2010

Synthesis and structural, magnetic, thermal, and transport properties of several transition metal oxides and arsenides

Supriyo Das
Iowa State University

Recommended Citation

Das, Supriyo, "Synthesis and structural, magnetic, thermal, and transport properties of several transition metal oxides and arsenides" (2010). *Graduate Theses and Dissertations*. 11194.
http://lib.dr.iastate.edu/etd/11194

Synthesis and structural, magnetic, thermal, and transport properties of several transition metal oxides and arsenides

by

Supriyo Das

A dissertation submitted to the graduate faculty
in partial fulfillment of the requirements for the degree of
DOCTOR OF PHILOSOPHY

Major: Condensed Matter Physics

Program of Study Committee:
David C. Johnston, Major Professor
Jörg Schmalian
Adam Kaminski
David Carter-Lewis
R. William McCallum

Iowa State University

Ames, Iowa

2010

DEDICATION

To my parents

TABLE OF CONTENTS

ACKNOWLEDGEMENTS

Firstly, I would like to thank my thesis advisor Dr. David C. Johnston for his constant guidance and support throughout the course of my PhD and also rigorously reading and correcting this thesis and the articles that I wrote.

I thank my committee members Dr. Jörg Schmalian, Dr. Adam Kaminski, Dr. David Carter-Lewis, and Dr. R. William McCallum for being in my committee and providing valuable suggestions regarding the improvement of this thesis.

I thank Dr. Asad Niazi for showing me how to operate the laboratory instruments. I also thank Asad, along with Dr. Yogesh Singh and Dr. Xiaopeng Zong for their help in various aspects of sample preparation and also putting up with me in the office for all these years.

I thank Dr. Andreas Kreyssig for his help and guidance during the high energy x-ray diffraction experiments and analyzing the diffraction data. I also thank Dr. Alan I. Goldman and Dr. Matthew J. Kramer for their help with the x-ray diffraction experiments.

Last but not the least, I thank my parents for all their support and encouragements with out which I couldn't have done this work. I dedicate this work to them.

Work at the Ames Laboratory was supported by the Department of Energy-Basic Energy Sciences under Contract No. DE-AC02-07CH11358.

CHAPTER 1. Introduction

Oxide compounds containing the transition metal vanadium (V) have attracted a lot of attention in the field of condensed matter physics owing to their exhibition of interesting properties including metal-insulator transitons, structural transitions, ferromagnetic and antiferromagnetic orderings, and heavy fermion behavior. Binary vanadium oxides V_nO_{2n-1} where $2 \leq n \leq 9$ have triclinic structures and exhibit metal-insulator and antiferromagnetic transitions.[1–6] The only exception is V_7O_{13} which remains metallic down to 4 K.[7] The ternary vanadium oxide LiV_2O_4 has the normal spinel structure, is metallic, does not undergo magnetic ordering and exhibits heavy fermion behavior below 10 K.[8] CaV_2O_4 has an orthorhombic structure[9, 10] with the vanadium spins forming zigzag chains and has been suggested to be a model system to study the gapless chiral phase.[11, 12] These provide great motivation for further investigation of some known vanadium compounds as well as to explore new vanadium compounds in search of new physics. This thesis consists, in part, of experimental studies involving sample preparation and magnetic, transport, thermal, and x-ray measurements on some strongly correlated eletron systems containing the transition metal vanadium. The compounds studied are LiV_2O_4, YV_4O_8, and YbV_4O_8.

The recent discovery of superconductivity in RFeAsO$_{1-x}$F$_x$ (R = La, Ce, Pr, Gd, Tb, Dy, Sm, and Nd), and AFe$_2$As$_2$ (A = Ba, Sr, Ca, and Eu) doped with K, Na, or Cs at the A site with relatively high T_c has sparked tremendous activities in the condensed matter physics community and a renewed interest in the area of superconductivity as occurred following the discovery of the layered cuprate high T_c superconductors in 1986. To discover more superconductors with hopefully higher T_c's, it is extremely important to investigate compounds having crystal structures related to the compounds showing high T_c superconductivity. Along with the vanadium oxide compounds described before, this thesis describes our investigations of magnetic, structural, thermal and transport properties of $EuPd_2Sb_2$ single crystals which have a crystal structure closely related to the $A\mathrm{Fe_2As_2}$ compounds and also a study of the reaction kinetics of the formation of $\mathrm{LaFeAsO}_{1-x}\mathrm{F}_x$.

1.1 Heavy fermion $\mathbf{LiV_2O_4}$

Heavy fermion materials are metallic materials where the current carriers behave as if their masses have been renormalized to $\sim 100 - 1000$ times the mass of a free electron. Most of the known heavy fermion compounds contain lanthanide or actinide atoms.[13] The mechanism of the heavy fermion formation in these compounds has been explained[14] using the Landau fermi liquid (FL) theory and the periodic Anderson model. According to the FL theory, the low level excitations (quasiparticles) of a system of interacting fermions are in a one-to-one correspondence with the excitations of the system without the interactions. As a result of the interactions, the effective mass of the quasiparticles is renormalized. For the case of the lanthanide or actinide heavy fermions, the localized f electrons of the lanthanide or actinide atoms at every lattice site are weakly hybridized with the itinerant s, p, and/or d electrons of other elements in the compound, resulting in screening of the f electron spins. This results in a large enhancement of the quasiparticle mass. The density of states at the Fermi energy $D(E_\mathrm{F})$ and the mass m^* of the quasiparticles can be obtained from heat capacity measurements. The Sommerfeld coefficient γ, which is the coefficient of the linear term of the expansion of the electronic heat capacity in temperature T, is related to m^* and $D(E_\mathrm{F})$ by the equations

$$\gamma(T=0) = \frac{\pi^2 k_\mathrm{B}^2}{3} D(E_\mathrm{F}), \tag{1.1}$$

$$D(E_\mathrm{F}) = \frac{m^* k_\mathrm{F} V}{\pi^2 \hbar^2}, \tag{1.2}$$

where k_B is Boltzmann constant, k_F is the Fermi wave vector, which in a single-band model is $k_\mathrm{F} = (3\pi^2 N_\mathrm{e}/V)^{1/3}$, N_e is the number of conduction electrons, V is the volume of the system, and $E_\mathrm{F} = \hbar^2 k_\mathrm{F}^2/(2m^*)$. Large quasiparticle masses $\sim$ 100–1000 times that of the free electron mass have been obtained from $\gamma(0)$. The magnetic susceptibility χ follows the Curie-Weiss law depicting local moment behavior at high temperatures and becomes mostly T independent with a large value in the low temperature heavy fermion regime where the local moment spins are screened by the conduction electron spins. The normalized ratio of $\gamma(0)$ and $\chi(0)$, called the Sommerfeld-Wilson ratio ($R_{\rm W}$), is given as

$$R_{\rm W} = \frac{\pi^2 2 k_{\rm B}^2 \chi(0)}{3\mu_{\rm eff}^2 \gamma(0)}, \tag{1.3}$$

where $\mu_{\rm eff}$ is the effective magnetic moment. For f-electron heavy fermion compounds, $R_{\rm W} \sim 2$ is of the order of unity as is typical for metals. Another universal relationship for the heavy fermion compounds is the Kadawaki-Wood's ratio[15] which is the ratio A/γ^2 where A is the coefficient of the T^2 term in the expansion of the resistivity ρ in T. For the f-electron heavy fermion compounds, that ratio $\sim 1.0\times10^{-5}$ $\mu\Omega$ cm (mol K^2)^2/(mJ)^2.

$\mathrm{LiV_2O_4}$ is a very special material as it shows heavy fermion behavior below 10 K in spite of being a d-electron metal.[8] This is very unusual because, unlike the f-orbitals, the d-orbitals have a large spatial extent and as such a much larger hybridization with the conduction electrons. $\mathrm{LiV_2O_4}$ has a face-centered-cubic crystal structure with space group $Fd\bar{3}m$. Figure 1.1 shows the crystal structure of $\mathrm{LiV_2O_4}$. It is a “normal” spinel structure with the vanadium atoms coordinated with six O atoms to form a slightly distorted octahedron. The edge-sharing $\mathrm{VO_6}$ octahedra form a three-dimensional network containing channels along the [110] directions. The Li atoms lie in these channels. The V atoms themselves form corner sharing tetrahedra, often called the “pyrochlore lattice”, which is strongly geometrically frustrated for antiferromagnetic ordering. Figure 1.2 shows the vanadium sublattice within the spinel structure.

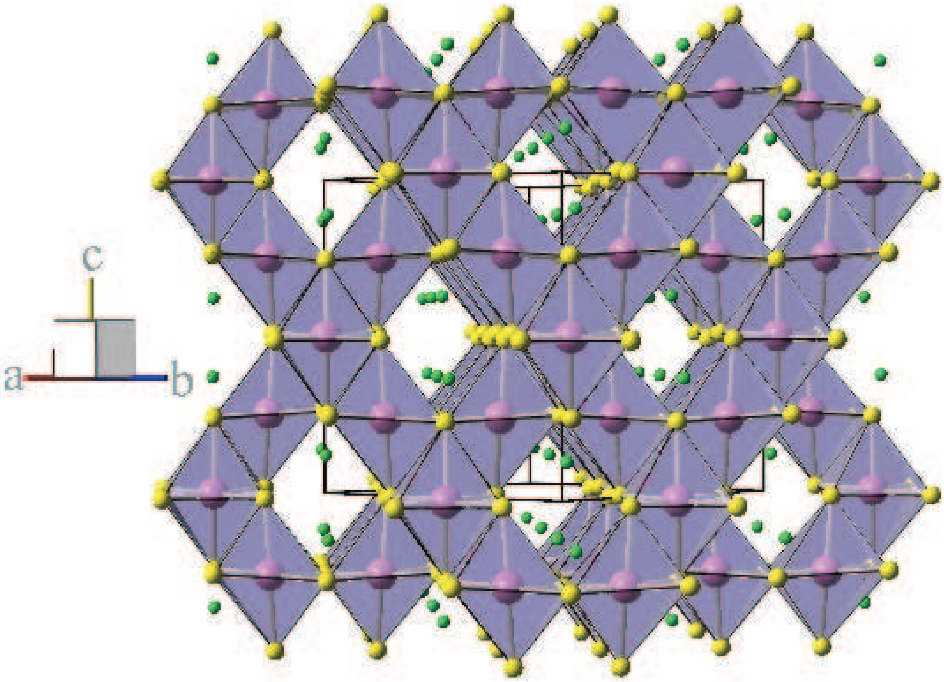

Figure 1.1 Crystal structure of LiV_2O_4. It is a normal spinel structure with the vanadium atoms coordinated to six O atoms that form a slightly distorted octahedron. The edge-sharing VO_6 octahedra form a three-dimensional network forming channels along the [110] directions. The Li atoms lie in these channels. In the figure, small, medium, and large spheres represent Li, O, and V atoms, respectively.

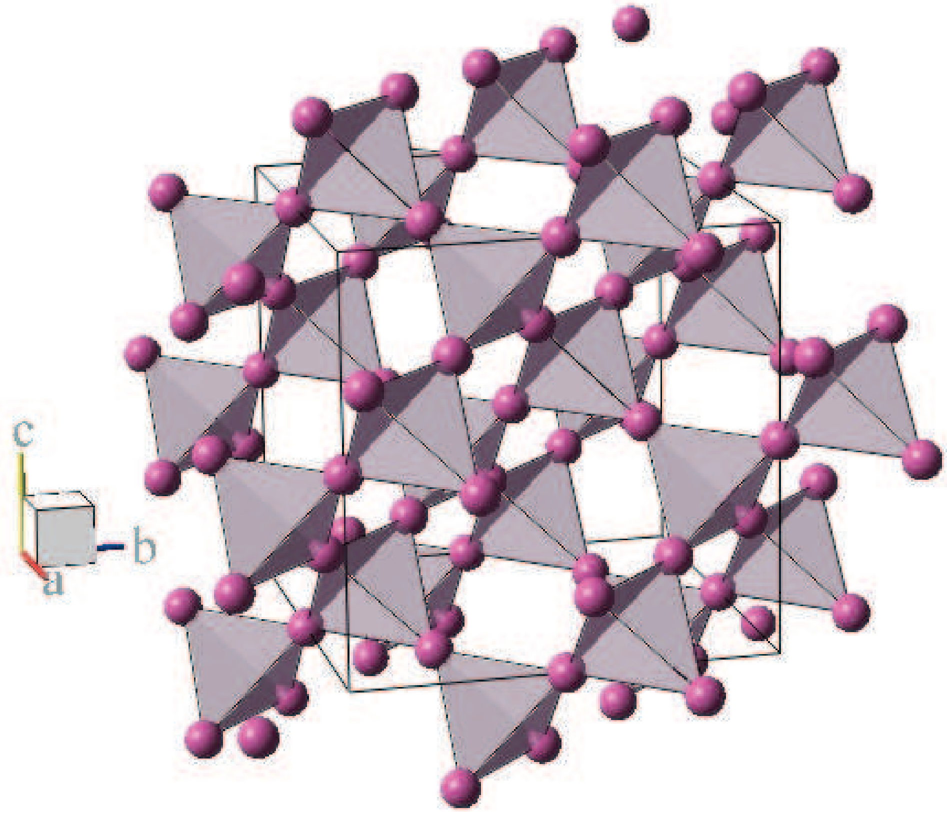

Figure 1.2 The vanadium sublattice in the spinel structure of LiV_2O_4. The vanadium atoms form a three-dimensional network of corner-sharing tetrahedra. The interaction between the vanadium spins is antiferromagnetic and thus antiferromagnetic ordering of the V spins is geometrically frustrated.

The vanadium atoms with nominal oxidation state of +3.5 and occupying equivalent sites in the structure make LiV_2O_4 metallic. The heavy fermion nature of LiV_2O_4 was discovered to occur from measurements of a large temperature-independent magnetic susceptibility $\chi \sim 0.01$ cm^3/mol and a large Sommerfeld coefficient $\gamma \sim 420$ mJ/mol K^2 below 10 K.[8] A sharp peak was observed in photoemission experiments just above the Fermi energy with a shape and temperature dependence very similar to those for f-electron heavy fermion compounds.[16]

There have been attempts to explain the heavy fermion behavior in LiV_2O_4 as analogous to that observed in the f-electron materials. The octahedral coordination of the O atoms around V atoms in LiV_2O_4 splits the $3d$ orbitals into three low-lying degenerate $t_{2\mathrm{g}}$ orbitals and two degenerate e_{g} orbitals that are 2 eV above the $t_{2\mathrm{g}}$ orbitals. The weak trigonal component of the crystal field arising from a slight elongation of the O_6 octahedra around the V atoms in the [111] directions splits the three degenerate $t_{2\mathrm{g}}$ orbitals into a lower nondegenerate $A_{1\mathrm{g}}$ orbital and two upper degenerate E_{g} orbitals. It has been proposed[17] that of 1.5 d electrons per V atom, one is localized in the $A_{1\mathrm{g}}$ orbital while the other 0.5 d electron per V atom partially fills the E_{g} orbitals to form a conduction band. This model matches the scenario for that in case of the f-electron heavy fermions. Now, there are two kinds of interactions present here. One is the on-site Hund's ferromagnetic coupling between the conduction electrons and the vanadium local moments. The other is the antiferromagnetic Kondo exchange coupling between the local moments and the spin of the conduction electron on neighboring sites. The above theory does not provide an explanation about how the strong ferromagnetic coupling is cancelled by the antiferromagnetic coupling to give a net antiferromagnetic behavior observed in the high-temperature magnetic susceptibility.[18]

There are also arguments in favor of the strong frustration[19] and mixed valence on the pyrochlore lattice[20] being the cause of the heavy fermion behavior. The vanadium spins in the lattice are strongly magnetically frustrated which prevents the system to order magnetically. There is no structural transition to lift the frustration.[8, 21] Yasufumi and co-workers[22] argued that spin-orbital fluctuations are responsible for the enhancement of the quasiparticle mass in LiV_2O_4. The spinel structure and strong short-range correlations between the d

electrons have been proposed by Fulde and co-workers[23] as the driving mechanism behind the heavy fermion behavior. Arita et al. [18] found from their calculations that the A_{1g} orbital in LiV_2O_4 is a lightly hole-doped Mott insulator (orbital-selective Mott insulator). They proposed that the mass of the quasiparticles is heavily enhanced because of the nearness to a doping-controlled Mott-Hubbard transition. However, there is still no consensus on the mechanism of heavy fermion behavior of LiV_2O_4.

1.1.1 Magnetic defects in LiV_2O_4

Magnetic defects present within the spinel structure have a pronounced effect on the properties of LiV_2O_4. The magnetic susceptibility of a LiV_2O_4 sample containing a high ($\lesssim$ 0.8 mol%) magnetic defect concentration shows a Curie-like upturn rather than becoming temperature independent at low temperatures.[24] The ^{7}Li nuclear spin-lattice relaxation rate $1/T_1$ of samples of LiV_2O_4 containing magnetic defects shows a peak at temperature ~ 1 K.[25] For magnetic defect-free samples, $1/T_1$ is proportional to T at low temperature (the Korringa law) which is typical for Fermi liquids. These observations raise the question whether the ground state of a LiV_2O_4 sample containing magnetic defects is still a Fermi liquid or is a non-Fermi liquid. If the ground state changes to a non-Fermi liquid, then there might be a critical defect concentration for the transition. Previously, LiV_2O_4 samples have been prepared with magnetic defect concentrations $n_{\rm defect}$ ranging from a low of 0.01 mol% to a high of 0.6 mol%.[24] $n_{\rm defect}$ and the spin of the magnetic defects S were found by analyzing the magnetization (M) versus magnetic field (H) isotherms at low temperatures $1.8 \leq T \lesssim 5$ K.[24] Large values of S ranging from 3–6 were obtained consistently from the M versus H measurements. Such large spin values suggest that the magnetic defects consist of more than one spin, or form a cluster of spins.

Johnston et al.[25] proposed a microscopic model which explains the large values of the spins of the magnetic defects. The only source of the magnetic defects is the crystal defects and a crystal defect can lift the geometric frustration of the spins around a small region around it. This allows a condensation of dynamic magnetic order in a finite region around the defect.

The condensation of spins around the defect forming a droplet explains the large values of the spins of the magnetic defects observed experimentally.

Zong and co-authors[26] performed extensive NMR measurements on samples of LiV_2O_4 with varying magnetic defect concentrations. Their experimental observations could be well explained by a model in which the magnetic defects are point-like and randomly distributed in the lattice. The assumptions behind the model are that the Fermi liquid still survives in LiV_2O_4 samples with high magnetic defect concentrations and that the properties of the Fermi liquid and the magnetic defects are separable.

1.1.2 Phase relations in the Li_2O-V_2O_3-V_2O_5 ternary system

To study the magnetic defects in detail, we need samples of LiV_2O_4 with varying concentrations $n_{\rm defect}$ of these defects. An important observation reported earlier was that there was a dependence of $n_{\rm defect}$ of samples of LiV_2O_4 on small amounts of impurity phases present in the sample.[24] It was observed that there was a sharp low-temperature Curie-like upturn in the susceptibility of a LiV_2O_4 sample containing a small amount of V_2O_3 as impurity phase and the analysis of the M versus H isotherms at low T yielded a large value of $n_{\rm defect}$. On the other hand, a sample with a small amount of V_3O_5 as impurity phase, the magnetic susceptibility was almost temperature independent at low temperature and the M versus H data yielded an extremely small value of $n_{\rm defect}$. From consideration of the magnetic susceptibilities of the impurity phases,[24, 27, 28] it was clear that the observed magnetic susceptibilities were intrinsic to LiV_2O_4 phase in the different samples. This motivated us to carry out a detailed phase relation analysis of LiV_2O_4 with other compounds which exist in equilibrium with it in the ternary phase diagram Li_2O-V_2O_3-V_2O_5, as described in Ch. 3 of this thesis. We mapped out the detailed phase relations in the Li_2O-V_2O_3-V_2O_5 ternary system in the vicinity of the LiV_2O_4 composition. From this study we proposed a model of formation of magnetic defects in LiV_2O_4.

1.1.3 Single crystal growth of LiV_2O_4

In addition to polycrystalline samples, high quality single crystals of LiV_2O_4 both magnetic defect free and containing magnetic defects would help resolve the question of the nature of the magnetic defects and also shed light on the mechanism for heavy fermion behavior in the pure material. Unfortunately, crystal growth reports of LiV_2O_4 are very rare. LiV_2O_4 melts incongruently and thus simply melting and resolidifying a polycrystalline sample of LiV_2O_4 will not produce crystals.

LiV_2O_4 crystals were previously grown by hydrothermal reaction of $LiVO_2$ and VO_2 in aqueous solutions 1N in LiOH sealed in gold tubes and heated to 500–700 °C under a pressure of 3 kbar for $\sim$ 24 hr.[29] Octahedra-shaped crystals were obtained that were $\sim$ 0.75 mm on an edge. Electrical resistivity measurements demonstrated for the first time that LiV_2O_4 is metallic down to a temperature T of at least 4 K, with a room temperature resistivity of 300 to 800 $\mu\Omega$ cm depending on the crystal.[29] Electrical resistivity measurements of magnetically pure LiV_2O_4 single crystals using crystals grown by this technique were recently reported[30, 31] down to 0.3 K revealing a T^2 dependence between 0.3 and $\sim$ 2 K as expected for a Fermi liquid. Heat capacity (C) measurements on these crystals yielded an extrapolated zero-temperature C/T value of 350 mJ/mol K^2 which was comparable to the value of $C/T \sim 430$ mJ/mol K^2 previously obtained at 1 K from measurements on polycrystalline samples.[8, 32] More recently, the first flux growth of single crystals of LiV_2O_4 was reported using $LiCl - Li_2MoO_4 - LiBO_2$ as the flux.[33] The crystals were reported to be of high quality but extremely reactive to air and/or moisture.[33]

From our study of the phase relations of the Li_2O-V_2O_3-V_2O_5 ternary system, we discovered a new flux which we used to grow high quality single crystals of LiV_2O_4, as described in Ch. 4 of this thesis. Our crystals had a maximum size of $\sim$ 2 mm on a side and did not show any reactivity towards air or moisture. We carried out magnetic, thermal, transport, x-ray, and NMR measurements on the crystals. From the magnetic susceptibility and magnetization measurements, we found that most of the crystals had magnetic defects in the structure with the defect concentration ranging from 0.2 mol% to 0.6 mol%. However, others with a different growth morphology showed extremely small $n_{\mathrm{defect}} \lesssim 0.01$ mol%.

1.1.4 High energy x-ray diffraction of LiV$_2$O$_4$ single crystals

Given the pronounced effects of the magnetic defects on the properties of LiV$_2$O$_4$, it is very important to examine if there are any periodic correlations in the distribution of the crystal defects which produce the magnetic defects or if they are randomly distributed. In particular, it will of great importance to investigate if there are short-range correlations among the magnetic defect spins as suggested by the droplet model in Ref. [25]. If we assume that a single crystal defect gives rise to a single magnetic defect, then the concentrations of crystal defects are too small ($<$ 0.8 mol%) to produce any observable change in the intensities of x-ray Bragg reflections. One way to look for such small effects is to map out complete reciprocal planes and search for features in addition to the normal Bragg reflections. Any long-range periodicity of the crystal defects would produce additional peaks in the x-ray diffraction patterns, and short-range ordering would cause streaking of the Bragg peaks. In Ch. 5, our high-energy x-ray diffraction study on our single crystals is described that was carried out to address these questions.

1.2 High pressure powder x-ray diffraction on LiV$_2$O$_4$ crystals

There have been suggestions in the literature of a possible structural phase transition under pressure in LiV$_2$O$_4$. Powder x-ray diffraction patterns obtained under increasing pressure and at a fixed temperature of 10 K showed a splitting of the single (440) cubic peak into two rhombohedral peaks at 12.8 GPa.[34] It was also observed that as the temperature was raised keeping the pressure constant at 12.8 GPa, the split peaks recombine into a single peak above 200 K.[34] Anomalies in NMR measurements were also observed under pressure up to 4.74 GPa. ^{7}Li NMR measurements in LiV$_2$O$_4$ under high pressure revealed an increase in the ^{7}Li nuclear spin-lattice relaxation rate $1/T_1$ at 4.74 GPa below 10 K.[35] Recently, extended x-ray absoption fine structure analysis suggested a cubic-to-rhombohedral structural transition above 12 GPa at room temperature.[36] To determine the high pressure structure, we carried out preliminary powder x-ray diffraction measurements at room temperature and at high pressure up to 24.5 GPa, as described in Ch. 6 of this thesis. These measurements were carried out at the Advanced Photon Source at Argonne National Laboratory in collaboration with M. Abliz and G. Shen. Additional high-pressure x-ray diffraction measurements of the structure are planned.

1.3 Magnetic, and thermal properties of the mixed valent vanadium oxides YV_4O_8 and LuV_4O_8

Geometric frustration often leads to exotic magnetic ground states in materials. As mentioned above, the unusual heavy fermion behavior in the three-dimensional normal-spinel LiV_2O_4 could be due to the strong geometrical frustration experienced by the vanadium spins. Frustration also plays a major role in altering the properties of low-dimensional spin chains with antiferromagnetic interactions. A spin $S = 1$ one-dimensional chain with antiferromagnetic (AF) nearest-neighbor (NN) interactions (J_1) shows a finite energy gap ("Haldane gap") between the ground state and the lowest excited magnetic states. However, when a next-nearest-neighbor (NNN) AF interaction is introduced, the low-temperature magnetic properties show different behaviors. Theoretical calculations have shown that for a one-dimensional spin $S = 1$ chain with antiferromagnetic nearest-neighbor interaction J_1 and frustrating next-nearest-neighbor antiferromagnetic interaction J_2, the magnetic ground state shows gapped or gapless chiral ordering depending on the the anisotropy of the spin chain being XY or XXZ and on the ratio J_2/J_1.[37–39] The system does not show any long-range ordering of the spins.

The frustrated spin $S = 1$ chain system with NN and NNN interactions discussed above is realized[11, 12] in the compound CaV_2O_4 which forms in the well-known $CaFe_2O_4$ structure. The V atoms have spin $S = 1$ and form a zigzag chain with antiferromagnetic nearest- and next-nearest-neighbor interactions. The crystal structure is shown in Figs. 1.3 and 1.4. The V atoms occupy two inequivalent sites to form two sets of V zigzag chains running along the *c*-axis. The Ca atoms are located in between these chains. The system undergoes an orthorhombic to monoclinic structural distortion at a sample-dependent $T_S \approx 108 - 145$ K and an antiferromagnetic transition with noncollinear spin structure at a sample-dependent $T_{\rm N} \approx 50 - 70$ K.[40–42] A peak in the heat capacity versus temperature at $T \sim 200$ K has been observed which might be the long-sought chiral phase transition. A detailed study involving synthesis of polycrystalline and single crystal samples of CaV_2O_4, and investigation of magnetic, structural, and thermal properties of the samples, is given in Appendix A of this thesis. I actively participated in the structural study of the single crystals which revealed the mentioned structural distortion. However, since the present author was not the primary author of this work, the description of this research is placed into an appendix.

Replacing Ca^{2+} in CaV_2O_4 by Na^{+1} which makes V mixed valent, the same $CaFe_2O_4$ structure is retained but the system becomes metallic even below the antiferromagnetic transition at 140 K.[43, 44] These and the above results on CaV_2O_4 motivated us to carry out further investigations of compounds having the same or similar $CaFe_2O_4$ structure in search of novel physics.

The compounds LV_4O_8 (L = Yb, Y, Lu) are nearly isostructural with $CaFe_2O_4$ with the modification that in LV_4O_8, only half of the L cation sites are occupied by L ions.[45] The L site vacancies are ordered, resulting in a decrease in the lattice symmetry from orthorhombic to monoclinic. YbV_4O_8 forms in two phases, the low temperature α-phase and the high temperature β-phase. At 185 K the β-YbV_4O_8 undergoes a magnetic phase transition with the vanadium spins separating into two classes that show Curie-Weiss type and spin-gap type behaviors, respectively. The magnetic transition is accompanied by a monoclinic to monoclinic structural phase transition at the same temperature which leads to complete charge ordering of the V^{+3} and V^{+4} ions.[46] YV_4O_8 also exists in α and β forms similar to YbV_4O_8. The magnetic susceptibilties of α-YV_4O_8 and β-YV_4O_8 show Curie-Weiss behavior in the high T region and drop sharply at temperatures between 50 and 80 K.[47] For α-YV_4O_8, the drop at 50 K suggests a first-order transition. This is very different from the magnetic susceptibility of the isostructural YbV_4O_8[46] or similiarly structured CaV_2O_4.[40, 41] This unusual magnetic susceptibility provided us with a strong motivation to further study this class of materials and the results are described in Ch. 7 of this thesis.

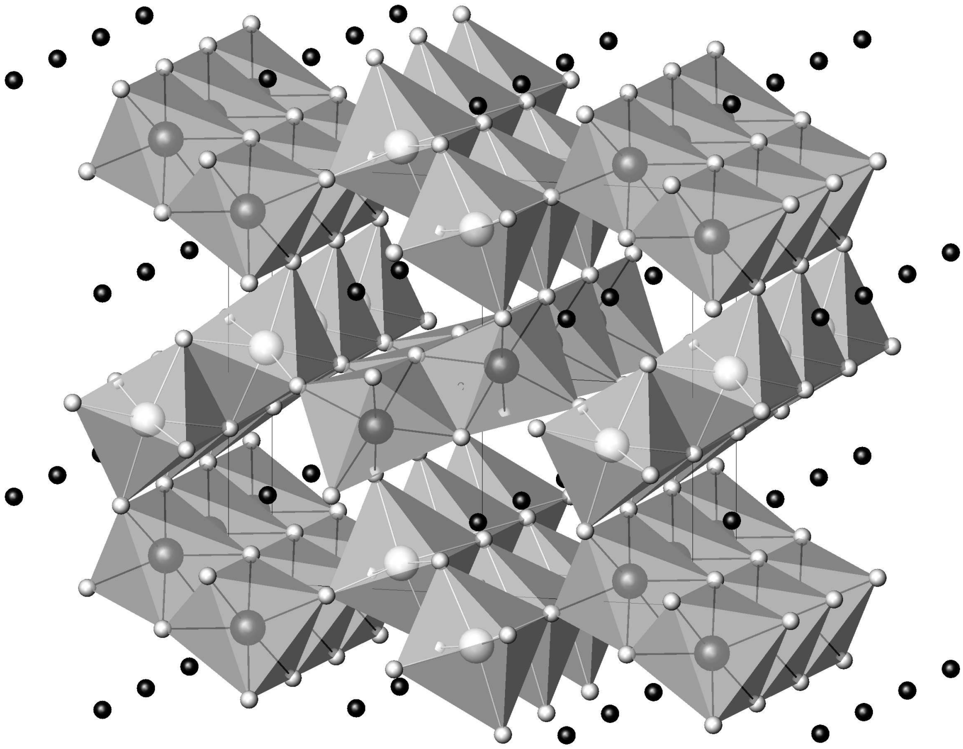

Figure 1.3 Inclined view along the *c*-axis of the crystal structure of CaV_2O_4. The VO_6 octahedra form zigzag chains running along the *c*-axis.

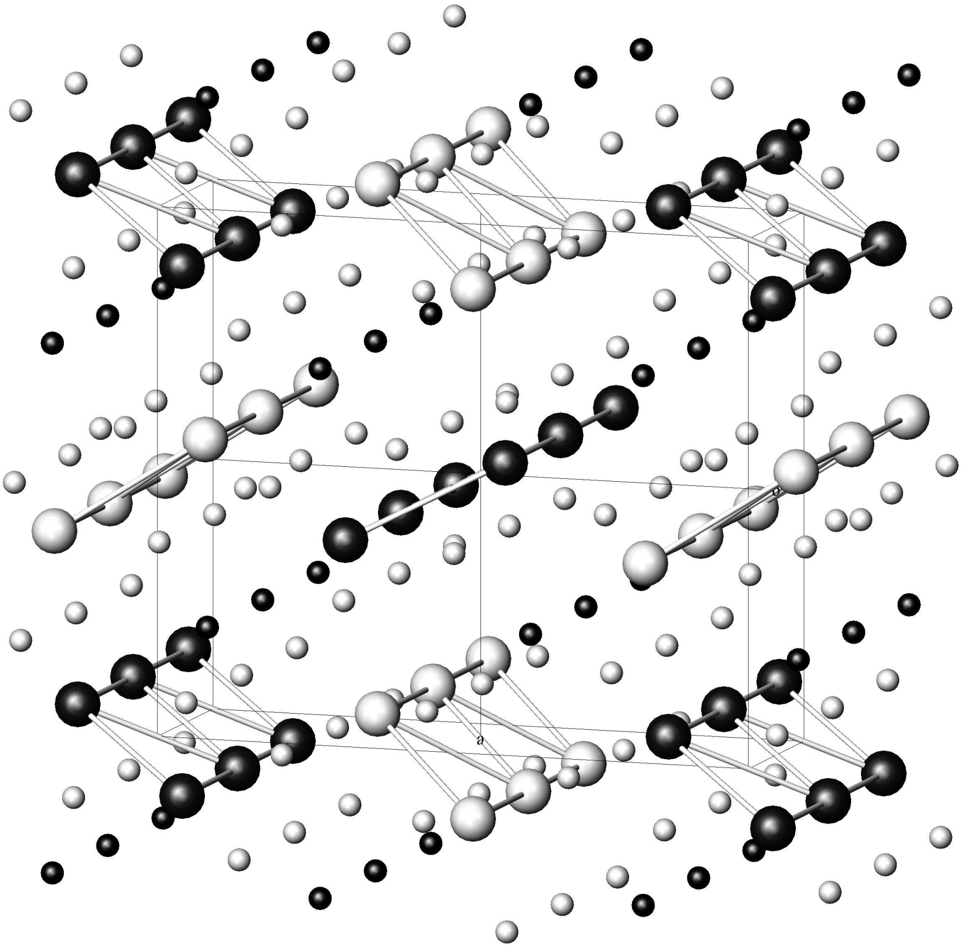

Figure 1.4 The V zigzag chains running along the c-axis in CaV_2O_4. There are two crystallographically inequivalent types of V atoms that reside in two inequivalent zigzag chains, respectively.

1.4 Iron Pnictide high T_{c} supercondctors

The recent discovery of high-temperature superconductivity in $R\mathrm{FeAsO}_{1-x}\mathrm{F}_x$ ($R =$ La, Ce, Pr, Nd, Sm, Gd, Tb, and Dy)[48–53] compounds with superconducting transition temperatures T_{c} as high as 56 K has sparked a lot of interest in the search for new superconductors. These materials crystallize in the tetragonal ZrCuSiAs-type structure with space group $P4/nmm$.[54] The structure consists of alternating FeAs and RO layers stacked along the crystallographic c axis. The parent componds RFeAsO exhibit a spin density wave (SDW) at $\sim 100-200$ K.[50, 55, 56] Upon doping with F, the SDW gets suppressed and superconductivity sets in.[49–53, 55, 57]

One of the biggest challenges in studying the properties of the $R\mathrm{FeAsO}_{1-x}\mathrm{F}_x$ compounds was the difficulty in preparing single phase high quality samples needed to study the intrinsic properties of these materials. The samples reported were made at high temperatures T $\sim$ 1100 °C and usually contained impurity phases along with the $R\mathrm{FeAsO}_{1-x}\mathrm{F}_x$ phase. I actively participated in a study of the reaction kinetics of the formation of $\mathrm{LaFeAsO}_{1-x}\mathrm{F}_x$. This x-ray diffraction study was carried out at the Advanced Photon Source at Argonne National Laboratory in collaboration with a large group of researchers at Iowa State University. The measurements were carried out using real-time high-energy x-ray diffraction on powder samples of the starting materials as they were heated. The details of the experimental procedure and results are described in Ref. [58].

Soon after the discovery of the $R\mathrm{FeAsO}_{1-x}\mathrm{F}_x$ compounds, another group of structurally related compounds with the chemical formula $A\mathrm{Fe}_2\mathrm{As}_2$ ($A =$ Ca, Sr, Ba, and Eu) was discovered to show superconductivity. The $A\mathrm{Fe}_2\mathrm{As}_2$ compounds crystallize in the tetragonal $\mathrm{ThCr}_2\mathrm{Si}_2$-type structure with space group $I4/mmm$ (No. 139) and the structure consists of alternating FeAs and A layers stacked along the c axis. In the FeAs layers, the Fe atoms form a square planar lattice. The $A\mathrm{Fe}_2\mathrm{As}_2$ compounds also show SDW and structural transitions at $\sim 100-200$ K[59–68] which are suppressed upon doping with K, Na, or Cs at the A site and superconductivity then sets in, with a maximum T_{c} of 38 K.[69–72]

In both classes of compounds described above, FeAs layers that are stacked along the c

axis seem to be the key chemical and structural element behind these compounds being superconductors with relatively high T_c. This gives us a strong motivation to investigate similarly structured compounds in a search for more parent compounds for high T_c superconductors.

The compound $EuPd_2Sb_2$ crystallizes in the $CaBe_2Ge_2$-type structure with space group $P4/nmm$ (space group number 129).[73] The structure is closely related to the $A$$Fe_2As_2$ structure. Alternating PdSb and Eu layers are stacked along the c axis, similar to the $A$$Fe_2As_2$ structure. However, there is a significant difference between the two structures. The PdSb layers are of two types. In one type, Pd atoms are arranged in a square planar lattice with two Sb sublayers on either side of the Pd layer, similar to the FeAs layers. In the other layer type, Pd and Sb switch positions. We synthesized single crystals of $EuPd_2Sb_2$ and studied their physical properties via magnetic susceptibility, magnetization, specific heat, and electrical transport measurements, as described in Ch. 8 of this thesis.

Powder X-ray diffraction measurements at room temperature reported in this thesis were done using a Rigaku Geigerflex diffractometer with Cu $K\alpha$ radiation. Temperature-dependent powder X-ray diffraction studies were done using a standard Rigaku TTRAX diffractometer system equipped with a theta/theta wide-angle goniometer and a Mo $K\alpha$ radiation source. Single crystal X-ray diffraction measurements were done using a Bruker CCD-1000 diffractometer with Mo K_α ($\lambda = 0.71073$ Å) radiation. High-energy X-ray diffraction measurements at room temperature were performed at the 6-ID-D station in the MU-CAT sector of the Advanced Photon Source, Argonne National Laboratory. Differential thermal analysis experiments were carried out using a Perkin-Elmer differential thermal analyzer (DTA-7). A Quantum Design Magnetic Property Measurement System (MPMS) was used for magnetization and magnetic susceptibility measurements. The theory of operation of the SQUID magnetometer is given in the Ph.D. thesis of Jullienne Hill.[74] Electronic transport and heat capacity measurements were done using a Quantum Design Physical Property Measurement System (PPMS). For resistivity and Hall coeffcient measurements, platinum or gold leads were attached to the samples using silver epoxy or spot welding. Standard AC four probe method was used for resistivity measurements, while, Hall coefficient measurements were carried out using the five-wire configuration supported by the PPMS. A description of the heat capacity measurement technique and analysis is described in Ch. 2.

CHAPTER 2. Heat capacity measurements using a Quantum Design Physical Property Measurement System (PPMS)

2.1 Introduction

Heat capacity at constant presssure C, electrical resistivity ρ, and Hall coefficient $R_{\rm H}$ versus temperature T measurements from 1.8–300 K were done using a Quantum Design PPMS. $C(T)$, $\rho(T)$, and $R_{\rm H}$ were measured in magnetic fields H ranging from 0–9 T. The Quantum Design PPMS measures the heat capacity of a sample using a thermal relaxation method.[75] The model employed in extracting the heat capacities of samples from the measurement data involves fitting the temperature response of the sample during both a heating period and a cooling period.[76] The Quantum Design PPMS heat capacity instrument and technique have been reviewed extensively.[77, 78] Here, we present a brief description of the heat capacity measurement process and our experimental results on the heat capacity measurements of a high purity copper standard.

2.2 Experimental setup and measurement process

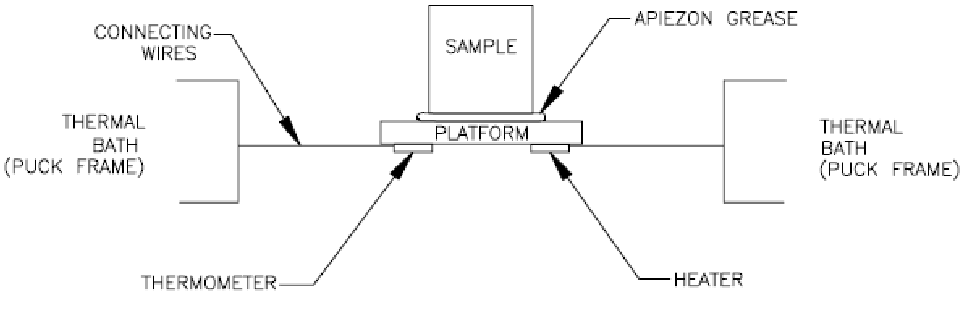

Figure 2.1 Schematic of the thermal connections to sample and sample platform in a PPMS heat capacity measurement. (Reproduced from the Quantum Design Heat Capacity Option Manual.[75])

Figure 2.1 shows the schematic of the PPMS heat capacity puck with the thermal connections to sample and sample platform. The components include a copper puck frame, a sample platform in the middle, and a copper cap (not shown in the figure) attached to the frame which encloses the sample platform with the sample on it. The sample platform is connected to the frame (which acts as a thermal bath) via eight platinum wires which also provide electrical connections to the platform and hold the platform in place. The temperature of the puck frame is measured using a 1050 Cernox thermometer. The platform has a $\mathrm{RuO_2}$ heater and a 1050 Cernox thermometer attached to its lower side as shown in Fig. 2.1. The sample is placed on the platform with a thin layer of Apiezon N thermal grease between the sample and the platform providing the required thermal contact between them. Heat capacity measurements are carried out in high vacuum to ensure that heat flow between the sample platform and the thermal bath takes place only through the platinum wires.

The determination of the heat capacity of each sample involves two separate measurements. First the heat capacity of the addenda, i.e., the sample platform plus the thermometer, heater, and the thermal grease on it, is measured. Second the heat capacity of the sample plus the addenda is measured. The heat capacity of the sample is obtained by subtracting the previously determined heat capacity of the addenda from the heat capacity of the sample plus addenda.

To do a heat capacity measurement at a temperature T_0 (of the puck frame), a heating/cooling sequence is applied as shown in Fig. 2.2. These data are analyzed as described in the following section to obtain the heat capacity at T_0.

2.3 Analysis of the thermal relaxation data

2.3.1 Introduction

Figure 2.3 shows the schematic of the heat flow model. The experimental setup involves a sample with unknown heat capacity C_{S} attached to the sample platform using Apiezon N grease which has a thermal conductance K_{G}. The sample platform, thermometer, heater, and N grease (the addenda) have a combined heat capacity C_{P}. Eight wires having a combined thermal conductance K_{W} connect the sample platform to a heat bath (the heat capacity puck

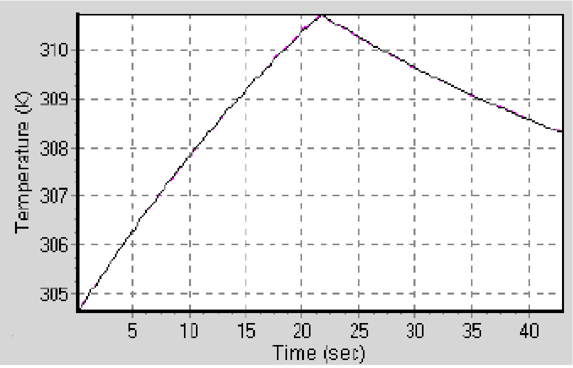

Figure 2.2 Typical temperature response of the sample platform obtained in a heat capacity measurement. A square heater power pulse is applied between times $t = 0$ and t_0 (here $t_0 \simeq 22$ s). (Reproduced from the Quantum Design Heat Capacity Option Manual.[75])

frame) maintained at a constant temperature T_0. A small heater attached to the sample platform supplies heat to the platform. With the heater supplying heat power $P(t)$ at time t to the platform, conservation of energy gives the coupled differential equations

$$P(t) = C_{\mathrm{P}} \, \frac{dT_{\mathrm{P}}(t)}{dt} + K_{\mathrm{G}}[T_{\mathrm{P}}(t) - T_{\mathrm{S}}(t)] + K_{\mathrm{W}}[T_{\mathrm{P}}(t) - T_0] \tag{2.1}$$

$$K_{\mathrm{G}}[T_{\mathrm{P}}(t) - T_{\mathrm{S}}(t)] = C_{\mathrm{S}} \, \frac{dT_{\mathrm{S}}(t)}{dt} \tag{2.2}$$

where $T_{\mathrm{P}}(t)$ and $T_{\mathrm{S}}(t)$ are the temperatures of the sample platform and the sample, respectively, at time t.

As the heater supplies a square pulse power of height P_0 and width t_0 to the sample platform, the temperature of the sample platform T_{P} first rises with time until time t_0 and then relaxes towards the bath temperature T_0 when the heater power is turned off. A typical temperature response of the sample platform obtained in the measurement is shown above in Fig. 2.2.

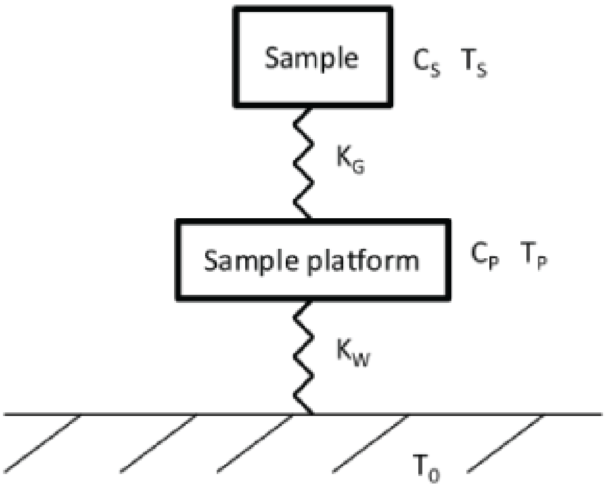

Figure 2.3 Shematic of the heat flow model used in the heat capacity measurement system. C_{S} and C_{P} are the heat capacities of the sample and the sample platform, respectively. T_{S}, T_{P}, and T_0 are the temperatures of the sample, sample platform and a constant temperature heat bath, respectively. K_{G} is the thermal conductance of the Apiezon N grease that attaches the sample to the sample platform, and K_{W} is the combined thermal conductance of the eight wires that attach the sample platform to the heat bath.

2.3.2 Simple model: $K_{\mathrm{G}} = \infty$

When the sample is in good thermal contact with the platform, one assumes $K_{\mathrm{G}} \to \infty$, which results in $T_{\mathrm{S}} = T_{\mathrm{P}}$. Under this condition, Eqs. (2.1) and (2.2) reduce to

$$C_{\mathrm{total}} \frac{dT_{\mathrm{P}}}{dt} = -K_{\mathrm{W}}(T_{\mathrm{P}} - T_0) + P(t) \tag{2.3}$$

where $C_{\mathrm{total}} = C_{\mathrm{S}} + C_{\mathrm{P}}$. The time dependence of this thermal relaxation of the platform-sample assembly is given by the solution of Eq. (2.3), which is[77]

$$T_{P\mathrm{on}}(t) = T_0 + \frac{P_0\tau}{C_{\mathrm{total}}}(1 - e^{-t/\tau}) \qquad (0 \leq t \leq t_0) \tag{2.4}$$

$$T_{P\mathrm{off}}(t) = T_0 + \frac{P_0\tau}{C_{\mathrm{total}}}(1 - e^{-t_0/\tau})e^{-(t-t_0)/\tau} \quad (t > t_0) \tag{2.5}$$

with initial conditions $T_{P\mathrm{on}}(0) = T_0$, $T_{P\mathrm{off}}(t_0) = T_{P\mathrm{on}}(t_0)$, where $T_{P\mathrm{off}}$ is the temperature of the sample platform with heater power $P = 0$, $T_{P\mathrm{on}}$ is the temperature of the sample platform with heater power $P = P_0$, and the time constant τ is given by

$$\tau = \frac{C_{\mathrm{total}}}{K_{\mathrm{W}}}. \tag{2.6}$$

During the sample heat capacity measurement, the temperature of the sample platform $T_{\rm P}$ versus time t is measured. The PPMS software then fits the relaxation ($T_{\rm P}$, t) data by Eqs. (2.4) and (2.5) using a nonlinear least-square fit alogorithm[76] to obtain the values of the unknowns $C_{\rm total} = C_{\rm S} + C_{\rm P}$, $K_{\rm W}$, and T_0. The addenda heat capacity $C_{\rm P}$ is obtained in a previous measurement without the sample. The heat capacity of the sample $C_{\rm S}$ is then obtained using $C_{\rm S} = C_{\rm total} - C_{\rm P}$. In the process mentioned above, only one relaxation described by τ takes place between the sample platform and the thermal bath due to the assumed perfect thermal contact of the sample and the sample platform. When measuring the heat capacity of the addenda, the software uses the simple model described above.

2.3.3 Two-tau model

When the thermal contact between the sample and the platform is not perfect, as is usually the case, then $T_{\rm S}(t) \neq T_{\rm P}(t)$. In this case, the solutions of Eqs. (2.1) and (2.2) obtained analytically are given by[77]

$$T_{P{\rm on}}(t) = T_0 + \frac{P_0}{K_{\rm W}} + \frac{P_0}{2\beta K_{\rm W}}\left[\frac{e^{t/\tau_2}}{\tau_1} - \frac{e^{t/\tau_1}}{\tau_2}\right] \qquad (0 \leq t \leq t_0) \tag{2.7}$$

$$T_{P{\rm off}}(t) = T_0 + \frac{P_0}{4\beta K_{\rm W}}\left[\frac{e^{-(t-t_0)/\tau_2}}{\tau_1} - \frac{e^{-(t-t_0)/\tau_1}}{\tau_2}\right]\left[2 - \frac{1}{\beta}\left(\frac{e^{-t_0/\tau_2}}{\tau_1} - \frac{e^{-t_0/\tau_1}}{\tau_2}\right)\right] \qquad (t > t_0) \tag{2.8}$$

for the time periods when the heater power is on and off, respectively (see Fig. 2.2), where

$$\tau_1 = \frac{1}{(\alpha - \beta)} \tag{2.9}$$

$$\tau_2 = \frac{1}{(\alpha + \beta)} \tag{2.10}$$

$$\alpha = \frac{K_{\rm G}}{2C_{\rm S}} + \frac{K_{\rm G} + K_{\rm W}}{2C_{\rm P}} \tag{2.11}$$

$$\beta = \frac{\sqrt{(C_{\rm P}K_{\rm G} + C_{\rm S}K_{\rm G} + C_{\rm S}K_{\rm W})^2 - 4C_{\rm P}C_{\rm S}K_{\rm W}K_{\rm G}}}{2C_{\rm P}C_{\rm S}}. \tag{2.12}$$

Now the temperature response involves two relaxation times τ_1 and τ_2. The relaxation time τ_2 is the faster relaxation time between the sample and the sample platform, while τ_1 is the slower relaxation time between the sample platform and the heat bath. With the value of $C_{\rm P}$ obtained from a measurement of the addenda, the PPMS software uses a nonlinear least square fit algorithm[76] to fit the $(t, T_{\rm P})$ relaxation data such as in Fig. 2.2 by Eqs. (2.7) and (2.8) to get the values of the unknowns $C_{\rm S}$, T_0, $K_{\rm W}$, and $K_{\rm G}$. If the deviation of the fit from the data using the two-tau model is smaller than that using the simple model, the software reports the values obtained using the two-tau model. Otherwise, the values obtained using the simple single-tau model are reported. If the fit to the data using the two-tau model does not converge, then also, the simple model is used. Such a divergence of the two-tau model fit parameters happens when the sample is perfectly attached to the platform (in which case the simple model is correct).

The software also reports a parameter Sample Coupling(%) $= 100 \times K_{\rm G}/(K_{\rm G} + K_{\rm W})$. During a heat capacity measurement of the addenda, a heat capacity measurement of a sample calculated using the simple single-tau model, and when the fit to the data using the two-tau model does not converge, the software reports the Sample Coupling to be exactly 100%, signifying that only the sungle-tau fitting method was used. For reliable measurements using the two-tau model, the Sample Coupling should be $> 90\%$ as mentioned by Quantum Design.

2.4 Heat capacity measurement of a copper standard

We measured the heat capacity of a copper (Puratronic, 99.999% pure, obtained from Alfa Aesar[79]) standard before measuring our samples in the PPMS. The sample was a 241.3 mg disk that was 5 mm in length and 0.125 in diameter. It was placed on the sample platform with one of its flat polished faces in thermal contact with the platform with Apiezon N grease. Figure 2.4(a) shows the heat capacity of the addenda $C_{\rm add}$ versus temperature T. Figure 2.4(b) shows the total heat capacity $C_{\rm total} = C_{\rm S} + C_{\rm add}$ versus T, where $C_{\rm S}$ is the sample heat capacity. Figure 2.4(c) shows $C_{\rm S}/C_{\rm total}$ versus T. Figure 2.4(d) shows the Sample Coupling versus T. Figures 2.5 and 2.6 show the measured high-T and low-T specific heat C versus T of the copper standard, respectively. The solid lines in Figs. 2.5 and 2.6 are the functions $C_{\rm fit} = \sum a_{\rm n}T^{\rm n}$ in the temperature range 30–300 K and 1.8–20 K representing the molar specific heat of copper reported in Refs. [80] and [81] at high-T and low-T, respectively. The insets in Figs. 2.5 and 2.6 show the percentage deviations $[C - C_{\rm fit}] \times 100/C$.

The accuracy of the measurement reported in Ref. [80] is 0.1% in the temperature range 30–300 K and the data were fitted by a polynomial which represented the data within 0.01% below 250 K and within 0.02% at 320 K. The accuracy reported in Ref. [81] is 0.5% for $T < 20$ K and the polynomial by which the data were fitted represented the data to within 0.01%. The maximum deviations of our measured data from the fitted polynomials in Refs. [80] and [81] are $< 1.5\%$ in the T range 30–300 K and $< 3\%$ for $T < 20$ K. Deviations up to 4% have been reported[78] below 4 K for the measured heat capacity of copper using the Quantum Design PPMS from a reference heat capacity function.[80–82] Around room temperature, a deviation of $< 1\%$ has been observed.[78] Our observations are consistent with these earlier observations. Quantum Design quotes a measurement accuracy $< 5\%$ in the temperature range 2–300 K with a “Typical” accuracy $< 2\%$.[83]

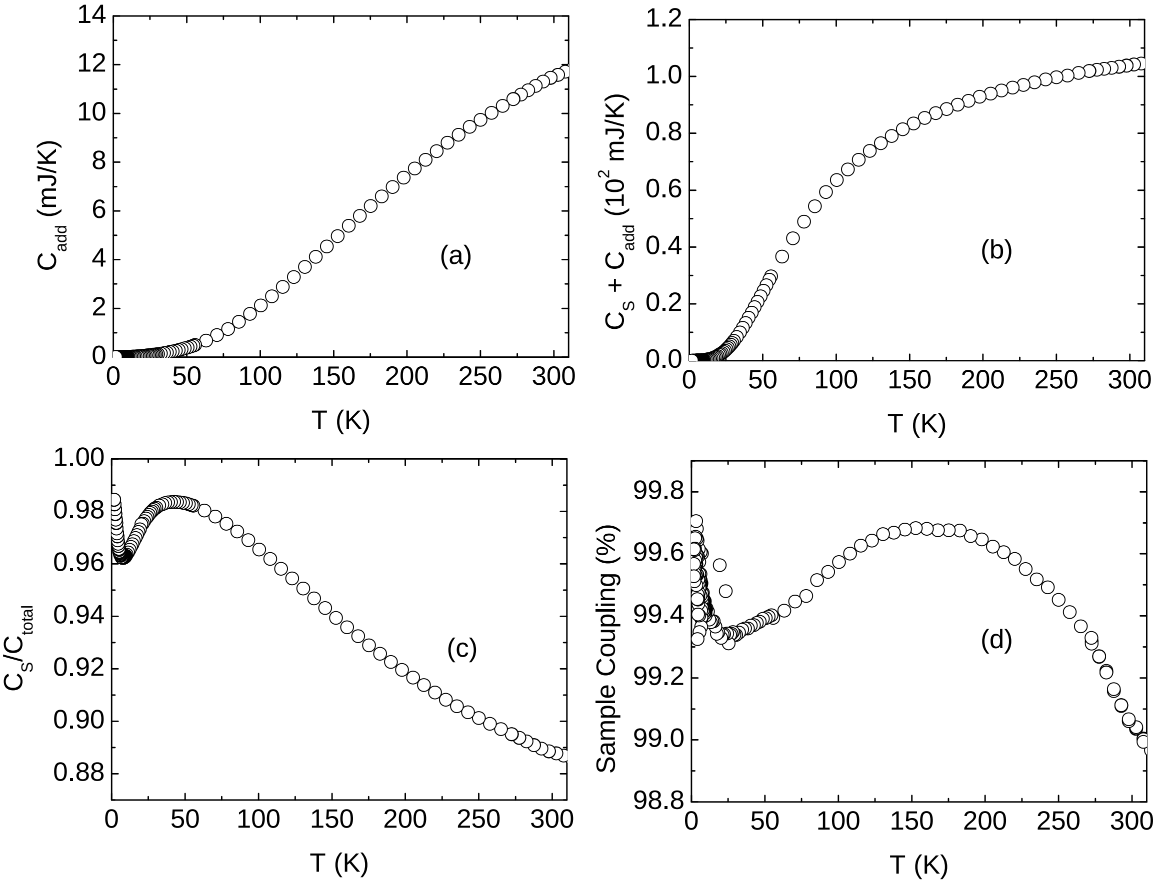

Figure 2.4 (a) The heat capacity of the addenda C_{add} versus temperature T. (b) The total heat capacity $C_{\text{total}} = C_{\text{S}} + C_{\text{add}}$ versus T, where C_{S} is the heat capacity of a copper standard. (c) The ratio $C_{\text{S}}/C_{\text{total}}$ versus T. (d) Sample Coupling parameter versus T.

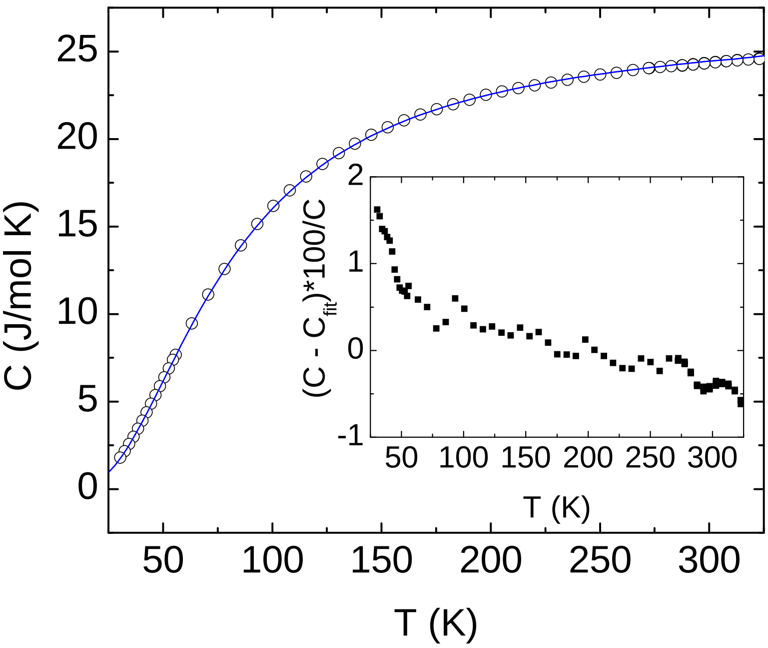

Figure 2.5 High temperature heat capacity C of a 243.1 mg copper standard. The solid line is a plot of $C^{\mathrm{high}}{}_{\mathrm{fit}} = \sum a_{\mathrm{n}} T^{\mathrm{n}}$ in the temperature range 30–300 K, where $C^{\mathrm{high}}{}_{\mathrm{fit}}$ is the accepted heat capacity of high purity copper in the temperature range 20–320 K.[80] The inset shows the percentage deviation $[C - C_{\mathrm{fit}}] \times 100/C$ versus T.

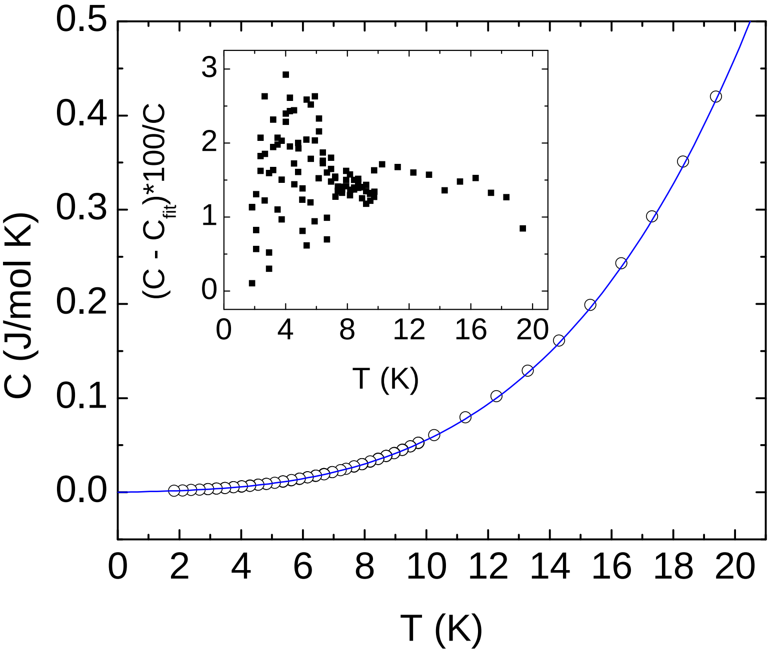

Figure 2.6 Low temperature heat capacity C of a 243.1 mg copper standard. The solid line is a plot of $C^{\rm low}{}_{\rm fit} = \sum a_{\rm n} T^{\rm n}$ in the temperature range 1.8–20 K, where $C^{\rm low}{}_{\rm fit}$ is the accepted heat capacity of copper below 30 K.[81] The inset shows the percentage deviation $[C - C_{\rm fit}] \times 100/C$ versus T.

CHAPTER 3. Phase Relations in the Li_2O-V_2O_3-V_2O_5 System at 700 °C: Correlations with Magnetic Defect Concentration in Heavy Fermion LiV_2O_4

This chapter is based on an article published in Phys. Rev. B **74**, 184417 (2006) by S. Das, X. Ma, X. Zong, A. Niazi, and D. C. Johnston.

Abstract

The phase relations in the Li_2O-V_2O_3-V_2O_5 ternary system at 700 °C for compositions in equilibrium with LiV_2O_4 are reported. This study clarified the synthesis conditions under which low and high magnetic defect concentrations can be obtained within the spinel structure of LiV_2O_4. We confirmed that the LiV_2O_4 phase can be obtained containing low (0.006 mol%) to high (0.83 mol%) magnetic defect concentrations $n_{\rm defect}$ and with consistently high magnetic defect spin S values between 3 and 6.5. The high $n_{\rm defect}$ values were obtained in the LiV_2O_4 phase in equilibrium with V_2O_3, Li_3VO_4, or $LiVO_2$ and the low values in the LiV_2O_4 phase in equilibrium with V_3O_5. A model is suggested to explain this correlation.

3.1 Introduction

Heavy fermion (HF) behavior has mostly been seen in f-electron metals. Such compounds are called heavy fermions because in these materials the current carriers behave as if they have a large mass ($\sim 10^2$–10^3 times the free electron mass). LiV_2O_4, first synthesized by Reuter and Jaskowsky,[84] is one of the few d-electron compounds to show HF behaviour at low temperatures.[8, 85] LiV_2O_4 has the face-centered-cubic spinel structure with the space group $Fd\bar{3}m$. The V atoms are coordinated by six O atoms in slightly distorted octahedron. The Li atoms are coordinated with four O atoms in a tetrahedron. The Li atoms are located in the gaps between chains of the VO_6 edge-sharing octahedra. From NMR measurements done on LiV_2O_4 samples it has been found that for magnetically pure samples the ^{7}Li nuclear spin-lattice relaxation rate $1/T_1$ is proportional to temperature T at low temperatures (the Korringa law) which is typical for Fermi liquids.[8, 35, 86] However for samples which contain magnetic defects within the spinel structure, the relaxation rate has a peak at ~ 1 K and also shows other signatures which do not agree with the behavior of Fermi liquids.[25] The occurrence of magnetic defects is easily seen as a low-T Curie-like upturn in the magnetic susceptibility rather than becoming nearly independant of T below ~ 10 K as observed for the intrinsic behavior.[24] The mechanism for the formation of the magnetic defects is not known yet.

Previously, polycrystalline samples of LiV_2O_4 had been prepared from the starting materials Li_2CO_3, V_2O_3 and V_2O_5 at 700 °C. Typically, the samples contain a concentration of magnetic defects $n_{\rm defect}$ within the structure of the spinel phase, ranging from $\lesssim 0.01$ to 0.7 mol%.[24] Magnetization M versus applied magnetic field H measurements at low T were carried out to estimate $n_{\rm defect}$ and the defect spin $S_{\rm defect}$. Low concentrations of defects were found in samples of LiV_2O_4 containing small amounts of V_3O_5 impurity phase while high defect concentrations were found in samples containing V_2O_3 impurity phase.[24] Though the reason behind this correlation is not known yet, these results pointed towards a controllable way to vary the magnetic defect concentration within the spinel structure. However, it was not clear that the above-noted V_2O_3 and V_3O_5 impurity phases were in equilibrium with the LiV_2O_4

spinel phase at 700 °C. In addition, it was unknown (in Ref. [24]) how the magnetic defect concentration in the spinel phase LiV_2O_4 varied if other impurity phases were present. To help resolve these questions, we report here the phase relations in the Li_2O–V_2O_3–V_2O_5 system at 700 °C, in the vicinity of the composition LiV_2O_4, and report the magnetic properties of a selection of such compositions.

There have been some studies of the Li_2O–V_2O_5 system which revealed the existence of three phases in the system, namely $LiVO_3$, Li_3VO_4 and LiV_3O_8. Reisman et al.[87] reported the existence of the congruently melting phases $LiVO_3$ (reported as $Li_2O{\cdot}V_2O_5$) and Li_3VO_4 (reported as $3Li_2O{\cdot}V_2O_5$) with melting points 616 °C and 1152 °C, respectively. LiV_3O_8 has been reported to be both congruently melting and incongruently melting.[87–89] Manthiram et al.[90] reported that $Li_{1-x}VO_2$ is single phase in the compositional range $0 \leq x \leq 0.3$ at 650 °C. LiV_2O_4 was reported to exist in equilibrium with the compounds VO_2 and $Li_{1-x}VO_2$ from room temperature to 1000 °C by Goodenough et al.[91] The lithium vanadium oxide system $Li_xV_2O_5$, also known as the lithium vanadium bronze phase, was reported to exist in a number of single-phase regions for $0 < x < 1$ and temperature $T < 500$ °C.[92]

The V_2O_3–V_2O_5 binary system has been extensively studied and a large number of phases have been reported. Hoschek and Klemm[93] first studied the system and suggested the presence of the phase V_2O_3, the β-phase ($VO_{1.65}$–$VO_{1.80}$), the α-phase ($VO_{1.80}$–VO_2), and the α'-phase ($VO_{2.09}$–$VO_{2.23}$). Andersson[94] reported phases with general formula V_nO_{2n-1} with $3 \leq n < 9$. Additional phases reported in this system are V_9O_{17} and $V_{10}O_{19}$[4]. The phases with general formula V_nO_{2n-1} with $3 \leq n \leq 9$ are called the Magnéli phases.[3] The triclinic structure of the Magnéli phases have been reported.[2, 4–6] The other V-O phases existing between VO_2 and V_2O_5 are V_6O_{13},[94, 95] V_4O_9[96] and V_3O_7.[97, 98] Combined with the work by Kachi and Roy[99], Kosuge[98] proposed a phase diagram of the V_2O_3-V_2O_5 system in the temperature-composition plane extending from room temperature to 1200 °C showing high melting points ($>$ 1200 °C) for V-O phases existing between V_2O_3 and VO_2, low melting points ($\lesssim$ 700 °C) for V-O phases existing between VO_2 and V_2O_5 and also the homogeneity ranges of all the phases existing between V_2O_3 and V_2O_5.

3.2 Experimental details

Our samples were prepared by conventional solid state reaction as described by Kondo et al.[24] The starting materials were Li_2CO_3 (99.995%, Alfa Aesar), V_2O_5 (99.995%, M V Laboratories Inc.) and V_2O_3 (99.999%, M V Laboratories Inc.). The samples were made in two stages. First a $(Li_2O)_x(V_2O_5)_y$ precursor was made by thoroughly mixing appropriate amounts of Li_2CO_3 and V_2O_5, pressing into a pellet and then heating in a tube furnace under oxygen flow at 525 °C until the expected weight loss occured due to the loss of CO_2 from Li_2CO_3. The precursor pellet was then crushed and the appropriate amount of V_2O_3 was added and mixed thoroughly inside a helium-filled glove box. The precursor-V_2O_3 mixture was then again pressed into a pellet, wrapped in a platinum foil, sealed in a quartz tube under vacuum and then heated at 700 °C for about ten days. The samples were taken out of the furnace and air-cooled to room temperature. The different phases present in the samples were identified from X-ray diffraction patterns at room temperature obtained using a Rikagu Geigerflex diffractometer with a curved graphite crystal monochromator. The diffraction patterns were matched with known phases from the JCPDS[100] database using the JADE 7 program.[101] The samples were repeatedly ground and heated until the X-ray patterns did not show any change to ensure that the samples were in thermal equilibrium at 700 °C. The magnetization $M_{\rm obs}$ measurements were done on the samples using a Quantum Design Superconducting Quantum Interference Device (SQUID) magnetometer over the temperature T range 1.8 K – 350 K and applied magnetic field H range 0.001 T – 5.5 T.

3.3 Results and analysis

3.3.1 Phase relations at 700 °C

The phase relations for phases in equilibrium with LiV_2O_4 at 700 °C are shown in Fig. 3.1. The black triangles represent the crystalline phases which exist singly in equilibrium at 700 °C. The solid dots represent the compositions of our samples from which the phase relations were determined. The solid straight lines connecting the phases are the tie lines. From a large

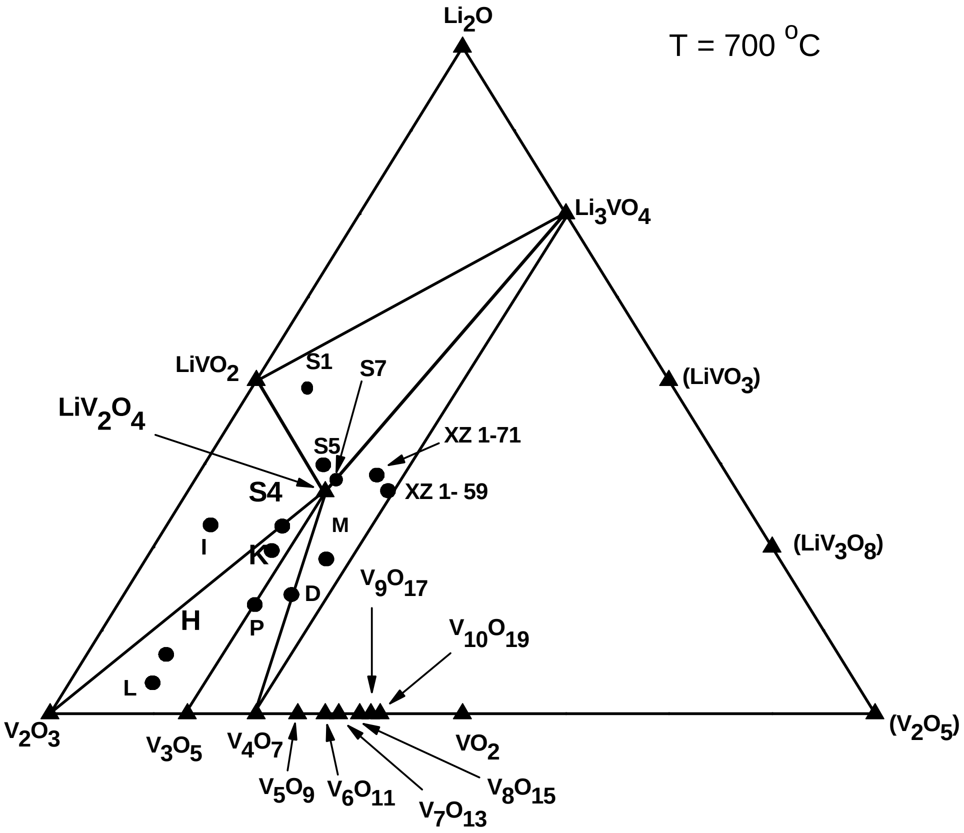

Figure 3.1 Phase relations in the Li_2O-V_2O_3-V_2O_5 system at 700 °C for phases in equilibrium with the LiV_2O_4 spinel phase. The triangles represent the crystalline phases which exist singly in equilibrium at 700 °C. The dots represent the compositions of our samples from which the phase relations were determined. The solid straight lines connecting the phases are the tie lines. The compounds in parentheses melt below 700 °C.

number of samples synthesized at the nominal stoichiometric composition LiV_2O_4, it has been found that LiV_2O_4 is a "line compound", i.e, this compound has an extremely small ($\lesssim$ 1 at.%) homogeneity range. This situation is very different from the large homogeneity range $0 \leq x \leq 1/3$ in the similiar spinel phase $Li[Li_xTi_{2-x}]O_4$.[102] According to the study of $Li_{1-x}VO_2$ by Goodenough et al.[91] mentioned above, there is a tie line between LiV_2O_4 and $LiVO_2$ at 700 °C, consistent with our results. However, our results conflict with their finding of a tie line between LiV_2O_4 and VO_2. In particular, the observed tie line in Fig. 1 between V_4O_7 and Li_3VO_4 precludes a tie line between LiV_2O_4 and VO_2 because the latter would have to cross the former which is not allowed.

3.3.2 Magnetic measurements

3.3.2.1 Magnetic susceptibility measurements

Here we present the magnetic susceptibility χ versus temperature T for some of our samples of LiV_2O_4 containing small amounts ($\lesssim$ 2 wt%) of impurity phases. Based on the X-ray diffraction patterns, the impurity phases present in the samples are V_2O_3 in sample 5A, V_3O_5 in sample 8 , $LiVO_2$ in sample 5B, and Li_3VO_4 in sample S7 as shown in Table 3.1. Sample 6B was the crystallographically purest sample synthesized and the X-ray diffraction pattern did not reveal any impurity phases. Figures 3.2 and 3.3 show expanded X-ray diffraction patterns of these samples.

The observed magnetic susceptibility $\chi_{\rm obs}$ versus T plots from T = 1.8 K to 350 K at magnetic field H = 1 T for the five samples are shown in Fig. 3.4 where $\chi_{\rm obs} \equiv M_{\rm obs}/H$. It can be clearly seen that the dependence of $\chi_{\rm obs}$ on T for the five samples is similar Curie-Weiss like for $T > 50$ K. However for $T < 50$ K the dependence is strikingly different. Sample 8 containing V_3O_5 impurity phase shows a broad peak at $T \approx 20$ K, which is characteristic of the intrinsic behavior of magnetically pure LiV_2O_4.[24] Sample 6B which is crystallographically pure also shows a broad peak but it is masked by a Curie-like upturn at $T < 10$ K. For sample 5A containing V_2O_3, S7 containing Li_3VO_4, and 5B containing $LiVO_2$ as impurity phases, the broad peak is totally masked by Curie contributions.

To interpret the origin of the Curie-like low-T contributions to $\chi(T)$ of these samples, it is important to consider the potential contributions of the impurity phases to this term. V_3O_5 orders antiferromagnetically with its susceptibility showing a very broad maximum between T = 120 K and 130 K[27, 28] which is much higher than its Néel temperature $T_{\rm N}$ = 75.5 K measured by Griffing.[103] The susceptibility for $T < T_{\rm N}$ decreases with decreasing T, has a value $< 2 \times 10^{-5}$ cm^3/mol at the lowest temperatures, and shows no evidence for a Curie-like term. V_2O_3 has a Curie-Weiss-like behaviour for $T > 170$ K where it is also metallic. Below 170 K it orders antiferromagnetically at a metal to insulator transition and the susceptibility remains constant at about 5×10^{-4} cm^3/mol down to $T \sim 80$ K. For $T < 80$ K, the susceptibility decreases with decreasing T with no sign of a Curie-like upturn.[12, 27] The susceptibility of

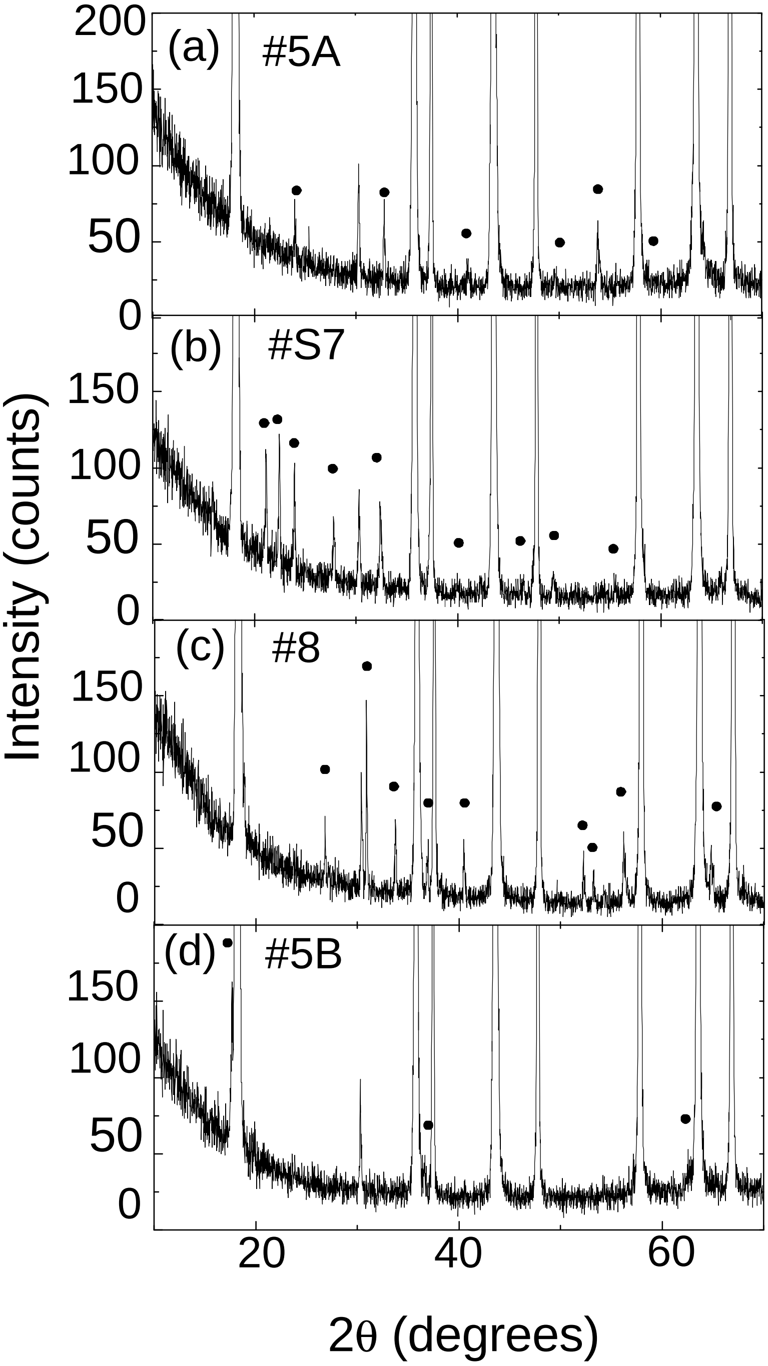

Figure 3.2 Expanded X-ray diffraction patterns of samples with compositions near LiV_2O_4. The impurity phase peaks are marked by solid circles. (a) Sample 5A has V_2O_3 impurity phase. (b) Sample S7 has Li_3VO_4 impurity phase. (c) Sample 8 has V_3O_5 impurity phase. (d) Sample 5B has $LiVO_2$ impurity phase.

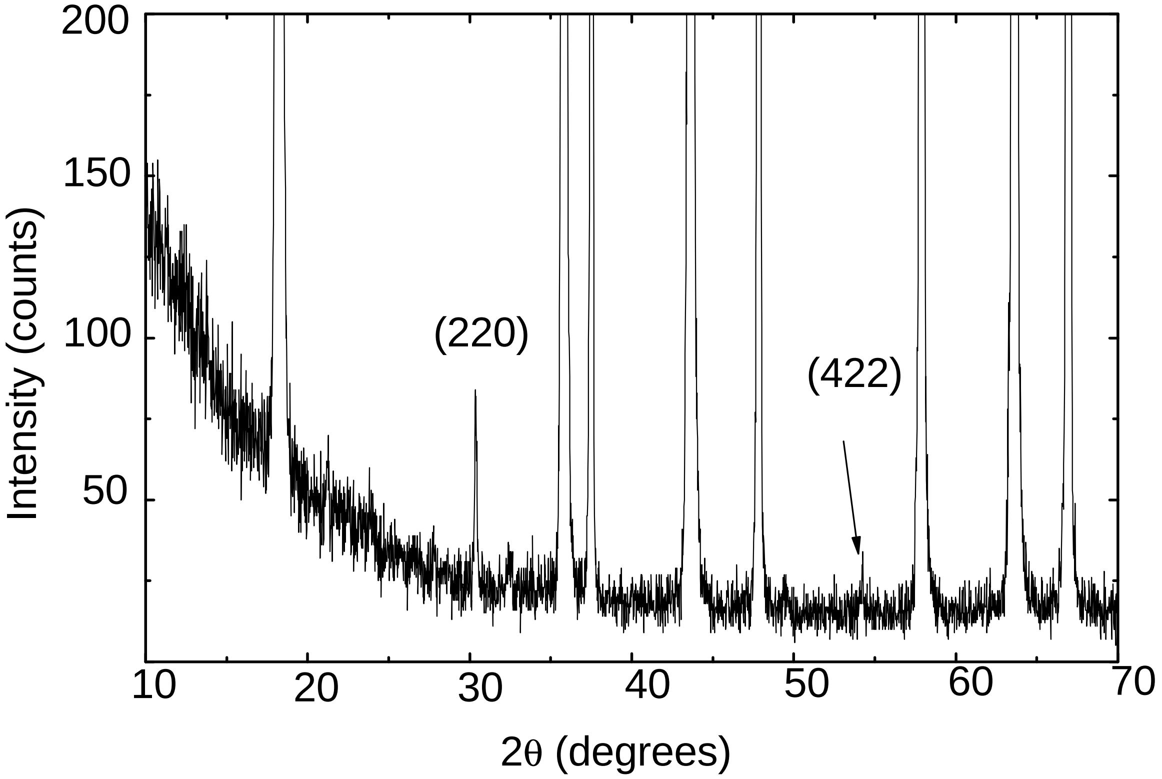

Figure 3.3 Expanded X-ray diffraction pattern of the LiV_2O_4 sample 6B. The two indexed peaks are of the LiV_2O_4 spinel phase. There are no observable impurity phases present.

$V_{2-y}O_3$ shows a peak at low T ($\sim$ 10 K) as it undergoes antiferromagnetic ordering at around 10 K with no evidence for a Curie-like term at lower T.[27] Li_3VO_4 is nonmagnetic since the vanadium atom is in the +5 oxidation state. The only impurity phase exhibiting a low-temperature Curie-like contribution to its susceptibility is $Li_{1-x}VO_2$, which shows a Curie-like upturn at $T < 50$ K due to Li deficiency of about 5%.[104, 105] However, the amounts of impurity phases in our LiV_2O_4 samples are small (< 2 wt%). Assuming that $x = 0.05$ in $Li_{1-x}VO_2$ impurity phase,[104] where each Li vacancy induces a V^{+4} ($S = 1/2$) defect in that phase, one obtains a Curie constant of $\simeq 4 \times 10^{-4}$ cm^3 K/mol, which is far smaller than observed (~ 0.1 cm^3 K/mol) in our sample 5B having $Li_{1-x}VO_2$ impurity phase. Thus we can conclude that the Curie-like upturn in the susceptibility of nearly single-phase LiV_2O_4 arises from magnetic defects within the spinel structure of this compound and not from impurity phases, which confirms the previous conclusion of Ref. [24].

3.3.2.2 Isothermal magnetization measurements

The observed magnetization $M_{\rm obs}$ versus applied magnetic field H isothermal measurements were done at different temperatures between 1.8 K and 350 K with H varying from 0.001 T to 5.5 T. However, to find $n_{\rm defect}$ only the low T (1.8 K, 2.5 K, 3 K and 5 K) isotherms were used. The $M_{\rm obs}$ versus H curves for different samples at 1.8 K are shown in Fig. 3.5. The samples showing a Curie-like upturn in the susceptibility show a negative curvature in their $M_{\rm obs}$ versus H curves, whereas the samples having a very small Curie-like upturn in the susceptibility show a hardly observable curvature. This correlation shows that the Curie contribution to the susceptibility is due to field saturable (paramagnetic) defects. The values of the defect concentrations and the values of the defect spins for different samples were determined according to the analysis done by Kondo et al.[24] The observed molar magnetization $M_{\rm obs}$ isotherms at low temperatures ($T \leq 5$ K) for each sample were simultaneously fitted by

$$M_{\rm obs} = \chi H + n_{\rm defect} N_{\rm A} g_{\rm defect} \mu_{\rm B} S_{\rm defect} B_S(x)\,, \tag{3.1}$$

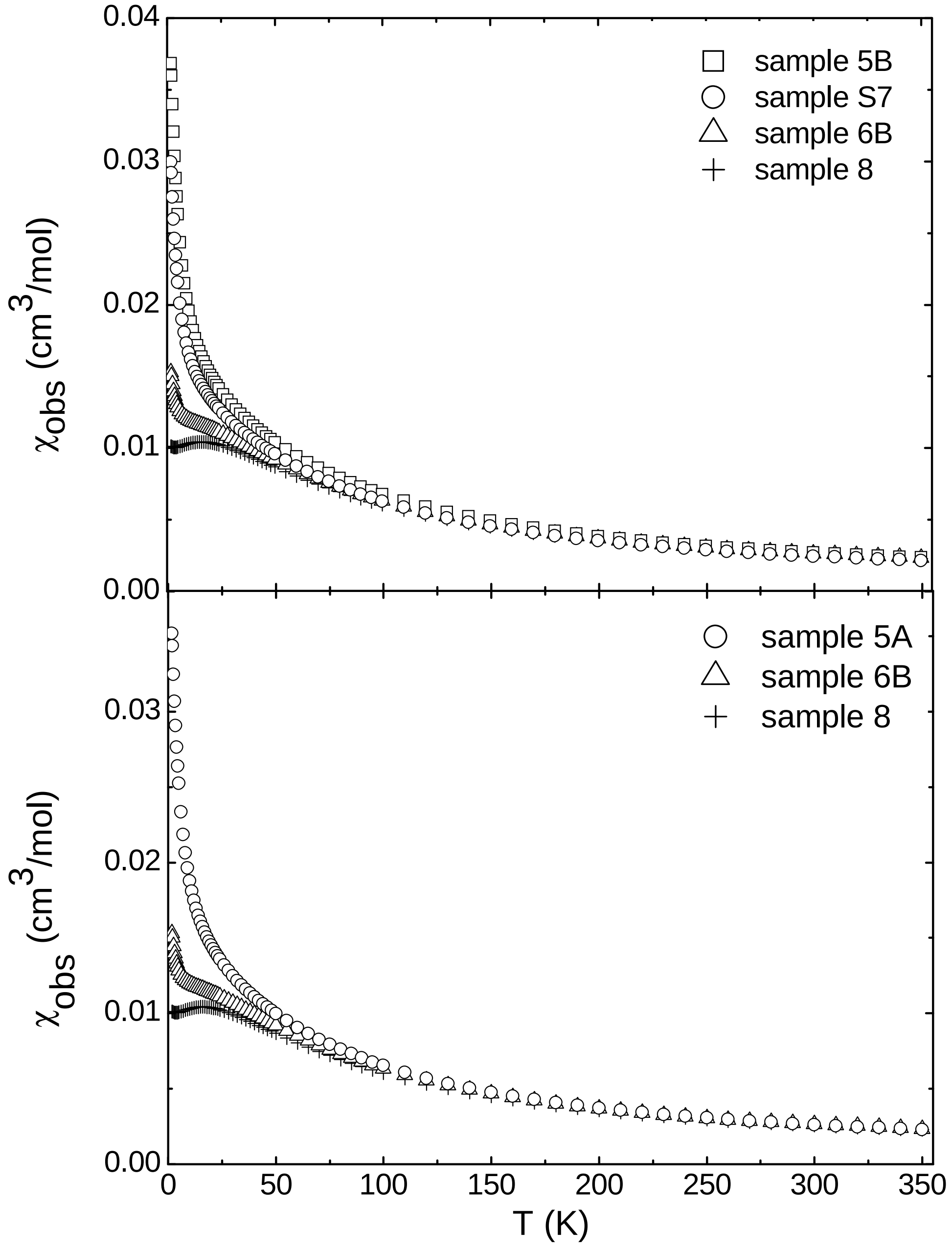

Figure 3.4 Observed magnetic susceptibility $\chi_{\rm obs}$ versus temperature T at $H = 1$ T for several samples in Table 3.1 that are nearly single-phase $\rm LiV_2O_4$.

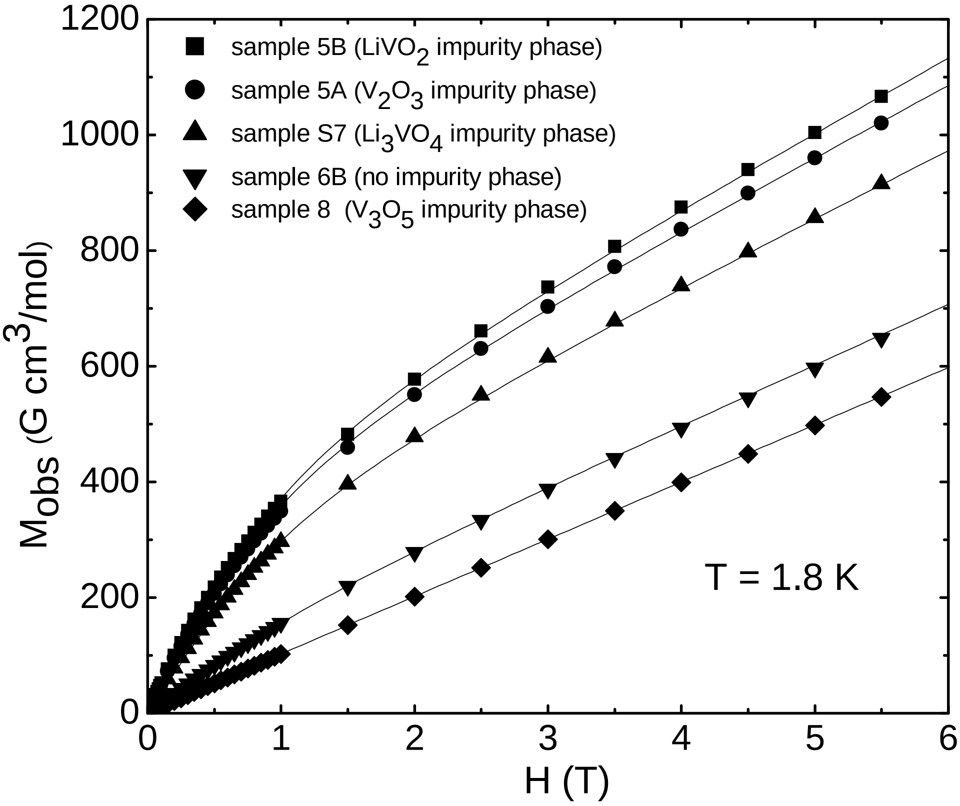

Figure 3.5 $M_{\rm obs}$ versus H isotherms of four samples at 1.8 K. The curves passing through the data points are fits by Eq. (1) with the values of the parameters given in Table 3.1.

where $n_{\rm defect}$ is the concentration of the magnetic defects, $N_{\rm A}$ Avogadro's number, $g_{\rm defect}$ the g-factor of the defect spins which was fixed to 2 (the detailed reasoning behind this is given in Ref. [24]), $S_{\rm defect}$ the spin of the defects, $B_S(x)$ the Brillouin function, and χ the intrinsic susceptibility of LiV$_2$O$_4$ spinel phase. The argument of the Brillouin function $B_S(x)$ is $x = g_{\rm defect}\mu_{\rm B}S_{\rm defect}H/[{\rm k_B}(T-\theta_{\rm defect})]$ where $\theta_{\rm defect}$ is the Weiss temperature. The four fitting parameters χ, $n_{\rm defect}$, $S_{\rm defect}$ and $\theta_{\rm defect}$ for each sample are listed in Table 3.1. Since the parameters $n_{\rm defect}$ and $S_{\rm defect}$ are strongly correlated in the fits, the products of these are also listed in Table 3.1.

The grain sizes of our samples were studied using a scanning electron microscope (SEM). The SEM pictures of some of our samples are shown in Fig. 3.6. As seen from the figure, the grain sizes are 1 – 10 μm, and from Table 3.1 there is no evident correlation between the sample grain sizes and the magnetic defect concentrations.

Table 3.1 Results of the analyses of the $M_{\rm obs}(H,T)$. The error in the last digit of a parameter is given in parentheses.

Sample no	Impurity	χ (cm^3/mol)	$n_{\rm defect}$ (mol%)	$S_{\rm defect}$	$\theta_{\rm defect}$ (K)	$n_{\rm defect}S_{\rm defect}$ (mol%)
5A	V_2O_3	0.0123(1)	0.77(3)	4.0(1)	−0.70(13)	3.08(13)
S7	Li_3VO_4	0.0115(1)	0.67(2)	3.7(1)	−0.59(9)	2.52(8)
8	V_3O_5	0.0098(1)	0.0067(28)	6.3(27)	−1.0(10)	0.04(18)
5B	$LiVO_2$	0.0127(2)	0.83(3)	3.9(1)	−0.65(12)	3.29(13)
6B	no impurity	0.0104(1)	0.21(1)	3.5(2)	−0.75(13)	0.73(4)

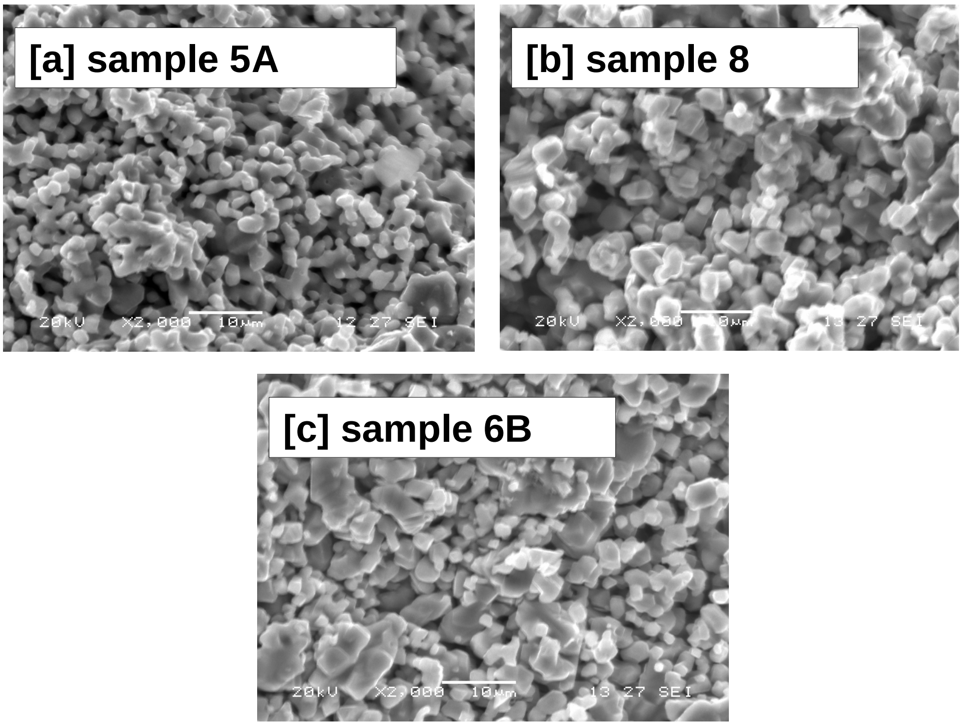

Figure 3.6 SEM pictures of our LiV_2O_4 powder samples. No evident correlation between the grain sizes and the defect concentrations was found. The bars at the bottom of each picture are 10 μm long. The grain sizes are in the range 1 to 10 μm.

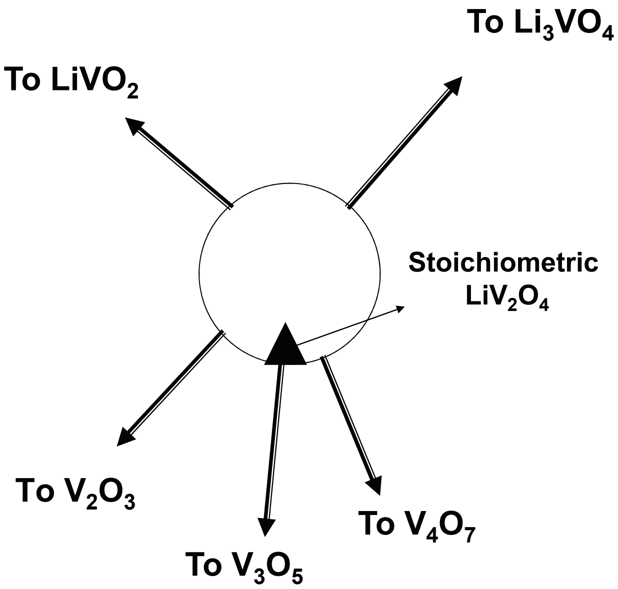

Figure 3.7 Suggested model for the mechanism of the crystal and magnetic defect formation in LiV_2O_4. The figure shows an enlarged region around LiV_2O_4 in the phase relation picture (Fig. 1) where the circle represents a possible small homogeneity range of the spinel phase and the filled triangle is stoichiometric LiV_2O_4.

3.4 Suggested model

The reason behind the correlation between the presence of the Li-V-O and V-O phases and the variation of the magnetic defect concentration in LiV_2O_4 is not known yet. We speculate that this is due to the formation of vacancies and/or interstitials in the spinel structure due to the variation of the sample composition from the ideal stoichiometry. A possible model is shown in Fig. 3.7. The black triangle is stoichiometric LiV_2O_4 while the circular region is a small ($\lesssim$ 1 at.%) homogeneity range of LiV_2O_4. Based on this model, the LiV_2O_4 phase in the samples having V_3O_5 impurity phase are very close to the ideal stoichiometric LiV_2O_4, the magnetic susceptibility is the intrinsic susceptibility for the ideal stoichiometric spinel phase and the magnetic defect concentration is very small. The composition of the spinel phase in samples having V_2O_3, Li_3VO_4 or $LiVO_2$ as impurity phases deviates from the ideal stoichiometry as can be seen in the figure. This variation from the ideal stoichiometry would cause the above vacancies and/or interstitial defects to form which in turn cause the formation of paramagnetic defects. The samples having chemical composition different from the black solid triangle (i.e. the ideal stoichiometric composition) but within the circular region will be by definition single phase LiV_2O_4 but not having the ideal stoichiometry. Thus some samples of LiV_2O_4 will have magnetic defects even if there are no impurity phases in them which might be the case for our sample 6B and also samples 3 and 7 studied by Kondo et al.,[24] where some samples were essentially impurity free but still had a strong Curie contribution in their susceptibility.

3.5 Conclusion

In this chapter we have reported the phase relations in the Li_2O-V_2O_3-V_2O_5 system at 700 °C for compositions in equilibrium with LiV_2O_4. This study helped us to determine the systhesis conditions under which polycrystalline samples of LiV_2O_4 could be prepared with variable magnetic defect concentrations ranging from $n_{\rm defect} = 0.006$ to 0.83 mol%. High magnetic defect concentrations were found in samples containing V_2O_3, Li_3VO_4, or $LiVO_2$ impurity phases while the samples containing V_3O_5 impurity phase had low defect concentration. We suggested a possible model which might explain this correlation. Our work shows how to systematically and controllably synthesize LiV_2O_4 samples with variable magnetic defect concentrations within the spinel structure. The results should be helpful to other researchers synthesizing samples for study of the physical properties of this system.

CHAPTER 4. Crystallography, magnetic susceptibility, heat capacity, and electrical resistivity of heavy fermion LiV_2O_4 single crystals grown using a self-flux technique

This chapter is based on an article published in Phys. Rev. B **76**, 054418 (2007) by S. Das, X. Zong, A. Niazi, A. Ellern, J.-Q. Yan, and D. C. Johnston.

Abstract

Magnetically pure spinel compound LiV_2O_4 is a rare *d*-electron heavy fermion. Measurements on single crystals are needed to clarify the mechanism for the heavy fermion behavior in the pure material. In addition, it is known that small concentrations (< 1 mol%) of magnetic defects in the structure strongly affect the properties, and measurements on single crystals containing magnetic defects would help to understand the latter behaviors. Herein, we report flux growth of LiV_2O_4 and preliminary measurements to help resolve these questions. The magnetic susceptibility of some as-grown crystals show a Curie-like upturn at low temperatures, showing the presence of magnetic defects within the spinel structure. The magnetic defects could be removed in some of the crystals by annealing them at 700 °C. A very high specific heat coefficient $\gamma = 450$ mJ/(mol K^2) was obtained at a temperature of 1.8 K for a crystal containing a magnetic defect concentration $n_{\rm defect} = 0.5$ mol%. A crystal with $n_{\rm defect}$ $= 0.01$ mol% showed a residual resistivity ratio of 50.

4.1 Introduction

The spinel lithium vanadium oxide LiV_2O_4 is a material of great interest as it shows heavy fermion behavior[8, 85] in spite of being a *d*-electron metal whereas most of the other heavy fermions are *f*-electron compounds. The origin of this heavy fermion behavior in LiV_2O_4 is controversial. LiV_2O_4 has the normal face-centered-cubic spinel structure with the space group $Fd\overline{3}m$. The V atoms are coordinated by six O atoms in a slightly distorted octahedron. The Li atoms are coordinated with four O atoms in a tetrahedron. The Li atoms are located in the gaps between chains of the VO_6 edge-sharing octahedra. A study of the phase relations in the Li_20-V_2O_3-V_2O_5 system at 700 °C (Ref. [106]) showed that the homogeneity range of LiV_2O_4 is smaller than the experimental resolution of $\sim$ 1 at%. From NMR measurements done on LiV_2O_4 samples it has been found that for magnetically pure samples the ^{7}Li nuclear spin-lattice relaxation rate $1/T_1$ is proportional to temperature T at low temperatures (the Korringa law) which is typical for Fermi liquids.[8, 35, 86] However for samples which contain magnetic defects within the spinel structure, the relaxation rate has a peak at $\sim$ 1 K and also shows other signatures which do not agree with the behavior of Fermi liquids.[25, 107] The occurrence of magnetic defects is easily seen as a low-T Curie-like upturn in the magnetic susceptibility rather than becoming nearly independent of T below $\sim$ 10 K as observed for the intrinsic behavior.[24] We have proposed a model in which the magnetic defects arise from a small homogeneity range of LiV_2O_4 in the spinel structure.[106] High quality crystals containing magnetic defects might help to resolve the question of the nature of these defects and may shed light on the mechanism for heavy fermion behavior in the pure material and on whether a Fermi liquid is still present in samples containing magnetic defects. In particular, there may be a critical concentration separating Fermi liquid from non-Fermi liquid behaviors.

Crystal growth reports of LiV_2O_4 are rare. LiV_2O_4 crystals were first grown by hydrothermal reaction of $LiVO_2$ and VO_2 in aqueous solutions 1N in LiOH sealed in gold tubes and heated to 500 – 700 °C under a pressure of 3 kbar for $\sim$ 24 hr.[29] Octahedra shaped crystals were obtained that were $\sim$ 0.75 mm on an edge. Electrical resistivity measurements demonstrated for the first time that LiV_2O_4 is metallic down to a temperature T of at least 4 K, with a room temperature resistivity of 300 to 800 $\mu\Omega$ cm depending on the crystal.[29] Electrical resistivity measurements of magnetically pure LiV_2O_4 single crystals using crystals grown by this technique were recently reported[30, 31] down to 0.3 K revealing a T^2 dependence between 0.3 and $\sim$ 2 K as expected for a Fermi liquid. Heat capacity (C) measurements on these crystals yielded an extrapolated zero-temperature C/T value of 350 mJ/mol K^2 which was comparable to the value of $C/T \sim 430$ mJ/mol K^2 previously obtained at 1 K from measurements on polycrystalline samples.[8, 32] More recently, the first flux growth of single crystals of LiV_2O_4 was reported using $LiCl - Li_2MoO_4 - LiBO_2$ as the flux.[33] The crystals were reported to be of high quality but extremely reactive to air and/or moisture.[33]

In this chapter we report a new self-flux growth method to obtain single crystals of LiV_2O_4 along with our initial magnetic, thermal, and transport properties of our crystals. Some of our as-grown crystals had magnetic defects in them while some were essentially defect free. Unlike the crystals grown in Ref. [33], our crystals did not show any reactivity towards air and moisture.

4.2 Experimental details

The starting materials of our samples of LiV_2O_4 and Li_3VO_4 were Li_2CO_3 (99.995%, Alfa Aesar), V_2O_5 (99.999%, M V Laboratories Inc.), and V_2O_3 (99.999%, M V Laboratories Inc.). The crystals of LiV_2O_4 were grown in a vertical tube furnace. The single crystal X-ray diffraction measurements were done using a Bruker CCD-1000 diffractometer with Mo K$_\alpha$ (λ = 0.71073 Å) radiation. Powder X-ray diffraction measurements at room temperature were done using a Rigaku Geigerflex diffractometer with a curved graphite crystal monochromator. Differential thermal analysis experiments were carried out using a Perkin-Elmer differential thermal analyzer (DTA-6). The magnetic measurements on the crystals were done using a Quantum Design superconducting quantum interference device (SQUID) magnetometer in the temperature range 1.8 K – 350 K and magnetic field range 0 – 5.5 T. The heat capacity and electrical resistivity measurements were done using a Quantum Design physical property measurement system (PPMS). For the heat capacity measurements, Apiezon N grease was used for thermal coupling between the samples and the sample platform. Heat capacity was measured in the temperature range 1.8 K – 300 K. For electrical resistivity measurements, 0.001 inch diameter platinum (99.999%) leads were put on polished crystals using single component Epotek P1011 epoxy glue for electrical connections. Electrical resistivity was measured in the temperature range 1.8 K – 300 K in 0 and 5 T magnetic fields.

4.3 Crystal growth and characterization

4.3.1 LiV_2O_4 – Li_3VO_4 Pseudobinary phase diagram

As a first step to find a self-flux for crystal growth of LiV_2O_4, we melted a prereacted powder sample under inert atmosphere. The product was a mixture primarily of V_2O_3 and Li_3VO_4. Since the phase relations in the solid state at 700 °C showed that LiV_2O_4 is in equilibrium with both V_2O_3 and Li_3VO_4,[106] this result indicated that Li_3VO_4 might be used as a flux to grow crystals of LiV_2O_4. We therefore determined the LiV_2O_4 – Li_3VO_4 pseudobinary phase diagram using a DTA under 1 atm He pressure, and the result is shown in Fig. 4.1. We find that LiV_2O_4 decomposes peritectically at 1040 °C. This temperature is comparable to the maximum stability temperature of 1020 °C for LiV_2O_4 in vacuum found in Ref. [33]. The eutectic temperature is about 950 °C and the eutectic composition is approximately 53 wt% LiV_2O_4 and 47 wt% Li_3VO_4. We see from Fig. 4.1 that by cooling a liquid with a composition of 53 – 58 wt% of LiV_2O_4 in Li_3VO_4, crystals of LiV_2O_4 should grow once the temperature reaches the liquidus temperature, until the growth temperature decreases to the eutectic temperature 950 °C. Our flux Li_3VO_4 has no other elements except Li, V and O, which eliminates the possibility of incorporating foreign elements in the LiV_2O_4 crystals. Also Li_3VO_4 did not evaporate at high temperatures $\sim$ 1000 – 1100 °C, nor did it react with or even wet platinum crucibles. The crystals could be separated from the flux by dissolving the flux in water (see below). All these data indicate that Li_3VO_4 is an ideal flux for LiV_2O_4 crystal growth.

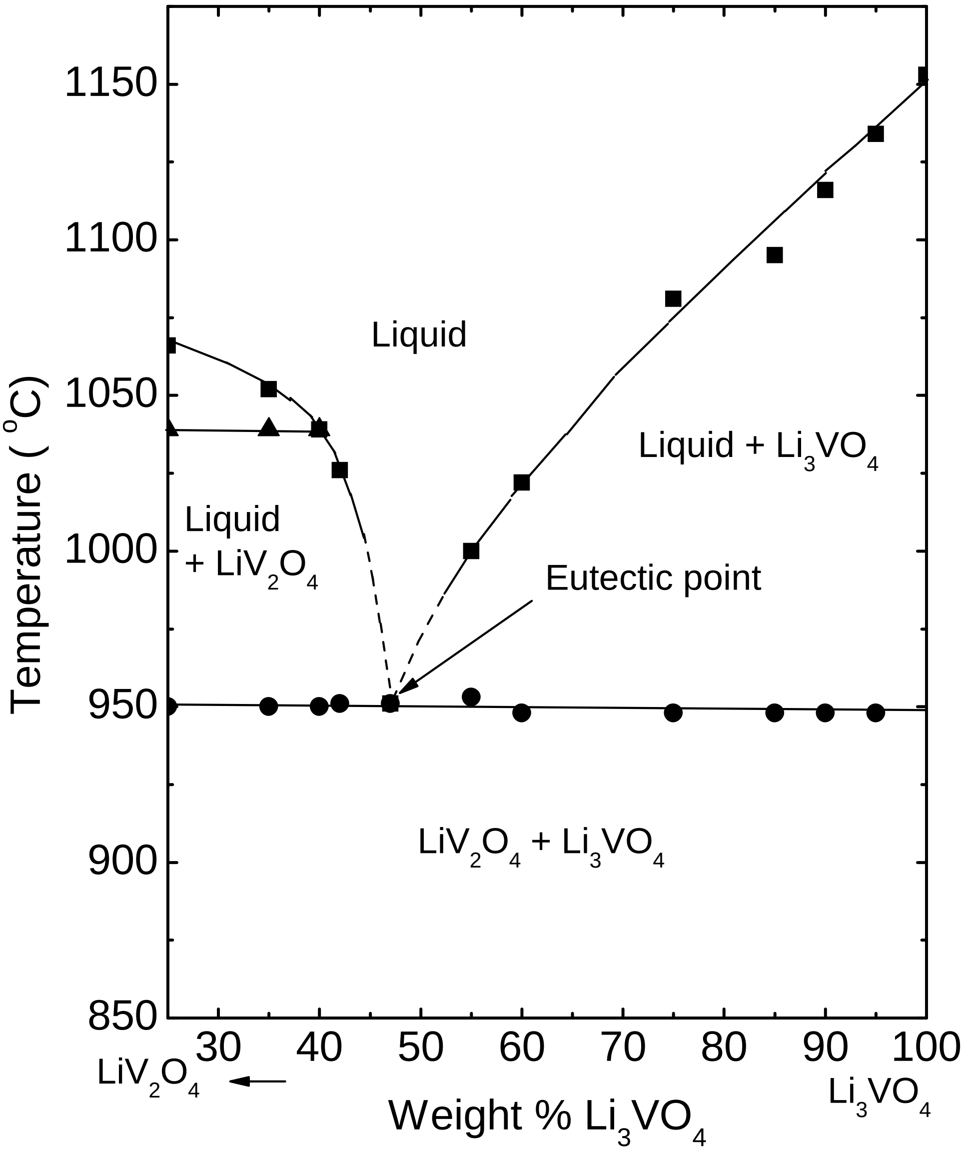

Figure 4.1 Pseudobinary phase diagram of the LiV_2O_4-Li_3VO_4 system. The arrow below the horizontal axis points towards pure LiV_2O_4, which is far to the left of the left-hand vertical axis. Note that LiV_2O_4 decomposes peritectically at 1040 °C.

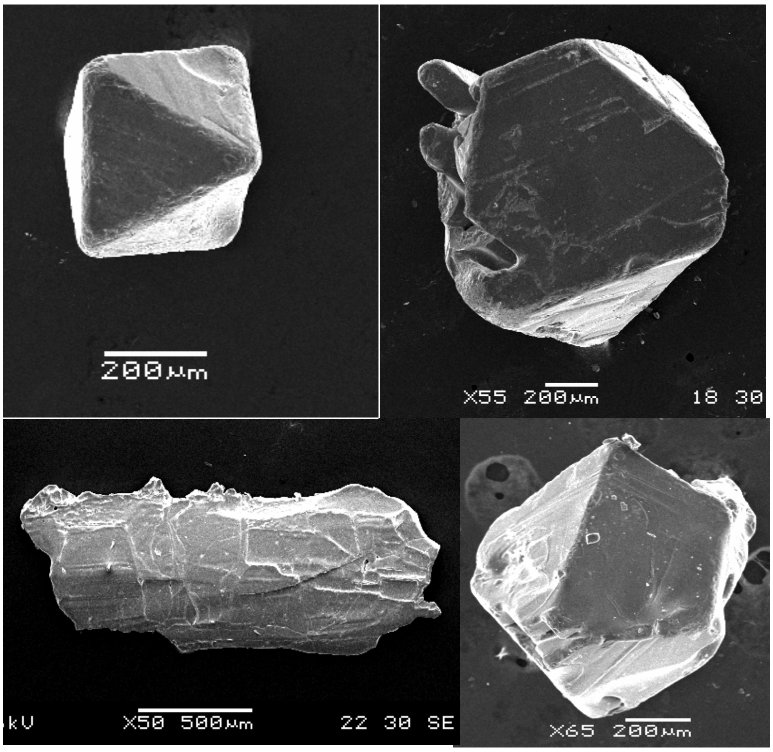

Figure 4.2 Scanning electron microscope pictures of the three LiV_2O_4 crystal morphologies obtained: octahedral (top left), irregular (top right and bottom right), and plate (bottom left).

4.3.2 Crystal growth

Polycrystalline LiV_2O_4 was prepared by the conventional solid state reaction of appropriate amounts of Li_2CO_3, V_2O_5 and V_2O_3.[24] Powder samples of the flux Li_3VO_4 were made by the solid state reaction of appropriate amounts of V_2O_5 and Li_2CO_3 at 525 °C in air for $\sim$ 5 days. To grow the crystals we mixed powdered samples of Li_3VO_4 and LiV_2O_4 with the composition of 58 wt% LiV_2O_4 and 42 wt% Li_3VO_4. The mass of the LiV_2O_4/Li_3VO_4 mixture was typically $\sim 5 - 8$ gm. The powder was placed in a platinum crucible which was then sealed under vacuum in a quartz tube. The quartz tube was then heated to 1038 – 1060 °C, was kept at that temperature for 12 – 24 hours, and then cooled to 930 °C at a slow rate. We obtained the largest (up to 2.5 mm on a side) crystals when the cooling rate was 1 °C/hour. At higher cooling rates of 2 °C/hour and 3 °C/hour the crystal size became smaller (0.2 – 0.5 mm on a side). From 930 °C the sample was furnace-cooled to room temperature. The crystals of LiV_2O_4 were extracted by dissolving the flux at 50 to 55 °C in a solution of $LiVO_3$ in deionized water or in pure deionized water in an ultrasonic bath. Finally the crystals were rinsed in acetone and dried.

Three different kinds of crystal morphologies were obtained. One was octahedral shaped crystals with well-developed faces and size $\sim$ 1 mm on a side. From Laue x-ray diffraction measurements, the flat faces of the octahedra were found to be [111] planes. Another was irregular shaped: they were partly octahedral shaped with a few well-developed faces but also had irregular faces. Crystals with these two described morphologies were obtained together in the crystal growth runs. In one of our growth runs, along with the two morphologies, some plate-shaped crystals were also obtained. These were $\sim$ 2 mm in length, $\sim$ 0.5 mm in width and about 0.1 mm in thickness. Figure 4.2 shows scanning electron microscope pictures of some of the crystals. X-ray diffraction measurements of powdered crystals showed single phase LiV_2O_4. Some of the crystals were annealed at 700 °C. To anneal, the crystals were wrapped in a platinum foil, embedded inside powder LiV_2O_4 and then sealed in a quartz tube under vacuum. The presence of the powdered LiV_2O_4 ensured that even trace amounts of oxygen in the tube would be taken up by the powder and the crystal would not become oxidized.

4.3.3 Chemical analysis and crystal structure determination

Chemical analysis was carried out on a collection of ~ 10 single crystals using inductively coupled plasma atomic emission spectroscopy (ICP-AES).[108] The results gave the composition Li: (3.67 ± 0.37) wt%; V: (54.6 ± 5.5) wt%; O, by difference: (41.7 ± 5.9) wt%. These values are consistent with the values calculated for LiV_2O_4: Li, 4.0 wt%; V, 59.0 wt%; O, 37.0 wt%.

A well-shaped octahedral crystal ($0.25 \times 0.25 \times 0.21$ mm^3) was selected for X-ray structure determination at $T = 293$ K and $T = 193$ K. The initial cell constants were obtained from three series of ω scans at different starting angles. The final cell constants were calculated from a set of strong reflections from the actual data collection. The data were collected using the full sphere routine by collecting four sets of frames with 0.3° scans in ω with an exposure time 10 sec per frame with detector-to-crystal distance 3.5 cm. This data set was corrected for Lorentz and polarization effects. The absorption correction was based on fitting a function to the empirical transmission surface as sampled by multiple equivalent measurements.[109] X-ray structure determination and refinement were performed using SHELXTL software package.[110]

Cell parameters and the systematic absences in the diffraction data were consistent with the space group $Fd\overline{3}m$ known for this compound. The Least-Squares refinement on F^2 converged to R1= 0.064 showing significant extinction, therefore extinction correction was applied. The final results, presented in Tables 4.1 and 4.2, are in a good agreement with earlier results on single crystals[33] and powder diffraction.[21]

4.4 Physical property measurements

4.4.1 Magnetic susceptibility

The magnetic susceptibilities of as-grown octahedral, irregular and plate-shaped crystals are shown in Fig. 4.3(a). The magnetic susceptibility of the octahedral and irregular crystals showed a sharp upturn at low temperatures which indicates that these as-grown crystals have magnetic defects in them, as also observed in some powder samples.[24] However the

Table 4.1 Crystal data and structure refinement of LiV_2O_4. Here R1 = $\sum||F_{\rm obs}| - |F_{\rm calc}||/\sum|F_{\rm obs}|$ and wR2 = $(\sum[\ w(|F_{\rm obs}|^2 - |F_{\rm calc}|^2)^2]/\sum[\ w(|F_{\rm obs}|^2)^2])^{1/2}$, where $F_{\rm obs}$ is the observed structure factor and $F_{\rm calc}$ is the calculated structure factor.

Temperature	193(2) K	293(2) K
Crystal system/Space group	Cubic, $Fd\bar{3}m$	Cubic, $Fd\bar{3}m$
Unit cell parameter	$a = 8.2384(6)$ Å	$a = 8.2427(7)$ Å
Volume	559.15(7) Å^3	560.03(7) Å^3
Z	8	8
Density (Calculated)	4.106 Mg/m^3	4.106 Mg/m^3
Absorption coefficient	6.485 mm^{-1}	6.485 mm^{-1}
F(000)	648	648
Data / restraints / parameters	80 / 0 / 8	80 / 0 / 8
Goodness-of-fit on F^2	1.392	1.401
Final R indices $[I > 2\sigma(I)]$	R1 = 0.0148	R1 = 0.0180
	wR2 = 0.0409	wR2 = 0.0527
Extinction coefficient	0.0205(15)	0.0280(3)

Table 4.2 Atomic coordinates (10^{-4}) and equivalent isotropic displacement parameters (10^{-3} Å^2) for LiV_2O_4 at 193 K. U(eq) is defined as one third of the trace of the orthogonalized $U_{\rm ij}$ tensor.

	x	y	z	U(eq)
V (1)	5000	5000	5000	2(1)
O (1)	2612(1)	2612(1)	2612(1)	3(1)
Li (1)	1250	1250	1250	2(2)

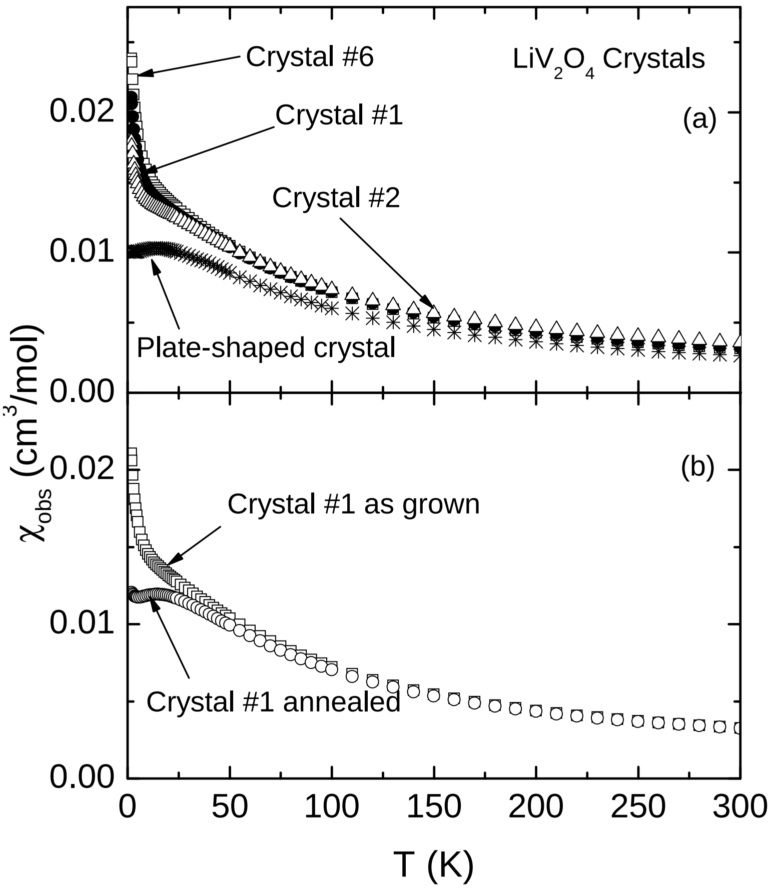

Figure 4.3 (a) Observed magnetic susceptibility of an octahedral (crystal #6), irregular (crystal #1 and #2) and a plate-shaped crystal of LiV_2O_4. The sharp Curie-like upturn at low T in the susceptibility of the octahedral and the irregular crystals show the presence of magnetic defects in the spinel structure of LiV_2O_4. (b) Magnetic susceptibility of crystal #1 (irregular shaped), as-grown and then annealed. The low T sharp upturn for the as-grown crystal disappears after annealing at 700 °C, showing the near-elimination of the magnetic defects by annealing.

magnetic susceptibility of the plate-shaped crystal was strikingly different. The susceptibility of the plate showed only a tiny low-temperature upturn and therefore revealed the intrinsic susceptibility[24] of LiV_2O_4.

The magnetic defect concentration in a crystal was calculated by fitting the observed molar magnetization $M_{\rm obs}$ isotherms at low temperatures[24] (< 10 K, not shown) by the equation

$$M_{\rm obs} = \chi H + n_{\rm defect} N_{\rm A} g_{\rm defect} \mu_{\rm B} S_{\rm defect} B_S(x)\,, \tag{4.1}$$

where $n_{\rm defect}$ is the concentration of the magnetic defects, $N_{\rm A}$ Avogadro's number, $g_{\rm defect}$ the g-factor of the defect spins which was fixed to 2 (the detailed reasoning behind this is given in Ref. [[24]]), $S_{\rm defect}$ the spin of the defects, $B_S(x)$ the Brillouin function, and χ the intrinsic susceptibility of LiV_2O_4 spinel phase. The argument of the Brillouin function $B_S(x)$ is $x = g_{\rm defect}\mu_{\rm B}S_{\rm defect}H/[{\rm k_B}(T-\theta_{\rm defect})]$ where $\theta_{\rm defect}$ is the Weiss temperature associated with the magnetic defects. Using the above analysis we obtained $n_{\rm defect} \sim 0.25 - 0.5$ mol% for the as-grown octahedral and irregular crystals and $n_{\rm defect} \lesssim 0.01$ mol% for the plate-shaped crystals.

In some of the octahedral/irregular crystals, annealing at 700 °C led to the near-elimination of the magnetic defects. The magnetic susceptibilities of one of the irregular shaped crystals, as-grown and then annealed, are shown in Fig. 4.3(b). The low T Curie-like upturn in the susceptibility for the as-grown crystal disappeared after annealing the crystal at 700 °C for five days, with the susceptibility becoming almost T-independent at low T, revealing the near-elimination of the magnetic defects. For the as-grown crystal we found $n_{\rm defect} = 0.38$ mol% and after annealing, the defect concentration $n_{\rm defect}$ became 0.01 mol%.

4.4.2 Heat capacity and electrical resistivity measurements

Figure 4.4(a) shows the heat capacity C and Fig. 4.4(b) shows the ratio $\gamma = C/T$ of as-grown octahedral crystal #6 [see also Fig. 4.3(a)]. Below 20 K, the γ increases with decreasing T and at the lowest temperature (1.8 K), it has a very high value of 450 mJ/mol K^2, comparable to the values[32] of 420–430 mJ/mol K^2 measured for powders. Figure 4.5 shows the low T $\gamma(T)$ of an octahedral, an irregular and a plate-shaped crystal with different magnetic defect

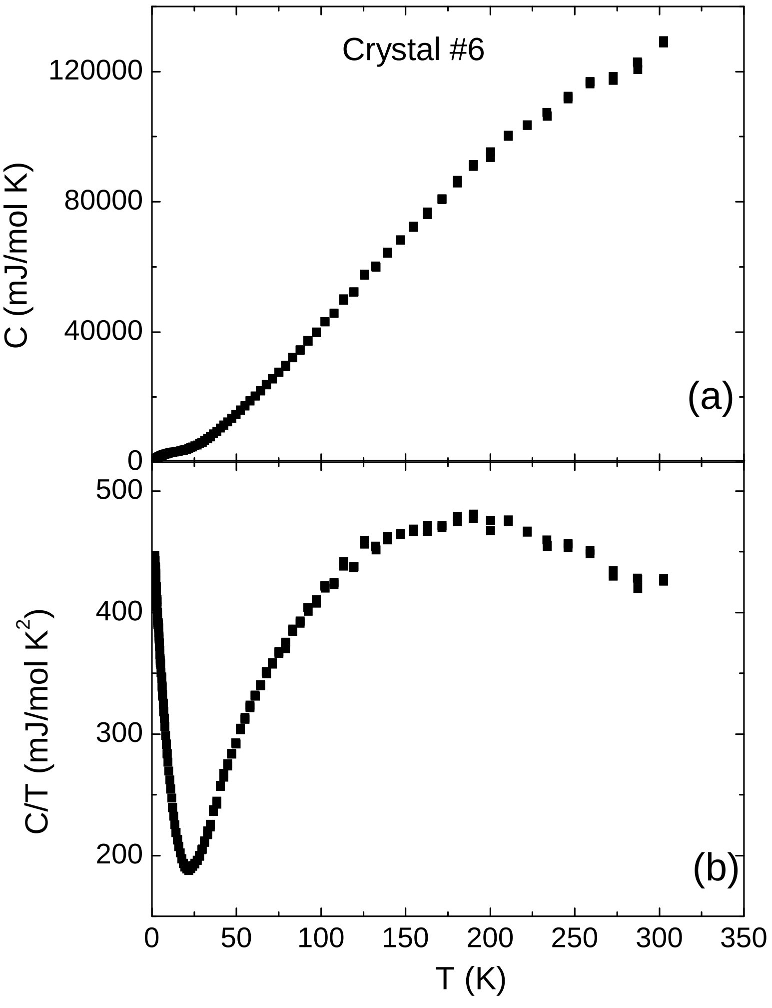

Figure 4.4 (a) Specific heat C versus temperature T for an octahedral crystal of LiV_2O_4 with magnetic defect concentration $n_{\rm defect} = 0.5$ mol%. (b) The data in (a) plotted as C/T versus T.

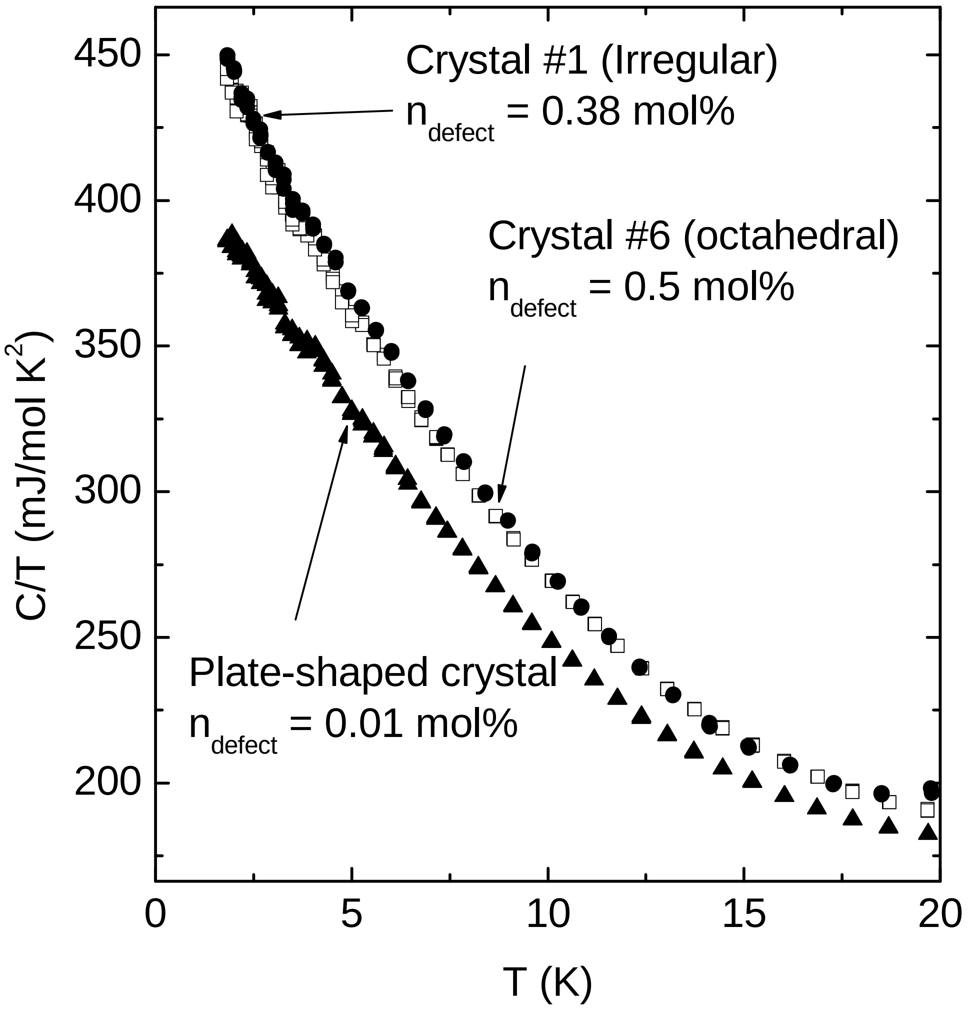

Figure 4.5 C/T versus T for crystals with varying n_{defect}: Crystal #1 (filled circles), crystal #6 (open squares), and a plate-shaped crystal (filled triangles).

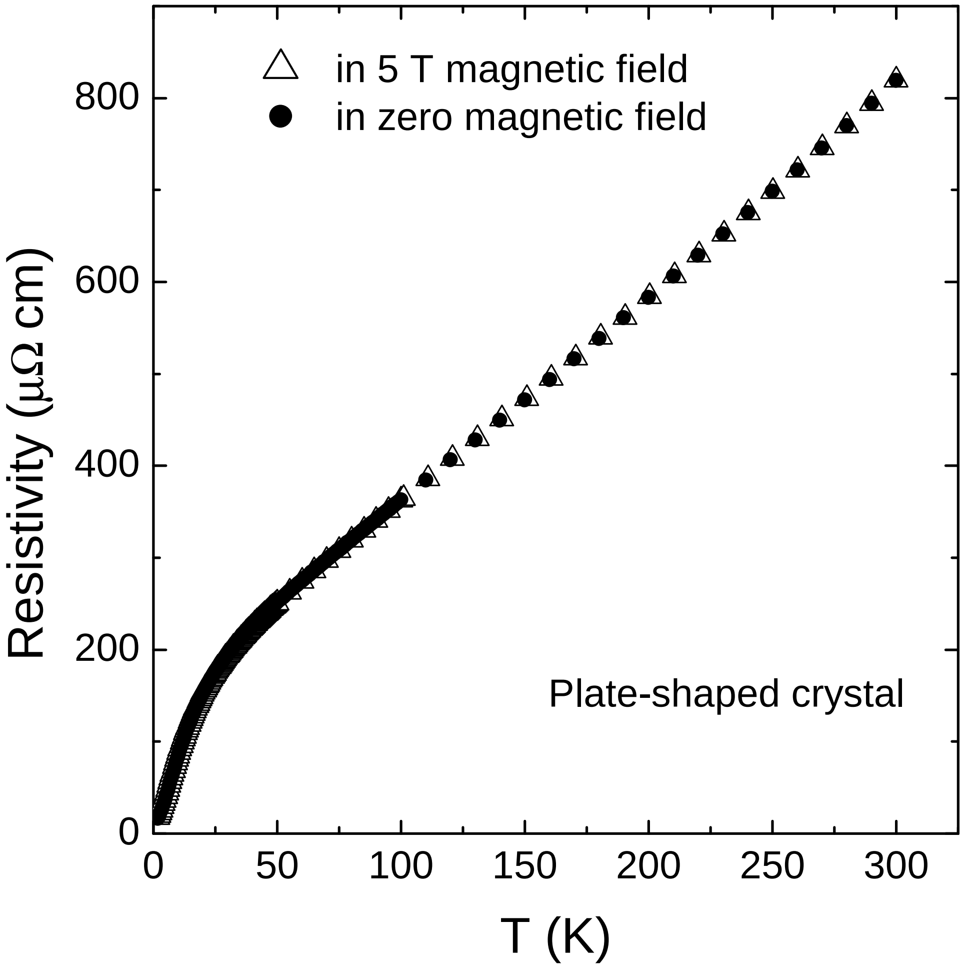

Figure 4.6 Temperature T variation of the resistivity of a plate-shaped crystal in zero field and in a 5 T magnetic field.

concentrations. The variations of γ with T for the octahedral and the irregular crystals are very similiar with the same value of γ at the lowest temperature. However, γ for the plate-shaped crystal is lower (380 mJ/mol K^2) at 1.8 K.

Figure 4.6 shows the temperature variation of the four-probe resistivity of a plate-shaped crystal both in zero magnetic field and in 5 T magnetic field. The applied field of 5 T is seen to have little influence on the resistivity. The resistivity decreases with decreasing T as expected for a metal. The residual resistivity ratio (RRR) for the plate-shaped crystal is 50, revealing its high crystal perfection. This value can be compared to the values of ≈ 2, ≈ 27 and ≈ 12 for the crystals in Refs. [29], [30] and [33], respectively.

4.5 Water treatment of LiV_2O_4

In view of the results in Ref. [33], we also performed an experiment to see if our crystals of LiV_2O_4 are sensitive to water exposure. We performed this experiment on both powdered samples and single crystals of LiV_2O_4. We selected a sample of LiV_2O_4 powder free of any magnetic defects. Then we put some of that powder into deionized water and some into a solution of $LiVO_3$ in deionized water for two weeks. The X-ray diffraction patterns of the two treated samples remained unchanged from the original sample. The magnetic susceptibilities of the two treated samples along with that of the original sample are plotted in Fig. 4.7(a). The susceptibilities of the three samples are nearly identical over the entire temperature range. With the single crystals, before dissolving the flux, a small crystal was broken off of the solified button of crystals embedded in the flux. The magnetic susceptibility of that small crystal was measured. Then it was put in water in an ultrasonic bath to dissolve the flux and after it was dried with acetone, it was left in water for 5 days. The magnetic susceptibility of that crystal before and after water treatment is shown in Fig. 4.7(b). Our findings for both powder and single crystal LiV_2O_4 contradict the results in Ref. [33] where the susceptibility of their LiV_2O_4 single crystals changes drastically after being exposed to air and moisture.

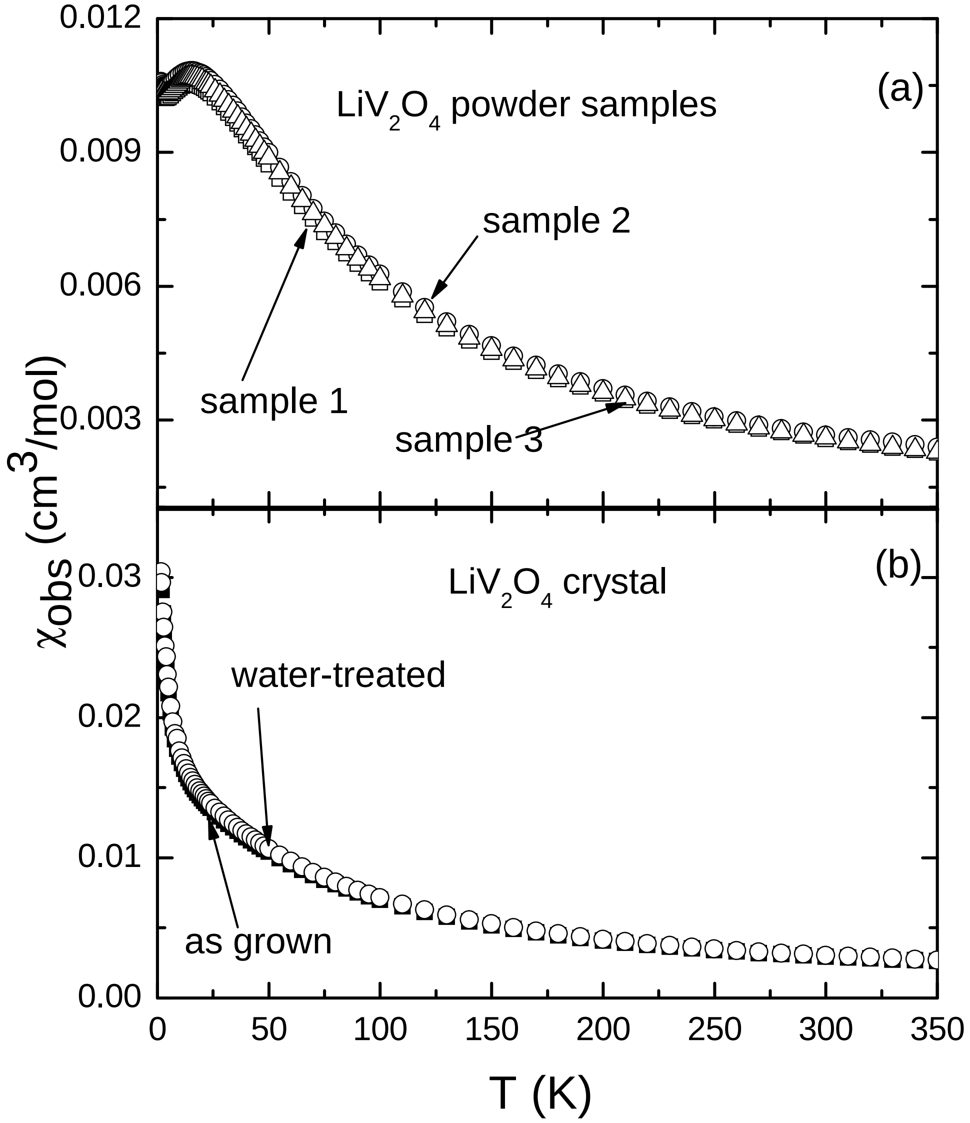

Figure 4.7 (a) Magnetic susceptibility of three LiV_2O_4 powder samples. Sample 1 (open squares) is the as-made LiV_2O_4 sample while samples 2 (open circles) and 3 (open triangles) are water treated and $LiVO_3$ solution treated, respectively. (b) Magnetic susceptibility of an as-grown (filled squares) and water treated (open circles) octahedral LiV_2O_4 single crystal.

4.6 Summary

In this chapter we have reported a new self-flux growth method to grow single crystals of LiV_2O_4 using the flux Li_3VO_4. The selection of Li_3VO_4 as the flux led to the study of the $LiV_2O_4 - Li_3VO_4$ pseudobinary phase diagram. LiV_2O_4 was found to decompose peritectically at 1040 °C. A eutectic was found with a eutectic temperature of 950 °C and the eutectic composition being approximately 53 wt% LiV_2O_4 and 47 wt% Li_3VO_4. The crystals are of high quality, and as with powder LiV_2O_4, are not reactive to air and moisture. The magnetic susceptibility of some of the crystals showed a Curie-like upturn at low T showing the presence of magnetic defects within the spinel structure. The defects could be nearly eliminated in some of the crystals by annealing them at 700 °C in vacuum. From the heat capacity measurements, a very large value of 450 mJ/mole K^2 was obtained for C/T for crystals having magnetic defects in them while a value of 380 mJ/mol K^2 was obtained for crystals which were free of any magnetic defects. The electrical resistivity measurement on a magnetically pure crystal revealed the expected metallic behavior down to 1.8 K.

In addition to the further study of heavy fermion behaviors in magnetically pure LiV_2O_4, the present method of crystal growth opens up new research areas associated with the physics of magnetic defects in LiV_2O_4. From detailed high resolution electron diffraction and/or synchrotron x-ray structural studies one may be able to determine the nature of the crystal defects giving rise to the magnetic defects. Important fundamental issues that can be addressed include whether the heavy Fermi liquid in magnetically pure LiV_2O_4 survives when magnetic defects are present and whether the crystal and magnetic defects drive a metal-insulator transition at some defect concentration. These questions can initially be addressed in the milliKelvin temperature range using electrical resistivity, magnetic susceptibility, NMR, and electrical resistivity measurements. A related question is whether a quantum critical point occurs versus magnetic defect concentration. These are exciting topics for future research.

CHAPTER 5. Absence of structural correlations of magnetic defects in the heavy fermion compound LiV_2O_4

This chapter is based on an article published in Phys. Rev. B **80**, 104401 (2009) by S. Das, A. Kreyssig, S. Nandi, A. I. Goldman, and D. C. Johnston.

Abstract

Magnetic defects arising from structural imperfections have pronounced effects on the magnetic properties of the face-centered cubic normal-spinel structure compound LiV_2O_4. High-energy x-ray diffraction studies were performed on LiV_2O_4 single crystals to search for superstructure peaks or other evidence of spatial correlations in the arrangement of the crystal defects present in the lattice. Entire reciprocal lattice planes were mapped out with the help of synchrotron radiation. No noticeable differences in the x-ray diffraction data between a crystal with high magnetic defect concentration and a crystal with low magnetic defect concentration were found. This indicates the absence of any long-range periodicity or short-range correlations in the arrangements of the crystal/magnetic defects.

5.1 Introduction

LiV_2O_4 is a material of great interest as it shows heavy fermion behavior at low temperatures ($T \lesssim 10$ K) in spite of being a d-electron metal.[8] This is of particular interest because most of the well known heavy fermion compounds have crystallographically ordered arrays of f-electron atoms. LiV_2O_4 has a face-centred cubic crystal structure (space group $Fd\bar{3}m$) with room temperature lattice parameters $a = b = c = 8.2393$ Å.[8] Each V atom is coordinated with six O atoms to form a slightly distorted octahedron.[111] The V atoms themselves form corner sharing tetrahedra, often called the "pyrochlore lattice", which is strongly geometrically frustrated for antiferromagnetic ordering. The vanadium atoms with nominal oxidation state of +3.5 occupy equivalent sites in the structure, making LiV_2O_4 metallic. The heavy fermion nature of LiV_2O_4 was discovered to occur below ~ 10 K from measurements of a large T-independent magnetic susceptibility $\chi \sim 0.01$ cm^3/mol and a large Sommerfeld heat capacity coefficient $\gamma \sim 420$ mJ/mol K^2.[8]

Magnetic defects in the structure have a pronounced effect on the magnetic properties of LiV_2O_4. For both polycrystalline samples and single crystals with extremely low magnetic defect concentration ($n_{\rm defect} \leq 0.01$ mol%), the low-T χ is T-independent.[8, 24, 33, 106] The heavy fermion behavior of LiV_2O_4 referred to above was inferred from measurements on such samples with extremely low $n_{\rm defect}$. However, in both powder and single crystal samples of LiV_2O_4 with high $n_{\rm defect}$ (up to a maximum of 0.8 mol%), the magnetic susceptibility shows a Curie-like upturn at low T.[8, 24, 106, 111] Crystal defects are the only possible source of these magnetic defects since magnetic impurity phases as the source of the low T Curie-like upturn was ruled out.[24, 106] Low T magnetization measurements on polycrystalline and single crystal LiV_2O_4 samples containing magnetic defects revealed large values of the average spins of these defects.[24, 106, 111] The spin values $S_{\rm defect}$ range from ~ 2 to 4.

The presence of magnetic defects has a dramatic influence on ^{7}Li NMR measurements of LiV_2O_4. NMR measurements on polycrystalline samples of LiV_2O_4 with extremely low $n_{\rm defect}$ show a linear variation of the ^{7}Li nuclear spin-lattice relaxation rate ($1/T_1$) versus T at low T.[25] This is typical for Fermi liquids. However, for polycrystalline samples of LiV_2O_4 with higher amounts of magnetic defects, the ^{7}Li $1/T_1$ shows a peak at ~ 1 K, and the relaxation recovery becomes strongly nonexponential.[25, 40] This observation raises the question whether the ground state of a $\mathrm{LiV_2O_4}$ sample with high $n_{\rm defect}$ is still a Fermi liquid or is a non-Fermi liquid. If the ground state changes to a non-Fermi liquid, then there might be a critical $n_{\rm defect}$ for the transition. The ^{7}Li NMR measurements indicated that the heavy Fermi liquid survives in the presence of a large concentration of magnetic defects.[40] Johnston et al.[25] suggested a model in which a crystal defect locally lifts the geometric frustration and thus allows magnetic order over a finite region around that defect, called a magnetic droplet. This model is qualitatively consistent with the large average values of $S_{\rm defect} \sim 2-4$ obtained from the low T magnetization measurements.

The only potential local magnetic moments in the system are $\mathrm{V^{+3}}$ ($S = 1$) and $\mathrm{V^{+4}}$ ($S = 1/2$) and from the observed values $S_{\rm defect} \sim 2-4$ of the spins of the magnetic defects, it is clear that a single V ion cannot give rise to a magnetic defect. The magnetic defects could be a group of V ions forming a cluster or having correlations among them. Given the pronounced effects of the magnetic defects on the properties of $\mathrm{LiV_2O_4}$, it is important to examine if there are any correlations in the spatial distribution of the crystal defects which produce the magnetic defects or if they are randomly distributed. One way to look for short and medium range spatial correlations in the defect structure is to map out complete reciprocal lattice planes and search for features in addition to the normal Bragg reflections. Long-range periodic ordering of the crystal defects would produce additional peaks in the x-ray diffraction patterns while short-range ordering can cause streaking of the Bragg peaks or diffuse broad signals. Here we report on high-energy x-ray studies of single crystals of $\mathrm{LiV_2O_4}$ with different magnetic defect concentrations.

5.2 Experimental details

High quality single crystals of $\mathrm{LiV_2O_4}$ used in the experiment were grown in a vertical tube furnace using $\mathrm{Li_3VO_4}$ as flux.[111] Three crystals, denoted as crystal 2, crystal 9, and crystal 10 with respective masses of 0.354 mg, 6.548 mg, and 2.1 mg were examined. The magnetic measurements on the crystals were done using a Quantum Design superconducting quantum interference device (SQUID) magnetometer in the temperature range 1.8 – 350 K and magnetic field range 0 – 5.5 T. The studied single crystals were selected based on typical magnetic behavior for low and high defect concentration. Crystals used in the measurements were of different sizes and shapes since as-grown crystals were used. Cutting or polishing the crystals would have given them a common size and shape and improve a quantitative analysis of the scattering data, but at the same time, this procedure had the potential to introduce additional crystal deformations due to strain and/or other mechanical effects. These could obscure the features due to the magnetic defects. We, therefore, decided on using as-grown single crystals. The high-energy x-ray diffraction measurements at room temperature were performed at the 6-ID-D station in the MU-CAT sector of the Advanced Photon Source, Argonne National Laboratory. The incident x-ray energy was set to 100 keV to ensure full penetration of the sample. The corresponding x-ray wavelength λ was 0.124 Å. The beam size was 0.3×0.3 mm^2. To record the full two-dimensional patterns, a MAR345 image-plate was positioned 705 mm behind the sample. During the experiments, the crystals were set between two pieces of thin kapton film and mounted on the sample holder.

5.3 Magnetic susceptibility and magnetization

Figure 5.1 shows the magnetic susceptibility χ versus temperature T of the crystals 2, 9, and 10 measured in a 1 T magnetic field. The magnetic defect concentrations of the crystals were calculated by fitting the observed molar magnetization M isotherms at low temperatures [$T \leq 5$ K, shown in Figs. 5.2(a), (b), and (c)] by the equation[24, 106]

$$M = \chi H + n_{\rm defect} N_{\rm A} g_{\rm defect} \mu_{\rm B} S_{\rm defect} B_S(x)\,, \tag{5.1}$$

where $n_{\rm defect}$ is the concentration of the magnetic defects, $N_{\rm A}$ is Avogadro's number, $g_{\rm defect}$ is the g-factor which was fixed to 2 for the spins of the magnetic defects (the detailed reasoning behind this is given in Ref. [24]), $\mu_{\rm B}$ is the Bohr magneton, $S_{\rm defect}$ is the average spin of the defects, $B_S(x)$ is the Brillouin function, χ is the intrinsic susceptibility of the pure LiV$_2$O$_4$ spinel phase in the absence of magnetic defects, and H is the applied magnetic field. The

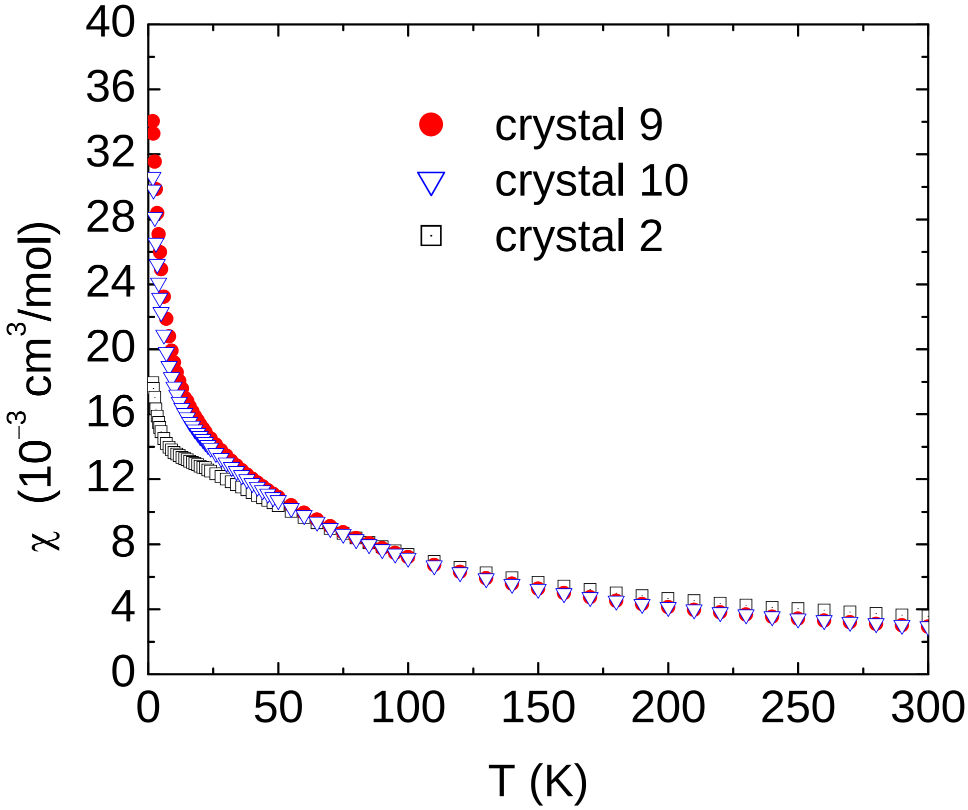

Figure 5.1 (Color online) Magnetic susceptibilities χ versus temperature T of LiV_2O_4 crystals containing different concentrations of magnetic defects (see Table 5.1). The susceptibilities are measured in 1 T magnetic field.

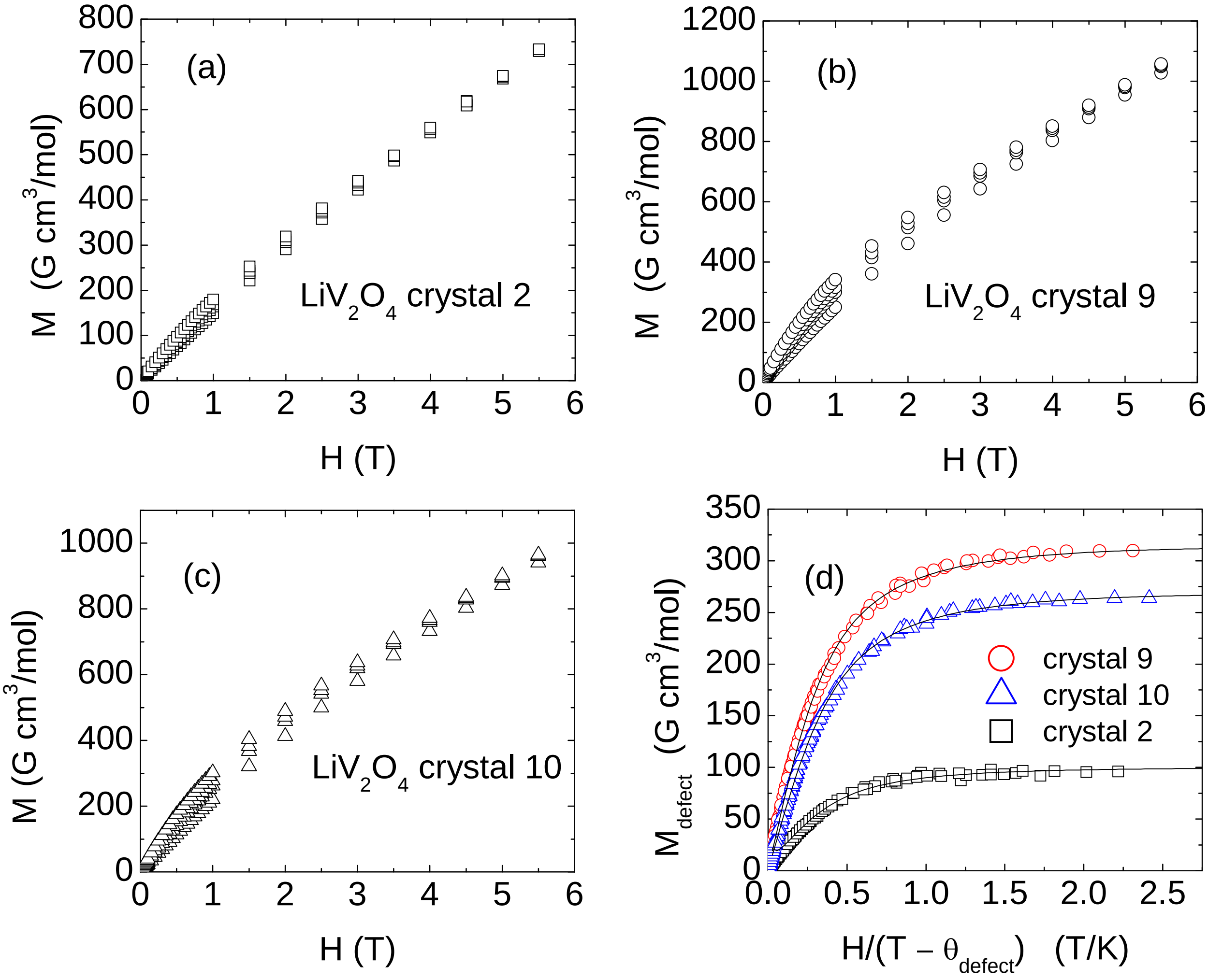

Figure 5.2 (Color online) Molar magnetization M versus applied magnetic field H isotherms at low temperatures ($T \leq 5$ K) for crystals (a) 2, (b) 9, and (c) 10, respectively. The four data sets shown in each of Figs. 5.2 (a), (b), and (c) are the $M(H)$ isotherms at four different temperatures 5 K, 3 K, 2.5 K, and 1.8 K. Figure 5.2(d) shows the magnetic defect contribution to the magnetization for each crystal $M_{\rm defect} = M - \chi H$ plotted versus $H/(T - \theta_{\rm defect})$. The solid lines are plots of the second term in Eq. (5.1) for each crystal with the parameters listed in Table 5.1.

Table 5.1 Magnetic parameters obtained from fits of Eq. (5.1) to the magnetization versus field measurements below 5 K in Fig. 5.1 of the three $\mathrm{LiV_2O_4}$ crystals. χ, $n_{\rm defect}$, $S_{\rm defect}$, and $\theta_{\rm defect}$ are magnetic susceptibility, magnetic defect concentration, spin of the magnetic defects, and Weiss temperature of the interactions among the magnetic defects, respectively. A number in parentheses indicates the error in the last digit of a quantity.

Sample no	χ (cm^3/mol)	$n_{\rm defect}$ (mol%)	$S_{\rm defect}$	$\theta_{\rm defect}$ (K)	$n_{\rm defect}S_{\rm defect}$ (mol%)
crystal 2	0.01158(6)	0.24(1)	3.6(2)	−0.7(1)	0.86(1)
crystal 9	0.0135(1)	0.71(3)	3.9(1)	−0.6(1)	2.78(7)
crystal 10	0.0127(1)	0.67(2)	3.6(1)	−0.5(1)	2.38(6)

argument of the Brillouin function $B_S(x)$ is $x = g_{\rm defect}\mu_{\rm B}S_{\rm defect}H/[{\rm k_B}(T-\theta_{\rm defect})]$ where $\theta_{\rm defect}$ is the Weiss temperature associated with the magnetic defects and $\mathrm{k_B}$ is Boltzmann's constant. The parameters fitted are χ, $n_{\rm defect}$, $S_{\rm defect}$, and $\theta_{\rm defect}$.

The best-fit parameters obtained from the fits of the $M(H)$ isotherm data in Figs. 5.2(a), (b), and (c) by Eq. (5.1) are tabulated in Table 5.1 for each crystal. Figure 5allimp(d) shows the defect contributions to the magnetization $M_{\rm defect} = M - \chi H$ for each crystal plotted versus $H/(T - \theta_{\rm defect})$. All the data points in Figs. 5allimp(a), (b), and (c) collapse onto a universal curve for each crystal, thus verifying the validity of the model and the fits. The solid lines in Fig. 5.2(d) are the plots of the second term in Eq. (fiteq) for the three crystals with the parameters listed in Table 5table1, respectively. Note that χ in Table 5.1 is constant to within ±8% as $n_{\rm defect}$ increases by nearly a factor of three. This indicates that the heavy Fermi liquid survives in the presence of the magnetic defects, consistent with the ^{7}Li NMR analysis in Ref. [26].

5.4 High-energy x-ray diffraction measurement

In order to search for long-range or short-range order in the arrangement of the crystal defects giving rise to the magnetic defects within the crystal structure, we carried out high-energy synchrotron x-ray diffraction measurements over a wide range of reciprocal space. The rocking technique used to record the diffraction intensities from planes in reciprocal space has been described in detail in Ref. [112]. Briefly, the patterns were obtained by recording the

Bragg reflections of all points of a reciprocal lattice plane intersecting the Ewald sphere. The orientation of the reciprocal lattice relative to the Ewald sphere is given by the orientation of the crystal with respect to the incident x-ray beam. Tilting the crystal through small angles allows complete reciprocal lattice planes of the crystal to intersect the Ewald sphere. In the experiment, diffraction patterns were obtained as in Fig. 5.3 below by tilting the crystal through two independent angles μ and η perpendicular to the incident x-ray beam by $\pm 3.2^\circ$. Patterns were recorded by continously scanning through μ as η was increased in small steps. By averaging the recorded patterns obtained at different values of μ and η, a considerable range of the designated reciprocal lattice planes was mapped out. This averaging over large parts of a Brillouin zone also enhances very weak broad scattering features making them detectable.

Depending on the kind of modification/deviation of the crystal structure arising from the crystal defects, we expect to see different modifications/deviations in the diffraction patterns of the reciprocal planes. A crystallographic superstructure, either commensurate or incommensurate, will produce weak additional Bragg reflections. Lower-dimensional or short-range order will produce broad features or diffuse scattering. For example, a two-dimensional order yields a rod-like scattering feature. If the incoming beam is parallel to the axis of the rod, we will see a spot in the diffraction pattern of that plane. The same feature, however, will yield a streak of intensity in the diffraction patterns of reciprocal planes perpendicular to the rod.

In our experiment, reflections from reciprocal lattice planes perpendicular to the three high symmetry directions, namely [001], $[\bar{1}01]$, and $[\bar{1}11]$ of the cubic structure, were recorded. Figures 5.3(a), (b), and (c) show the room temperature diffraction patterns from planes in the reciprocal space of crystal 2 ($n_{\text{defect}} = 0.24$ mol%) perpendicular to [001], $[\bar{1}01]$, and $[\bar{1}11]$ directions, respectively. The lattice planes perpendicular to the $[\bar{1}11]$ direction are very closely spaced. Thus in this direction, when we tilt the crystal, higher order reciprocal planes will also intersect the Ewald sphere and be observed.[112] This out-of-plane scattering was minimized by limiting the range of the tilts to $\pm 2.8^\circ$. Nevertheless, the reflections enclosed by the white lines in (c) and (f) are from the reciprocal layer through the origin which is perpendicular to the $(\bar{1}11)$ direction $[(hkl)$ reflections with $(hkl)\cdot[\bar{1}11] = 0]$. The outer spots are from the next layers $[(hkl)\cdot[\bar{1}11] = \pm 1]$.

In Figs. 5.3(a), (b), and (c), all the spots observed are allowed by the space group of the crystal. The intensity at the center of the Bragg reflections are 3–6 orders of magnitude higher than the intensity shown in black at the maximum in the scale for the contour map. We used iron slabs, up to 3 cm in thickness, to increase the dynamic range from 10^4 (intrinsic for the detector) to 10^7 by attenuating the incident x-ray beam. The greytone in Fig. 3 represents the intensity on a logarithmic scale. In each pattern, the scale has been chosen in such a manner that as much as possible, the details in low signals can be visualized. No extra spots or Bragg reflections were observed in the patterns. We conclude that there are no other single crystals or grains oriented in other directions or satellite reflections related to a superstructure of the given normal spinel structure. The shape of the spots is also as expected for the given resolution conditions.

Figures 5.3(d), (e), and (f) show the room temperature x-ray diffraction patterns from reciprocal planes of crystal 9 with high magnetic defect concentration ($n_{\text{defect}} = 0.62$ mol%) perpendicular to [001], $[\bar{1}01]$, and $[\bar{1}11]$ directions, respectively. For the planes perpendicular to the [001] and $[\bar{1}01]$ directions, there are no differences between the patterns obtained for crystal 2 and crystal 9. From the positions of the Bragg reflections, the lattice parameters of these two crystals are same to within our precision of one part in one thousand. For the plane perpendicular to the $[\bar{1}11]$ direction, a few spots were observed marked by solid circles in Fig. 5.3(f), which are not allowed by the symmetry of the space group and are missing in Fig. 5.3(c). These extra features are linearly extended compared to the circular spots and have an intensity 10^{-5} times that of the Bragg reflections. The position of these extra spots is close to the expected position of reflections from higher layers (e.g. (311) and symmetry equivalent reflections). By reducing or increasing the range of the rocking angles, the contribution from the higher layers can be modified. The intensity and shape of the additional features did not change when the patterns were recorded with different ranges for the rocking angles. This suggests that the additional features are located on the reciprocal plane close to the origin and eliminates significant contributions from Bragg reflections of higher layers or from the halos around them. We note that twinning or stacking faults of similiarly oriented crystals can allow such features to appear. Furthermore, as seen from the spots outside the white polygon, these features are not present in the other Brillouin zones with the same orientation. This excludes the possibility of periodic arrangement of such crystal defects.

The observed halos surrounding the Bragg reflections are partially caused by exposure of the adjacent pixels in the detector material due to light scattering between pixels within the detector for strong signals. The diffuse scattering dominating at lower count rates also contributes to the formation of the halos. Distinguishing between diffuse scattering arising from static disorder and thermal diffuse scattering arising from uncorrelated lattice vibrations would require extensive temperature-dependent studies including detailed two-dimensional profile analysis and is beyond the scope of the present study. The halos around the Bragg reflections are similar for both samples with high and low magnetic defect concentrations, respectively. Unfortunately, the visibility of the halos in the different patterns is handicapped by the different signal to background ratios which vary by up to a factor of twenty between the different patterns. This is due to different sizes and shapes of the samples and the resulting different scattering strengths of the samples and different absorptions of the primary beam and background signals. As a consequence, the halos in Fig. 5.3(b) are barely visible and barely separable from the background signal. A comparison of the intensity of the halos around strong reflections [e.g. (404) and (131)] with the intensity of the Bragg reflections themselves yields a similar ratio for both samples for patterns measured perpendicular to the $[\bar{1}01]$ direction shown in Figs. 3(b) and (e). The intensities at several data points in the halo of each Bragg reflection were compared with the maximum value in the center of the Bragg reflection itself. As long as the count rate in the halo was significantly above the background from incoherent and air scattering and the reflections were of comparable strength, the variation in the ratio was minimal. The ratio deviates slightly (by up to a factor of 1.6) for strong reflections, likely due to extinction effects. A comparison of the intensity of the halos and that of the corresponding Bragg reflections shows no obvious deviation from the expected scaling between the intensities. The similarity in the strength of the halos relative to the Bragg reflections for both types of samples, with low and high magnetic defect concentrations, suggests that the diffuse scattering is likely dominated by thermal diffuse scattering and cannot explain the observed difference in their magnetic properties.

To test if the appearance of the extended extra features for crystal 9 [shown in Fig. 5.3(f)] is an artifact of the particular crystal or is intrinsic, we performed the same experiment on crystal 10 which was grown under similiar conditions and has a similiar magnetic defect concentration as that of crystal 9. The x-ray diffraction pattern for the reciprocal lattice plane perpendicular to the $[\bar{1}11]$ direction of crystal 10 is shown in Fig. 5.4. We note that the additional spots present in Fig. 5.3(f) are missing here. There are a few very weak spots other than those allowed for the plane perpendicular to $[\bar{1}11]$ direction. These are caused by other misaligned crystals of the same material or impurities and illustrate the very high sensitivity of the technique to the smallest deviations/differences in the pattern from that expected for a perfect crystal. If we focus our beam onto different spots on the same crystal surface, the extra peaks vary in intensity or disappear.

5.5 Summary

No noticeable difference in the high-energy x-ray diffraction patterns of the reciprocal lattice planes of a crystal with high magnetic defect concentration and a crystal with low magnetic defect concentration has been found. This indicates the absence of any long-range periodicity or order in the arrangement of the crystal defects giving rise to the magnetic defects. We also did not observe any difference in the diffuse scattering in reciprocal space for both samples and thus exclude any long-range low-dimensional order or short-range order of the crystal defects related to the different magnetic defect concentrations. Thus we conclude that the crystal defects in LiV_2O_4 which produce the magnetic defects are randomly distributed within the spinel structure.

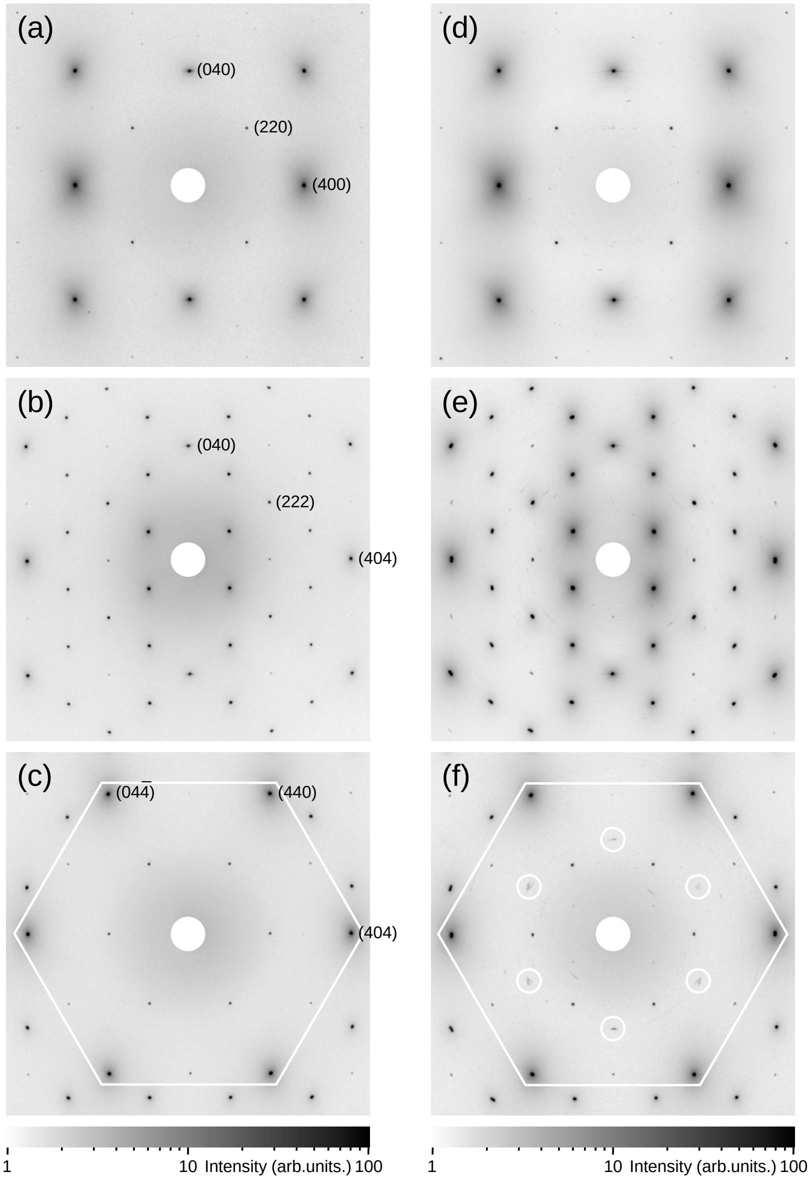

Figure 5.3 High-energy x-ray diffraction patterns of LiV_2O_4 single crystals 2 and 9. Figures 5.3(a), (b), and (c) show the patterns for reciprocal planes of crystal 2 perpendicular to the [001], [$\bar{1}$01], and [$\bar{1}$11] directions, respectively. Figures 5.3(d), (e), and (f) show the patterns for reciprocal planes of crystal 9 perpendicular to the [001], [$\bar{1}$01], and [$\bar{1}$11] directions, respectively. In (f), the extended features indicated by white circles are reflections that are not allowed by the symmetry. The reflection spots enclosed by the white lines in (c) and (f) are from the reciprocal (hkl) layer through the origin which is perpendicular to the [$\bar{1}$11] direction with $(hkl)\cdot[\bar{1}11] = 0$. The outer spots are from the next layers with $(hkl)\cdot[\bar{1}11] = \pm1$. The patterns shown have the same aspect ratio as that of the patterns recorded in the detector.

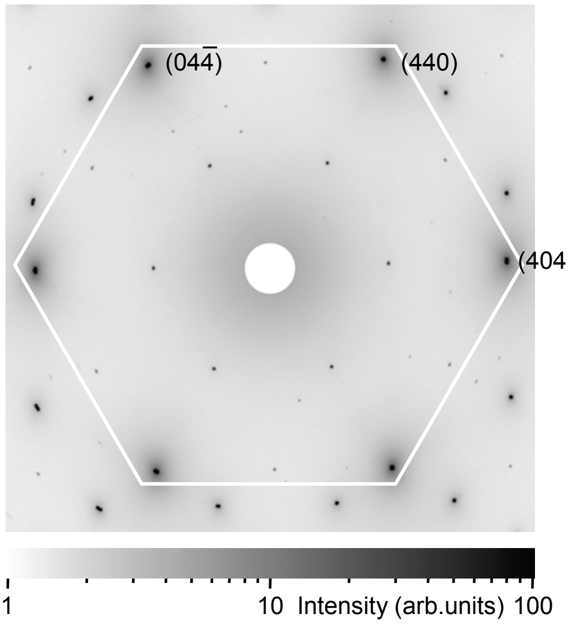

Figure 5.4 High-energy x-ray diffraction pattern of the reciprocal lattice plane perpendicular to the [$\bar{1}$11] direction of LiV_2O_4 crystal 10.

CHAPTER 6. Structural measurements under high pressure in the heavy fermion compound LiV_2O_4

This preliminary work was carried out in collaboration with M. Abliz and G. Shen at the Advanced Photon Source, Argonne National Laboratory.

6.1 Introduction

LiV_2O_4 is a material of great interest as it shows heavy fermion behavior at low temperatures ($T \lesssim 10$ K) in spite of being a d-electron metal.[8] This is of particular interest because most of the well known heavy fermion compounds have crystallographically ordered arrays of f-electron atoms. LiV_2O_4 has a face-centred cubic crystal structure (space group $Fd\bar{3}m$) with room temperature lattice parameters $a = b = c = 8.2393$ Å.[8] Each V atom is coordinated with six O atoms to form a slightly distorted octahedron.[111] The V atoms themselves form corner sharing tetrahedra, often called the "pyrochlore lattice", which is strongly geometrically frustrated for antiferromagnetic ordering. The vanadium atoms with nominal oxidation state of +3.5 occupy equivalent sites in the structure, making LiV_2O_4 metallic. The heavy fermion nature of LiV_2O_4 was discovered to occur below $\sim$ 10 K from measurements of a large T-independent magnetic susceptibility $\chi \sim 0.01$ cm^3/mol and a large Sommerfeld heat capacity coefficient $\gamma \sim 420$ mJ/mol K^2.[8]

Powder x-ray diffraction patterns obtained under increasing pressure and at a fixed temperature of 10 K showed a splitting of the single (440) cubic peak into two rhombohedral peaks at 12.8 GPa.[34] It was also observed that as the temperature was raised keeping the pressure constant at 12.8 GPa, the split peaks recombine into a single peak above 200 K.[34] ^{7}Li NMR measurements in LiV_2O_4 under high pressure revealed an enhanced nuclear spin-lattice relaxation rate $1/T_1$ in 4.74 GPa below 10 K.[35] Recently, extended x-ray absoption fine structure analysis suggested a cubic to rhombohedral structural transition above 12 GPa at room temperature.[36] To accurately determine the high pressure structure with all the structural parameters, we carried out preliminary powder x-ray diffraction measurements at room temperature and at high pressure.

6.2 Experimental

A symmetric diamond-anvil cell with two anvils of 300 micron culets was used to preindent a Re gasket from an original thickness of 250 μm to 22 μm central thickness. A 150 micron diameter hole was drilled at the center of the gasket indent to form the sample chamber. A single crystal sample LiV_2O_4 was crushed into powder with about 5 micron average grain size. Then, the powder was pressed into a thin disk and a 40 micron diameter sample was loaded into the hole of the gasket on the diamond. The sample was Ar gas loaded for a pressure medium to get a uniform pressure on the sample. The initial pressure was 1.5 GPa after gas loading. A few 5–10 micron diameter ruby spheres were added to a quadrant of the sample chamber for pressure measurement. High pressure angle-dispersive diffraction experiments were performed at the 16BMD station of the HPCAT Sector, Advanced Photon Source, Argonne National Laboratory. A monochromatic x-ray beam was focused to a diameter of $\sim$ 20 micron at the sample position. Pressure was measured by the ruby R1 fluorescence with an Ar-ion laser. The diffraction patterns were collected using a MAR3450 image plate and the exposure time was typically 300 s. The two-dimensional diffraction rings on the image plate were integrated with the FIT2D program to produce diffraction patterns of intensity versus Bragg angle 2θ, and the lattice parameters were obtained by Rietveld refinement of these diffraction patterns using the GSAS program suite.[113]

6.3 Results

Figure 6.1 shows the powder x-ray diffraction pattern of powder LiV_2O_4 at a pressure of 1.5 GPa. Figure 6.2 shows intensity versus 2θ obtained by integrating the pattern in Fig. 6.1

versus the azimuthal angle. The solid line in Fig. 6.2 is the fitted pattern using the normal spinel structure of $\mathrm{LiV_2O_4}$. All the observed peaks could be indexed using the normal spinel structure. Figure 6.3 shows the x-ray diffraction pattern in 20 GPa. A new structure is revealed from the splitting of the third bright ring. Figure 6.4 shows the lattice parameter a versus applied pressure P, where a is obtained by fitting the integrated intensity versus 2θ patterns using Rietveld analysis for pressures up to 13 GPa. The dotted line in Fig. 6.4 is the linear fit to the data in the pressure range 1.5–6.17 GPa while the solid line is the linear fit to data in the pressure range 8.31–13.17 GPa. The two fitted straight lines have different slopes as seen in Fig. 6.4. There might be a structural transition at 5.8 GPa where the two fitted straight lines intersect, as shown by a vertical arrow in Fig. 6.4. Extrapolation of the dotted line to ambient pressure yields a lattice parameter $a = 8.310(2)$ Å. This value is significantly higher than the value of the lattice parameter $a = 8.24$ Å at room temperature and at ambient pressure reported earlier,[21, 111] indicating the presence of a systematic error of unknown origin in the measurements. The calculated bulk modulus in the low-pressure region is $B = -V dP/dV = 124(4)$ GPa. The obtained bulk modulus is comparable to the bulk modulus of the spinel $\mathrm{MgAl_2O_4}$.[114]

6.4 Summary

We have carried out preliminary high pressure powder x-ray diffraction measurements on polycrystalline $\mathrm{LiV_2O_4}$ obtained by powdering single crystals, and found evidence that structural phase transitions occur at high pressure. The lattice parameter at ambient pressure obtained by extrapolation of the a versus P data to zero P yields $a = 8.31$ Å which is significantly higher than the lattice parameter at ambient pressure reported in the literature. The reason behind this deviation is not understood at this point. The background intensities in the two-dimensional diffraction patterns were also very high resulting in the mid and high angle peaks in the patterns being barely visible. More detailed powder and single crystal x-ray diffraction measurements at high pressures are required to accurately determine the symmetry and the structural parameters of the high-pressure phase(s).

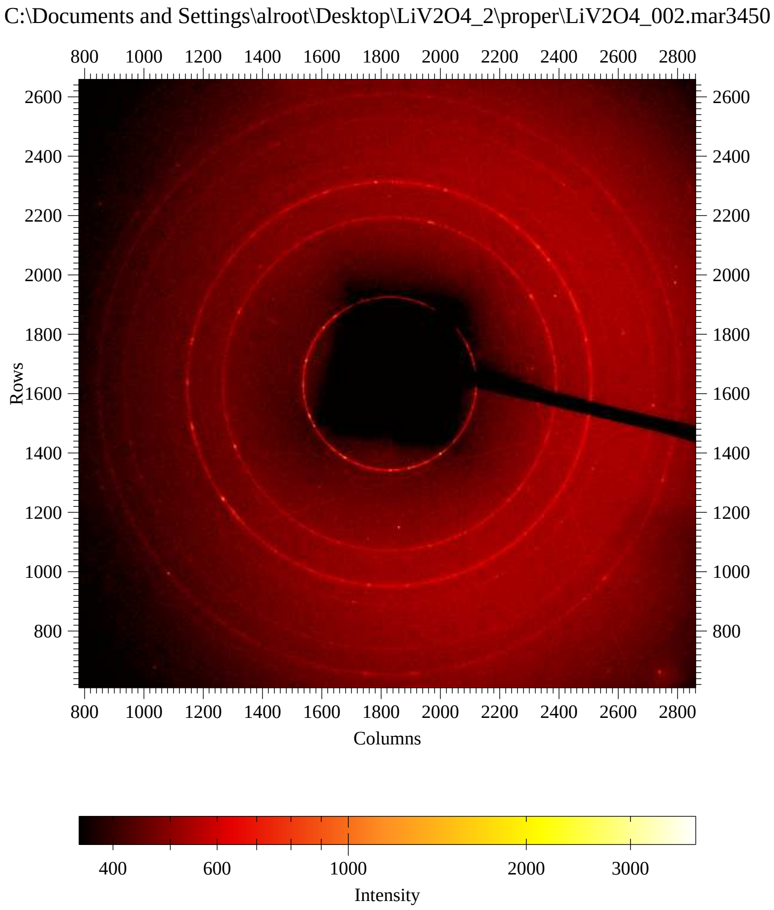

Figure 6.1 X-ray diffraction data of powder LiV_2O_4 at 1.5 GPa pressure.

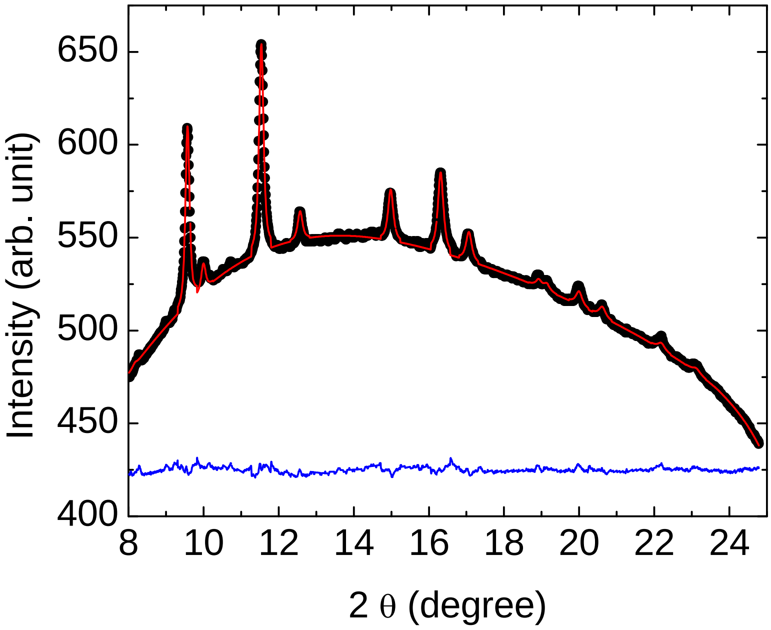

Figure 6.2 Observed intensity versus 2θ obtained by integrating the diffraction rings of the powder x-ray diffraction pattern of LiV_2O_4 at 296 K and 1.5 GPa, along with the calculated pattern using Reitveld refinement. The lower trace shows the difference between the observed and calculated intensities versus 2θ.

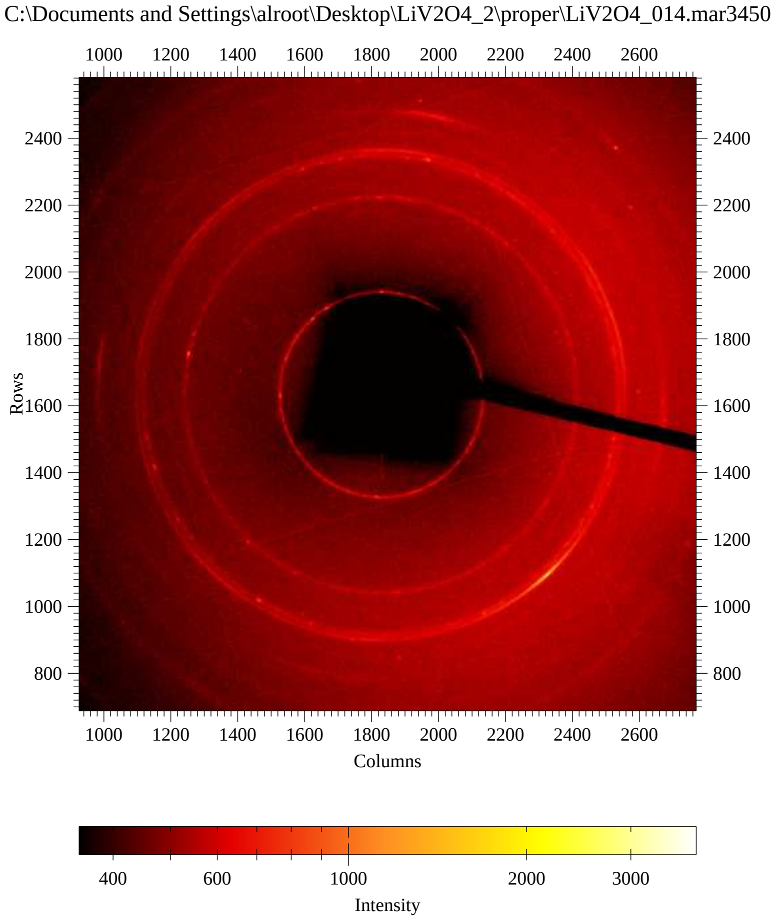

Figure 6.3 X-ray diffraction data of powder LiV_2O_4 at 20 GPa pressure. There is a clear splitting of the third bright ring.

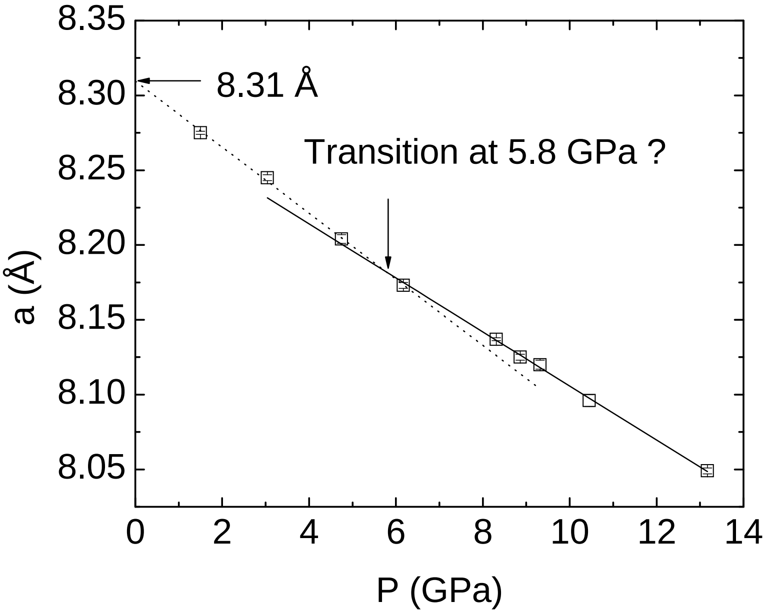

Figure 6.4 Cubic lattice parameter a vs pressure P for polycrystalline $\mathrm{LiV_2O_4}$. The dotted line is a linear fit to the data in the pressure range 1.5–6.17 GPa while the solid line is the linear fit to the data in the pressure range 8.31–13.17 GPa. The vertical arrow points to the pressure where the the two fitted lines intersect on extrapolation. The horizontal arrow points to the lattice parameter at ambient pressure obtained by extrapolating the dotted line to zero pressure.

CHAPTER 7. Magnetic, thermal, and transport properties of the mixed valent vanadium oxides $\mathbf{LuV_4O_8}$ and $\mathbf{YV_4O_8}$

This chapter is based on an article submitted to Phys. Rev. B that is currently under review, by S. Das, A. Niazi, Y. Mudryk, V. K. Pecharsky, and D. C. Johnston.

Abstract

LV$_4$O$_8$ (L = Yb, Y, Lu) compounds are reported to crystallize in a structure similar to that of the orthorhombic $CaFe_2O_4$ structure-type, and contain four inequivalent V sites arranged in zigzag chains. We confirm the structure and report the magnetic, thermal, and transport properties of polycrystalline YV_4O_8 and LuV_4O_8. A first-order like phase transition is observed at 50 K in both YV_4O_8 and LuV_4O_8. The symmetry remains the same with the lattice parameters changing discontinously. The structural transition in YV_4O_8 leads to partial dimerization of the V atoms resulting in a sudden sharp drop in the magnetic susceptibility. The V spins that do not form dimers order in a canted antiferromagnetic state. The magnetic susceptibility of LuV_4O_8 shows a sharp peak at $\sim$ 50 K. The magnetic entropies calculated from heat capacity versus temperature measurements indicate bulk magnetic transitions below 90 K for both YV_4O_8 and LuV_4O_8.

7.1 Introduction

Vanadium oxides have been of broad interest owing to their interesting properties. Binary vanadium oxides V_nO_{2n-1} where $2 \leq n \leq 9$ exhibit metal to insulator and paramagnetic to antiferromagnetic transitions on cooling.[115] The only exception is V_7O_{13} which remains metallic down to 4 K.[7] Among ternary vanadium oxides, the normal spinel mixed valent LiV_2O_4 does not show any magnetic ordering, remains metallic down to 0.5 K and surprisingly shows heavy fermion behavior below 10 K.[8] This is very different from the similar normal spinel $LiTi_2O_4$ which shows superconductivity below 13 K.[116]

The compound CaV_2O_4 forms in the well-known $CaFe_2O_4$ type structure with orthorhombic space group *Pnam* and lattice parameters $a = 9.206$ Å, $b = 10.674$ Å, and $c = 3.009$ Å.[9, 10, 117] The V atoms have spin $S = 1$ and form a zigzag chain system. The compound undergoes an orthorhombic to monoclinic structural distortion below 150 K and an antiferromagnetic transition at 63 K, and is an insulator.[40, 117, 118] The low dimensionality of the V spin structure is very interesting since this can give rise to exotic magnetism. Indeed, there is a suggestion that a phase transition at $\simeq$ 200 K in CaV_2O_4 arises from a long- to short-range chiral ordering transition with no long-range spin order either below or above this temperature.[117] In a spin $S = 1$ zigzag chain system, depending on the ratio of the nearest-neighbor and next-nearest-neighbor interactions, there can be ground states with a Haldane gap, as well as gapless or gapped chiral ordering.[39] Replacing Ca^{2+} by Na^{+1}, the same $CaFe_2O_4$ structure is retained but becomes metallic even below the antiferromagnetic transition at 140 K.[43, 44] Further investigations of compounds having the $CaFe_2O_4$-type and related structures are clearly warranted.

The compounds LV_4O_8 (L = Yb, Y, Lu) have structures similar to the $CaFe_2O_4$-type structure but with the modification that in LV_4O_8, only half of the L cation sites are occupied by L ions in an ordered manner.[45] This results in a reduction of the unit cell symmetry from orthorhombic to monoclinic with space group $P12_1/n1$ (which is a nonisomorphic subgroup of the orthorhombic space group *Pnam* of CaV_2O_4) and lattice parameters $a = 9.0648$ Å, $b = 10.6215$ Å, $c = 5.7607$ Å, and $\beta = 90.184°$ for the room temperature α-phase (see below)

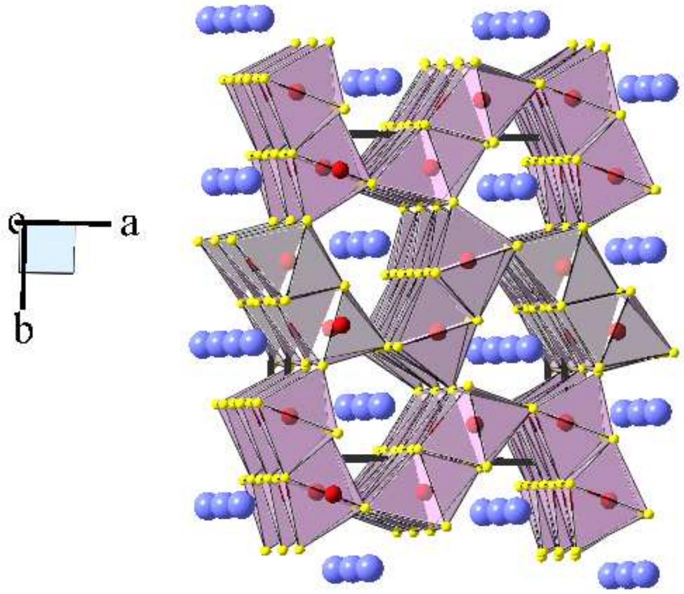

Figure 7.1 (Color online) Crystal structure of the low-temperature α-phase of $L\mathrm{V}_4\mathrm{O}_8$ viewed along the c-axis. The large blue, intermediate red, and small yellow circles represent L, V and O atoms, respectively. The VO_6 octahedra share edges to form V zigzag chains running along the c-axis. The L ions occupy half of the cation sites in the $\mathrm{CaV}_2\mathrm{O}_4$ structure in an ordered fashion while the other half is vacant.

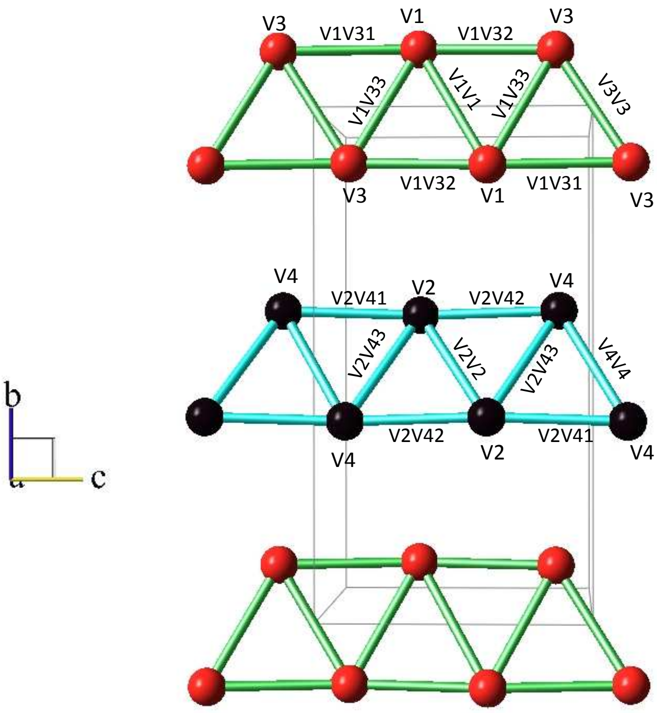

Figure 7.2 (Color online) The arrangment of V atoms in the structure as viewed along the *a*-axis. Two distinct chains are formed by V atoms in four inequivalent sites labelled V1, V2, V3, and V4, respectively. The bond lengths between different V atoms are labelled as V1V1, V2V2, V3V3, V4V4, V1V31, V1V32, V1V33, V2V41, V2V42, and V2V43, respectively.

of the Yb compound.[45] Note that the monoclinic angle β is close to 90° and that the a-axis and b-axis lattice parameters are nearly the same as in the above orthorhombic room-temperature structure of CaV_2O_4. Figure 7.1 shows the structure of α-LV_4O_8 viewed along the c axis. The slightly distorted VO_6 octahedra share edges and corners to form zigzag chains along the c axis. The four V atoms in the structure occupy four inequivalent positions and form two distinct chains with two inequivalent V positions in each chain. The V-V zigzag chains as viewed along the a axis are shown in Fig. 7.2.

YbV_4O_8 forms in two monoclinic phases, the low temperature α-phase with space group $P12_1/n1$ and lattice parameters $a = 9.0648$ Å, $b = 10.6215$ Å, $c = 5.7607$ Å, and $\beta = 90.184°$ and the high temperature β-phase with space group $P2_1/n11$ and lattice parameters $a = 9.0625$Å, $b = 11.0086$ Å, $c = 5.7655$ Å, and $\alpha = 105.070°$.[45] The two phases differ crystallographically by the z atomic position of the Yb ions, but both contain similar zigzag chains. At 185 K the β-YbV_4O_8 undergoes a magnetic phase transition with magnetic behavior of the vanadium cations separating into Curie-Weiss and spin gap types. The magnetic transition is accompanied at the same temperature by a monoclinic to monoclinic structural phase transition arising from complete charge ordering of the V^{+3} and V^{+4} ions.[46] YV_4O_8 also cystallizes in α and β forms isomorphous with α- and β-YbV_4O_8.[47] LuV_4O_8 was reported to have a homogeneity range from $LuV_4O_{7.93}$ to $LuV_4O_{8.05}$[119] and its structure is isostructural with α-YbV_4O_8.[45]

The structures of the above LV_4O_8 compounds are closely related to the Hollandite-type structure with either tetragonal or monoclinic crystal symmetry and chemical formula $A_xB_8O_{16}$ (A = K, Li, Sr, Ba, Bi; B = Ti, V, Mn, Ru, Rh; $1 \leq x \leq 2$).[120, 121] In the Hollandites, edge-sharing BO_6 octahedra form zigzag chains running parallel to the crystallographic c axis. The Hollandite $K_2V_8O_{16}$ undergoes a metal-isulator and a structural transition at 170 K which leads to possible dimerization of the V spins.[122] The presence of a quantum phase transition from a weakly localized state to a metallic state in $BaRu_6O_{12}$ has been reported.[123]

The magnetic susceptibilties of α-YV_4O_8 and β-YV_4O_8 show Curie-Weiss behavior in the high T region and drop sharply on cooling to temperatures between 50 and 80 K.[47] For

α-YV_4O_8, the drop at 50 K appears to be a first order transition. This is different from the magnetic susceptibility of the isostructural YbV_4O_8 or similiarly structured CaV_2O_4.[40] Curie-Weiss fits to the high T susceptibilities yielded negative Weiss temperatures indicating dominant antiferromagnetic interactions among the V spins and Curie constants much lower than expected for three V^{+3} ($S = 1$) and one V^{+4} ($S = 1/2$) spins per formula unit for both α- and β-YV_4O_8. In order to investigate the origin of the first order-like transition in YV_4O_8 and to search for interesting magnetic ground states in these zigzag spin chain systems with modified $CaFe_2O_4$ crystallographic structure, we have synthesized polycrystalline samples of YV_4O_8 and LuV_4O_8 and report their structure, magnetic susceptibility χ, magnetization M, specific heat C, and the electrical resistivity ρ.

The remainder of the chapter is organized as follows. In Sec. 7.2, the synthesis procedure and other experimental details are reported. The structures from room temperature down to 10 K, magnetic susceptibility, magnetization, heat capacity, and electrical resistivity measurements are presented in Sec. 7.3. We also carried out bond valence analysis to estimate the valences of the inequivalent V atoms in the mixed valent YV_4O_8 and LuV_4O_8 compounds. The results of this analysis are reported following the x-ray diffraction measurements in Sec. 7.3. In Sec. 7.4, we suggest a model to explain the observed magnetic susceptibility and heat capacity behaviors of YV_4O_8 in light of the structural studies reported in Sec. 7.3, whereas a model to explain the magnetic susceptibility and heat capacity behaviors of LuV_4O_8 is elusive. A summary of our results is given in Sec. 7.5.

7.2 Experimental details

The samples of LV_4O_8 (L = Y, Lu) were prepared by solid state reaction. The starting materials for our samples were Y_2O_3 (99.995%, Alfa Aesar), Lu_2O_3, V_2O_5 (99.999%, MV Laboratories Inc.), and V_2O_3 (99.999%, MV Laboratories Inc.). Stoichiometeric amounts of L_2O_3,V_2O_5, and V_2O_3 were thoroughly mixed together in a glove box filled with helium gas, and pressed into pellets. The pellets were wrapped in platinum foils, sealed in evacuated quartz tubes and heated at 520 °C for 8–10 d. The temperature was then raised to 800 °C for another

5–7 d. Finally the samples were heated at 1200 °C for another 7 d. The quartz tubes were then taken out of the furnace at 1200 °C and quenched in air to room temperature.

Powder x-ray diffraction measurements at room temperature were done using a Rigaku Geigerflex diffractometer with a curved graphite crystal monochromator. Temperature-dependent powder x-ray diffraction studies were done in the temperature range 10 K – 295 K using a standard Rigaku TTRAX diffractometer system equipped with a theta/theta wide-angle goniometer and a Mo $K\alpha$ radiation source.[124] The magnetic measurements were done using a Quantum Design superconducting quantum interference device (SQUID) magnetometer in the temperature range 1.8 K – 350 K and magnetic field range 0 – 5.5 T. The heat capacity and electrical resistivity measurements were done using a Quantum Design physical property measurement system (PPMS). For the heat capacity measurements, Apiezon N grease was used for thermal coupling between the samples and the sample platform. Heat capacity was measured in the temperature range 1.8 K – 320 K in zero, 5 T, and 9 T magnetic fields. Electrical resistivity measurements were carried out using a standard dc 4-probe technique. Platinum leads were attached to rectangular shaped pieces of sintered pellets using silver epoxy. An excitation current of 10 mA was used in the resistivity measurements in the temperature range 1.8 K – 300 K.

7.3 Results

7.3.1 X-ray diffraction measurements

Figures 7.3(a) and (b) show the room temperature x-ray diffraction (XRD) patterns of powder samples of YV_4O_8 and LuV_4O_8, respectively, along with the calculated patterns. The calculated patterns were obtained by Rietfeld refinements of the observed patterns using the GSAS program suite.[113, 125] The refinements for both YV_4O_8 and LuV_4O_8 were done with space group $P12_1/n1$ (No. 14) (the same space group as for the low-T α-phase of YbV_4O_8) with one position for the L atom, four different positions for V atoms, and eight different positions for O atoms. All the fractional atomic positions, the lattice parameters, and the overall thermal parameter for all the atoms were varied in the refinement. The obtained best-

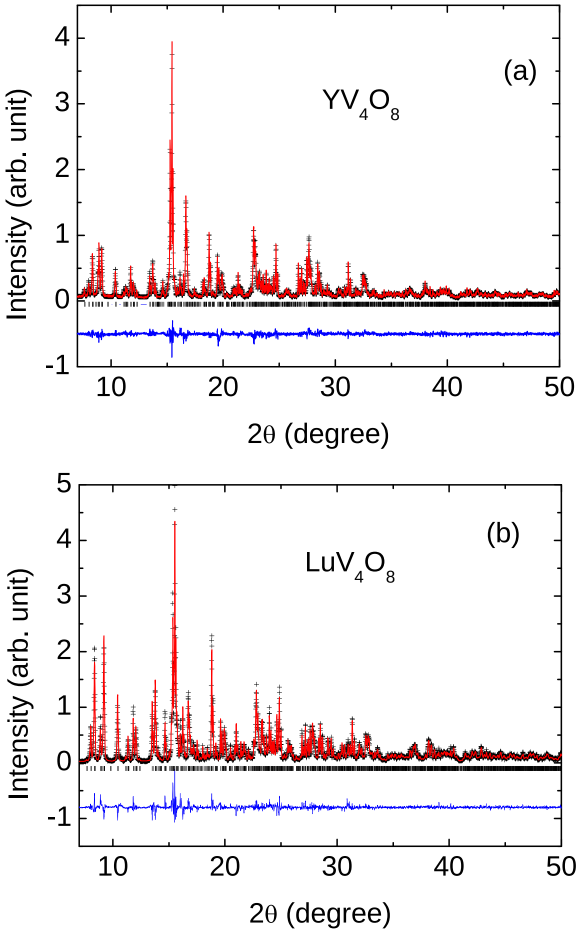

Figure 7.3 (Color online) X-ray diffraction patterns of YV_4O_8 (a) and LuV_4O_8 (b), respectively, at room temperature. The solid crosses are the observed data points while the solid lines are the Rietveld fits to the data. The tic marks below the data indicate the peak positions. The solid lines below the tick marks are the difference between the observed and the calculated intensities. Small amounts ($<$ 4 wt%) of V_2O_3 impurity phases are present in both YV_4O_8 and LuV_4O_8 samples.

Table 7.1 Lattice parameters and the fractional atomic positions of YV_4O_8 at 295 K, obtained by Rietveld refinement of powder XRD data. Space group: $P12_1/n1$ (No. 14); $Z = 4$ formula units/unit cell; lattice parameters: $a = 9.1186(2)$ Å, $b = 10.6775(2)$ Å, $c = 5.7764(1)$ Å, and monoclinic angle $\beta = 90.206(1)°$; $R(F^2) = 0.083$. All atoms are in general Wyckoff positions $4(e)$: x, y, z. A number in parentheses gives the error in the last or last two digits of the respective quantity.

	x	y	z
Y1	0.7574(2)	0.6581(2)	0.1257(4)
V1	0.4282(3)	0.6175(3)	0.1266(8))
V2	0.4107(3)	0.0989(3)	0.1235(9)
V3	0.4537(3)	0.6111(3)	0.6263(8)
V4	0.4193(3)	0.1043(3)	0.6252(9)
O1	0.1977(9)	0.1516(1)	0.0977(21)
O2	0.1154(9)	0.4760(10)	0.1266(29)
O3	0.5278(9)	0.7744(9)	0.1285(30)
O4	0.4238(11)	0.4297(9)	0.1177(33)
O5	0.2198(9)	0.1492(10)	0.6164(22)
O6	0.1195(10)	0.4800(11)	0.6227(27)
O7	0.5119(10)	0.7934(9)	0.6155(28)
O8	0.4130(11)	0.4287(9)	0.6450(30)

Table 7.2 Lattice parameters and the fractional atomic positions of LuV_4O_8 at 295 K, obtained by Reitveld refinement of powder XRD data. Space group: $P12_1/n1$ (No. 14); $Z = 4$ formula units/unit cell; lattice parameters: $a = 9.0598(2)$ Å, $b = 10.6158(2)$ Å, $c = 5.7637(1)$ Å, and monoclinic angle $\beta = 90.189(2)^\circ$; $R(F^2) = 0.095$. All atoms are in general Wyckoff positions 4(e): x, y, z. A number in parentheses gives the error in the last or last two digits of the respective quantity.

	x	y	z
Lu1	0.7573(2)	0.6583(1)	0.159(2)
V1	0.4269(4)	0.6170(4)	0.1281(11)
V2	0.4103(4)	0.0976(4)	0.1217(13)
V3	0.4549(4)	0.6107(4)	0.6332(11)
V4	0.4182(4)	0.1046(4)	0.6230(12)
O1	0.2019(13)	0.1609(13)	0.1091(33)
O2	0.1250(15)	0.4698(14)	0.1278(42)
O3	0.5299(14)	0.7774(14)	0.1258(45)
O4	0.4158(16)	0.4237(12)	0.1341(42)
O5	0.2098(13)	0.1670(12)	0.6358(34)
O6	0.1221(16)	0.4747(14)	0.6311(41)
O7	0.5135(14)	0.7938(14)	0.6283(42)
O8	0.4095(16)	0.4314(14)	0.6382(43)

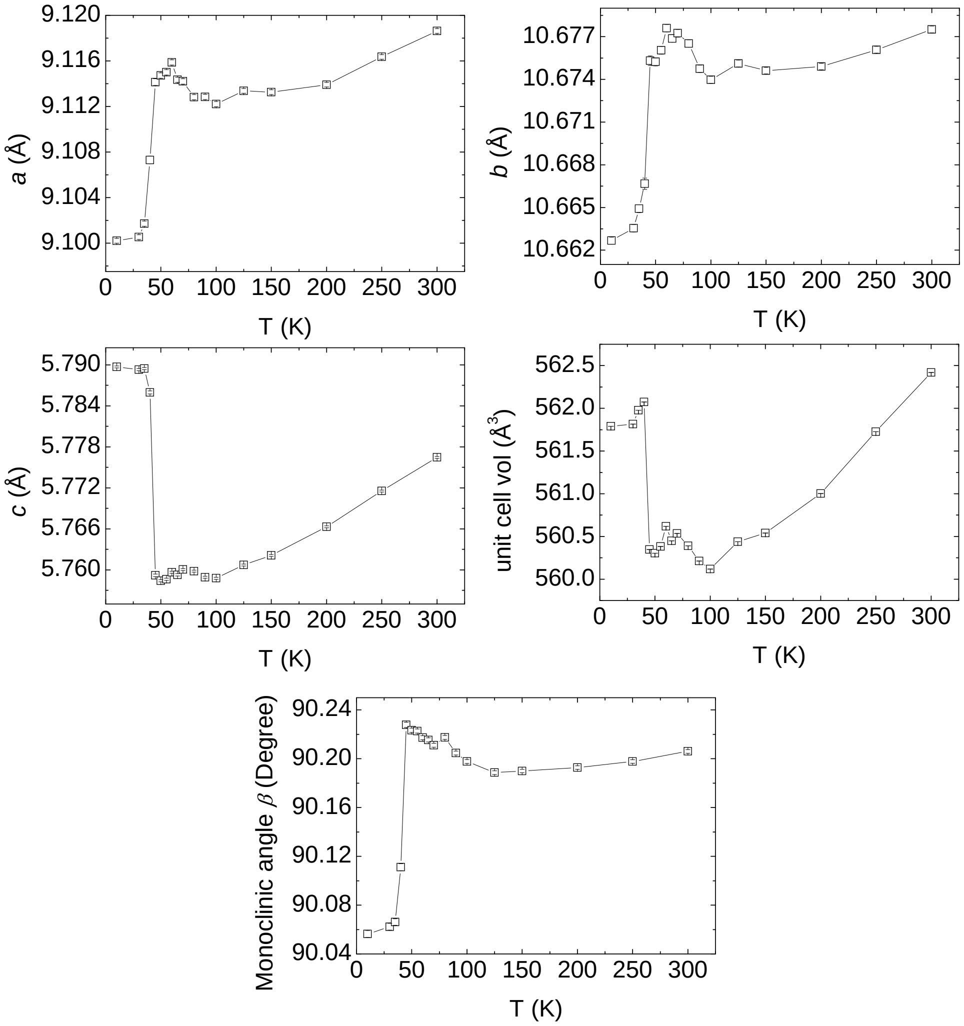

Figure 7.4 Lattice parameters a, b, c, unit cell volume, and the monoclinic angle β of YV_4O_8 versus temperature T.

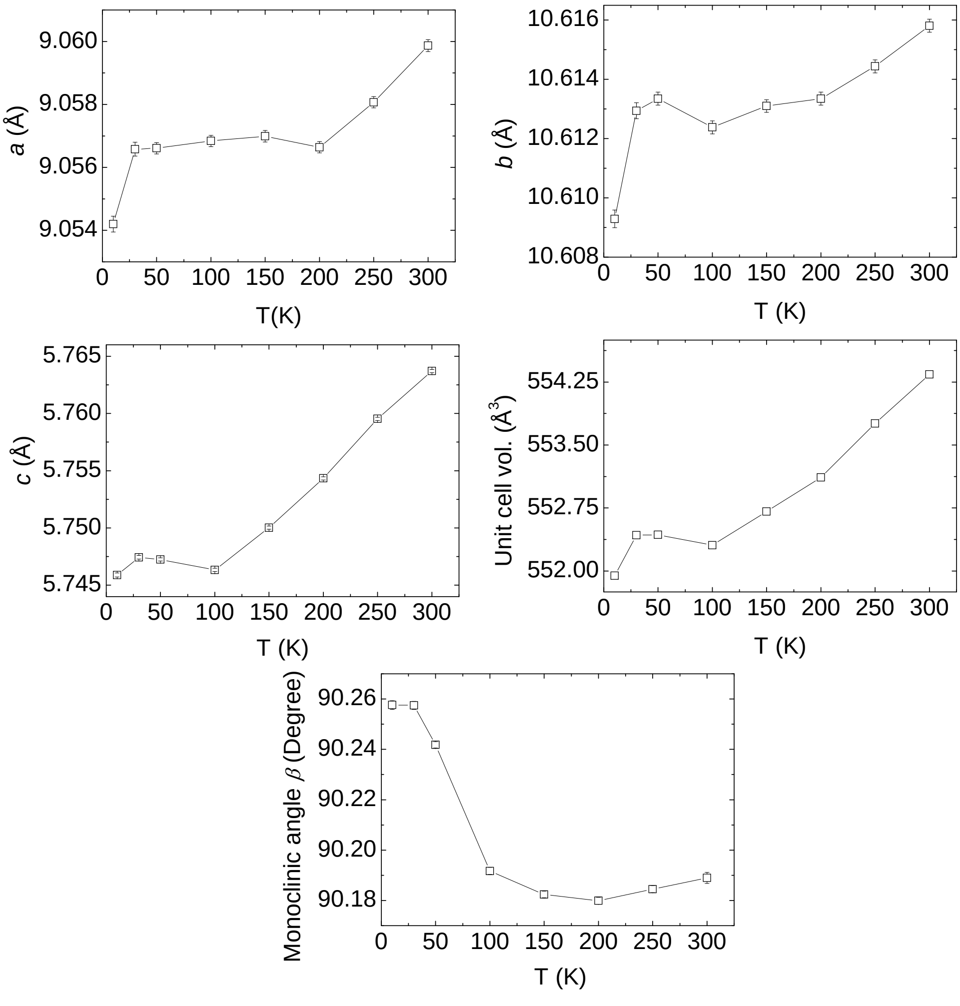

Figure 7.5 Lattice parameters a, b, c, unit cell volume, and the monoclinic angle β of LuV_4O_8 versus temperature T.

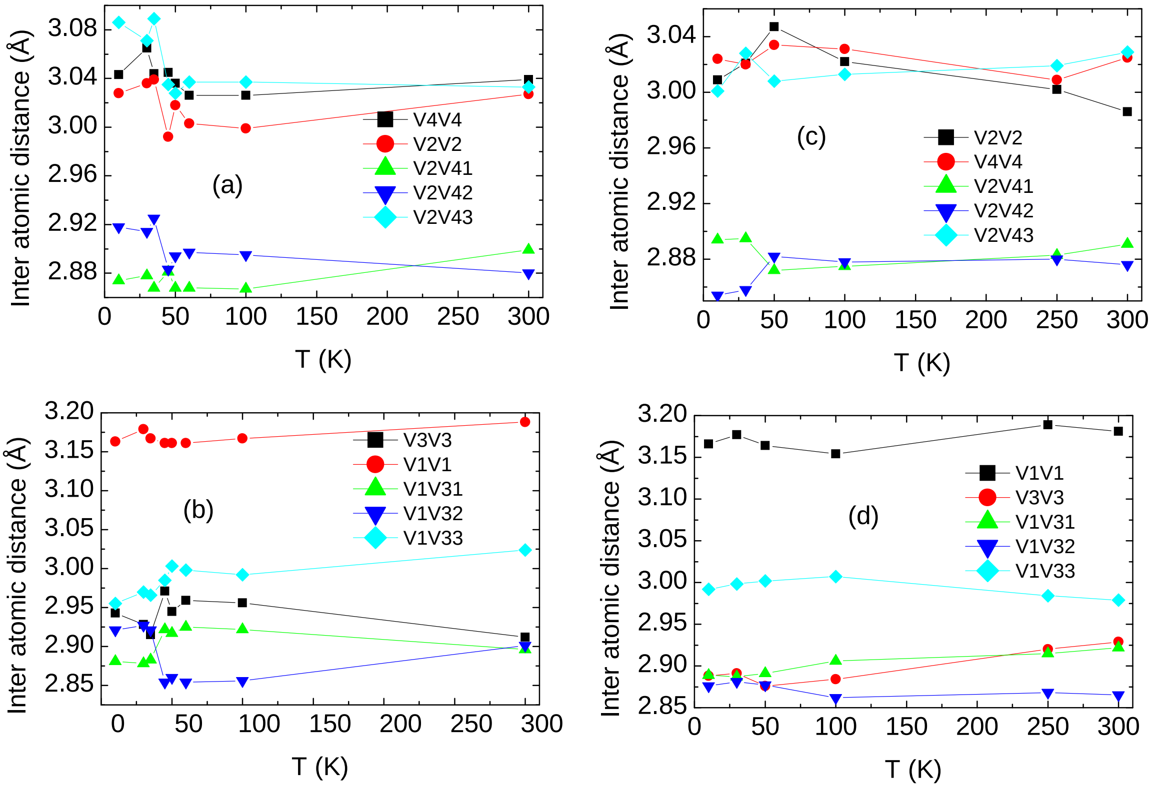

Figure 7.6 (Color online) V-V bond lengths in (a)-(b) YV_4O_8 and (c)-(d) LuV_4O_8. For the atom notations see Fig. 7.2.

fit lattice parameters and fractional atomic positions at 300 K are listed in Tables 7.1 and 7.2 for YV_4O_8 and LuV_4O_8, respectively. From the refinements, small amounts ($<$ 4 wt%) of V_2O_3 impurity phases were found in both YV_4O_8 and LuV_4O_8 samples.

Figure 7.4 shows the lattice parameters a, b, c, unit cell volume, and the monoclinic angle β respectively, of YV_4O_8 versus temperature. At $\sim$ 50 K the a and b axes and the monoclinic angle α decrease sharply while the c axis and the unit cell volume increase. There is no change in the symmetry of the unit cell. The sharp change in the lattice parameters and the unit cell volume indicate a first order phase transition.

For LuV_4O_8, as shown in Fig. 7.5, the a and b lattice parameters decrease sharply below 45 K while the c lattice parameter and the unit cell volume show a broad peak at $\sim$ 45 K. The monoclinic angle β increases below 100 K.

Figures 7.6(a)-(b) and 7.6(c)-(d) show the V-V bond lengths versus temperature for different inequivalent V atoms in YV_4O_8 and LuV_4O_8, respectively. For both YV_4O_8 and LuV_4O_8, the V atoms at the four inequivalent sites form two different kinds of chains V1-V3 and V2-V4 running along the c axis as shown in Fig. 7.2. For the V1-V3 chain in YV_4O_8, the V1V32 distance increases while the V1V31 distance decreases below 50 K. The other V1-V3 distances also decrease below 50 K. For LuV_4O_8, the V2V42 distance decreases while the V2V41 distance increases below 50 K.

Bond valence analysis

The bond-valence method is used to calculate the valences of individual atoms in a chemical compound.[126] The atomic valence of an atom is taken to be the sum of the bond valences of all bonds between that particular atom and the neighbouring atoms to which it is bonded. The bond-valence is defined as $v_i = \exp[(r_0 - r_i)/B]$ where B is fixed to the value 0.37, r_i is the interatomic distance between the particular atom and the neighbouring atom it is bonded to and r_0 is the bond-valence parameter which is obtained empirically.[127, 128] The valence for the given atom is then

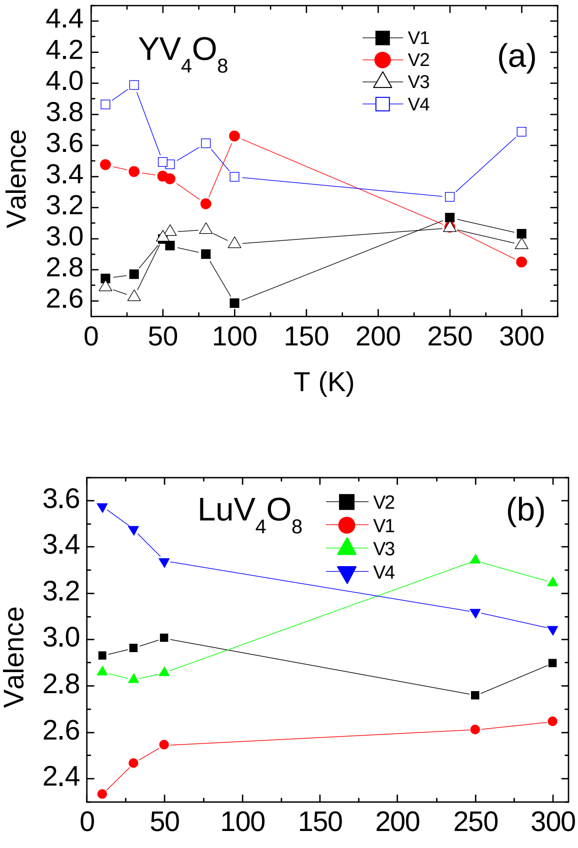

Figure 7.7 (Color online) Valences of the different inequivalent V atoms versus temperature T in (a) YV_4O_8 and (b) LuV_4O_8.

$$v = \sum_i v_i = \sum_i \exp[(r_0 - r_i)/B], \tag{7.1}$$

where the sum is over all the nearest-neighbors to the atom of interest.

For YV_4O_8 and YV_4O_8, we used the bond-valence method to calculate the valences v of the different inequivalent V atoms. The V atoms are bonded only to the O atoms and the V–O interatomic distances r_i for the different V–O bonds at different temperatures were determined by the above Rietveld refinements of the structures of the two compounds at different temperatures. The bond-valence parameters r_0 for V–O bonds are listed for V^{3+}–O^{2-}, V^{4+}–O^{2-}, and V^{5+}–O^{2-} bonds in Ref. [127]. We obtained an expression for $r_0(v_i)$ by fitting the three r_0 versus v_i values for V–O bonds[127] by a second order polynomial. The valences of the four inequivalent V atoms at different temperatures for YV_4O_8 and LuV_4O_8 from Eq. (7.1) are shown in Fig. 7.7.

7.3.2 Magnetic measurements

7.3.2.1 Magnetic susceptibility

Figure 7.8(a) shows the magnetic susceptibility $\chi \equiv M/H$ versus temperature T of YV_4O_8 in magnetic field $H = 100$ G. These data are in good agreement with the $\chi(T)$ of YV_4O_8 reported in Ref. [47]. There is a sharp fall in the susceptibility at $T = 50$ K followed by a bifurcation in the zero-field-cooled (ZFC) and field-cooled (FC) susceptibility $\chi(T)$ below 16 K. In addition, there are two small anomalies at $T = 90$ K and $T = 78$ K. The field dependence of χ is shown in Fig. 7.8(b). The sharp peak at 16 K and the small anomaly at 90 K for $H = 100$ G disappear at $H = 5000$ G.

Figure 7.8(d) shows the ZFC and FC magnetic susceptibilities of LuV_4O_8 in $H = 100$ G. The FC susceptibility shows a sudden slope change at ~ 100 K, a broad peak at ~ 70 K and then a sharp peak at 49 K followed by an almost T-independent behavior below 25 K. There is a strong bifurcation in the FC and ZFC susceptibility for $T < 100$ K. The magnetic field dependence of the peak at 49 K and the small anomaly at ~ 100 K are shown in Fig. 7.8(e). Overall, the behavior of $\chi(T)$ of YV_4O_8 and LuV_4O_8 are distinctly different.

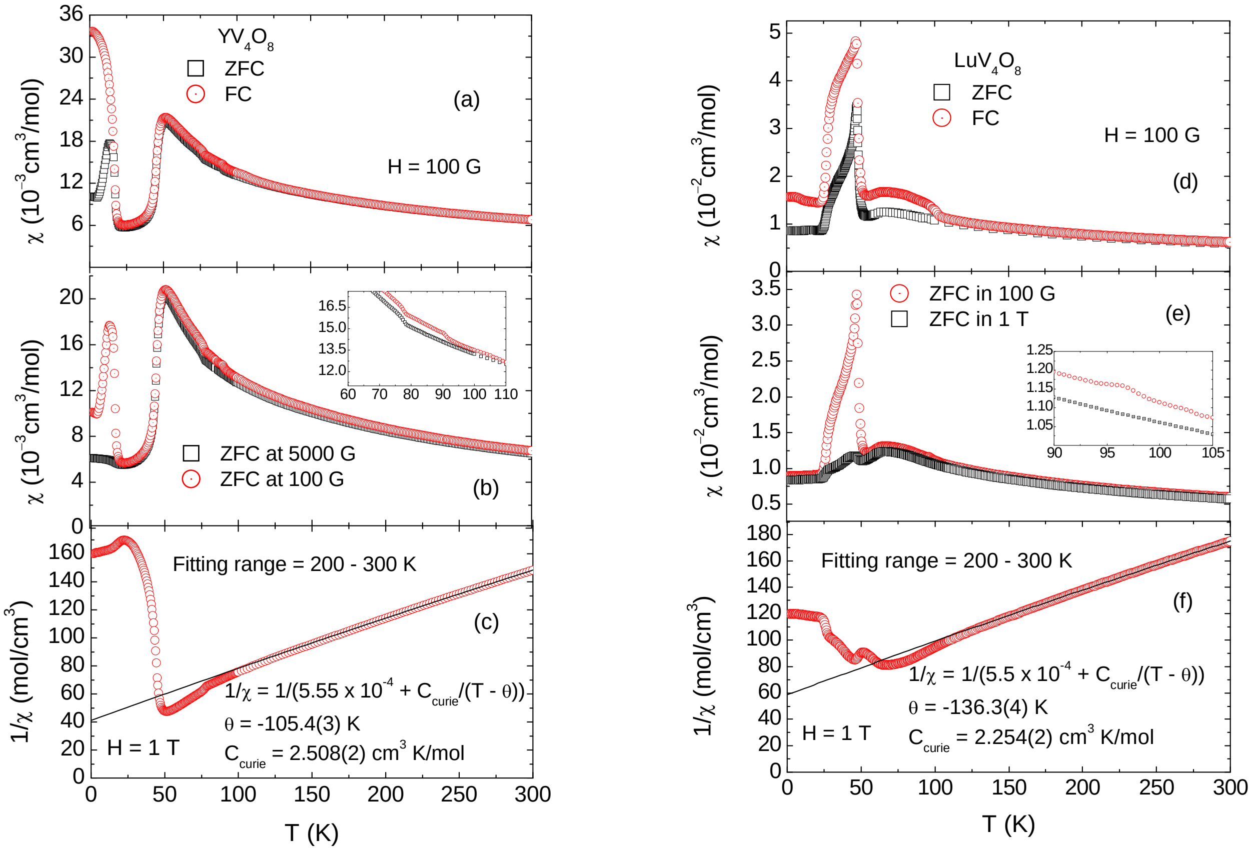

Figure 7.8 (Color online) Zero-field-cooled (ZFC) and field-cooled (FC) magnetic susceptibility (a) YV_4O_8 and (d) LuV_4O_8. (b) ZFC $\chi(T)$ in 5000 G and 100 G fields of YV_4O_8 and (e) ZFC χ in 100 G and 1 T fields of LuV_4O_8. The insets in (b) and (e) show the the anomalies in χ at 90 K and 78 K for YV_4O_8 and at 96 K for LuV_4O_8, respectively. The inverse susceptibilities $1/\chi$ versus T in 1 T of YV_4O_8 and LuV_4O_8 are shown in (c) and (f), respectively, where the solid lines are Curie-Weiss fits to the data in the temperature range 200 – 300 K.

Table 7.3 Curie constant $C_{\rm Curie}$, Weiss temperature θ, and temperature independent susceptibility χ_0 of YV_4O_8 and LuV_4O_8 obtained from different types of Curie-Weiss fits to the inverse susceptibility $1/\chi$ versus temperature T data in the range 200 to 300 K. The numbers in parentheses give the error in the last digit of a quantity. The parameters which do not have errors in their values were fixed during the fittings. σ^2/DOF is the goodness of fit where $\sigma^2 = \sum_i [1/\chi(T_i) - f(T_i)]^2$ and DOF (degrees of freedom) = number of data points minus the number of fit parameters. Here $\chi(T_i)$ is the measured susceptibility χ at temperature $T = T_i$ and $f(T_i)$ is the value of the fit function f at $T = T_i$.

Compound	σ^2/DOF $(10^{-1}$ mol/cm$^3)^2$	$C_{\rm Curie}$ (cm^3 K/mol)	χ_0 $(10^{-4}$ cm^3/mol)	θ (K)
YV_4O_8	0.062	2.08(1)	11.8(2)	−74(1)
	0.66	2.508(2)	5.55	−105.4(3)
	1.89	2.917(5)	0	−133.0(7)
	3.67	3.375	−5.7(1)	−161.9(5)
LuV_4O_8	0.12	1.71(1)	12.9(2)	−87(1)
	1.39	2.254(2)	5.5	−136.3(4)
	3.32	2.698(4)	0	−172.4(7)
	5.96	3.375	−6.78(8)	−216.8(5)

The high temperature $\chi(T)$ of both YV_4O_8 and LuV_4O_8 were fitted by the Curie-Weiss law

$$\chi(T) = \chi_0 + C_{\rm Curie}/(T-\theta)\,, \tag{7.2}$$

where χ_0 is the T-independent magnetic susceptibility, $C_{\rm Curie}$ is the Curie constant, and θ is the Weiss temperature. The temperature range over which the data were fitted is $T = 200 - 300$ K. For YV_4O_8, when we let all the parameters vary, we obtained $\chi_0 = 11.8\times10^{-4}$ cm^3/mol, $C_{\rm Curie}$ = 2.08 cm^{3}K/mol, and $\theta = -74$ K. If we assume YV_4O_8 to be an insulator, then $\chi_0 = \chi_{\rm VV} + \chi_{\rm dia}$ where $\chi_{\rm VV}$ is the paramagnetic Van Vleck susceptibility and $\chi_{\rm dia}$ is the diamagnetic core susceptibility. From the standard tables,[20] we have for YV_4O_8, $\chi_{\rm dia} = -1.45\times10^{-4}$ cm^3/mol. The V^{3+} compound V_2O_3 has a $\chi_{\rm VV} \sim 2\times10^{-4}$ cm^3/mol V.[129, 130] The V^{4+} compound VO_2 has $\chi_{\rm VV} \sim 1\times10^{-4}$ cm^3/mol V.[131] Thus, considering that there are three moles of V^{3+} and one mole of V^{4+} ions in one mole of YV_4O_8, we get an estimate of $\chi_0 = 5.55\times10^{-4}$ cm^3/mol for YV_4O_8. For LuV_4O_8, we have an estimate of $\chi_0 = 5.5\times10^{-4}$ cm^3/mol. Thus, the above value of $\chi_0 = 11.8\times10^{-4}$ cm^3/mol for YV_4O_8 that we obtained by fitting the data by Eq. (7.2) with all the parameters varying is much too large. Keeping the value of χ_0 fixed to 5.55×10^{-4} cm^3/mol, we obtain a $C_{\rm Curie} = 2.476(2)$ cm^3 K/mol which is much less than the value 3.375 cm^3 K/mol expected for 3 V^{3+} (spin $S = 1$) and 1 V^{4+} ($S = 1/2$) atoms per formula unit with g-factor $g = 2$. Keeping χ_0 fixed to zero, we obtain a $C_{\rm Curie} = 2.917(5)$ cm^3 K/mol which is closer to the expected $C_{\rm Curie} = 3.375$ cm^3 K/mol. A similar analysis was done for LuV$_4$O$_8$. Table 7.3 lists the best-fit values of the parameters $C_{\rm Curie}$, χ_0, and θ for YV$_4$O$_8$ and LuV$_4$O$_8$ obtained in these different fits. The solid lines in Figs. 7.8(c) and 7.8(f) are the Curie-Weiss fits to the $1/\chi$ data in the temperature range 200–300 K with χ_0 fixed to 5.55×10^{-4} cm^3/mol and 5.5×10^{-4} cm^3/mol, respectively. As shown in Figs. 7.8(c) and 7.8(f), the observed inverse susceptibilities $1/\chi$ show stronger negative curvatures than the fits for both YV$_4$O$_8$ and LuV$_4$O$_8$. The reason might be that the temperature range of the fits is still not high enough for the Curie-Weiss law to hold. For all the fits for each compound, we see that θ is consistently negative indicating predominantly antiferromagnetic interactions between the V spins in both compounds.

7.3.2.2 Magnetization versus applied magnetic field isotherms

Figures 7.9(a) and (b) show the magnetization M versus applied magnetic field H isotherms at selected temperatures for LuV$_4$O$_8$ and LuV$_4$O$_8$, respectively. The saturation magnetization $M_{\rm S}$ is obtained by fitting the high field (1.5 T $\leq H \leq$ 5.5 T) $M(H)$ data by

$$M(H,T) = M_{\rm S}(T) \ + \chi(T)H. \tag{7.3}$$

The solid lines in Figs. 7.9(a) and (b) are the fits of the data by Eq. (7.3). The fitted $M_{\rm S}(T)$ for YV$_4$O$_8$ and LuV$_4$O$_8$ are shown in Fig. 7.9(c).

For YV$_4$O$_8$, $M_{\rm S}$ varies rapidly with temperature below 50 K. As temperature decreases, $M_{\rm S}$ goes to a positive value of 4.13×10^{-4} $\mu_{\rm B}$/F.U. (F.U. means formula unit) at 50 K, where $\mu_{\rm B}$ is the Bohr magneton. In view of the negative Weiss temperature found in Sec. 3 B1, this suggests a canted antiferromagnetic (AF) state. Then at 45 K, $M_{\rm S}$ decreases sharply to a negative value of 4.35×10^{-4} $\mu_{\rm B}$/F.U. which arises from an upward curvature to $M(H)$ which suggests the disappearance of canting and a sudden development of purely antiferromagnetic ordering. This is consistent with the observed susceptibility χ where χ was increasing with

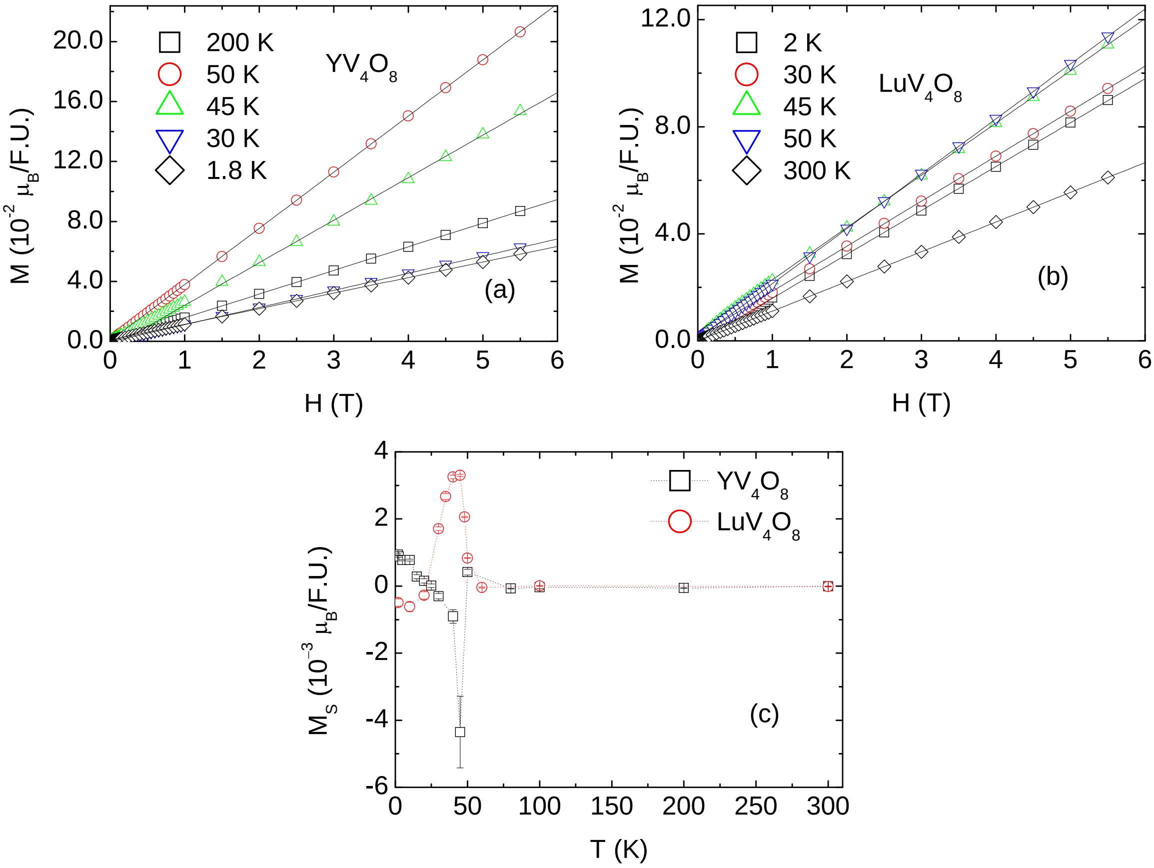

Figure 7.9 (Color online) Magnetization M versus magnetic field H at different temperatures of (a) YV_4O_8 and (b) LuV_4O_8. The solid lines are the fits of the high field (1.5 T $\leq$ H $\leq$ 5.5 T) $M(H)$ data by Eq. (7.3). The values of the saturation magnetization M_S versus T obtained from the fits are shown in (c).

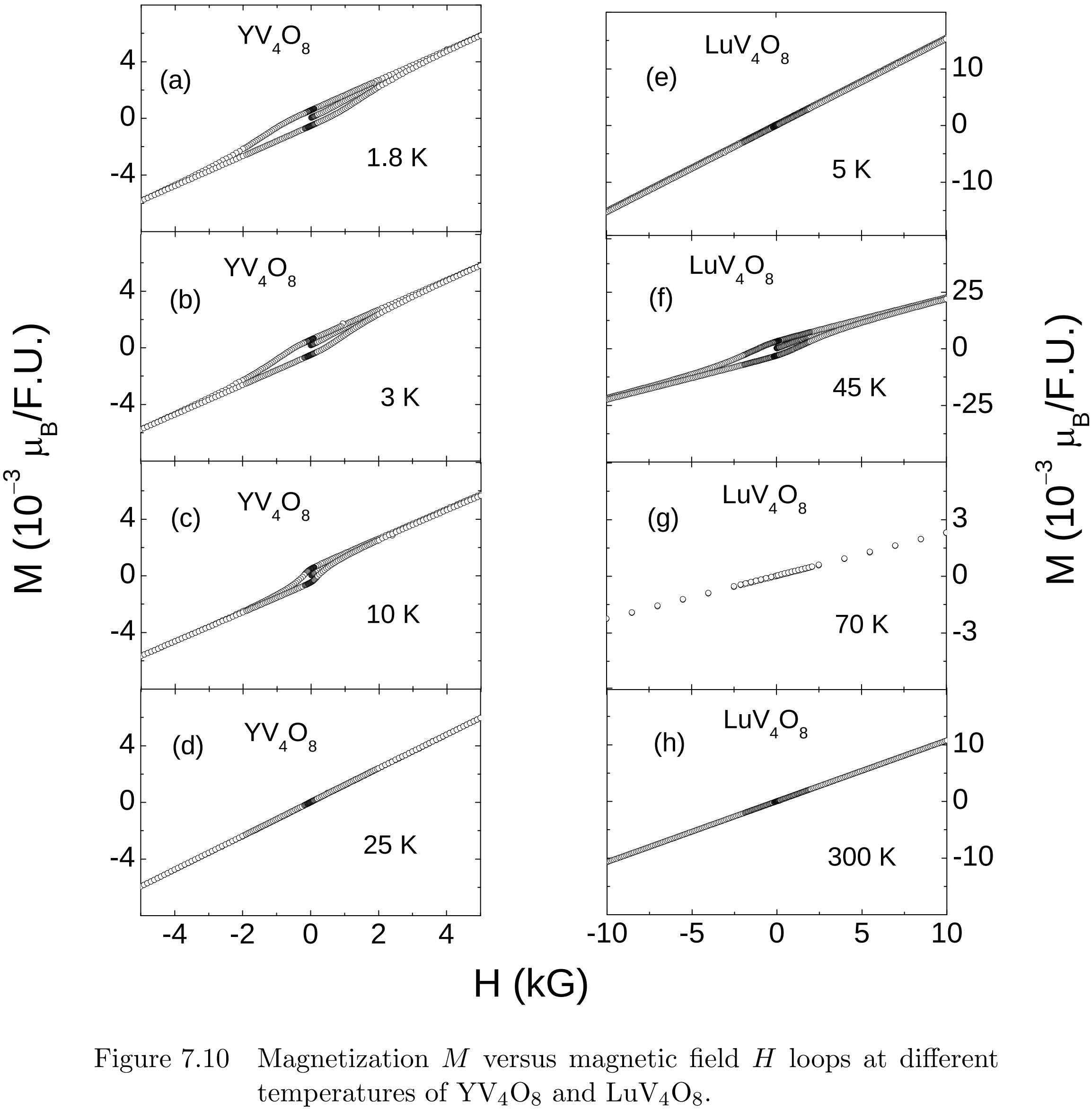

Figure 7.10 Magnetization M versus magnetic field H loops at different temperatures of YV_4O_8 and LuV_4O_8.

decreasing temperature but suddenly drops sharply at 49 K. As the temperature is further lowered, $M_{\rm S}$ gradually increases and finally becomes positive at 25 K and goes to a small positive value of 6.36×10^{-4} $\mu_{\rm B}$/F.U. at 1.8 K.

For $\rm LuV_4O_8$, the behavior of $M_{\rm S}(T)$ versus T is distinctly different from that of $\rm YV_4O_8$. As temperature decreases, $M_{\rm S}$ increases sharply from zero to 3.3×10^{-3} $\mu_{\rm B}$/F.U. at 45 K in what appears to be a first-order transition. The data suggest the development of a canted AF state below 50 K, where the canting continuously goes to zero by 20 K, which can also be observed in the susceptibility data in Fig. 7.8(d) where χ increases sharply at 49 K. Then, as the temperature is further lowered, $M_{\rm S}$ starts decreasing, becoming negative at 25 K and then remaining almost constant down to 1.8 K.

Figures 7.10(a)–(d) and 7.10(e)–(h) show the $M(H)$ loops at different temperatures for $\rm YV_4O_8$ and $\rm LuV_4O_8$, respectively. For $\rm YV_4O_8$, measurable hysteresis is observed below 16 K. At 1.8 K, the remanent magnetization is 0.0007 μ_B/F.U. and the coercive field is 400 G. For $\rm LuV_4O_8$, on the other hand, hysteresis is observed only around the transition at 50 K. At 45 K, the magnetization loop shows a remanent magnetization of 0.003 μ_B/F.U. and a coercive field of 1050 G. As we move away from the transition at 50 K, the hysteresis disappears.

7.3.3 Heat capacity measurements

Figure 7.11(a) shows the molar heat capacity C versus temperature T of $\rm YV_4O_8$ in zero and 9 T magnetic fields. $C(T)$ shows a sharp peak at $T = 77$ K and two small anomalies at $T = 81$ K (pointed by the arrow) and $T = 45$ K. There is a small magnetic field dependence of $C(T)$ at 45 K as shown in the inset of Fig. 7.11(a).

The magnetic contribution to the heat capacity $C_{\rm mag}(T)$ was obtained by $C_{\rm mag}(T) = C(T) - C_{\rm latt}(T)$ where the lattice heat capacity $C_{\rm latt}(T)$ is estimated from the Debye model

$$C_{\rm latt}(T) = 9xnN_{\rm A}k_{\rm B}\left(\frac{T}{\theta_{\rm D}}\right)^3 \int_0^{\theta_{\rm D}/T} \frac{y^4 e^y}{(e^y-1)^2}dy\,, \tag{7.4}$$

where n is the number of atoms per formula unit, $N_{\rm A}$ is Avagadro's number, $k_{\rm B}$ is Boltzman's constant, $\theta_{\rm D}$ is the Debye temperature, and x is a scaling factor which we had to introduce to

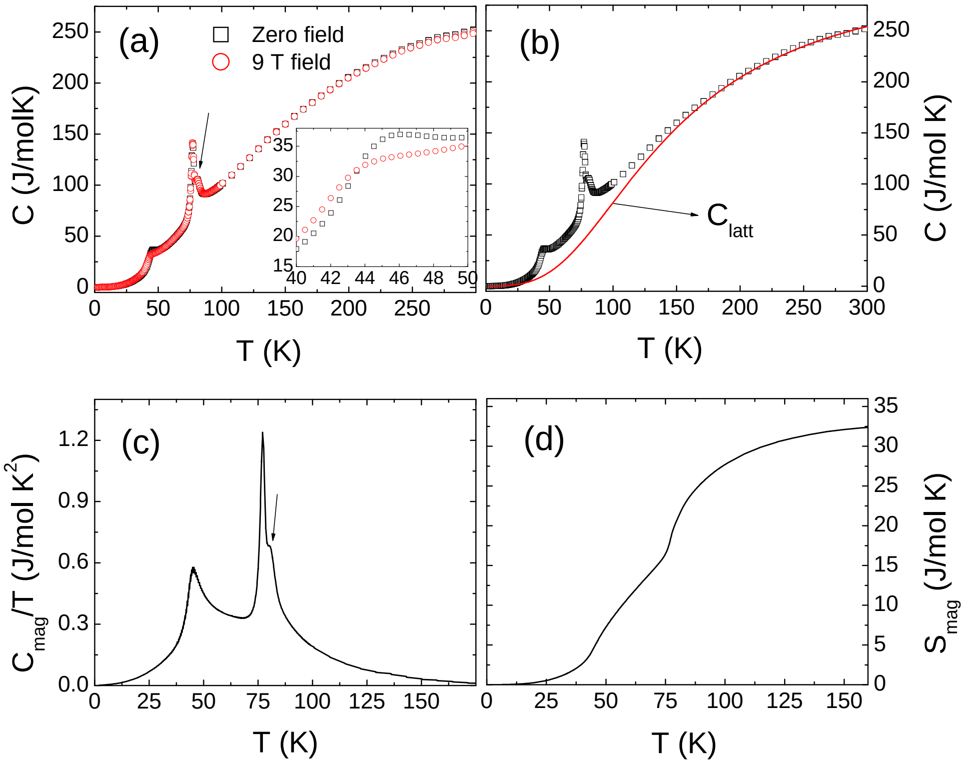

Figure 7.11 (Color online) (a) Heat capacity C versus temperature T of YV_4O_8 in 0 and 9 T magnetic fields. The arrow points to a tiny anomaly at 81 K. The inset shows a small magnetic field dependence of the heat capacity anomaly at 45 K. (b) The $C(T)$ in zero field from (a) along with the $C_{\rm latt}(T)$ obtained using Eq. (7.4) with $x = 0.96$ and $\theta_{\rm D} = 600$ K. (c) $C_{\rm mag}(T)/T$ versus T. The arrow points to the tiny anomaly at 81 K also seen in Fig. 7.11(a). (d) Magnetic entropy $S_{\rm mag}(T)$ obtained from Eq. (7.5).

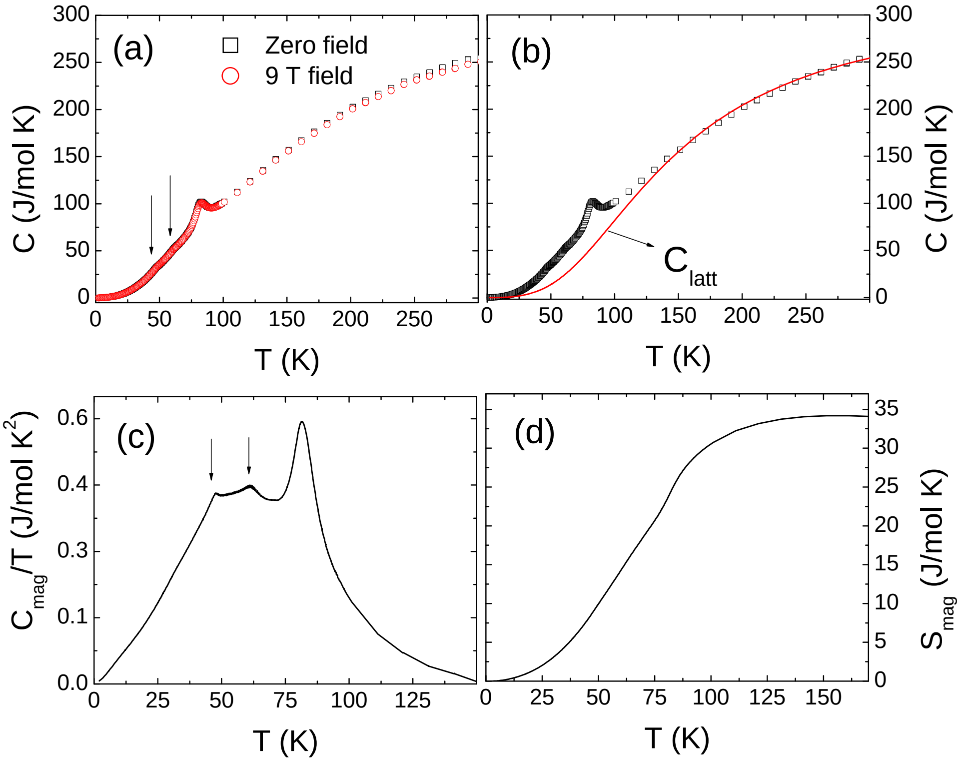

Figure 7.12 (Color online) (a) Heat capacity C versus temperature T of LuV_4O_8 in 0 and 9 T magnetic fields. The arrows point to two kinks at 62 K and 48 K, respectively. (b) The heat capacity $C(T)$ from (a) in zero field along with the $C_{\rm latt}(T)$ obtained from Eq. (7.4) with $x = 0.96$ and $\theta_{\rm D} = 600$ K. (c) $C_{\rm mag}(T)/T$ versus T. The arrows point to the kinks at 62 K and 48 K also seen in Fig. 7.12(a). (d) Magnetic entropy $S_{\rm mag}(T)$ obtained from Eq. (7.5).

get a considerable overlap of Eq. (7.4) with the measured C at high T. Plots of $C_{\rm latt}$ versus T were obtained for various values of the Debye temperature $\theta_{\rm D}$ and x, and were compared to the plot of measured $C(T)$ versus T. The $C_{\rm latt}(T)$ with the maximum overlap with the plot of $C(T)$ data at high temperatures was chosen.

For YV_4O_8, we obtained the best fit of $C_{\rm latt}(T)$ by Eq. (7.4) with $\theta_{\rm D} = 600$ K and $x = 0.96$ for $T > 200$ K. Figure 7.11(b) shows the plot of $C_{\rm latt}(T)$ along with the measured $C(T)$ for YV_4O_8. Figure 7.11(c) shows the magnetic contribution to the heat capacity $C_{\rm mag}(T)/T \equiv [C(T) - C_{\rm latt}(T)]/T$ for YV_4O_8 and Fig. 7.11(d) shows the magnetic entropy $S_{\rm mag}(T)$ versus T of YV_4O_8 given by

$$S_{\rm mag}(T) = \int_0^T \frac{C_{\rm mag}(T)}{T} dT\,. \tag{7.5}$$

The change in $S_{\rm mag}$ over the temperature range 0 K to 90 K in which the magnetic transitions occur is 32.5 J/mol K. If the V spins order, then the magnetic entropy associated with the spin ordering $S_{\rm spin}$ is given by

$$S_{\rm spin} = \sum_i n_i R \ln(2S_i + 1)\,, \tag{7.6}$$

where the sum is over V spins S_i in a formula unit, n_i is the number of spins S_i, and R is the molar gas constant. Using $n_i = 3$ V^{+3} ($S = 1$) and 1 V^{+4} ($S = 1/2$) per formula unit gives $S_{\rm mag} = 33.14$ J/mol K which is very close (within 2%) to the value of $S_{\rm mag}$ obtained above. This indicates that our estimation of $C_{\rm latt}(T)$ is reasonable.

Figure 7.12(a) shows the $C(T)$ of LuV_4O_8 in zero and 9 T magnetic fields. There is a peak at $T = 80$ K and two small kinks at 62 K and 48 K, pointed out by two arrows, respectively. The magnetic field dependence of $C(T)$ is negligible. Figure 7.12(b) shows the zero field $C(T)$ and the $C_{\rm latt}(T)$ for LuV_4O_8 from Eq. (7.4). For LuV_4O_8, the values $\theta_{\rm D} = 600$ K and $x = 0.96$ produced the $C_{\rm latt}(T)$ with the maximum overlap with $C(T)$ at high $T > 150$ K. Figure 7.12(c) shows $C_{\rm mag}(T)/T$ versus T for LuV_4O_8. The two kinks pointed out by the arrows in Fig. 7.12(a) can be seen prominently here. The magnetic entropy $S_{\rm mag}$ calculated from Eq. (7.5) versus T is shown in Fig. 7.12(d). The total magnetic entropy change up to 150 K is 34.0 J/mol K, which again agrees very well with the the above value of 33.1 J/mol K

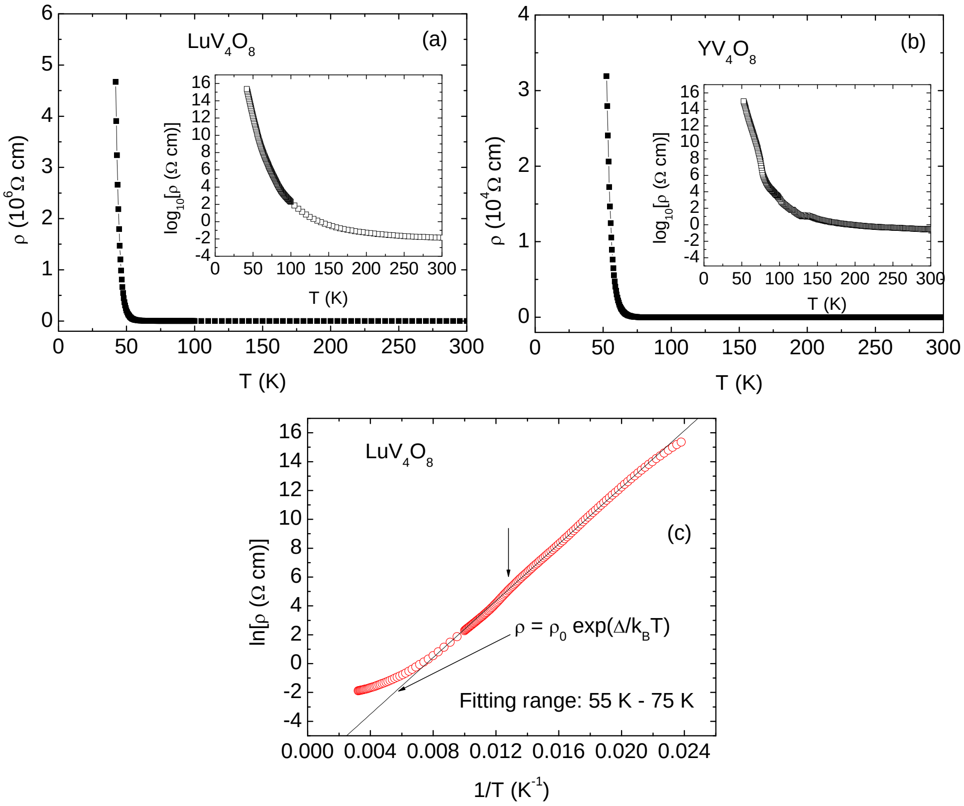

Figure 7.13 Electrical resistivity ρ versus temperature T measured on sintered pellets of (a) LuV_4O_8 and (b) YV_4O_8. Insets in (a) and (b) show $\log(\rho)$ versus T for LuV_4O_8 and YV_4O_8, respectively. (c) $\ln(\rho)$ versus $1/T$ for LuV_4O_8. The solid line in (c) is the fit to the data by Eq. (7.7) in the temperature range 55 K ($1/T$ = 0.018 K) to 75 K ($1/T$ = 0.0133 K) where the data are approximately linear.

for disordered V spins. A sharp peak occurs in $C_{\rm mag}(T)$ at $\approx$ 80 K with two additional kinks highlighted by two vertical arrows at 45 K and $\approx$ 60 K, respectively, as shown in Fig. 7.12(c).

7.3.4 Electrical resistivity measurements

Figures 7.13(a) and (b) show the electrical resistivity ρ versus temperature T measured on pieces of sintered pellets of LuV_4O_8 and YV_4O_8, respectively. On the scale of the figures, the resistivities are nearly temperature-independent above 50 K and 60 K, respectively, and strongly increase below those temperatures, suggesting the occurrence of metal to insulator transitions upon cooling below those temperatures. The insets in Figs. 7.13(a) and (b) show

Table 7.4 Different temperatures at which anomalies were observed in $\chi(T)$, $C(T)$, and $\rho(T)$, respectively, for YV_4O_8.

	χ	C	ρ
T_1	16		
T_2	50	45	
T_3			60
T_4	78	77	
T_5		81	
T_6	90		

Table 7.5 Different temperatures at which anomalies were observed in $\chi(T)$, $C(T)$, and $\rho(T)$, respectively, for LuV_4O_8.

	χ	C	ρ
T_1	25		
T_2	50	48	50
T_3		62	
T_4		80	
T_5	100		

the respective $\log_{10}(\rho)$ versus T for the two compounds. For both compounds, $\log_{10}(\rho)$ increases with decreasing T showing apparent semiconducting behaviors over the whole T range. However, the nearly T-independent behaviors at the highest temperatures suggest metallic behavior as just noted. Polycrystalline pellets of metallic oxides are notorious for showing semiconducting-like behavior due to insulating material in the grain boundaries. A plot of $\ln(\rho)$ versus $1/T$ for LuV_4O_8 is shown in Fig. 7.13(c). We fitted these data by

$$\rho = \rho_0 \exp[\Delta/k_{\rm B}T], \tag{7.7}$$

where Δ is the activation energy, ρ_0 is a constant, and $k_{\rm B}$ is Boltzmann's constant. The solid line in Fig. 7.13(c) is the fit in the T range 55 K ($1/T$ = 0.018 K) to 75 K ($1/T$ = 0.0133 K) where the $\ln[\rho(1/T)]$ data are approximately linear. The obtained fit parameters are $\rho_0 = 7.44(3)$ Ω cm and $\Delta = 84.6(1)$ meV.

7.4 Discussion

Tables 7.4 and 7.5 list the temperatures at which anomalies were observed in the $\chi(T)$, $C(T)$, and $\rho(T)$ measurements of YV_4O_8 and LuV_4O_8, respectively. Upon cooling below

$\approx$ 50 K, a sharp decrease of the V1V31 distance, increase of the V1V32 distance, and an increase in the other V1-V3 distances as shown in Fig. 7.6(b) suggest dimerization of the V1 and V3 spins in the V1-V3 chain (see Fig. 7.2) in YV_4O_8. The valences of V1 and V3 from Fig. 7.7(a) are close to 3 suggesting that both have spin $S = 1$. From the Curie-Weiss fit of the magnetic susceptibility in Fig. 7.8(c), the dominant interactions between the V spins are antiferromagnetic. We infer that the dimerization leads to a suppression of the magnetic susceptibility in the V1-V3 chain below 50 K. For the other V2-V4 chain, below 50 K, all the V-V interatomic distances increase as shown in Fig. 7.6(a), allowing the spins to order antiferromagnetically. The calculated valences of the V2 and V4 atoms in Fig. 7.7(a) point towards a decrease in the spin states of those V atoms. Both effects probably contribute to the sudden sharp drop in the magnetic susceptibility below 50 K in Figs. 7.8(a) and (b).

The transition observed in $\chi(T)$ at 50 K in Figs. 7.8(a) and (b) for YV_4O_8 also appears in $C_{\rm mag}(T)$ and $\rho(T)$ for this compound at a similar temperature in Figs. 7.11(a), (c), and Fig. 7.13(b). The presence of the anomaly in $C(T)$ strengthens our interpretation of dimerization due to structural transition and long range antiferromagnetic ordering at 50 K. However, there is no anomaly in $C_{\rm mag}$ at 16 K where the ZFC-FC $\chi(T)$ data in Fig. 7.8(a) show a strong bifurcation which disappears at high fields as shown in Fig. 7.8(b). No change in $C_{\rm mag}(T)$ in Fig. 7.11(c) is observed at 16 K, suggesting that the bifurcation of the ZFC-FC $\chi(T)$ may be due to weak canting of the antiferromagnetically ordered V spins. The presence of magnetic hysteresis with a very small (0.0007 $\mu_{\rm B}$/F.U.) remnant magnetization at 2 K shown in Fig. 7.10(a) and a small almost T-independent $M_{\rm S}(T)$ below 16 K shown in Fig. 7.9(c) are all consistent with the occurrence of canted antiferromagnetism below 16 K. There are two additional anomalies at 75 K and 90 K which appear in both $\chi(T)$ and $C_{\rm mag}(T)$, the origins of which are unclear.

The dimerization of the V spins in one of the chains and formation of spin singlets in YV_4O_8 is very similar to the spin-Peierls transition observed in $CuGeO_3$ at 14 K.[132] The occurrence of a metal to insulator transition at 60 K (which is very close to the temperature of the spin singlet formation) as shown in Fig. 7.13(b) suggests that YV_4O_8 is a rare example where a metal to spin singlet insulator transition takes place. Such a Peierls-like transition has been observed in the tetragonal rutile VO_2 at 340 K[133, 134] and in the spinel $MgTi_2O_4$ at 260 K.[135, 136] In both VO_2 and $MgTi_2O_4$, a complete structural transition occurs at the temperature of the metal to spin singlet transition,[135, 137] unlike YV_4O_8, where only the lattice parameters change without a lowering of the crystal symmetry.

For LuV_4O_8, the magnetic susceptibility in Figs. 7.8(d) and (e) shows no evidence of formation of spin singlets. There is no anomaly in $C_{\rm mag}(T)$ in Fig. 7.12(c) at $\approx$ 100 K at which a slope change occurs in $\chi(T)$ in Fig. 7.8(d). On the other hand, a sharp peak occurs in $C_{\rm mag}(T)$ at $\approx$ 80 K, where no anomaly in $\chi(T)$ occurs. This might indicate the onset of short-range ordering at $\approx$ 100 K followed by long-range ordering at $\approx$ 80 K. From Figs. 7.8(d) and (e), the $\chi(T)$ shows a sharp increase at $\approx$ 50 K, whereas in Fig. 7.12(c) there is only a small kink in $C_{\rm mag}(T)$ at this T. The absence of a sharp anomaly in $C_{\rm mag}$ at 50 K might indicate the development of a canted AF state at that temperature.

The Curie-Weiss fits to the high T χ for both YV_4O_8 and YV_4O_8 yield Curie constants that are considerably lower than expected, which leads to the possibility of both these compounds being metallic.

7.5 Summary

We have synthesized powder samples of YV_4O_8 and LuV_4O_8 whose crystallographic structure consists of two distinct one-dimensional zigzag chains running along the crystallographic c-axis. X-ray diffraction measurements down to 10 K reveal a first-order-like phase transition with a sudden change in the lattice parameters and unit cell volume at 50 K in YV_4O_8. However, the high and low temperature structures could be refined using the same space group indicating no lowering of the symmetry of the unit cell due to the structural transition. As a result of the transition, one of the chains dimerizes. The magnetic susceptibility of YV_4O_8 exhibits a sharp first-order-like decrease at 50 K followed by a bifurcation in the ZFC-FC susecptibility below 16 K. The anomaly at 50 K is suggested to arise from the dimerization of the $S = 1$ chain and antiferromagnetic (AF) ordering of the other chain. The AF ordered spins then become canted below 16 K. The change in the magnetic entropy calculated from heat capacity measurements also agrees very well with ordering of three $S = 1$ and one $S = 1/2$ disordered spins per formula unit. The lattice parameters of $\mathrm{LuV_4O_8}$ exhibit a small anomaly at $\sim$ 50 K but not as sharp as in $\mathrm{YV_4O_8}$. The magnetic susceptibility of $\mathrm{LuV_4O_8}$ shows a broad peak at $\sim$ 60 K followed by a sharp first order-like increase at 50 K. The 50 K anomaly is suppressed at higher fields. For both compounds, Curie-Weiss fits to the high T susceptibilities yield Curie constants which are much lower than expected. Electrical resistivity measurements on sintered pellets indicate metal to insulator-like transition at 60 K and 50 K for $\mathrm{YV_4O_8}$ and $\mathrm{LuV_4O_8}$, respectively. It would be very interesting to study single crystals of these compounds. Single crystal resistivity measurements are needed to determine if these materials are metallic or not at high temperatures. Measurements such as NMR or neutron scattering that would provide microscopic information about the spin dynamics would also be valuable to clarify the nature of the magnetic ordering transitions in $\mathrm{YV_4O_8}$ and $\mathrm{LuV_4O_8}$.

CHAPTER 8. Structure and magnetic, thermal, and electronic transport properties of single crystal EuPd$_2$Sb$_2$

This chapter is based on an article to be submitted to Phys. Rev. B by S. Das, K. McFadden, Y. Singh, R. Nath, A. Ellern, and D. C. Johnston.

Abstract

Single crystals of EuPd$_2$Sb$_2$ have been grown from PdSb self-flux. The properties of the single crystals have been investigated by x-ray diffraction, magnetic susceptibility χ, magnetization M, electrical resistivity ρ, Hall coefficient $R_{\rm H}$, and heat capacity $C_{\rm p}$ measurements versus temperature T and magnetic field H. Single crystal x-ray diffraction studies confirmed that EuPd$_2$Sb$_2$ crystallizes in the CaBe$_2$Ge$_2$-type structure. The $\chi(T)$ measurements suggest antiferromagnetic ordering at 6.0 K with the easy axis or plane in the crystallographic *ab* plane. An additional transition occurs at 4.5 K that may be a spin reorientation transition. The $C_{\rm p}(T)$ data also show the two transitions at 6.1 K and 4.4 K, respectively, indicating the bulk nature of the transitions. The 4.4 K transition is suppressed below 1.8 K while the 6.1 K transition moves down to 3.3 K in $H = 8$ T. The $\rho(T)$ data show metallic behavior down to 1.8 K along with an anomaly at 5.5 K in zero field. The anomaly is suppressed to 2.7 K in an 8 T field. The $R_{\rm H}$ measurements indicated that the dominant charge carriers are electrons. The $M(H)$ isotherms show three field-induced transitions at 2.75 T, 3.90 T, and 4.2 T magnetic fields parallel to the *ab* plane at 1.8 K. No transitions are observed in $M(H)$ for fields parallel to the *c* axis.

8.1 Introduction

The recent discovery of high-temperature superconductivity in RFeAsO$_{1-x}$F$_x$ ($R =$ La, Ce, Pr, Nd, Sm, Gd, Tb, and Dy)[48–53] compounds with superconducting transition temperatures $T_{\rm c}$ as high as 55 K has sparked a lot of interest in the search for new superconductors. These materials crystallize in the tetragonal ZrCuSiAs-type structure with space group $P4/nmm$.[54] The structure consists of alternating FeAs and RO layers stacked along the crystallographic c axis. The parent compounds RFeAsO exhibit spin density wave (SDW) transitions at temperatures $\lesssim$ 200 K.[50, 55, 56] Upon doping with F, the SDW is suppressed and superconductivity appears.[49–53, 55, 57]

Another group of structurally related parent compounds with the chemical formula AFe$_2$As$_2$ (A = Ca, Sr, Ba, and Eu) was soon discovered to show superconductivity upon doping or application of pressure. These compounds crystallize in the tetragonal ThCr$_2$Si$_2$-type structure with space group $I4/mmm$ (No. 139). The structure consists of alternating FeAs and A layers stacked along the c axis as shown in Fig. 8.1(a). In the FeAs layers, the Fe atoms form a square planar lattice. The AFe$_2$As$_2$ compounds also show SDW and structural transitions at high temperatures[59–68] which are suppressed by doping with K, Na, and Cs at the A site and accompanied by the onset of superconductivity.[69–72]

In both classes of RFeAsO$_{1-x}$F$_x$ and AFe$_2$As$_2$ compounds described above, FeAs layers that are stacked along the c axis are evidently a key building block yielding superconductors with relatively high $T_{\rm c}$. This gives a strong motivation to investigate similarly structured compounds in a search for additional high-$T_{\rm c}$ superconductors.

The compound EuPd$_2$Sb$_2$ crystallizes in the CaBe$_2$Ge$_2$-type structure with space group $P4/nmm$ (No. 129),[73] as shown in Fig. 8.1(b). The structure is closely related to the AFe$_2$As$_2$ structure. Alternating PdSb and Eu layers are stacked along the c axis, similar to the AFe$_2$As$_2$ structure. However, there is a distinct difference between the two structures. In half of the PdSb layers in the EuPd$_2$Sb$_2$ structure, the Pd atoms are arranged in a planar square lattice with two Sb layers on either side of each Pd layer, resulting in a tetrahedral coordination of Pd by Sb as in the FeAs-type layers. However, alternating with these layers are layers in which

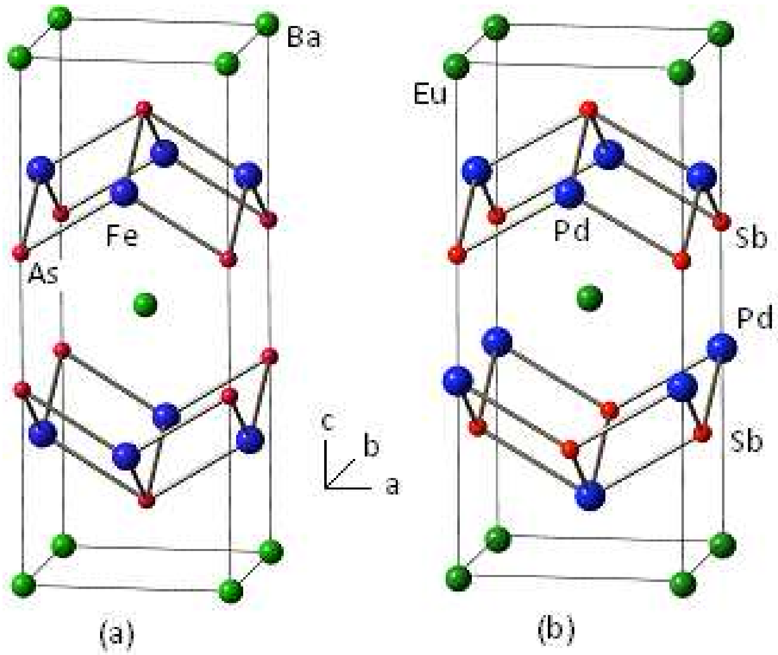

Figure 8.1 (Color online) (a) Crystal structure of $BaFe_2As_2$ with the tetragonal $ThCr_2Si_2$-type structure. The structure consists of alternating FeAs and Ba layers stacked along the crystallographic c axis. (b) Crystal structure of $EuPd_2Sb_2$ with the origin of the unit cell shifted by (1/4 1/4 1/4) compared to that in the space group $P4/nmm$, for comparison purposes. The structure consists of alternating PdSb and Eu layers stacked along the crystallographic c axis similar to the $BaFe_2As_2$ shown in (a). However, half of the PdSb layers are inverted (the Pd and Sb atoms switch positions) with respect to the FeAs-type layers.

the Pd and Sb positions are switched, as shown in Fig. 8.1(b).

There have been reports of structural instabilities and antiferromagnetic ordering in some compounds forming in the $CaBe_2Ge_2$-type structure. $UCu_{1.5}Sn_2$ orders antiferromagnetically at 110 °C which is very high among uranium intermetallics.[138] $CePd_2Ga_2$ undergoes a tetragonal to monoclinic second order structural transition at 125 K and orders antiferromagnetically at 2.3 K.[139] $LaPd_2Ga_2$ is superconducting below 1.9 K. [139] Eu was reported to be in a mixed valent state between Eu^{+2} (spin $S = 7/2$) and Eu^{+3} (spin $S = 0$) in polycrystalline samples of $EuPd_2Sb_2$.[73] In this chapter, we report the synthesis and structure of single crystals of $EuPd_2Sb_2$ and their physical properties including magnetic susceptibility, magnetization, specific heat, and electronic transport measurements.

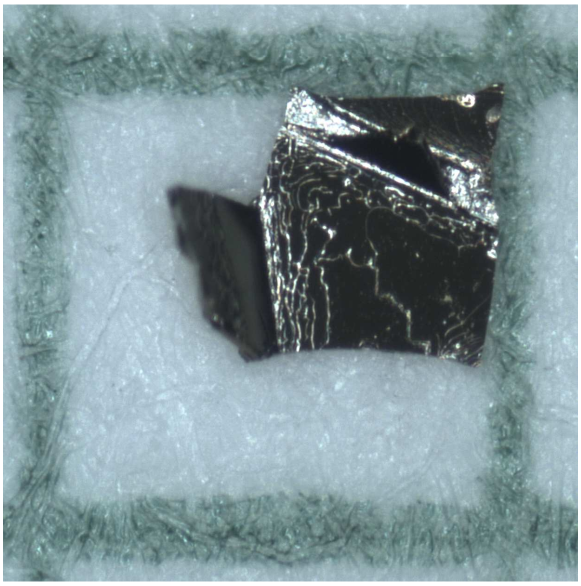

Figure 8.2 An as-grown crystal of $EuPd_2Sb_2$. The grid size in 1 mm.

8.2 Experimental details

Single crystals of $EuPd_2Sb_2$ were grown using PdSb self-flux which melts at $\sim$ 805 °C. The Eu (99.999% pure) was obtained from the Ames Laboratory Materials Preparation Center. The Pd (99.95% pure) and Sb (99.999% pure) were obtained from Alfa-Aesar. Pd and Sb powders were thoroughly mixed inside a helium-filled glove box, and then poured on top of a chunk of Eu ($\sim$ 0.1 g) that was placed at the bottom of a 2 mL alumina crucible. The elements were in the atomic ratio Eu:Pd:Sb = 1:5:5. The top of the crucible was packed with quartz wool. The crucible was then sealed in a quartz tube under vacuum and was placed vertically in a box furnace and heated to 1000 °C at a rate of 76 °C/h and held there for 6 h. The tube was then cooled to 850 °C at the rate of 1.5 °C/h and at this temperature the tube was removed from the oven and centrifuged to partially separate the crystals from the flux. A single conglomerated chunk (about 0.4 g) was found in the crucible after removing the quartz wool. Plate-like gold-colored crystals were isolated mechanically. The largest crystals had dimensions $\sim 2\times2\times0.1$ mm^3. The crystals are brittle and are easily broken into smaller pieces. Figure 8.2 shows an as-grown crystal on a mm grid.

Single crystal x-ray diffraction measurements were done using a Bruker CCD-1000 diffractometer with Mo K_α ($\lambda = 0.71073$ Å) radiation. Magnetic measurements on the crystals were carried out using a Quantum Design superconducting quantum interference device (SQUID) magnetometer in the temperature T range 1.8–350 K and magnetic field H range 0–5.5 T. Heat capacity, electrical resistivity, and Hall coefficient measurements were done using a Quantum Design physical property measurement system (PPMS). For the heat capacity measurements, Apiezon N grease was used for thermal coupling between a sample and the sample platform. The heat capacity was measured in the temperature range 1.8–300 K in $H = 0$, 2, 5, 7, and 9 T. For electrical resistivity and Hall coefficient measurements, platinum leads were attached to the crystals using silver epoxy. Electrical resistivity measurements were carried out using the standard AC four probe method with 10 mA excitation current in the temperature range 1.8–300 K and magnetic field range 0–8 T. Hall coefficient measurements were carried out using the five-wire configuration supported by the PPMS ACT[75] option with 100 mA excitation current in the temperature range 1.8–310 K and magnetic field range 0–8 T. The Hall voltage was computed at each temperaure from the odd part of the measured transverse voltage upon reversing the sign of the applied magnetic field. The even part was much smaller than the odd part at each measured temperature.

8.3 Results

8.3.1 Structure and chemical composition determination

A well-shaped crystal with dimensions $0.21 \times 0.18 \times 0.11$ mm^3 was selected for single crystal x-ray diffraction at 173 K. X-ray structure determination and refinement were performed using the SHELXTL software package.[110] The refined unit cell parameters, the isotropic thermal parameters, and the atomic positions are listed in Tables 8.1 and 8.2. Our results confirm that $EuPd_2Sb_2$ crystallizes in the $CaBe_2Ge_2$ structure.[73] The unit cell dimensions and the atomic positions are similar to those found from single crystal x-ray diffraction measurements at room temperature in Ref. [73], which were $a = 4.629(1)$ Å, $c = 10.568(2)$ Å, Eu: $z = 0.2424(1)$; Pd(2): $z = 0.6284(2)$; Sb(2): $z = 0.8745(1)$. The significant difference between the lattice parameters in Ref. [73] and lattice parameters obtained by us suggests a difference in crystal

Table 8.1 Crystal data and structure refinement of $EuPd_2Sb_2$ at a temperature of 173 K. Here $R1 = \sum||F_{\mathrm{obs}}| - |F_{\mathrm{calc}}||/\sum|F_{\mathrm{obs}}|$ and $wR2 = (\sum[\ w(|F_{\mathrm{obs}}|^2 - |F_{\mathrm{calc}}|^2)^2]/\sum[\ w(|F_{\mathrm{obs}}|^2)^2])^{1/2}$, where F_{obs} is the observed structure factor and F_{calc} is the calculated structure factor.

Crystal system/Space group	Tetragonal, $P4/nmm$
Unit cell parameters	$a = 4.653(2)$ Å
	$c = 10.627(4)$ Å
Unit cell volume	230.1(3) Å^3
Z (formula units/unit cell)	2
Density (Calculated)	8.779 Mg/m^3
Absorption coefficient	32.47 mm^{-1}
$F(000)$	514
Goodness-of-fit on F^2	1.235
Final R indices $[I > 2\sigma(I)]$	R1 = 0.0737
	wR2 = 0.02506
Extinction coefficient	0.033(9)

Table 8.2 Atomic coordinates x, y, and z (10^{-4}) and equivalent isotropic displacement parameters U (10^{-3} Å^2) for $EuPd_2Sb_2$ at 173 K.

	x	y	z	U(eq)
Eu	2500	2500	2425(1)	13(1)
Pd(1)	7500	2500	0	16(1)
Pd(2)	2500	2500	6292(2)	17(1)
Sb(1)	7500	2500	5000	13(1)
Sb(2)	2500	2500	8738(1)	14(1)

stoichiometry between the samples in Ref. [73] and ours, although both studies indicate nearly stoichiometric compositions. The temperature difference between the two studies cannot be responsible, since the lattice parameter differences are opposite to expectation in that case.

The stoichiometry of a representative crystal was checked by semiquantitative energy-dispersive x-ray (EDX) microanalysis. The results gave the following composition: Eu, 24.9 ± 1.1 wt%; Pd, 35.5 ± 0.8 wt%; Sb, 39.7 ± 1.0 wt%. These values are consistent with the values calculated for the composition $\mathrm{EuPd_2Sb_2}$: Eu, 24.98 wt%; Pd, 34.98 wt%; Sb, 40.03 wt%.

8.3.2 Magnetic measurements

8.3.2.1 Magnetic susceptibility measurements

Figure 8.3(a) shows the magnetic susceptibility χ of $\mathrm{EuPd_2Sb_2}$ versus temperature T with the magnetic field H parallel to the crystallographic c axis ($\chi_{||}$) and to the ab plane ($\chi_{\perp}$), respectively. At high-T, the $\chi(T)$ shows nearly isotropic paramagnetic behavior. Figure 8.3(b) shows the inverse susceptibility $1/\chi$ for $H \parallel c$ versus T. An excellent fit to the data in the T range 125 – 300 K was obtained using the Curie-Weiss behavior

$$\frac{1}{\chi} = \frac{1}{\chi_0 + C/(T-\theta)}, \tag{8.1}$$

where χ_0 is the T-independent susceptibility, C is the Curie constant, and θ is the Weiss temperature. The values of the parameters obtained from the fit are $C = 7.333(8)$ cm^3 K/mol, $\theta = -12.9(2)$ K, and $\chi_0 = -0.00024(3)$ cm^3/mol. Keeping χ_0 fixed to zero, the Curie-Weiss fits to the $1/\chi_{||}(T)$ data in the different temperature ranges between 25–300 K and 200–300 K yielded $C = 7.23(3)$ cm^3 K/mol and $\theta = -11.8(8)$ K. The obtained Curie constants are significantly lower than the value $C = 7.88$ cm^3 K/mol expected for Eu^{+2} (spin $S = 7/2$) with g-factor $g = 2$. This indicates that Eu is in an intermediate valent state Eu$^{+2.07}$ as previously suggested in Ref. [73]. The negative Weiss temperature indicates dominant antiferromagnetic interactions between the nearest-neighbor Eu spins.

At low temperatures, $\chi_{||}$ becomes almost T-independent below 6.0 K with a cusp at $T =$ 4.5 K as shown in the inset of Fig. 8.3(a). $\chi_{\perp}$ shows a peak at 6.0 K and decreases monotonically

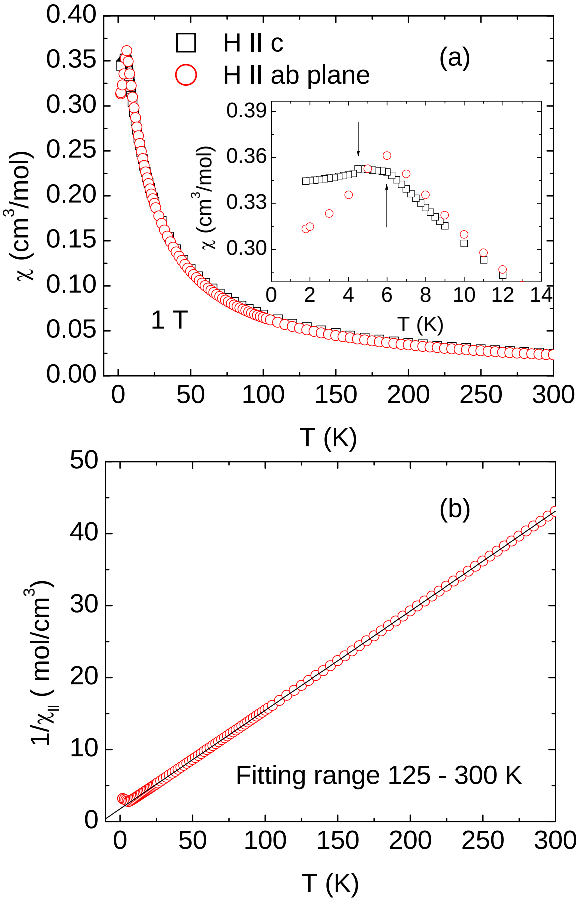

[h]

Figure 8.3 (Color online) (a) Magnetic susceptibility χ versus temperature T of EuPd$_2$Sb$_2$ with the magnetic field H parallel to the crystallographic c axis and to the ab plane, respectively. The inset shows the low-T part of the $\chi(T)$ plot. The two transitions at 4.5 K and 6.0 K are indicated by the vertical arrows. (b) Inverse susceptibility $1/\chi(T)$ for $H \parallel c$. The solid curve is the Curie-Weiss fit [Eq. (8.1)] to the $1/\chi_{\|}(T)$ data in the temperature range 125–300 K with the parameters listed in the text.

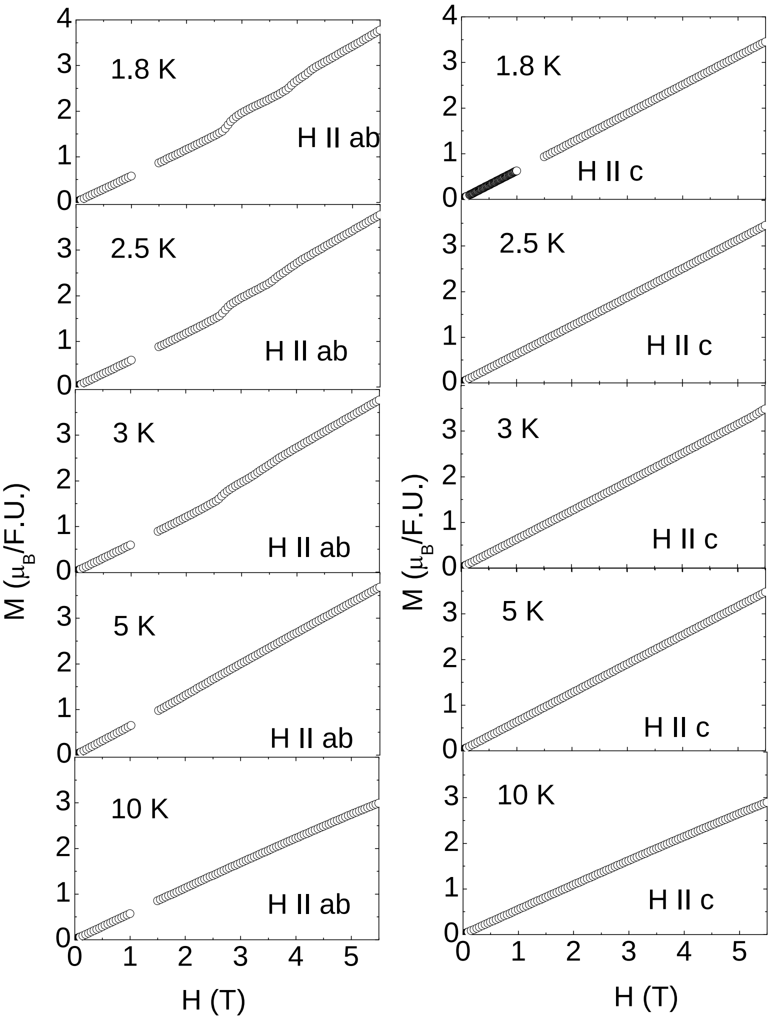

Figure 8.4 Magnetization M versus applied magnetic field H of EuPd$_2$Sb$_2$ with H parallel to the crystallographic c axis (left-hand panels) and to the ab plane (right-hand panels), respectively.

at lower T. The data suggest antiferromagnetic ordering of the Eu spins at 6.0 K with the easy axis or plane within the ab plane, with a possible spin reorientation transition at 4.5 K.

8.3.2.2 Magnetization versus applied magnetic field isotherm measurements

Figure 8.4 shows the magnetization M of EuPd$_2$Sb$_2$ versus magnetic field H with H parallel to the crystallographic c axis (right-hand panels) and to the ab plane (left-hand panels), respectively. For $H \parallel ab$, anomalies in $M(H)$ are clearly visible for $T < 5$ K. Above 10 K, $M(H)$ is proportional to H. To illustrate the anomalies more clearly, Fig. 8.5(a) shows the

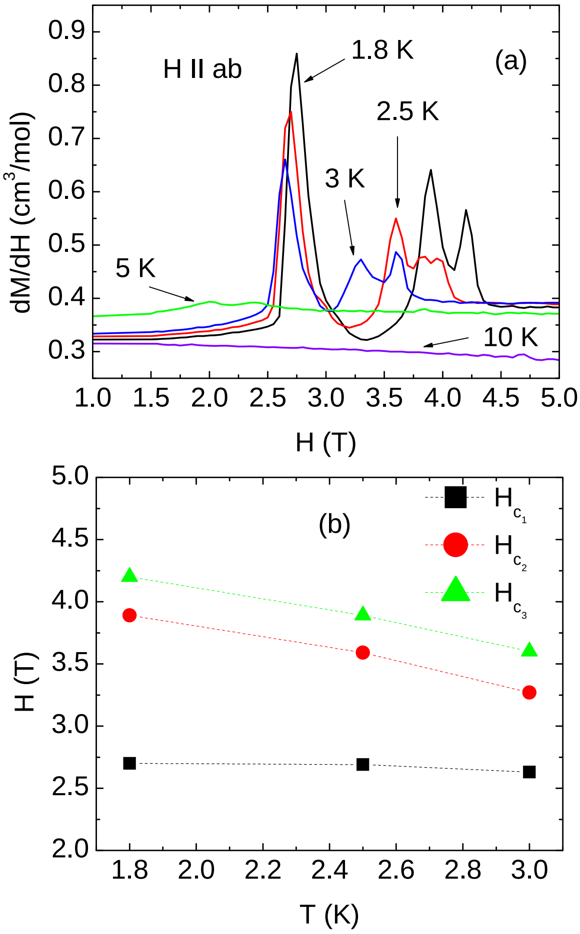

Figure 8.5 (a) Derivative dM/dH of the magnetization M with respect to the applied field H versus H with H parallel to the crystallographic ab plane. (b) The fields H_{c_1}, H_{c_2}, and H_{c_3}, at which transitions are observed in dM/dH, versus T. The dotted lines are guides to the eye.

derivative dM/dH versus H with $H \parallel ab$. The dM/dH data for $M \parallel ab$ show three peaks at $H_{c_1} = 2.75$ T, $H_{c_2} = 3.90$ T, and $H_{c_3} = 4.20$ T, respectively, at 1.8 K. The temperature dependences of the fields at which these field-induced transitions occur are shown in Fig. 8.5(b). The transition fields are seen to decrease with increasing T, and disappear between 5 and 10 K. At 1.8 K in $H = 5.5$ T, the value of $M \parallel ab$ in Fig. 8.4 is 3.8 $\mu_{\rm B}$/f.u. This value is much less than the expected Eu^{+2} saturation moment of 7 $\mu_{\rm B}$. This difference suggests that the metamagnetic transitions take place between different antiferromagnetic states. In contrast, $M \parallel c$ is proportional to H at all T. Qualitatively similar $M(H)$ observations were previously reported for single crystals of $\rm EuRh_2As_2$.[140]

8.3.3 Heat capacity measurements

Figure 8.6(a) shows the heat capacity $C_{\rm p}$ of a 2.619 mg $\rm EuPd_2Sb_2$ crystal versus temperature T in zero magnetic field. The inset of Fig. 8.6(a) shows $C_{\rm p}/T$ versus T for $T < 10$ K. Two anomalies are observed at 6.1 K and 4.4 K, respectively, indicating that the transitions observed in $\chi(T)$ in the inset of Fig. 8.3(a) at similar temperatures are bulk long-range magnetic ordering transitions. The data at high $T \sim 300$ K approach the Dulong-Petit classical lattice heat capacity value of $15R \simeq 125$ J/mol K, where R is the molar gas constant.

Figure 8.6(b) shows the calculated magnetic entropy $S_{\rm mag} = \int\limits_0^T [C_{\rm mag}(T)/T]dT$ versus T at low temperatures $T < 10$ K, where $C_{\rm mag} = C_{\rm p} - C_{\rm latt}$ is the magnetic contribution and $C_{\rm latt}$ is the lattice contribution to the specific heat. We assumed $C_{\rm latt} = \beta T^3$ for $T < 10$ K with $\beta = 1.93(4)$ mJ/mol K^4 obtained for $\rm BaRh_2As_2$ from Ref. [141]. A linear extrapolation to zero of $C_{\rm mag}/T$, as shown by the dotted straight line in the inset of Fig. 8.6(b), was assumed in order to approximate the missing $C_{\rm mag}/T$ data between 0 K and 1.8 K. The magnetic entropy $S_{\rm mag} =$ 16.4 J/mol K at 10 K is close to the expected entropy $S_{\rm mag} = R\ln(2S + 1) = 17.3$ J/mol K due to ordering of one spin $S = 7/2$ per formula unit.

Figures 8.7(a)–(e) show $C_{\rm p}(T)$ in different magnetic fields parallel to the crystallographic c axis. For $H = 0$ T, $C_{\rm p}(T)$ shows a jump at $T_{\rm N1} = 6.1$ K and then a cusp at $T_{\rm N1} = 4.4$ K. The shapes of the $C_{\rm p}$ anomalies at the two transitions are thus distinctly different. As H is

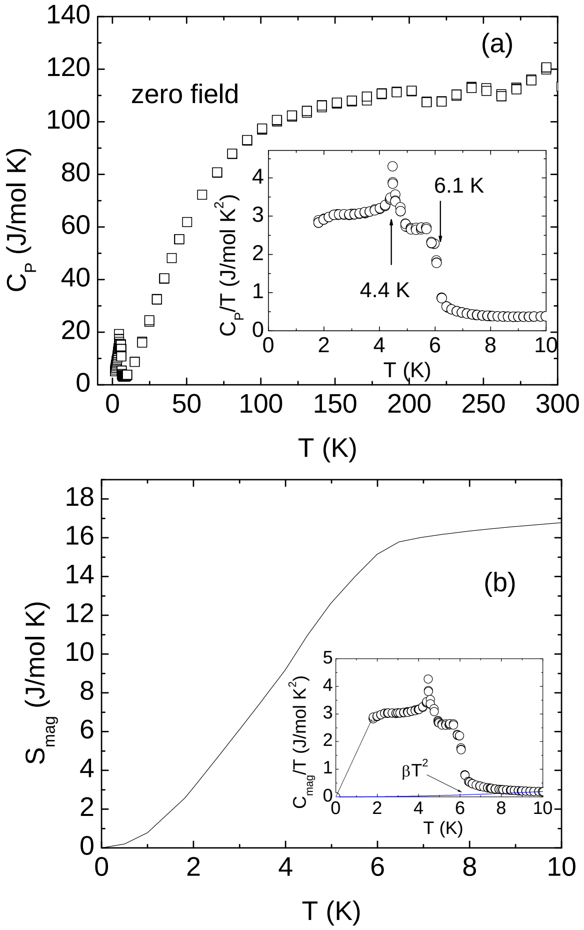

Figure 8.6 (Color online) (a) Heat capacity $C_{\rm p}$ versus temperature T of $\rm EuPd_2Sb_2$ in zero magnetic field. The inset shows $C_{\rm p}/T$ versus T for $T < 10$ K. Two anomalies in $C_{\rm p}(T)/T$ are observed at 4.4 K and 6.1 K indicated by vertical arrows in the inset. (b) Calculated magnetic entropy $S_{\rm mag} = \int\limits_0^T [C_{\rm mag}(T)/T]dT$ versus T. A linear extrapolation to zero of $C_{\rm p}(T)/T$ as shown by the dotted straight line in the inset was used to approximate the missing $C_{\rm p}/T$ data between 0 K and 1.8 K. The solid line in the inset is a plot of the lattice contribution $C_{\rm latt} = \beta T^2$ with $\beta = 1.92$ mJ/mol K^4 obtained for $\rm BaRh_2As_2$ in Ref. [141]. The inset shows that the lattice heat capacity is negligible compared to the magnetic heat capacity below 10 K.

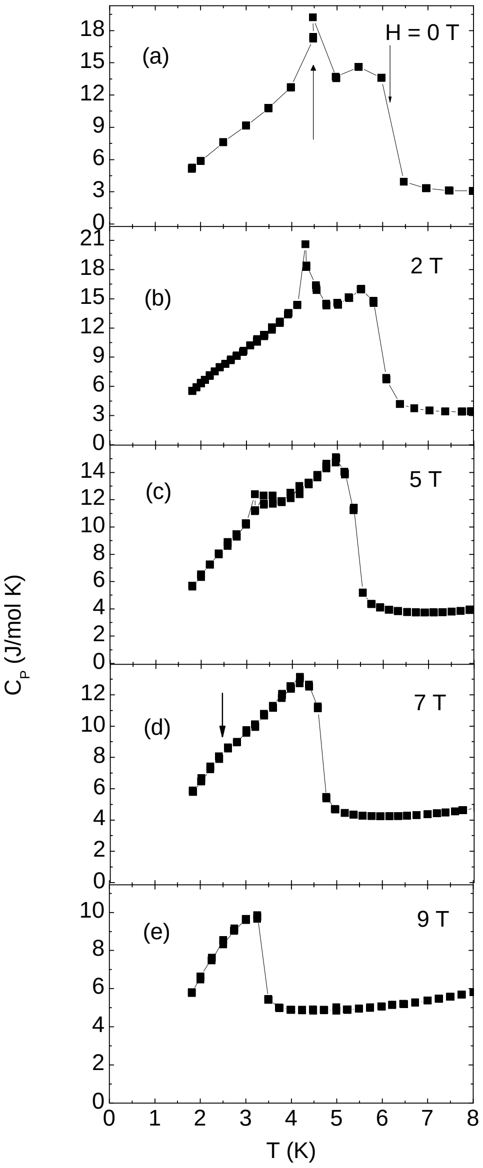

Figure 8.7 Heat capacity C_p versus temperature T of $\mathrm{EuPd_2Sb_2}$ in different magnetic fields parallel to the c axis. The two transitions at temperatures $T_{\mathrm{N}1}$ and $T_{\mathrm{N}2}$, respectively, are indicated in panel (a). The vertical arrow in (d) points to T_{N_2} in $H = 7$ T.

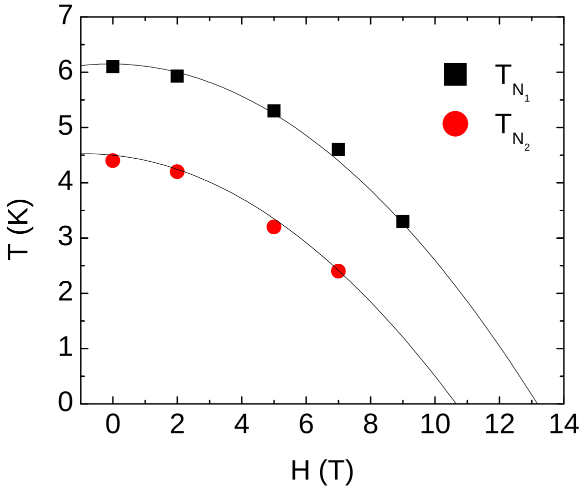

Figure 8.8 (Color online) Transition temperatures T_{N_1} and T_{N_2} of $\mathrm{EuPd_2Sb_2}$ versus magnetic field $H \parallel c$ as determined from the heat capacity measurements versus H in Fig. 8.7. The solid curves are guides to the eye.

increased, T_{N_2} decreases below 1.8 K at 9 T, while the T_{N_1} goes down to 3.2 K in 9 T. The transition at T_{N_1} remains sharp while the transition at T_{N_2} broadens for $H > 2$T. Figure 8.8 shows plots of T_{N_1} and T_{N_2} versus H.

8.3.4 Electronic transport measurements

8.3.4.1 Electrical resistivity measurements

Figure 8.9 shows the electrical resistance ratio ρ/ρ_{300} of $\mathrm{EuPd_2Sb_2}$ for current parallel to the ab-plane versus temperature T in 0 and 8 T magnetic fields parallel to the c axis, where ρ is the resistance at temperature T and $\rho_{300} = (50 \pm 25)\mu\Omega$ cm is the resistance at 300 K. The large fractional uncertainty in ρ_{300} arises due to the uncertainty in the geometric factor for the irregularly-shaped crystal. The inset shows the low-T region below 10 K. The resistance data exhibit metallic behavior down to the lowest temperature. The residual resistance ratio $RRR = \rho(300\ \mathrm{K})/\rho(2\ \mathrm{K}) \approx 10$. This value is comparable to the values found in the ab-plane resistivity for single crystals of other layered pnictides.[59, 60, 63, 67] From the inset of Fig. 8.9, in zero magnetic field $\rho(T)$ shows an anomaly at 5.4 K which gets suppressed to 2.9 K in $H = 8$ T. The anomaly is evidently due to the antiferromagnetic ordering at $T_{N_1} = 6.1$ K

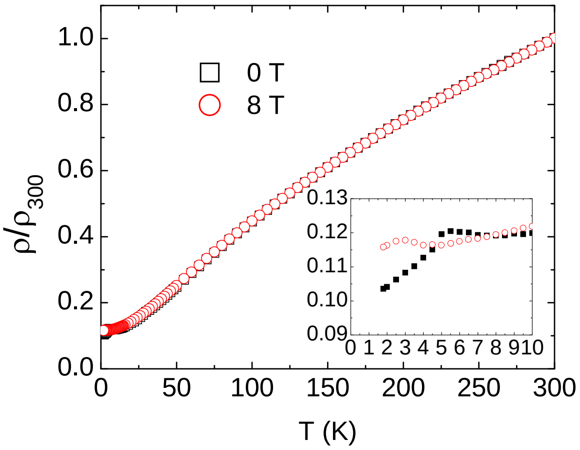

Figure 8.9 (Color online) Electrical resistance ratio ρ/ρ_{300} versus temperature T of $EuPd_2Sb_2$ for current in the ab-plane in 0 and 8 T magnetic fields parallel to the c axis where ρ is the resistance at temperature T and $\rho_{300} = (50 \pm 25)$ $\mu\Omega$ cm is the resistance at 300 K. The inset shows the low-T region below 10 K.

as observed from the $C_\mathrm{p}(T)$ and $\chi(T)$ measurements.

8.3.4.2 Hall coefficient measurements

Figure 8.10(a) shows the Hall resistivity $\rho_\mathrm{H} = V_\mathrm{H}A/Il$ versus H where V_H is the measured Hall voltage, A is the cross sectional area of the sample, l is the separation of the transverse voltage leads, and I is the longitudinal current. In Fig. 8.10(a), ρ_H versus magnetic field H is seen to deviate from a proportional behavior below 100 K. This behavior is more clearly seen in the plot of ρ_H/H versus H in Fig. 8.10(b). The measured $\rho_\mathrm{H}(H)$ data were fitted by the function $\rho_\mathrm{H}(H) = a_1H + a_3H^3 + a_5H^5$ and a_1 (the coefficient of the linear term) is the Hall coefficient R_H. R_H versus T is shown in Fig. 8.10(c), where R_H becomes more negative by a factor of 3 on cooling from 310 K to 2 K. The temperature dependence is very similar to $R_\mathrm{H}(T)$ of $BaRh_2As_2$ (Ref. [141]) which crystallizes in the tetragonal $ThCr_2Si_2$-type structure. The consistently negative R_H indicates that the dominant charge carriers are electrons. If one uses a single band model, one obtains a conduction electron concentration $n = (R_\mathrm{H}e)^{-1} = 3$ and 11 $(\mathrm{f.u.})^{-1}$ at 310 K and 2 K, respectively.

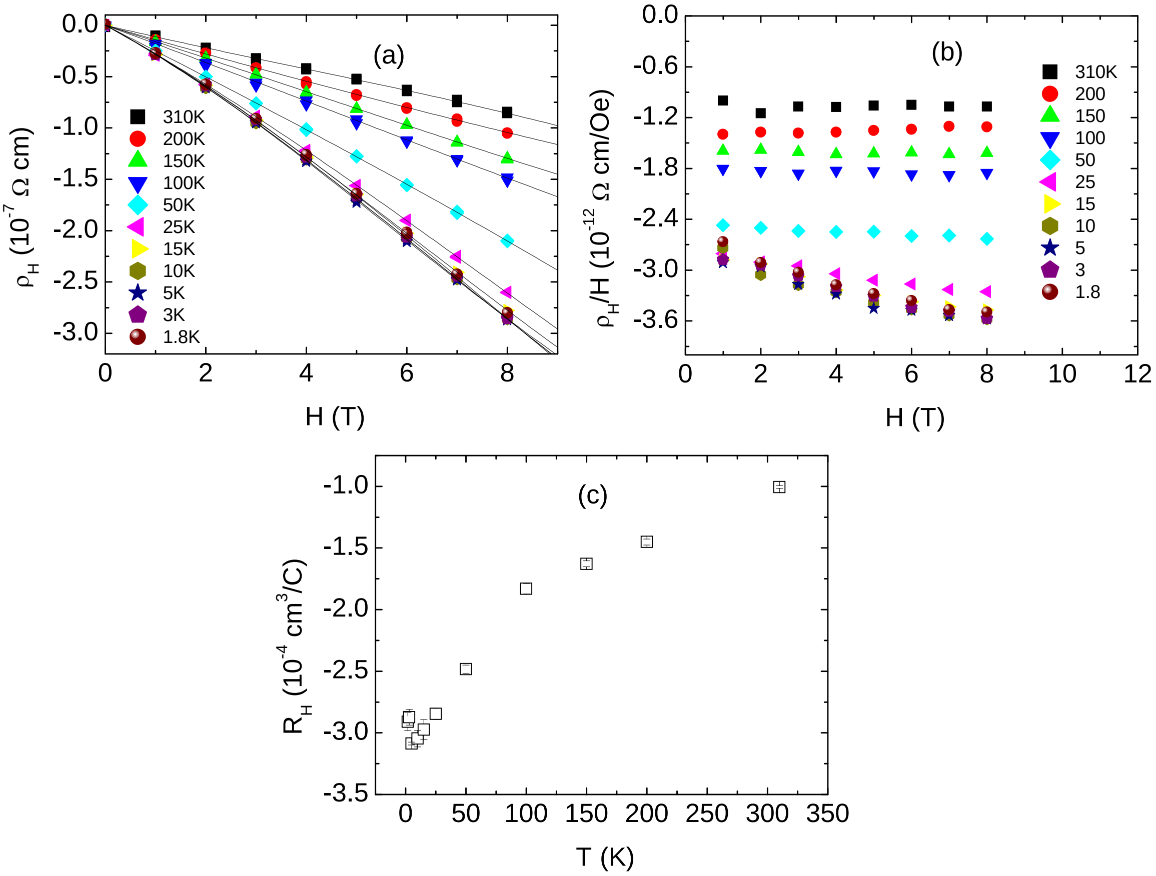

Figure 8.10 (Color online) (a) Hall resistivity $\rho_{\rm H}$ of $\rm EuPd_2Sb_2$ versus applied magnetic field H at the indicated temperatures T. The solid curves are polynomial fits to the data (see text). (b) $\rho_{\rm H}/H$ versus H at the indicated values of T. (c) Hall coefficient $R_{\rm H}$ versus T. The consistently negative $R_{\rm H}$ indicates that the dominant current carriers are electrons.

8.4 Summary and discussion

We have synthesized single crystals of $EuPd_2Sb_2$ and characterized them using single crystal x-ray diffraction, anisotropic magnetic susceptibility and magnetization, specific heat, electrical resistivity, and Hall coefficient measurements. The magnetic susceptibility indicates antiferromagnetic ordering at 6.0 K with an easy axis or plane within the crystallographic *ab* plane followed by another transition at 4.5 K. The transitions are also observed in heat capacity measurements indicating their bulk nature. The transition at 4.5 K is suppressed below 1.8 K in a magnetic field of 8 T as observed from the heat capacity and electrical resistivity measurements. The transition at 6 K is pushed down to 3.5 K in a field of 8 T. $M(H)$ isotherms show three field-induced transitions at 2.75 T, 3.90 T, and 4.2 T for magnetic fields parallel to the *ab* plane below 5 K. No transitions are observed for fields parallel to the *c* axis. The Hall coefficient is consistently negative from 1.8 to 310 K indicating electrons as the dominant charge carriers.

The related compound $EuFe_2As_2$ forms in the $ThCr_2Si_2$-type structure and shows superconducting behavior under pressure[142] as well as under doping at the Eu site.[71] The antiferromagnetic ordering temperature of $EuPd_2Sb_2$ is 6 K compared to the AF ordering temperature of 20 K of $EuFe_2As_2$. Thus the Eu-Eu spin interactions are different in the two compounds. The c/a ratio in $EuPd_2Sb_2$ is 2.28, which is quite different from 3.10 in $EuFe_2As_2$. In $Eu_{0.5}K_{0.5}Fe_2As_2$ which is superconducting below 32 K, however, AF ordering of the Eu spins take place below 10 K. The calculated effective moment 7.67 μ_B/f.u of the Eu spins in $EuPd_2Sb_2$ is close to the calculated effective moment 7.79 μ_B/f.u.[67] of Eu spins in $EuFe_2As_2$. The Hall coefficient of $EuPd_2Sb_2$ remains negative between 1.8 – 300 K like that in the superconducting $Ba(Fe_{1-x}Co_x)_2As_2$ and $Ba(Fe_{1-x}Cu_x)_2As_2$.[143] However, in $EuFe_2As_2$, the Hall coefficient changes sign from negative to positive at $\sim$ 175 K.

CHAPTER 9. Summary

We have synthesized polycrystalline samples as well as single crystals of very interesting vanadium compounds LiV_2O_4, YV_4O_8, and LuV_4O_8, and also of $EuPd_2Sb_2$ which has a crystal structure closely related to the recently discovered AFe$_2$As$_2$ high T_c superconductors. We carried out detailed investigations of their physical properties via magnetic, thermal, structural, and electrical transport measurements.

We studied the phase relations in the Li_2O-V_2O_3-V_2O_5 system at 700 °C for compositions in equilibrium with LiV_2O_4. This study helped us to determine the synthesis conditions under which polycrystalline samples of LiV_2O_4 could be prepared with variable magnetic defect concentrations ranging from $n_{\rm defect} = 0.006$ to 0.83 mol%. High magnetic defect concentrations were found in samples containing V_2O_3, Li_3VO_4, or $LiVO_2$ impurity phases while the samples containing V_3O_5 impurity phase had low defect concentration. Based on our findings, we suggested a model which might explain this correlation. Our work shows how to systematically and controllably synthesize LiV_2O_4 samples with variable magnetic defect concentrations within the spinel structure.

In the course of our study of the phase relations in the Li_2O-V_2O_3-V_2O_5 ternary system, we discovered that LiV_2O_4 exists in equilibrium with Li_3VO_4 at 700 °C. This led to the possibility of using Li_3VO_4 as a flux to grow single crystals of LiV_2O_4. Following up on this idea, we studied the LiV_2O_4–Li_3VO_4 pseudobinary phase diagram. LiV_2O_4 was found to decompose peritectically at 1040 °C. A eutectic was found with a eutectic temperature of 950 °C and with the eutectic composition being approximately 53 wt% LiV_2O_4 and 47 wt% Li_3VO_4. The discovery of the eutectic lead to our succesful growth of LiV_2O_4 single crystals using Li_3VO_4 as the flux. The crystals were of high quality, and as with powder LiV_2O_4, are not reactive to air and moisture. While the magnetic susceptibility of some of the crystals showed a Curie-like upturn at low T showing the presence of magnetic defects within the spinel structure, the susceptibility of a few crystals with a different morphology showed almost temperature independent behavior at low temperatures, indicating absence of magnetic defects in them. From the heat capacity measurements, a very large value of 450 mJ/mole K^2 was obtained for C/T for crystals having magnetic defects in them while a value of 380 mJ/mol K^2 was obtained for crystals which were free of any magnetic defects. The electrical resistivity measurements on magnetically pure crystals as well as crystals with magnetic defects revealed the expected metallic behavior down to 1.8 K.

To investigate if there were any periodic correlations among the magnetic defects present within the LiV_2O_4 spinel structure, we carried out high energy x-ray diffraction experiments on the crystals. No noticeable difference in the x-ray diffraction patterns of the reciprocal lattice planes of a crystal with a high magnetic defect concentration and a crystal with a low magnetic defect concentration was found. This observation points towards the absence of any long-range or short-range periodicity or order in the arrangement of the crystal defects giving rise to the magnetic defects. We observed some diffuse scattering in our diffraction patterns. However, the observed diffuse scattering was similar for crystals with high and low magnetic defect concentrations. We thus exclude any long-range order or short-range order of the crystal defects related to the different magnetic defect concentrations. Our observations lead to the conclusion that the crystal defects in LiV_2O_4 which produce the magnetic defects are randomly distributed within the spinel structure. Preliminary high pressure x-ray diffraction studies on LiV_2O_4 crystals revealed possible phase crystallographic phase transition(s) around 6 and 20 GPa. Additional measurements to determine the structure(s) are planned.

Important fundamental issues regarding LiV_2O_4 include whether the heavy Fermi liquid in magnetically pure LiV_2O_4 survives when magnetic defects are present and whether the crystal and magnetic defects drive a metal-insulator transition at some defect concentration. These questions can initially be addressed in the millikelvin temperature range using electrical resistivity, magnetic susceptibility, NMR, and electrical resistivity measurements. A related question is whether a quantum critical point occurs versus magnetic defect concentration. Professor Ruslan Prozorov's group tried to measure the electrical resistivity of some of the our LiV_2O_4 crystals in the milliKelvin temperature range using a dilution refrigerator. However, they did not obtain usable results due to low signal-to-noise ratio. The measurements of the physical properties of LiV_2O_4 with magnetic defects in the milliKelvin temperature range are exciting topics for future research.

Apart from the spinel LiV_2O_4, we also studied some low dimensional vanadium spin chain compounds as spin chain compounds often show interesting magnetism. Interesting crystallographic and magnetic phase transitions were found in CaV_2O_4 as described in Appendix A. We have also synthesized single phase powder samples of YV_4O_8 and LuV_4O_8 whose crystallographic structure consist of two distinct one dimensional zigzag chains running along the crystallographic c-axis and carried out a detailed investigation of their structure, magnetic susceptibility, magnetization, specific heat, and electrical transport.

X-ray diffraction measaurements exhibit a first order-like phase transition with a sudden change in the lattice parameters and unit cell volume at 50 K in YV_4O_8. Interestingly, the high and low temperature structures have the same monoclinic symmetry. As a result of the transition, one of the chains dimerizes. The dimerization is also observed in the magnetic susceptibility which shows a sharp drop at 50 K. The other chain undergoes antiferromagnetic ordering at 50 K and the ordered spins then become canted below 16 K. The change in the magnetic entropy calculated from heat capacity measurements agrees very well with ordering of three $S = 1$ and one $S = 1/2$ disordered spins per formula unit. The lattice parameters of LuV_4O_8 exhibit a small anomaly at ~ 50 K but not as sharp as in YV_4O_8. The magnetic susceptibility of LuV_4O_8 shows a broad peak at ~ 60 K followed by a sharp first order-like increase at 50 K. The 50 K anomaly is suppressed at higher fields. For both compounds, Curie-Weiss fits to the high T susceptibilities yield Curie constants which are much lower than expected. Electrical resistivity measurements on sintered pellets indicate metal to insulator-like transition at 60 K and 50 K for YV_4O_8 and LuV_4O_8, respectively. It would be very interesting to study single crystals of these compounds. Single crystal resistivity measurements are needed to determine if these materials are metallic or not. Measurements like NMR or neutron scattering that would provide microscopic information about the spin dynamics would also be valuable to clarify the nature of the magnetic ordering transitions in YV_4O_8 and LuV_4O_8.

Our x-ray diffraction study of the reaction kinetics of the formation of $LaFeAsO_{1-x}F_x$ componds, as described in Ref. [58], revealed that $LaFeAsO_x$ forms over a range of oxygen stoichiometry with $0.1 \leq x \leq 0.3$ at high temperatures. We also found that the control of the reaction in the proximity of the Fe-Fe_2As eutectic temperature is essential for high reaction rates and sample homogeneity.

Magnetic susceptibility and heat capacity measurements on $EuPd_2Sb_2$ single crystals revealed long-range antiferromagnetic ordering below 6 K in the crystallographic *ab* plane and a possible spin reorientation transition at 4.5 K. Magnetization versus magnetic field measurements at 1.8 K showed anomalies at 2.75 T, 3.90 T, and 4.2 T magnetic field parallel to the *ab* plane which point towards metamagnetic transitions between antiferromagnetic states. Hall coefficient measurements indicated that electrons are the dominant charge carriers in $EuPd_2Sb_2$. No spin density waves or structural transitions were observed. It will be very interesting to grow single crystals of $EuPd_{1-x}Fe_xSb_2$ and study their physical properties. The doping of Fe at the Pd site will eventually make the Pd(Fe)-Sb layers magnetic, like they are in the $A\mathrm{Fe_2As_2}$ compounds. In addition, synthesizing polycrystalline and single crystal samples of other compounds which form in the $CaBe_2Ge_2$-type structure and with magnetic ions at the Be site might lead to new high T_c superconductors.

APPENDIX A. Single Crystal Growth, Crystallography, Magnetic Susceptibility, Heat Capacity, and Thermal Expansion of the Antiferromagnetic S = 1 Chain Compound $\mathbf{CaV_2O_4}$

This appendix is based on a paper published in Phys. Rev. B **79**, 104432 (2009) by A. Niazi, S. L. Budko, D. L. Schlagel, J.-Q. Yan, T. A. Lograsso, A. Kreyssig, S. Das, S. Nandi, A. I. Goldman, A. Honecker, R. W. McCallum, M. Reehuis, O. Pieper, B. Lake, and D. C. Johnston.

Abstract

The compound CaV_2O_4 contains V^{+3} cations with spin $S = 1$ and has an orthorhombic structure at room temperature containing zigzag chains of V atoms running along the c-axis. We have grown single crystals of CaV_2O_4 and report crystallography, static magnetization, magnetic susceptibility χ, ac magnetic susceptibility, heat capacity $C_{\rm p}$, and thermal expansion measurements in the temperature T range of 1.8–350 K on the single crystals and on polycrystalline samples. An orthorhombic to monoclinic structural distortion and a long-range antiferromagnetic (AF) transition were found at sample-dependent temperatures $T_{\rm S} \approx 108$–145 K and $T_{\rm N} \approx 51$–76 K, respectively. In two annealed single crystals, another transition was found at ≈ 200 K. In one of the crystals, this transition is mostly due to V_2O_3 impurity phase that grows coherently in the crystals during annealing. However, in the other crystal the origin of this transition at 200 K is unknown. The $\chi(T)$ shows a broad maximum at ≈ 300 K associated with short-range AF ordering and the anisotropy of χ above $T_{\rm N}$ is small. The anisotropic $\chi(T \to 0)$ data below $T_{\rm N}$ show that the (average) easy axis of the AF magnetic structure is the b-axis. The $C_{\rm p}(T)$ data indicate strong short-range AF ordering above $T_{\rm N}$, consistent with the $\chi(T)$ data. We fitted our χ data by a J_1-J_2 $S = 1$ Heisenberg chain model,

where $J_1(J_2)$ is the (next)-nearest-neighbor exchange interaction. We find $J_1 \approx 230$ K, and surprisingly, $J_2/J_1 \approx 0$ (or $J_1/J_2 \approx 0$). The interaction $J_\perp$ between these $S = 1$ chains leading to long-range AF ordering at $T_{\rm N}$ is estimated to be $J_\perp/J_1 \gtrsim 0.04$.

A.1 Introduction

Low-dimensional frustrated spin systems have rich phase diagrams arising from a complex interplay of thermal and quantum fluctuations and competing magnetic interactions at low temperatures. While spin $S = 1/2$ antiferromagnetic (AF) chains[144] and odd-leg ladders[85, 145] have gapless magnetic excitations, $S = 1$ chains and $S = 1/2$ even-leg ladders with nearest-neighbor (NN, J_1) interactions exhibit a finite energy gap between the ground state and the lowest excited magnetic states. However, numerical calculations have shown that the influence of frustrating next-nearest-neighbor (NNN, J_2) interactions play a significant role and depending on the J_2/J_1 ratio, can lead to incommensurate helical spin structures which may be gapped or gapless. [37, 38, 146–148] Such a system is described by the XXZ Hamiltonian [38]

$$\mathcal{H} = \sum_{\rho=1}^{2} J_\rho \sum_l (S_l^x S_{l+\rho}^x + S_l^y S_{l+\rho}^y + \lambda S_l^z S_{l+\rho}^z), \tag{A.1}$$

where $\mathbf{S}_l$ is the spin operator at the lth site, J_ρ is the AF interaction between the NN ($\rho = 1$) and NNN ($\rho = 2$) spin pairs, and λ is the exchange anisotropy. For $j \equiv J_2/J_1 > 1/4$, the classical AF chain exhibits incommensurate helical long-range ordering described by the wave vector $q = \arccos[-1/(4j)]$ and a finite *vector chirality* $\vec{\kappa} = \mathbf{S}_i \times \mathbf{S}_{i+1}$ which describes the sense of rotation (left or right handed) of the spins along the helix. In the large-j, small-λ limit of the $S = 1$ chain, one finds a corresponding phase[146] where spin correlations decay, as required for a one-dimensional system, although only algebraically, but chirality is still long-range ordered. This phase is called the *chiral gapless phase* and is seen to exist for all spin quantum numbers S.[37, 147] For smaller j, a *chiral gapped phase* is observed in the $S = 1$ chain,[146] with chiral long-range order and exponentially decaying spin correlations.

The above chiral phases are ground state phases of a spin system. In a related prediction, Villain suggested three decades ago that a long-range ordered vector chiral phase can exist above the Néel temperature T_{N} of a quasi-one-dimensional spin chain system showing helical magnetic ordering below T_{N}.[149] This chiral phase would have a transition temperature $T_0 > T_{\mathrm{N}}$ that could be detected using heat capacity measurements.[149]

The compound CaV_2O_4, containing crystallographic V^{+3} spin $S = 1$ zigzag chains, has been suggested as a model experimental system to study the above chiral gapless phase. [11, 12] CaV_2O_4 crystallizes in the $CaFe_2O_4$ structure at room temperature[9, 10] with the orthorhombic space group *Pnam* and with all the atoms in distinct Wyckoff positions $4(c)$ $(x, y, 1/4)$ in the unit cell. As shown in Figs. A.1 and A.2, two zigzag chains of distorted edge- and corner-sharing VO_6 octrahedra occur within the unit cell and run parallel to the c-axis, with the Ca ions situated in tunnels between the chains. Two sets of crystallographically inequivalent V atoms occupy the two zigzag chains, respectively. The VO_6 octahedra within a zigzag chain share corners with the octahedra in the adjacent zigzag chain. Within each zigzag chain, in order to be consistent with our theoretical modeling later in Sec. A.4 of the paper, the nearest neighbors are *defined* to be those on different legs of the zigzag chain where the NN V-V distance is 3.07 Å. The NNN V-V distance (3.01 Å) is *defined* to be along a leg of the zigzag chain. The similarity between these two distances in CaV_2O_4 suggests that $J_1 \approx J_2$, which would result in geometrically frustrated AF interactions in this insulating low-dimensional system.[11, 12]

Previous studies on polycrystalline samples of CaV_2O_4 have offered contrasting views on the nature of the magnetic ground state. Magnetic neutron diffraction measurements on CaV_2O_4 (Ref. [10]) gave clear evidence for the presence of long-range antiferromagnetic ordering at 4.2 K (the temperature dependence was not studied, and the Néel temperature was not determined). A doubled magnetic unit cell along the b and c directions was found with AF propagation vector $(0\ \frac{1}{2}\ \frac{1}{2})$ and three collinear AF models with the V ordered moments parallel to the b-axis were considered. Interestingly, the ordered moment was found to be 1.06(6) μ_B/(V atom), where μ_B is the Bohr magneton. This value is a factor of two smaller than the value $gS\mu_B = 2.0\ \mu_B$/(V atom) expected for a spin $S = 1$ with spectroscopic splitting factor (g-factor) $g = 2$. Magnetic susceptibility measurements[11, 12] showed a broad maximum at ~ 250 K, indicating the onset of strong short-range AF ordering in a low-dimensional spin system upon cooling. The data also showed a finite value at the lowest temperatures, indicating that an energy gap for spin excitations did not occur, consistent with the neutron diffraction measurements.

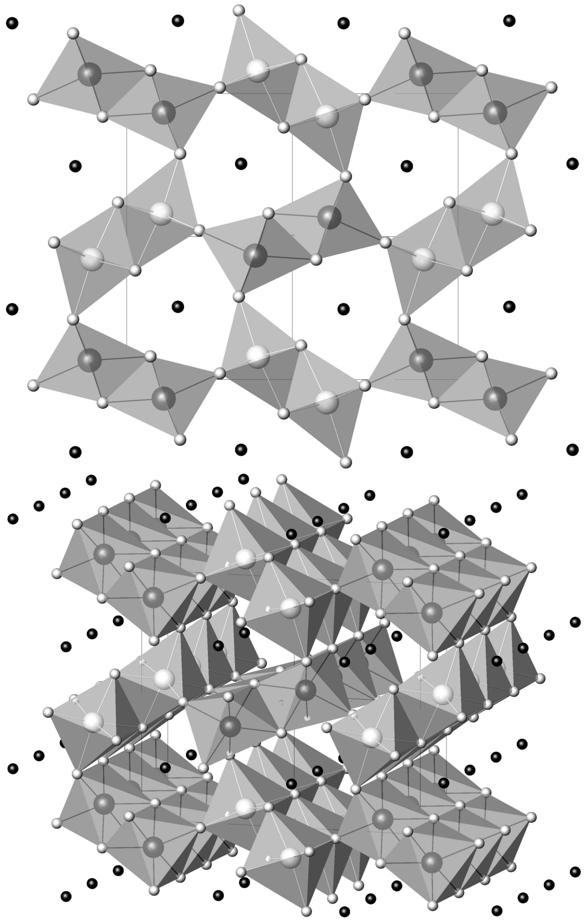

Figure A.1 End-on (top) and inclined (bottom) views along the *c*-axis of the CaV_2O_4 structure showing the V zigzag chains with the V atoms in distorted edge- and corner-sharing octahedral coordination by oxygen.

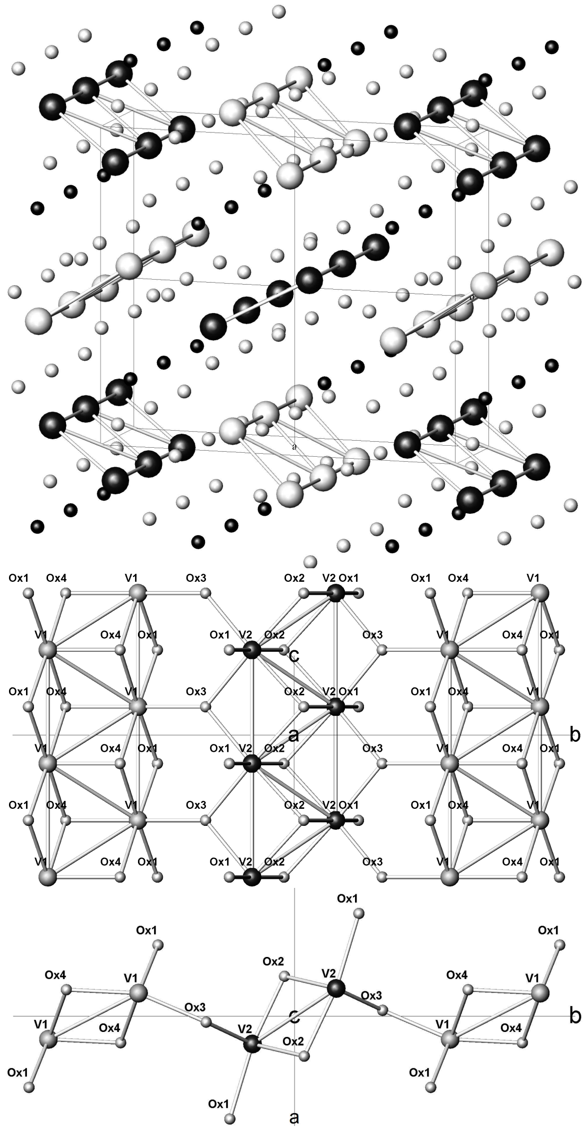

Figure A.2 Top panel: the skeletal structure of CaV_2O_4 showing the zigzag V-V chains. The large spheres represent V atoms, the small dark spheres Ca atoms, and the small light spheres O atoms. Middle and bottom panels: cross-sections of the *b*-*c* and *a*-*b* planes, with the V and O atoms labeled as described in Table A.2. The Ca atoms have been omitted for clarity.

However, these magnetic susceptibility data also showed a bifurcation below ~ 20 K between low field (100 Oe) zero-field-cooled and field-cooled measurements that was suggestive of a spin-glass-like freezing rather than long-range AF ordering. ^{51}V nuclear magnetic resonance (NMR) measurements[11, 12] showed a nuclear spin-lattice relaxation rate $1/T_1 \propto T$ at low temperatures from 2 K to 30 K, of unknown origin, but again indicating lack of an energy gap for magnetic excitations. The authors[11, 12] proposed a *chiral gapless ordered* phase at low temperatures in accordance with theoretical predictions for a $S = 1$ frustrated XY or XXZ chain. The chiral phase implies a helical spin arrangement in contrast to the collinear spin models proposed[10] in the neutron diffraction study. Furthermore, the observation of a ^{51}V nuclear resonance at the normal ^{51}V Larmor frequency[11, 12] at temperatures at and below 4 K is not consistent with the long-range antiferromagnetic ordering found at 4 K from the neutron diffraction measurements,[10] since such ordering produces a very large static local magnetic field of order 20 T at the positions of the V nuclei.

In order to resolve the above inconsistencies regarding the magnetic ground state of $\mathrm{CaV_2O_4}$ and to search for interesting physics in this system associated with possible geometric frustration within the zigzag spin chains, we have for the first time (to our knowledge) grown single crystals of this compound, and report herein crystal structure, static magnetization and magnetic susceptibility $\chi(T)$, ac magnetic susceptibility $\chi_{\rm ac}(T)$, heat capacity $C_{\rm p}(T)$, and anisotropic linear thermal expansion $\alpha_i(T)$ $(i = x, y, z)$ measurements over the temperature T range 1.8 to 350 K on polycrystalline and single crystal samples. Our $\chi(T)$ and $\chi_{\rm ac}(T)$ measurements do not show any signature of a spin-glass transition around 20 K as previously reported.[11, 12] We instead observe long-range antiferromagnetic (AF) ordering at sample-dependent Néel temperatures $T_{\rm N} \approx 51$–76 K.

We have recently reported elsewhere the results of ^{17}O NMR measurements on a polycrystalline sample of $\mathrm{CaV_2O_4}$ and find a clear signature of AF ordering at $T_{\rm N} \approx 78$ K.[150] We find no evidence of a ^{51}V NMR signal at the normal Larmor frequency at temperatures between 4 K and 300 K, in conflict with the above previous ^{51}V NMR studies which did find such a resonance.[11, 12] In single crystals, at temperatures below 45 K we do find a *zero-field* ^{51}V

NMR signal where the ^{51}V nuclei resonate in the static component of the local magnetic field generated by the long-range AF order below $T_{\rm N} \approx 70$ K.[150] The ordered moment at 4.2 K in the crystals was estimated from the zero-field ^{51}V NMR measurements to be 1.3(3) $\mu_{\rm B}$/(V atom), somewhat larger than but still consistent with the value 1.06(6) $\mu_{\rm B}$/(V atom) from the above neutron diffraction measurements. [10] An energy gap Δ for antiferromagnetic spin wave excitations was found with a value $\Delta/k_{\rm B} = 80(20)$ K in the temperature range 4–45 K, where $k_{\rm B}$ is Boltzmann's constant. This energy gap was proposed to arise from single-ion anisotropy associated with the $S = 1$ V^{+3} ion. A model for the antiferromagnetic structure at 4 K was formulated in which the magnetic structure consists of two substructures, each of which exhibits collinear antiferromagnetic order, but where the easy axes of the two substructures are at an angle of 19(1)° with respect to each other. The *average* easy axis direction is along the b-axis, consistent with our magnetic susceptibility measurements to be presented here, and with the easy-axis direction proposed in the earlier neutron diffraction measurements.[10] Our magnetic neutron diffraction studies of the antiferromagnetic structure of CaV_2O_4 single crystals are qualitatively consistent with the NMR analyses; these results together with high-temperature ($T \leq 1000$ K) magnetic susceptibility measurements and their analysis are presented elsewhere.[151]

We also find that CaV_2O_4 exhibits a weak orthorhombic to monoclinic structural distortion upon cooling below a sample-dependent temperature $T_{\rm S} = 108$–147 K, discovered from our neutron and x-ray diffraction measurements to be reported in detail elsewhere.[152] In our two *annealed single crystals* only, anomalies in the heat capacity and thermal expansion are also found at $T_{\rm S1} \approx 200$ K. From high-energy x-ray diffraction measurements reported here, we find that in one of the crystals the anomaly is most likely primarily due to the metal-insulator and structural transitions in V_2O_3 impurity phase that grows coherently in the crystal when it is annealed. In the other crystal, we still find a small anomaly in the heat capacity at $T_{\rm S1}$ but where the transition in the V_2O_3 impurity phase is at much lower temperature. Hence we infer that there is an intrinsic transition in our two annealed CaV_2O_4 crystals at $T_{\rm S1}$ with an unknown origin. We speculate that this transition may be the long-sought chiral ordering transition envisioned by Villain[149] that was mentioned above.

From our inelastic neutron scattering results to be published elsewhere,[153] we know that the magnetic character of $\mathrm{CaV_2O_4}$ is quasi-one-dimensional as might be inferred from the crystal structure. The largest dispersion of the magnetic excitations is along the zigzag chains, which is along the orthorhombic c-axis direction, with the dispersion along the two perpendicular directions roughly a factor of four smaller. This indicates that the exchange interactions perpendicular to the zigzag chains are roughly an order of magnitude smaller than within a chain. We therefore analyze the magnetic susceptibility results here in terms of theory for the $S = 1$ J_1-J_2 linear Heisenberg chain, where $J_1(J_2)$ is the (next-)nearest-neighbor interaction along the chain. With respect to the interactions, this chain is topologically the same as a zigzag chain where J_1 is the nearest-neighbor interaction between spins in the two different legs of the zigzag chain and J_2 is the nearest-neighbor interaction between spins within the same leg. We utilize exact diagonalization to calculate the magnetic susceptibility and magnetic heat capacity for chains containing up to 14 spins $S = 1$, and quantum Monte Carlo simulations of the magnetic susceptibility and heat capacity for chains of 30 and 60 spins. We obtain estimates of J_1, J_2/J_1, the temperature-independent orbital susceptibility χ_0, and the zero-temperature spin susceptibilities in $\mathrm{CaV_2O_4}$ from comparison of the theory with the experimental $\chi(T)$ data near room temperature. Remarkably, we find that one of the two exchange constants is very small compared to the other near room temperature, as opposed to $J_1/J_2 \approx 1$ that is expected from the crystal structure. Thus, with respect to the magnetic interactions, the zigzag crystallographic chain compound acts instead like a linear $S = 1$ Haldane spin chain compound. In Ref. [151], we propose that partial orbital ordering is responsible for this unexpected result, and suggest a particular orbital ordering configuration. In Ref. [151], we also deduce that below $T_{\mathrm{S}} \sim 150$ K, the monoclinic distortion results in a change in the orbital ordering that in turn changes the nature of the spin interactions from those of a Haldane chain to those of a $S = 1$ two-leg spin ladder. Here we also compare the theory for the magnetic heat capacity with the results of our heat capacity experiments. We estimate the coupling $J_\perp$ between these chains that leads to the long-range AF order at T_{N}.

The remainder of this paper is organized as follows. The synthesis and structural studies are presented in Sec. A.2. The magnetization, magnetic susceptibility, heat capacity and thermal expansion measurements are presented in Sec. A.3. In Sec. A.4 we consider the origin of the heat capacity and thermal expansion anomalies at $T_{\rm S1} \approx 200$ K. We then analyze the $\chi(T)$ data in terms of the predictions of exact diagonalization calculations and quantum Monte Carlo simulations to obtain J_1, J_2/J_1 and χ_0. Using the same J_1 and J_2/J_1 parameters, we compare the predicted behavior of the magnetic heat capacity with the experimentally observed heat capacity data. We also obtain an estimate of the interchain coupling $J_\perp$ giving rise to long-range AF order at $T_{\rm N}$. A summary of our results is given in Sec. A.5.

A.2 Synthesis, single crystal growth, and crystal structure of CaV_2O_4

A.2.1 Synthesis and Crystal Growth

Polycrystalline CaV_2O_4 was synthesized via solid state reaction by first mixing V_2O_3 (99.995%, MV Labs) with $CaCO_3$ (99.995%, Aithaca Chemicals) or CaO obtained by calcining the $CaCO_3$ at 1100 °C. The chemicals were ground inside a He glove-box, pressed and sintered at 1200 °C for 96 hours in flowing 4.5%H_2-He, as well as in sealed quartz tubes when using CaO, with intermediate grindings. Phase purity was confirmed by powder x-ray diffraction (XRD) patterns obtained using a Rigaku Geigerflex diffractometer with Cu Kα radiation in the angular range $2\theta = 10$–90° accumulated for 5 s per 0.02° step. Thermogravimetric analysis (TGA) at 800 °C using a Perkin Elmer TGA 7 was used to check the oxygen content by oxidizing the sample to CaV_2O_6. A typical oxygen content of $CaV_2O_{3.98\pm0.05}$ was determined, consistent with the initial stoichiometric composition CaV_2O_4.

CaV_2O_4 was found to melt congruently in an Ar arc furnace with negligible mass loss by evaporation. Therefore crystal growth was attempted by pulling a crystal from the melt in a triarc furnace (99.995% Ar) using a tungsten seed rod.[154] The triarc furnace was custom made for us by Materials Research Furnaces, Inc. Using 15–20 g premelted buttons of CaV_2O_4, pulling rates of 0.2–0.5 mm/min were used to grow ingots of about 3–6 mm diameter and 3.0–4.7 cm length. The length of the ingot was limited by contraction of the molten region as power was lowered to control the crystal diameter. Obtaining a single grain was difficult because small fluctuations in the arcs coupled with high mobility of the CaV_2O_4 melt easily caused nucleation of new grains. Out of multiple growth runs, a reasonably large single grain section could be cut out of one of the ingots. The as-grown ingot from the triarc furnace and a single crystal isolated and aligned from it are shown in Figs. A.3(a) and (b), respectively. Due to the tendency for multiple nucleations in the triarc furnace, an optical floating zone (OFZ) furnace was subsequently used for crystal growth.[154] Growth rates and Ar atmosphere flow rates were optimized to successfully grow large crystals of 4–5 mm diameter and 4–5 cm length starting from sintered polycrystalline rods with masses of 8–10 g. An as-grown rod from the OFZ furnace is shown in Fig. A.3(c).

Powder XRD of crushed sections from the triarc grown ingots as well as from the OFZ grown crystals showed single phase CaV_2O_4. Laue x-ray diffraction patterns of a single-grain section confirmed its single-crystalline character and the crystal was found to grow approximately along its crystallographic *c*-axis. The crystals were oriented and cut to obtain faces aligned perpendicular to the principal axes. They were measured as grown (only for the triarc grown crystals) as well as after annealing in flowing 5%H_2-He gas at 1200 °C for up to 96 hours.

A.2.2 Powder and Single Crystal X-ray and Neutron Diffraction Measurements

Rietveld refinements of the powder x-ray diffraction data obtained at room temperature were carried out using the program DBWS9807a.[155] The refined powder XRD patterns from a polycrystalline sample and crushed pieces of the triarc and optical floating zone grown crystals are shown in Fig. A.4 and the refinement results are presented in Tables A.1, A.2, and A.3. The XRD of the powdered *annealed* single crystal samples showed a trace amount ($\sim$ 1–2 mol%) of V_2O_3. It is curious that no trace was found of V_2O_3 impurity phase in the as-grown crystals, and that this impurity phase only formed after annealing the crystals. From the refinement results, the structural parameters remain relatively unchanged between polycrystalline samples prepared by the solid state route and both as-grown and annealed single crystals grown from the melt.

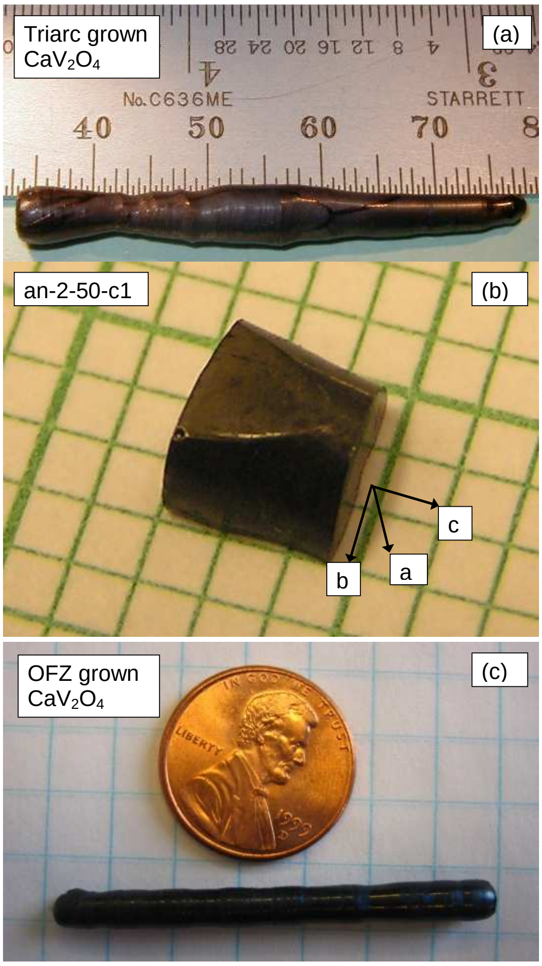

Figure A.3 (Color online) Single crystals of CaV_2O_4 grown using (a), (b) a triarc furnace (a numbered division on the scale is 1 mm) and (c) an optical floating zone furnace (compared with a U.S. penny).

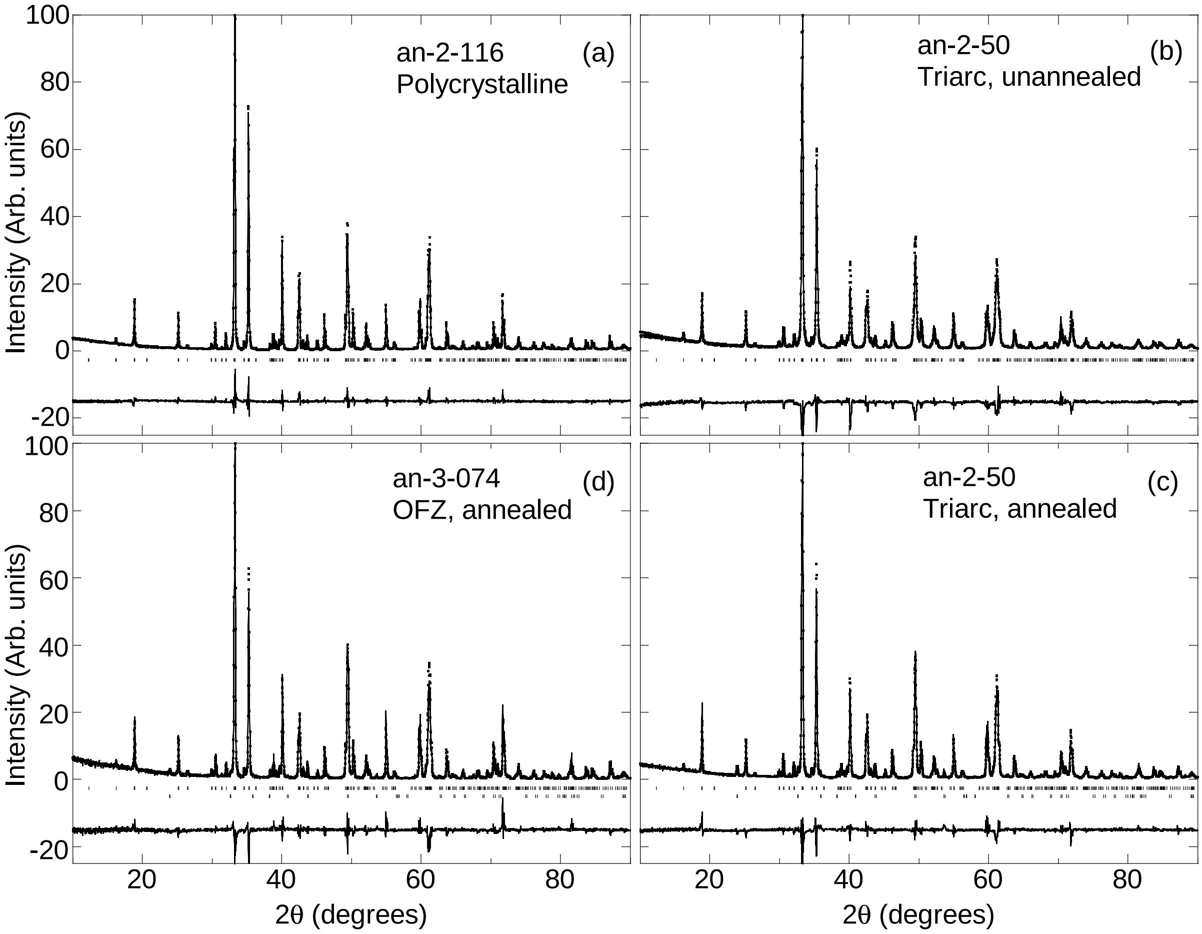

Figure A.4 Rietveld refinement of room temperature powder XRD data of CaV_2O_4 showing I_{obs} (+) I_{calc} (.), difference (–), and peak positions (|) for (a) a polycrystalline sample, (b) an as-grown triarc crystal, (c) an annealed triarc crystal, and (d) an annealed optical floating zone (OFZ) crystal. The annealed single crystal samples contain small XRD peaks from ∼ 1–2 mol% of V_2O_3, shown as the lower sets of peak position markers.

Single-crystal neutron diffraction data were collected on the four-circle diffractometer E5 at the BERII reactor of the Helmholtz-Zentrum Berlin, Germany. A pyrolytic graphite monochromator was used to select the neutron wavelength $\lambda = 2.36$ Å. Second order contamination was suppressed below 10^{-3} of first order by a pyrolytic graphite filter. Bragg reflections of CaV_2O_4 were measured with a two-dimensional position sensitive ^{3}He detector, 90×90 mm^2 in area. The sample was mounted in a closed-cycle refrigerator, where the temperature was controlled between 290 K and 6 K. A structural phase transition at temperature T_S from the high temperature orthorhombic structure to a low temperature monoclinic structure was found.[152] This transition is reflected in Fig. A.5 by a sudden change in the (0 3 1) Bragg peak intensity which occurs at a temperature $T_S \approx 112$ K for the as-grown triarc crystal, and ≈ 141 K and ≈ 147 K for the annealed triarc and OFZ-grown crystals, respectively. Due to twinning the orthorhombic (0 3 1) reflection splits below the structural phase transition into the (0 3 1) and (0 $\bar{3}$ 1) monoclinic reflections. The total integrated intensity at this position increases at T_S because of the increased mosaic which results in a reduction of the extinction effect. The peak in the intensity at 105 K for the as-grown triarc crystal is an experimental artifact due to multiple scattering. The lattice parameters of the low temperature monoclinic phase differ very little from the orthorhombic phase and the monoclinic angle $\alpha \approx 89.3°$ is close to 90°. This result and the smoothly varying signatures in the thermodynamic properties suggest that the structural transition is of second order and involves a small distortion of the orthorhombic structure. Full details of the neutron and x-ray diffraction structural measurements and results will be presented elsewhere.[152]

A higher temperature anomaly in the temperature dependence of the lattice parameters of a powder sample was observed by x-ray diffraction over a temperature range of 175–200 K. This transition with $T_{S1} \approx 200$ K was also observed in the magnetic susceptibility, thermal expansion, and heat capacity measurements of two *annealed single crystals* as described in Sec. A.3 below. In the next section we investigate whether there is a structural aspect to this phase transition.

Table A.1 Structure parameters at room temperature for CaV_2O_4 forming in the $CaFe_2O_4$ structure, refined from powder XRD data. Space Group: $Pnam$ (#62); $Z = 4$; Atomic positions: 4(c), $(x, y, 1/4)$; Profile: Pseudo-Voigt. The overall isotropic thermal parameter B is defined within the temperature factor of the intensity as $e^{-2B\sin^2\theta/\lambda^2}$.

Sample	Synthesis	a (Å)	b (Å)	c (Å)	B (Å^2)	R_{wp}(%)	R_{p} (%)
an-2-116	1200 °C solid state	9.2064(1)	10.6741(1)	3.0090(1)	2.33(4)	11.17	8.24
an-2-50	Triarc as grown	9.2241(11)	10.6976(13)	3.0046(4)	1.72(5)	12.05	9.27
an-2-50	Triarc annealed 1200 °C	9.2054(3)	10.6748(3)	3.0042(1)	1.58(5)	14.54	10.95
an-3-074	OFZ annealed 1200 °C	9.2089(2)	10.6774(3)	3.0067(1)	0.75(5)	17.46	12.77

Table A.2 Atomic positions $(x, y, 1/4)$ for CaV_2O_4 obtained by Rietveld refinement of powder XRD data at room temperature for four samples.

Sample No.	an-2-116	an-2-50-c1	an-2-50-c1	an-3-074
Synthesis	Solid State	Triarc	Triarc	OFZ
	(1200 °C)	(as grown)	(annealed)^1	(annealed)^1
	x, y	x, y	x, y	x, y
Ca	0.7550(3), 0.6545(2)	0.7562(4), 0.6536(3)	0.7542(4), 0.6544(3)	0.7536(4), 0.6550(3)
V1	0.4329(2), 0.6117(1)	0.4320(3), 0.6120(2)	0.4336(3), 0.6120(2)	0.4331(3), 0.6114(2)
V2	0.4202(2), 0.1040(1)	0.4204(3), 0.1041(2)	0.4200(3), 0.1043(2)	0.4209(3), 0.1043(2)
O1	0.2083(6), 0.1615(5)	0.2128(8), 0.1593(7)	0.2049(8), 0.1603(8)	0.2074(9), 0.1635(9)
O2	0.1176(5), 0.4744(5)	0.1157(7), 0.4745(8)	0.1144(7), 0.4756(8)	0.1181(9), 0.4738(9)
O3	0.5190(7), 0.7823(5)	0.5153(11), 0.7812(7)	0.5166(0), 0.7806(7)	0.5169(11), 0.7797(8)
O4	0.4203(6), 0.4270(5)	0.4207(8), 0.4282(7)	0.4244(8), 0.4325(7)	0.4280(9), 0.4251(9)

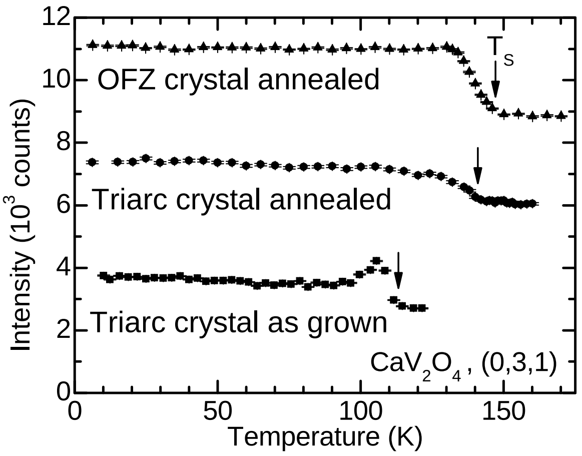

Figure A.5 Temperature variation of intensity of the (0 3 1) structural Bragg peak across the orthorhombic to monoclinic structural transition temperature (T_S) in single crystal samples of CaV_2O_4 measured by neutron diffraction. The (0 3 1) peak is present in both the orthorhombic and monoclinic phases.

Table A.3 Bond angles V–O–V and bond lengths V–V for CaV_2O_4 at room temperature refined from powder XRD data and calculated using Atoms for Windows, version 5.0. The V_1–O and V_2–O bond lengths varied from 1.92 Å to 2.08 Å. The accuracy of the bond angles calculated is ±0.1 °.

Sample Number	an-2-116	an-2-50-c1	an-2-50-c1	an-3-074
Synthesis	Sintered powder (1200 °C)	Triarc (as grown)	Triarc (annealed)	Optical float zone (annealed)
V_1–O_1–V_1 (NN)(°)	93.9	92.9	95.0	93.7
V_1–O_4–V_1 (NN)(°)	93.6	93.0	94.4	96.6
V_1–V_1 (NN)(Å)	3.009	3.005	3.004	3.004
V_1–O_4–V_1 (NNN)(°)	99.3	99.9	101.8	100.3
V_1–V_1 (NNN)(Å)	3.078	3.094	3.077	3.071
V_2–O_2–V_2 (NN)(°)	93.1	93.0	93.7	92.5
V_2–O_3–V_2 (NN)(°)	96.8	95.6	95.6	97.5
V_2–V_2 (NN)(Å)	3.009	3.005	3.004	3.004
V_2–O_3–V_2 (NNN)(°)	97.3	98.0	98.3	97.1
V_2–V_2 (NNN)(Å)	3.058	3.062	3.062	3.055
V_1–O_1–V_2 (°)[1]	121.7	122.9	121.8	121.0
V_1–V_2 (Å)[1]	3.583	3.581	3.582	3.589
V_1–O_3–V_2 (°)[2]	131.6	132.2	132.2	132.2
V_1–V_2 (Å)[2]	3.647	3.652	3.652	3.643

A.2.3 High Energy X-ray Diffraction Measurements on Annealed CaV_2O_4 Single Crystals

In order to unambiguously determine the crystallographic structure of CaV_2O_4 at various temperatures, to characterize structural phase transitions, and to check the crystal perfection, high-energy x-ray diffraction measurements ($E = 99.43$ keV) using an area detector were performed on two annealed single crystals at the Advanced Photon Source at Argonne National Laboratory. At this high energy, x-rays probe the bulk of a crystal rather than just the near-surface region and, by rocking the crystal about both the horizontal and vertical axes perpendicular to the incident x-ray beam, an extended range of a chosen reciprocal plane can be recorded.[156] For these measurements, a crystal was mounted on the cold-finger of a closed-cycle refrigerator surrounded by the heat shield and vacuum containment using Kapton windows to avoid extraneous reflections associated with Be or the aluminum housing. Two orientations of the crystal, with either the [001] or [100] direction parallel to the incident beam, were studied allowing the recording of the $(hk0)$ or $(0kl)$ reciprocal planes. For each data set, the horizontal angle, μ, was scanned over a range of ± 2.4 deg for each value of the vertical angle, η, between ± 2.4 deg with a step size of 0.2 deg. The total exposure time for each frame was 338 sec. The x-ray diffraction patterns were recorded with different intensities of the incident beam that were selected by attenuation to increase the dynamic range to a total of 10^7 counts. A beam size of 0.3×0.3 mm^2 was chosen to optimize the intensity/resolution condition and to allow probing different sections of the crystal by stepwise translations of the crystal in directions perpendicular to the incident beam.

A.2.3.1 Annealed Triarc-Grown Crystal

Figure A.6 shows the $(hk0)$ diffraction plane of the annealed triarc sample an-2-50-c1 at 205 K. The reciprocal space image reveals well-defined diffraction spots that correspond to the "primary" CaV_2O_4 lattice, as well as spots that can be indexed to an impurity phase inclusion of V_2O_3 coherently oriented with respect to the CaV_2O_4. No additional reflections were observed. Indeed, we find two coherent twins of V_2O_3 related by an inversion across

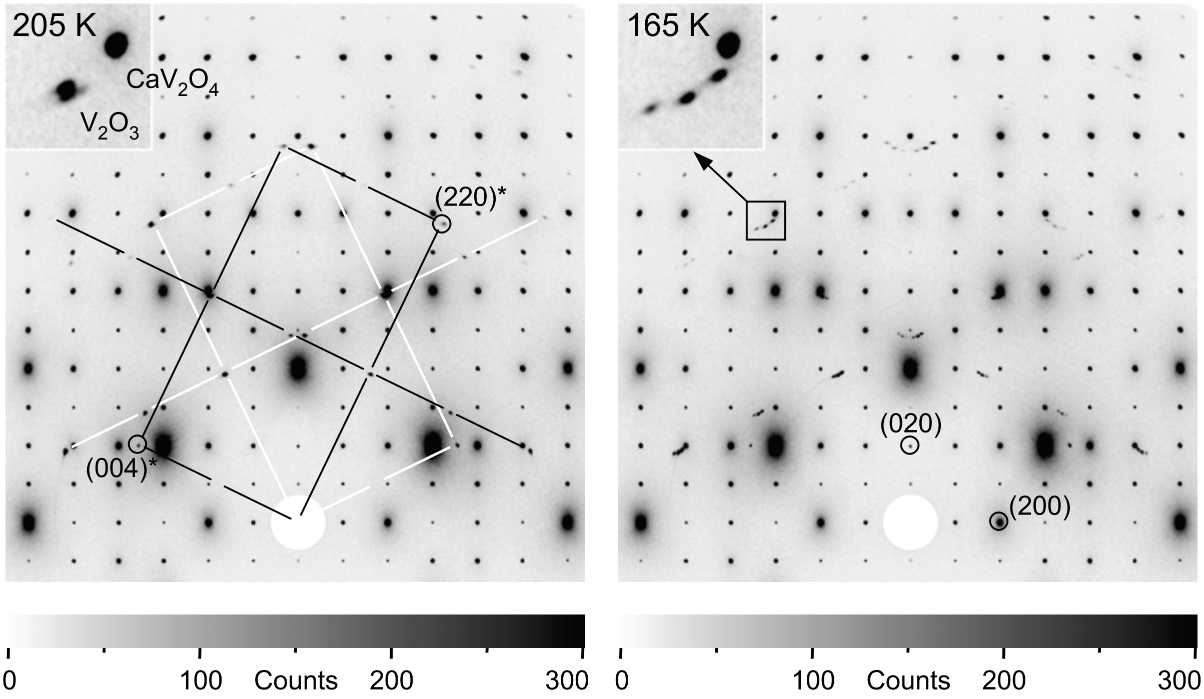

Figure A.6 High-energy x-ray diffraction patterns of the annealed triarc CaV_2O_4 crystal (an-2-50-c1), oriented with the ($hk0$) plane coincident with the scattering plane at $T = 205$ K (left panel) and 165 K (right panel). The white circles in the lower center of each pattern depict the excluded areas around the primary x-ray beam direction. Several peaks corresponding to the main phase, CaV_2O_4, as well as the coherently oriented second phase, V_2O_3, are labeled by indices (hkl) and $(hkl)^*$, respectively. For V_2O_3, the hexagonal Miller indices for the rhombohedral lattice are used. The insets of both panels display enlarged regions of the diffraction pattern to highlight the rhombohedral-to-monoclinic transition for V_2O_3.

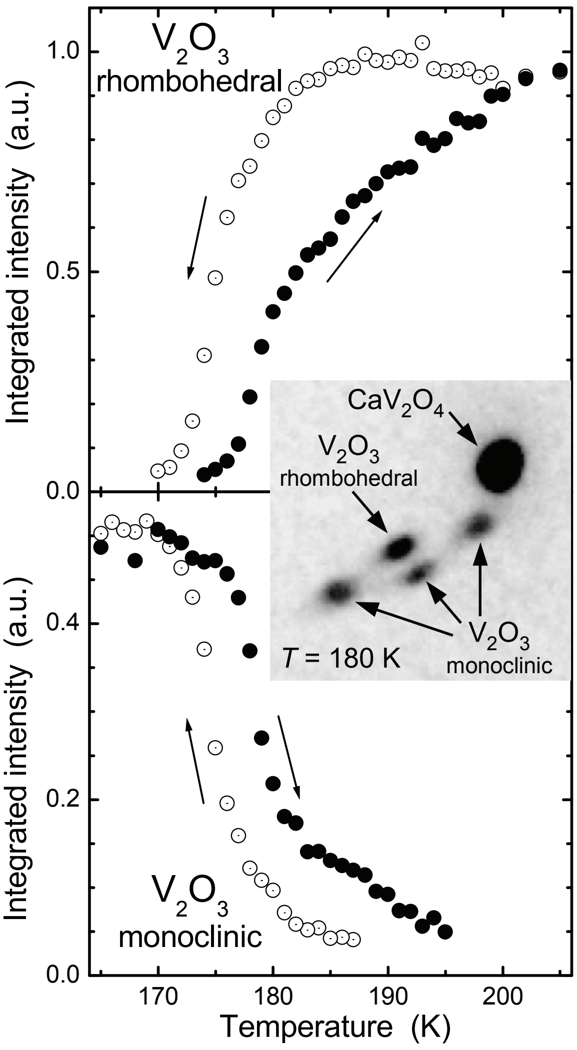

Figure A.7 Integrated intensity of selected reflections in the high-energy x-ray diffraction pattern related to the rhombohedral (top panel) and monoclinic (bottom panel) phases of V_2O_3 as a function of temperature for the annealed triarc crystal (an-2-50-c1). The direction of the temperature change is indicated by arrows. The inset displays the pattern observed at 180 K (with increasing temperature) for the (220) reflection from V_2O_3 in the coexistence temperature range. This region is the same as that displayed in the insets of Fig. A.6.

a mirror plane of the CaV_2O_4 lattice as depicted by the black and white rectangles in the left panel of Fig. A.6. By comparing the integrated intensities of reflections from the two phases, we estimate that V_2O_3 comprises a volume fraction of approximately 1–2 percent of the sample. This is in excellent agreement with the result of the x-ray diffraction analysis of the polycrystalline sample prepared from the same annealed crystal that was described above. The volume fraction of V_2O_3 varies only slightly in different parts of the crystal probed by scanning the x-ray beam over the crystal. This indicates that the inclusions of V_2O_3 are approximately equally distributed over the volume of the crystal.

Upon lowering the temperature of the crystal to 165 K, below $T_{S1} \sim 200$ K, we observe changes in the V_2O_3 structure consistent with the known first-order rhombohedral-to-monoclinic structural transition at 170 K (measured on heating). [157, 158] In particular, the upper left corners of both panels of Fig. A.6 show enlarged views of the region near the $(\bar{3}80)$ reflection from CaV_2O_4 and the (220) reflection (in hexagonal notation) for the rhombohedral lattice of V_2O_3. Below T_{S1} the (220) reflection splits into three reflections in the monoclinic phase. The temperature dependence of this transition is displayed in Fig. A.7. Here, we note that there is a finite range of coexistence between the rhombohedral and monoclinic phases of V_2O_3 (see the inset to Fig. A.7) and the transition itself has a hysteresis of roughly 5–10 K.

Several points regarding Figs. A.6 and A.7 are relevant to our interpretation of the specific heat and thermal expansion measurements of the annealed triarc crystal (an-2-50-c1) to be presented below in Figs. A.15 and A.16, respectively. First, we note that over the temperature range encompassing the features at $T_{S1} \sim 200$ K, there is no apparent change in the diffraction pattern of CaV_2O_4. These anomalies are instead strongly correlated with the rhombohedral-to-monoclinic transition in V_2O_3. We further note that the temperature for this latter transition is somewhat higher than the accepted value of ≈ 170 K (determined on warming) found in the literature.[157, 159, 160] This difference is, perhaps, due to the fact that the V_2O_3 and CaV_2O_4 lattices are coupled, as evidenced by the coherent orientation relationship between them, so that strains at the phase boundaries come into play and can raise the transition temperature.[161] In addition, it is reported[159, 160] that deviations of the stoichiometry from V_2O_3 can affect the transition temperature significantly.

We now turn our attention to changes in the diffraction pattern of CaV_2O_4 associated with anomalies in the heat capacity and thermal expansion measurements at temperatures $T_S \sim 150$ K in Figs. A.15 and A.16 below, respectively. The annealed triarc crystal (an-2-50-c1) was reoriented so that the CaV_2O_4 $(0kl)$ reciprocal lattice plane was set perpendicular to the incident beam. Figure A.8 shows the diffraction patterns obtained at 205 K (above T_S) and 13 K (well below T_S). The strong reflections in Fig. A.8 are associated with the main CaV_2O_4 lattice while the weaker diffraction peaks are, again, associated with the coherently oriented V_2O_3 second phase. At low temperatures, we observe a splitting of the main reflections that is the signature of the orthorhombic-to-monoclinic transition at T_S for the CaV_2O_4 lattice. The splitting of reflections associated with the transition at T_{S1} for V_2O_3, in this reciprocal lattice plane, is not readily observed.

For the low-temperature monoclinic phase of CaV_2O_4 two possible space groups have been considered.[152] The space groups $P\ 2_1/n\ 1\ 1$ and $P\ n\ 1\ 1$ can be separated by testing the occurrence or absence of $(0k0)$ reflections with k odd, respectively. The systematic absence of such reflections was proven by recording $(hk0)$ planes with varying conditions to evaluate the sporadic occurrence of these reflections by Rengers or multiple scattering. The space group $P\ 2_1/n\ 1\ 1$ is confirmed for the low-temperature phase of the studied CaV_2O_4 crystal. No changes in the diffraction pattern were observed related to the onset of antiferromagnetic order in CaV_2O_4 below $T_N = 69$ K.

The details of the orthorhombic-to-monoclinic transition at T_S for CaV_2O_4 are shown in Fig. A.9 where we plot the monoclinic distortion angle as a function of temperature. The monoclinic angle was determined from the splitting of the peaks along the **b**-direction through the position of the $(04\bar{2})$ reflection. Below $T_S = 138(2)$ K, the monoclinic angle evolves continuously, consistent with a second order transition, and saturates at approximately 89.2 deg at low temperatures.

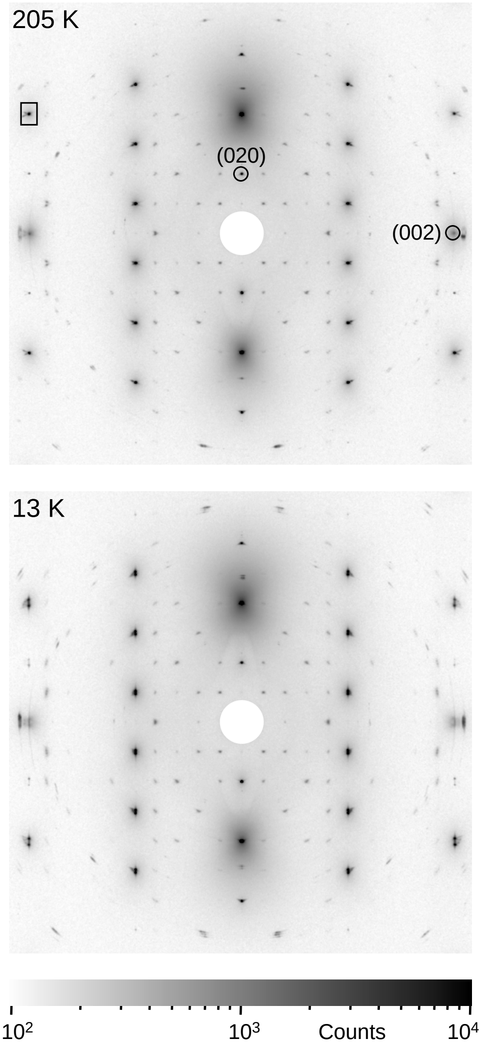

Figure A.8 High-energy x-ray diffraction patterns of the $(0kl)$ reciprocal lattice plane of CaV_2O_4 from the annealed triarc crystal (an-2-50-c1) at 205 K (top panel) and 13 K (bottom panel). The white circles in the center of the patterns depict the excluded areas around the primary x-ray beam direction. Most of the reflections related to CaV_2O_4 show intensities above 10^4 counts (see intensity scale). The (020) and (002) reflections of CaV_2O_4 are marked in the top panel. The area bounded by the black rectangle in the top panel depicts the region close to the orthorhombic $(04\bar{2})$ reflection of CaV_2O_4, analyzed in Fig. A.9.

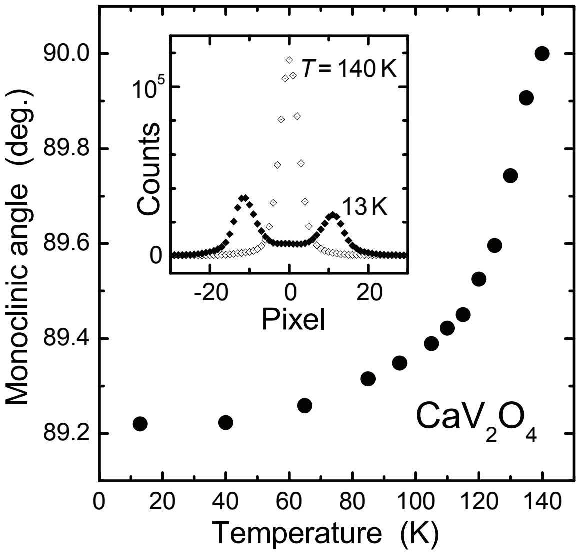

Figure A.9 Temperature dependence of the monoclinic angle in the low-temperature phase of CaV$_2$O$_4$, extracted from diffraction data such as shown in the inset for temperatures of 140 K and 13 K. Such diffraction line scans were extracted from high--energy x-ray diffraction patterns by summing up the intensity perpendicular to the **b** direction for the sector marked by the rectangle in the top panel of Fig. A.8.

A.2.3.2 Annealed OFZ-Grown Crystal

The annealed optical floating zone crystal (an-3-074 OFZ) shows a diffraction pattern similar to that of the annealed triarc-grown crystal (an-2-50-c1) in measurements of ($hk0$) planes at room temperature. The observed V$_2$O$_3$ inclusions are again coherently oriented with respect to the CaV$_2$O$_4$ lattice. The intensities of the diffraction peaks related to V$_2$O$_3$ are similar to those in the annealed triarc crystal (an-2-50-c1) and also vary only slightly upon scanning different spots of the crystal which indicates a homogeneous distribution of the V$_2$O$_3$ inclusions with a similar volume fraction. However, the temperature dependence of the diffraction pattern is different for the two crystals. Measurements taken on cooling show that in the annealed floating-zone crystal (an-3-074 OFZ), the shape and position of the peaks originating from V$_2$O$_3$ are stable from room temperature down to 130 K where the onset of the structural transition occurs. Around 120 K strong changes are observed similar to the observations around 180 K in the annealed triarc crystal (an-2-50-c1). Below 110 K, the transition to the low-temperature monoclinic structure of V_2O_3 is complete. Therefore, the temperature for the rhombohedral-to-monoclinic transition is reduced by $\sim$ 60 K compared to the corresponding temperature in the annealed triarc crystal (an-2-50-c1).

A.3 Magnetization, Magnetic Susceptibility, Heat Capacity and Thermal Expansion Measurements

In the following, we describe our results of magnetization, magnetic susceptibility, heat capacity, and thermal expansion measurements of both polycrystalline and single crystal samples. These and additional measurements consistently identify temperatures at which the antiferromagnetic transition ($T_{\rm N}$), the orthorhombic-to-monoclinic structural transition ($T_{\rm S}$) and the transition at $\sim$ 200 K ($T_{\rm S1}$) occur in these samples. In Table A.4, we summarize these transition temperatures for the different samples obtained using the various measurements.

A.3.1 Magnetization and Magnetic Susceptibility Measurements

The static magnetic susceptibility versus temperature $\chi(T) \equiv M(T)/H$ of a polycrystalline sample as well as of the oriented crystals was measured using a Quantum Design MPMS SQUID magnetometer in a 1 T field from 1.8 K to 350 K, where M is the magnetization of the sample and H is the magnitude of the applied magnetic field. In addition, low field (100 Oe) zero-field-cooled and field-cooled (zfc, fc) measurements of $M(T)$ at fixed H were carried out from 1.8 K to 100 K. A Quantum Design MPMS ac SQUID magnetometer was used to measure the ac susceptibility $\chi_{\rm ac}(T)$ of the annealed triarc grown crystal from 5 to 100 K in an ac field $H_{\rm ac} = 1$ Oe and frequency 10 Hz. The powder was contained in polycarbonate capsules mounted in clear plastic straws. Each crystal was glued to a small piece of clear plastic transparency sheet with GE 7031 varnish or Duco cement, which was then aligned inside the plastic straws with the a, b or c axis direction parallel to the external magnetic field. $M(H)$ isotherms were measured in fields up to $H = 5.5$ T at various temperatures.

The $\chi(T)$ in $H = 1$ T is plotted in Fig. A.10 for a CaV_2O_4 polycrystalline sample and for aligned single crystals grown using a triarc furnace and using an optical floating zone (OFZ)

Table A.4 Antiferromagnetic ordering (Néel) temperature ($T_{\rm N}$), high temperature orthorhombic to low-temperature monoclinic structural transition temperature ($T_{\rm S}$), and the transition temperature at $\sim$ 200 K ($T_{\rm S1}$) observed by static magnetic susceptibility χ (peak of $d(\chi T)/dT$), heat capacity $C_{\rm p}$ (peak of $\Delta C_{\rm p}$), thermal expansion α [peak of $\alpha(T)$, except for $T_{\rm S1}$ where the onset of α slope change is used], powder synchrotron x-ray diffraction (XRD), single crystal neutron diffraction (ND), and single crystal high-energy x-ray diffraction (HEXRD) measurements for polycrystalline (powder) and single crystal CaV_2O_4 samples. The single crystals were grown using either a triarc furnace or an optical floating zone (OFZ) furnace.

Sample	Synthesis	Method	$T_{\rm N}$ (K)	$T_{\rm S}$ (K)	$T_{\rm S1}$ (K)
an-2-116	powder	χ	76	147	^{1}
	1200 °C	$C_{\rm p}$	75	144	^{1}
		XRD	–	150	200
an-2-50	Triarc crystal	χ	51	108	^{1}
	as-grown	$C_{\rm p}$	51	108	^{2}
		ND	53	112	^{2}
an-2-50	Triarc crystal	χ	68	133	195
	annealed 1200 °C	$C_{\rm p}$	68	133	193
		α	68	136	198
		ND	69	141	^{2}
		HEXRD	–	138(2)	192(7)^3
an-3-074	OFZ crystal	χ	69	136	192
	annealed 1200 °C	$C_{\rm p}$	71	132	191
		ND	69	147	^{2}

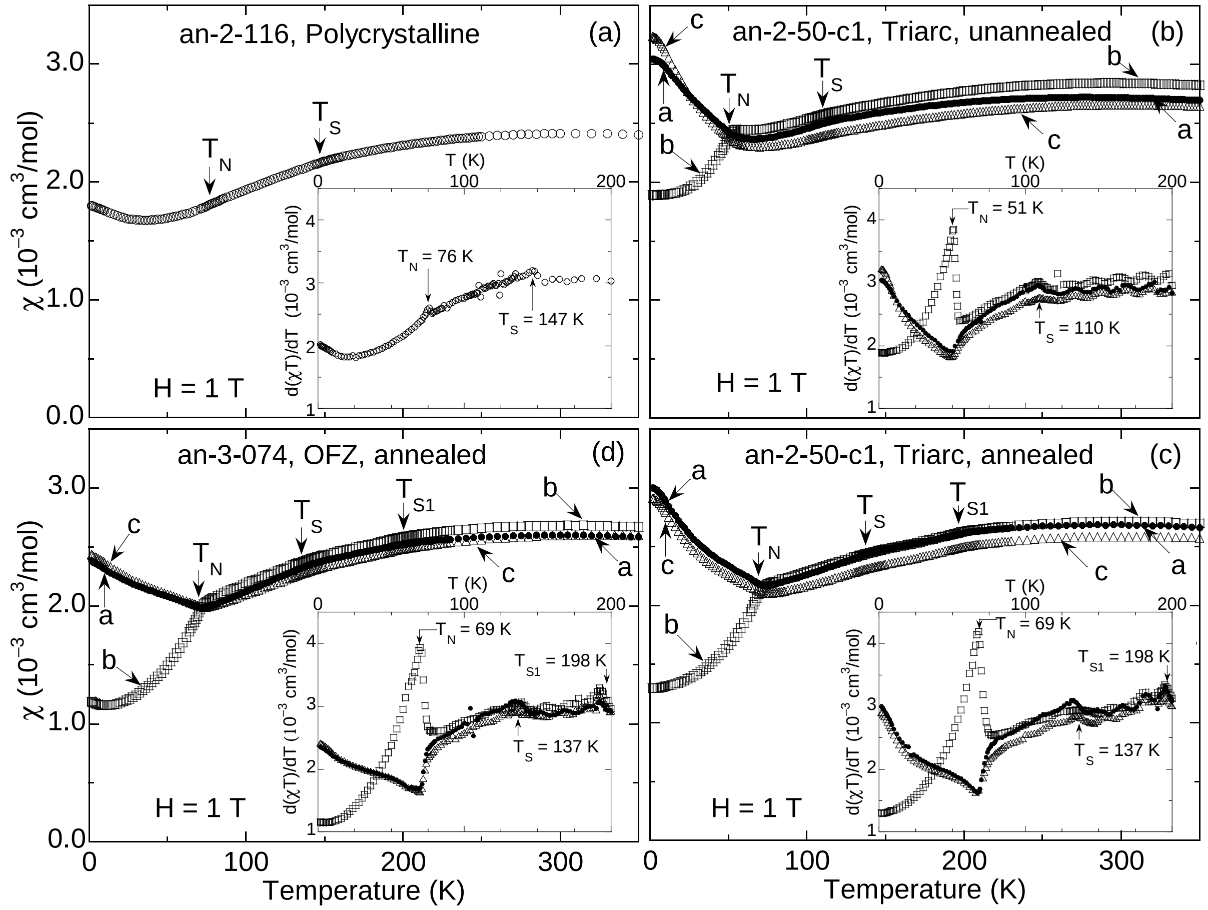

Figure A.10 Magnetic susceptibility χ versus temperature in a field of 1 T of CaV_2O_4 (a) polycrystalline sample, (b) as-grown triarc–grown single crystal, (c) annealed triarc-grown single crystal, and (d) annealed OFZ-grown single crystal. The axes (a, b, or c) along which the measurements were carried out are as indicated. The insets show $d(\chi T)/dT$ versus T to highlight the transition temperatures. The oscillatory behavior of $d(\chi T)/dT$ at the higher temperatures, most pronounced in the inset in (b), is an artifact generated by the SQUID magnetometer.

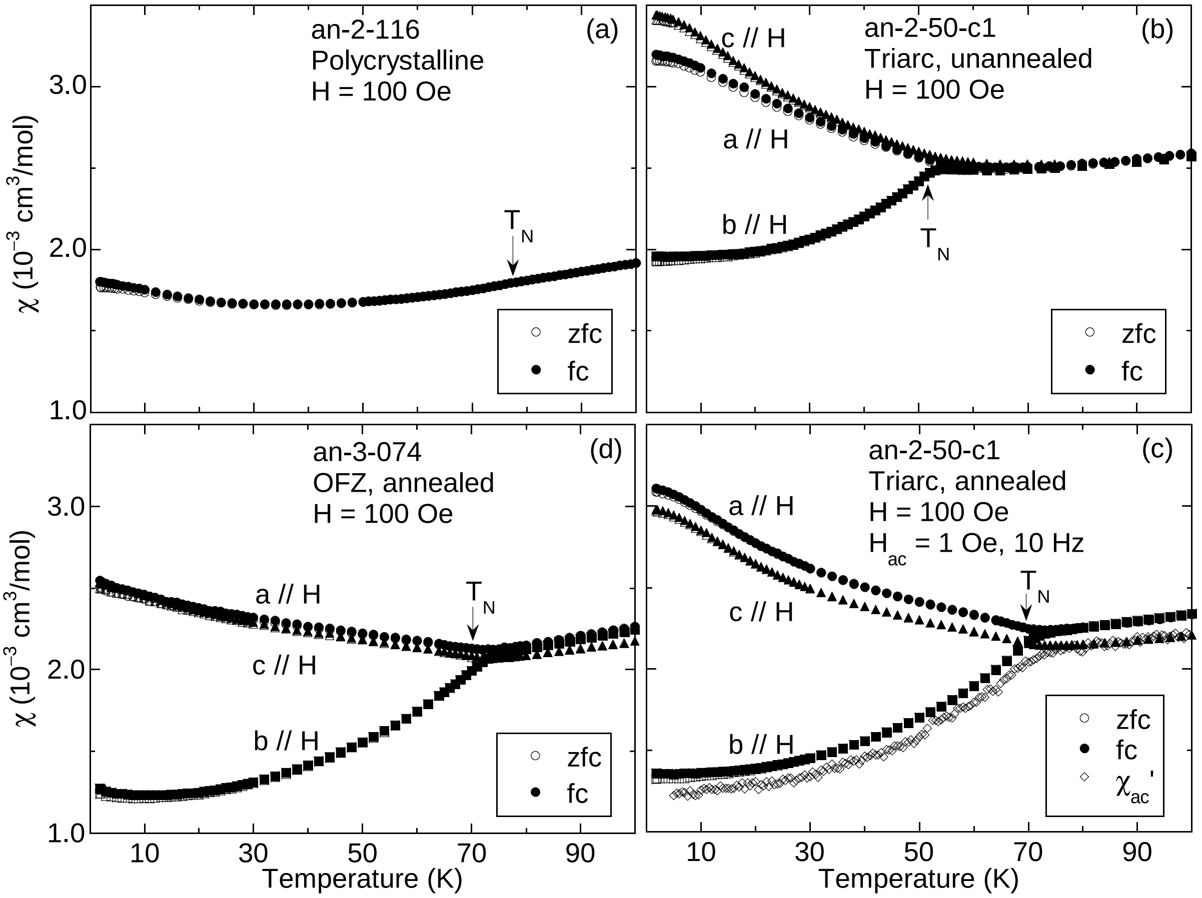

Figure A.11 Zero-field-cooled and field-cooled susceptibility of CaV_2O_4 in a field of 100 Oe measured on (a) polycrystalline powder, (b) unannealed triarc grown single crystal (c) annealed triarc grown single crystal, and (d) annealed OFZ grown single crystal. Part (c) also shows the ac-susceptibility $\chi'_{\rm ac}(T)$ along the easy b-axis of the annealed crystal measured in a field $H_{\rm ac} = 1$ Oe at a frequency of 10 Hz. The antiferromagnetic transition temperatures $T_{\rm N}$ are marked as shown.

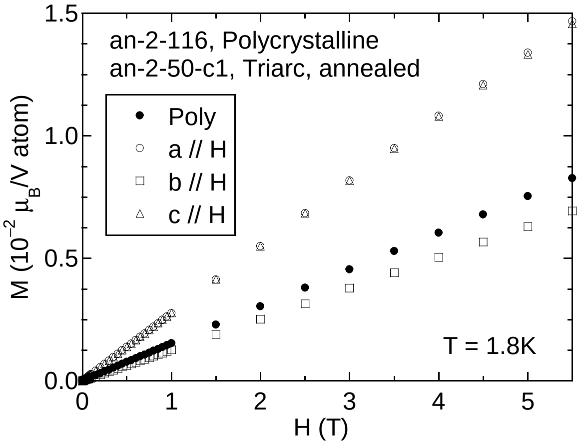

Figure A.12 Magnetization M versus applied magnetic field H isotherms at a temperature of 1.8 K of a polycrystalline sample and of an annealed triarc grown single crystal of CaV_2O_4.

furnace. The broad maximum in $\chi(T)$ around 300 K is characteristic of a low-dimensional spin system with dominant antiferromagnetic exchange interactions with magnitude of order 300 K. For the single crystal samples, clear evidence is seen for long-range antiferromagnetic ordering at Néel temperatures $T_N = 51$ to 69 K, depending on the sample. The easy axis of the antiferromagnetic ordering (with the lowest susceptibility as $T \to 0$) is seen to be the *b*-axis, perpendicular to the zigzag V chains. At temperatures above T_N, the susceptibility of the crystals is nearly isotropic, but with small anisotropies which typically showed $\chi_b > \chi_a > \chi_c$. However, occasionally variations of ±5% in the absolute value of $\chi_i(T)$ were observed between different runs for the same crystal axis i that we attribute to sample size and positioning effects (radial off-centering) in the second order gradiometer coils of the Quantum Design MPMS SQUID magnetometer.[162, 163]

The ordering temperatures observed are marked by vertical arrows in Fig. A.10 and are highlighted in the plots of $d(\chi T)/dT$ versus T shown in the insets. The various transition temperatures are summarized in Table A.4. As is typical for a low-dimensional antiferromagnetic system, the polycrystalline sample shows only a very weak cusp at $T_N = 76$ K due to averaging over the three principal axis directions, but it is still well-defined as observed in the $d(\chi T)/dT$ *vs* T plot shown in the inset of Fig. A.10(a). In a related study, ^{17}O NMR measurements on a polycrystalline sample of ^{17}O-enriched CaV_2O_4 gave a clear signature of antiferromagnetic ordering at 78 K.[150] In contrast to the polycrystalline sample, the as-grown crystal in Fig. A.10(b) shows a clear and distinct antiferromagnetic ordering temperature but with a much lower value $T_{\rm N} \approx 51$ K. After annealing the crystals, Figs. A.10(c) and A.10(d) show that $T_{\rm N}$ increases to ≈ 69 K, closer to that observed in the polycrystalline sample. However, the powder average of the annealed single crystal susceptibility below $T_{\rm N}$ does not match the susceptibility of the polycrystalline sample. The reason for this disagreement is unclear at this time. In any case the slow upturn in the susceptibility of the powder sample below 40 K in Fig. A.10 is evidently intrinsic, due to the powder average of the anisotropic susceptibilities, and is not due to magnetic impurities.

The zero-field-cooled (zfc) and field-cooled (fc) $\chi(T)$ measured in a field of 100 Oe for polycrystalline and single crystal samples of $\rm CaV_2O_4$ are plotted in Figs. A.11(a)–(d). Also shown in Fig. A.11(c) is the real part of the ac susceptibility $\chi'_{\rm ac}(T)$ along the easy b-axis direction of the annealed triarc crystal measured in an ac field of amplitude 1 Oe at a frequency of 10 Hz. A small irreversibility is observed in Fig. A.11 in all samples between the zfc and fc susceptibilities below ~ 30 K. However, the $\chi'_{\rm ac}(T)$ measurement in Fig. A.11(c) does not show any peak in that temperature region, ruling out spin glass-like spin freezing which was suggested to occur in powder samples from earlier reports.[11, 12] The slight irreversibility observed may be associated with antiferromagnetic domain wall effects.

In Fig. A.12 we show isothermal $M(H)$ measurements up to $H = 5.5$ T measured at 1.8 K for the polycrystalline sample and for the annealed triarc-grown single crystal. The behavior is representative of all samples measured. We find that M is proportional to H at fields up to at least ~ 2 T, indicating the absence of any significant ferromagnetic impurities and the absence of a ferromagnetic component to the ordered magnetic structure.

A.3.2 Heat Capacity Measurements

The heat capacity $C_{\rm p}$ versus temperature T of a sintered polycrystalline pellet of $\rm CaV_2O_4$ as well as of crystals (as-grown and annealed) was measured using a Quantum Design PPMS system at $T = 1.8$ to 200–300 K in zero applied magnetic field. The $C_{\rm p}(T)$ was also measured of

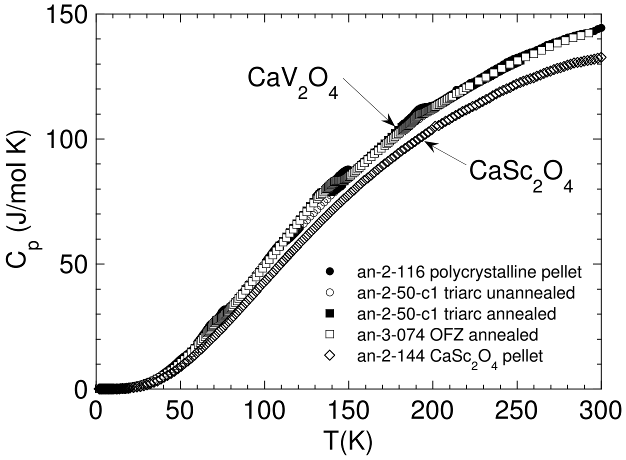

Figure A.13 Heat Capacity $C_{\rm p}$ versus temperature T in zero magnetic field of one polycrystalline sample and three single crystal samples of $\rm CaV_2O_4$ and of a polycrystalline sample of isostructural nonmagnetic $\rm CaSc_2O_4$. On this scale, the data for the four $\rm CaV_2O_4$ samples are hardly distinguishable.

a polycrystalline sintered pellet of isostructural (at room temperature) nonmagnetic $\rm CaSc_2O_4$ whose lattice parameters and formula weight are very similar to those of $\rm CaV_2O_4$.[164] The $\rm CaSc_2O_4$ sample was synthesized from $\rm Sc_2O_3$ (99.99%, Alfa) and $\rm CaCO_3$ (99.995%, Aithaca) by reacting a stoichiometric mixture in air at 1000 °C for 24 hr and then at 1200 °C for 96 hr with intermediate grindings, and checked for phase purity using powder XRD.

In Fig. A.13 we plot the measured $C_{\rm p}(T)$ of four $\rm CaV_2O_4$ samples and of isostructural nonmagnetic $\rm CaSc_2O_4$. The difference $\Delta C_{\rm p}$ versus T for the four $\rm CaV_2O_4$ samples is plotted in Fig. A.14(a). Here $\Delta C_{\rm p}$ is the difference between the heat capacity of $\rm CaV_2O_4$ and that of $\rm CaSc_2O_4$, but where the temperature axis of $C_{\rm p}$ for $\rm CaSc_2O_4$ was multiplied by a scaling factor to take account of the difference in the formula weights of $\rm CaV_2O_4$ and $\rm CaSc_2O_4$. This factor is given by $[M_{\rm M}({\rm CaSc_2O_4})/M_{\rm M}({\rm CaV_2O_4})]^{1/2}$=0.9705 where $M_{\rm M}$ is the molar mass of the respective compound. If the lattice heat capacity of $\rm CaV_2O_4$ and the (renormalized) heat capacity of $\rm CaSc_2O_4$ had been the same, the difference $\Delta C_{\rm p}(T)$ would presumably have been the magnetic heat capacity of $\rm CaV_2O_4$. However, due to the structural transition at $T_{\rm S}$ and the transition at $T_{\rm S1}$, $\Delta C_{\rm p}(T)$ contains a lattice contribution as well. The lattice contribution to $\Delta C_{\rm p}$ is expected to be minimal at low temperatures, where only the long wavelength acoustic

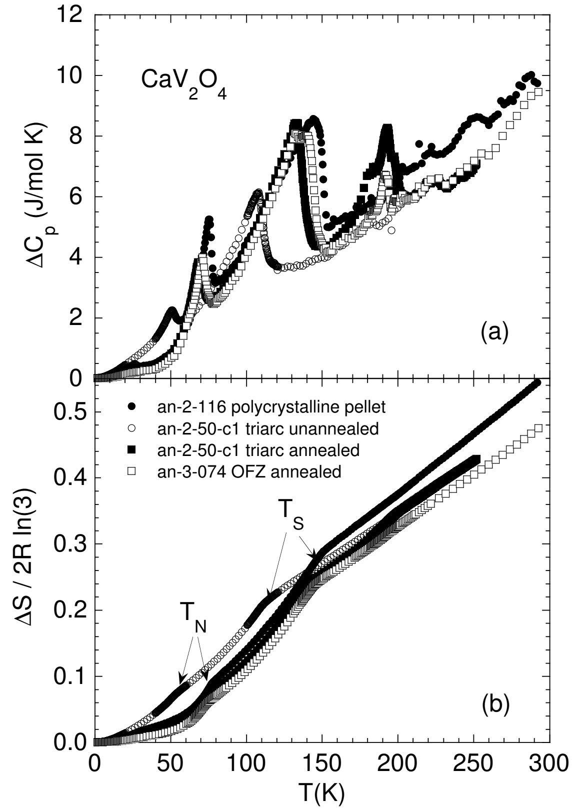

Figure A.14 (a) ΔC_p versus temperature T for four CaV$_2$O$_4$ samples. Here ΔC_p is the difference between the heat capacity of CaV$_2$O$_4$ and that of CaSc$_2$O$_4$, but where the temperature axis of C_p for CaSc$_2$O$_4$ was multiplied by 0.9705 to take account of the difference in the formula weights of CaV$_2$O$_4$ and CaSc$_2$O$_4$. (b) Entropy $\Delta S(T)$ associated with the $\Delta C_\mathrm{p}(T)$ data in (a), obtained by integrating $\Delta C_\mathrm{p}/T$ in (a) versus T. The ΔS is normalized by the entropy 2R ln(3) of two moles of disordered spins $S = 1$, where R is the molar gas constant.

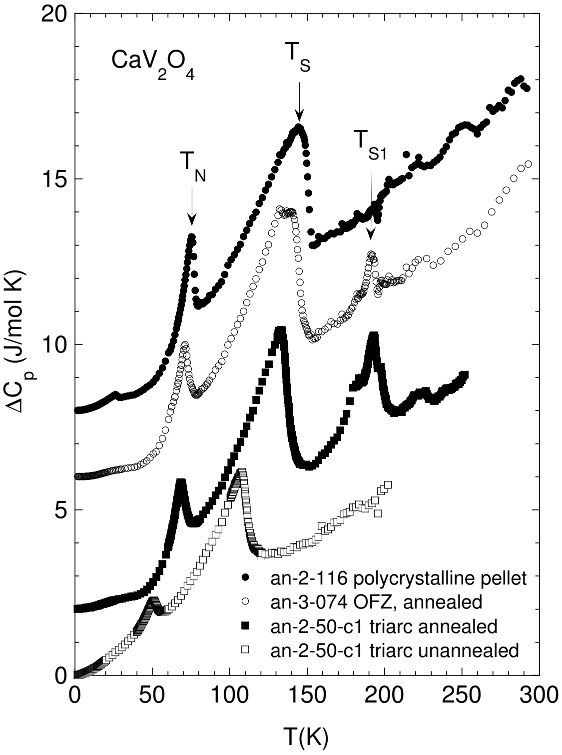

Figure A.15 ΔC_p versus temperature T for four CaV$_2$O$_4$ samples. The data are the same as in Fig. A.14(a) except for vertical offsets to separate the data sets. The symbol T_N labels the long-range antiferromagnetic transition and T_S labels the high temperature orthorhombic to low temperature monoclinic structural transition. An additional transition at $T_\mathrm{S1} \sim 200$ K is seen in the two annealed single crystals. The small anomaly for the AFZ crystal and for the triarc crystal that rides on top of the broader peak appear to be intrinsic to CaV$_2$O$_4$. The broad peak in the latter crystal appears to be due to coherently grown V$_2$O$_3$ impurity phase that grows during annealing (see text).

phonon modes are excited, and possibly also above T_{S1} where the two compounds are known to be isostructural.

Figure A.14(a) shows that the $\Delta C_{\mathrm{p}}(T)$ data for the four $\mathrm{CaV_2O_4}$ samples are similar except for the different sizes and temperatures of the anomalies associated with three transitions. In order to more clearly illustrate the differences between samples, Fig. A.15 shows the same data for each sample but vertically displaced from each other to avoid overlap. The magnetic ordering transition at T_{N} as well as the ordering temperatures T_{S} and T_{S1} are clearly evident from the $\Delta C_{\mathrm{p}}(T)$ data in Fig. A.15. The ordering temperatures observed are summarized above in Table A.4.

The entropy versus temperature associated with the $\Delta C_{\mathrm{p}}(T)$ data of each sample in Fig. A.14(a) is shown in Fig. A.14(b), obtained from $\Delta S(T) = \int_0^T [\Delta C_{\mathrm{p}}(T)/T]dT$. In Fig. A.14(b), ΔS is normalized by the entropy $2\mathrm{R}\ln(2S+1) = 2\mathrm{R}\ln(3)$ for two moles of fully disordered spins $S = 1$, where R is the molar gas constant. As noted above, at least at low temperatures, we associate $\Delta S(T)$ with the magnetic entropy of the system. At the antiferromagnetic ordering temperature T_{N}, the normalized value of $\Delta S(T_{\mathrm{N}})/2\mathrm{R}\ln(3) \approx$ 6–8% is very small and is about the same for all samples. This small value indicates that short-range antiferromagnetic ordering is very strong above T_{N} and the data in Fig. A.14(b) indicate that the maximum spin entropy of the system is not attained even at room temperature. This is qualitatively consistent with our estimate $J_1 \approx 230$ K obtained below in Sec. A.4 by comparison of our $\chi(T)$ data with calculations of $\chi(T)$.

The small observed magnetic entropy at T_{N} is consistent with the values of the heat capacity discontinuities ΔC_{AF} at T_{N} in Fig. A.15, as follows. In mean field theory, for a system containing N spins S the discontinuity in the magnetic heat capacity at the ordering temperature for either ferromagnetic or antiferromagnetic ordering is predicted to be[165]

$$\Delta C_{\mathrm{AF}} = \frac{5}{2} N k_{\mathrm{B}} \frac{(2S+1)^2 - 1}{(2S+1)^2 + 1}, \tag{A.2}$$

where N is the number of spins and k_{B} is Boltzmann's constant. Using $S = 1$ relevant to V^{+3} and $Nk_{\mathrm{B}} = 2\mathrm{R}$, where R is the molar gas constant, one obtains $\Delta C_{\mathrm{AF}} = 4\mathrm{R} = 33.3$ J/mol K, where a "mol" refers to a mole of $\mathrm{CaV_2O_4}$ formula units. From Fig. A.15, the experimental

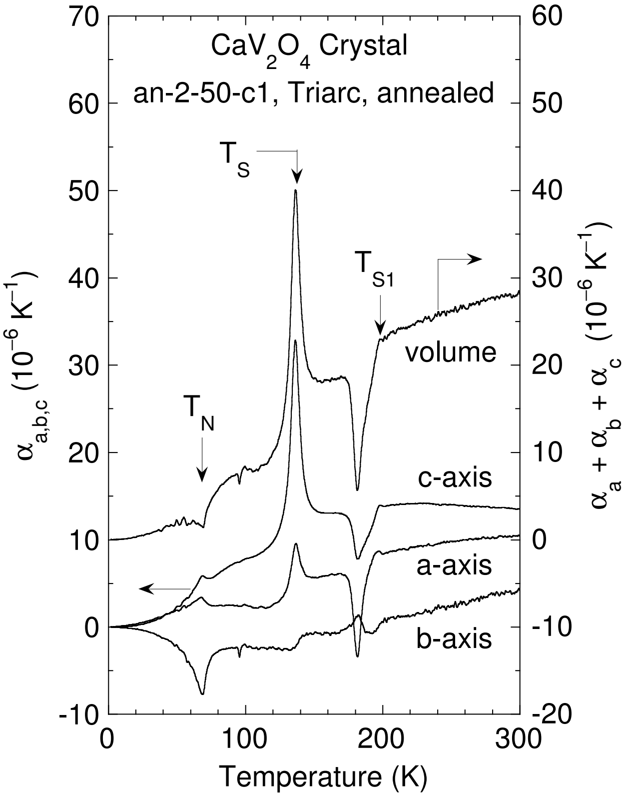

Figure A.16 Coefficients of linear thermal expansion $\alpha_{a,b,c}$ of an annealed single crystal of CaV$_2$O$_4$ measured along the orthorhombic a, b, and c-axes versus temperature (left-hand scale), and the volume expansion coefficient $\alpha_a + \alpha_b + \alpha_c$ versus temperature (right-hand scale).

$\Delta C_{\rm AF}$ is about 0.5 to 2 J/mol K, which is only 1.5–6% of the mean field value. This small jump in $C_{\rm p}(T_{\rm N})$ is consistent with the above small value of $S(T_{\rm N})$. When short range magnetic ordering removes most of the magnetic entropy of a system at high temperatures, then thermal effects associated with three-dimensional magnetic ordering of the system at low temperatures will necessarily be much smaller than otherwise expected.

A.3.3 Thermal Expansion Measurements

The thermal expansion of the annealed triarc grown CaV$_2$O$_4$ crystal an-2-50-c1 was measured versus temperature using capacitance dilatometry[166] from 1.8 to 300 K along the three orthorhombic axes a, b and c. The crystal is the same annealed triarc crystal measured by magnetic susceptibility and heat capacity in Figs. A.10 and A.11(c) and in Figs. A.13–A.15,

Table A.5 Relative length changes along the orthorhombic *a*-, *b*- and *c*-axis directions and of the volume V that are associated with the three transitions at $T_{\rm N} \approx 70$ K, $T_{\rm S} \approx 140$ K, and $T_{\rm S1} \approx 195$ K in annealed triarc CaV_2O_4 single crystal an-2-50-c1. The temperature T range over which the changes were measured are as indicated.

	$T_{\rm N}$	$T_{\rm S}$	$T_{\rm S1}$
T range (K)	52–75	120–153	174–198
$\Delta a/a$ (10^{-5})	1.2	4.9	−7.5
$\Delta b/b$ (10^{-5})	−4.3	−0.9	−0.1
$\Delta c/c$ (10^{-5})	1.1	19.6	−6.3
$\Delta V/V$ (10^{-5})	−2.0	23.6	−13.9

respectively. In Fig. A.16 the linear coefficients of thermal expansion are plotted versus temperature (left-hand scale), along with the volume thermal expansion coefficient (right-hand scale). At high temperatures $T \sim 300$ K the α values tend to become temperature independent. Below 200 K, the ordering transitions observed above in the magnetic susceptibility and heat capacity are reflected in distinct anomalies in the thermal expansion coefficients at the corresponding temperatures. The ordering temperatures observed are summarized above in Table A.4.

The normalized length changes along the orthorhombic a, b and c axis directions and the normalized change in the volume V associated with the three transitions at $T_{\rm N}$, $T_{\rm S}$ and $T_{\rm S1}$ are listed in Table A.5. These changes were calculated by determining the areas under the respective peaks in the thermal expansion coefficients in Fig. A.16, and then subtracting the estimated respective background changes over the same temperature intervals.

A.4 Analysis of Experimental Data

A.4.1 Origin of the Transition at $T_{\rm S1} \sim 200$ K in Annealed CaV_2O_4 Single Crystals

From Table A.5 above, the relative volume change of the annealed triarc crystal an-2-50-c1 on heating through $T_{\rm S1}$ from the thermal expansion data is $\Delta V/V \approx -1.4 \times 10^{-4}$. This value is about 1% of the value for pure V_2O_3 at its transition.[157] The height of the heat capacity anomaly above “background” in Fig. A.15 for this crystal is ≈ 2.5 J/mol K, which is about

0.8% of the value[159] at the structural transition for pure V_2O_3. These estimates are both consistent with our estimates from x-ray diffraction data in Sec. A.2 of a 1–2 percent volume fraction of V_2O_3 in this crystal. Our data therefore indicate that for the annealed triarc-grown crystal (an-2-50-c1), the anomalous features found above in the heat capacity and thermal expansion data at $T_{\rm S1}$ arise mainly from this transition in the V_2O_3 impurity phase.

Furthermore, the temperature dependences of the linear thermal expansion coefficients at the transition $T_{\rm S1} \approx 200$ K in Fig. A.16 are significantly different than near the transitions $T_{\rm N} \approx 70$ K and $T_{\rm S} \approx 140$ K. There appears to be a discontinuity in the slopes of $\alpha_i(T)$ as the transition $T_{\rm S1}$ is approached from above, whereas a continuous change in the slopes occurs as $T_{\rm S}$ and $T_{\rm N}$ are approached from above. The reason for this difference is evidently that the former transition is mainly due to the *first order* structural transition in the V_2O_3 coherently-grown impurity phase in this annealed crystal as investigated previously in Sec. A.2.3.1, whereas the latter two transitions are *second order*.

However, we also found in Sec. A.2 that for the annealed floating-zone crystal (an-3-074 OFZ), the structural transition of the V_2O_3 impurity phase was reduced by ~ 60 K from that of the V_2O_3 impurity phase in the annealed triarc grown crystal, and hence cannot be responsible for heat capacity anomaly at $T_{\rm S1} \sim 200$ K for the annealed float-zone crystal in Fig. A.15. Indeed, the relatively small heat capacity anomaly at $T_{\rm S1}$ in Fig. A.15 for the float-zone crystal appears to also be present at the same temperature for the annealed triarc-grown crystal, but rides on top of a broader anomaly that is evidently due to the structural transition of the V_2O_3 impurity phase in that crystal. Furthermore, the double peak structure in the heat capacity for the annealed triarc crystal at $T_{\rm S} \approx 140$ K evidently arises due to the overlap of the onsets of the structural transitions in V_2O_3 and CaV_2O_4.

An issue of interest is the cause(s) of the variability in the structural rhombohedral-to-monoclinic transition temperature of the coherently grown V_2O_3 impurity phase in our annealed CaV_2O_4 crystals. Due to the first order nature of the transition, the transition is hysteretic. The transition temperature of bulk stoichiometric V_2O_3 has been reported to be at ≈ 170 K on heating and ≈ 150 K on cooling.[159, 167–169] The transition temperature *decreases* rapidly under pressure.[170] A pressure of only 9 kbar lowers the transition temperature by 60 K, and the transition is completely suppressed at a pressure of ≈ 20 kbar.[170] The transition temperature is also rapidly *suppressed* if the sample contains V vacancies; a crystal of composition $V_{1.985}O_3$ showed a transition temperature of ≈ 50 K.[169] Furthermore, it was found that when V_2O_3 is epitaxially grown on $LiTaO_3$, the transition temperature is *enhanced* from the bulk value by 20 K.[161] Given the possibilities of compressive or tensile forces acting on the V_2O_3 due to the epitaxial relationship of the V_2O_3 impurity with the CaV_2O_4 host and the possibility of nonstoichiometry of the V_2O_3 impurity phase, one can see how the transition temperature of the V_2O_3 might be *depressed or enhanced* from the bulk value by ≈ 30 K as we found for the coherently grown V_2O_3 impurity phases in our two annealed crystals in Sec. A.2.3.

In summary, then, it appears that there is an intrinsic phase transition in the two annealed CaV_2O_4 crystals at about 200 K that has no obvious source. We speculate that this transition may be the long-sought chiral phase transition originally postulated by Villain,[149] where there is long-range chiral order but no long-range spin order below the transition temperature, and the long-range chiral order is lost above the transition temperature.

A.4.2 Magnetic Susceptibility and Magnetic Heat Capacity

In separate experiments to be described elsewhere,[153] we have carried out inelastic neutron scattering measurements of the magnetic excitation dispersion relations for CaV_2O_4 single crystals. We find that the dispersion along the c-axis (in the vanadium chain direction) is significantly larger than in the two perpendicular directions. Above the Néel temperature $T_{\rm N}$, the magnetic susceptibility in Fig. A.10 is nearly isotropic. Thus a quasi-one-dimensional Heisenberg model appears to be appropriate for the spin interactions in CaV_2O_4.

The crystal structure suggests the presence of spin $S = 1$ zigzag spin chains along the orthorhombic c-axis. We report here exact diagonalization (ED) calculations of the magnetic spin susceptibility versus temperature $\chi(T)$ and the magnetic heat capacity $C(T)$ of spin $S = 1$ J_1-J_2 Heisenberg chains containing $N = 8$, 10, and 12 spins for J_2/J_1 ratios from -1 to 5, and containing 14 spins for $J_2/J_1 = 0$. We also report the results of quantum Monte Carlo (QMC) simulations of $\chi(T)$ and $C(T)$. These simulations were carried out with the ALPS directed loop application[171] in the stochastic series expansion framework[172] for chains with $N = 30$ and 60 spins and $J_2/J_1 = 0$. Here J_1 and J_2 are the nearest-neighbor and next-nearest-neighbor interactions on a linear chain, respectively. The spin Hamiltonian is the $\lambda = 1$ special case of Eq. (A.1), given by

$$\mathcal{H} = \sum_{i=1}^{N} (J_1 \mathbf{S}_i \cdot \mathbf{S}_{i+1} + J_2 \mathbf{S}_i \cdot \mathbf{S}_{i+2}), \tag{A.3}$$

where $\mathbf{S}$ is a spin-1 operator. Periodic boundary conditions are imposed, so the chains become rings. J_1 is always positive (antiferromagnetic) whereas J_2 was taken to be either positive or negative (ferromagnetic). This chain is topologically the same as a zigzag chain in which J_1 is the nearest-neighbor interaction between the two legs of the zigzag chain and J_2 is the nearest-neighbor interaction along either leg of the zigzag chain. For $J_2 = 0$, the N spins are all part of the same nearest-neighbor exchange (J_1) chain. For $J_1 = 0$, two independent isolated equivalent chains are formed, each containing $N/2$ spins and with nearest-neighbor exchange J_2. This effect can be quantified using the $T = 0$ correlation length ξ which has been computed in Ref. [173]. We find that we can reach ratios N/ξ which are at least 2 for $J_2/J_1 \lesssim 0.6$ whereas ξ becomes comparable to or even bigger than the system sizes N which are accessible by ED for larger J_2/J_1. Accordingly, our finite chain data become a poorer approximation to the infinite J_1-J_2 chain for large J_2/J_1. This is exemplified below in Fig. A.20 where the data for chains containing different numbers N of spins exhibit an increasing divergence from each other with increasing J_2/J_1.

We will compare the spin susceptibility calculations with the experimental magnetic susceptibility data to estimate the J_1 and J_2/J_1 values in the J_1-J_2 chain model for CaV_2O_4. These values will also be used as input to compare the calculated magnetic heat capacity versus temperature with the experimental heat capacity data.

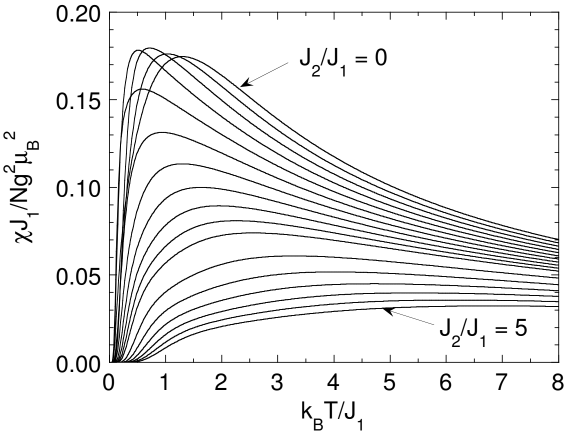

Figure A.17 Calculated magnetic spin susceptibility χ for spin $S = 1$ J_1-J_2 Heisenberg chains containing $N = 12$ spins versus temperature T, where J_1 and J_2 are the nearest-neighbor and next-nearest-neighbor exchange interactions in the chain. The curves from top to bottom on the right are for $J_2/J_1 = 0$, 0.2, 0.4, . . . , 2.0, 2.5, . . . , 5.0.

A.4.2.1 Magnetic Susceptibility

The calculated magnetic spin susceptibility $\chi(T)$ data for the spin $S = 1$ J_1-J_2 Heisenberg chain model are in the dimensionless form

$$\frac{\chi J_1}{Ng^2\mu_{\rm B}^2} \quad \text{versus} \quad \frac{k_{\rm B}T}{J_1}, \tag{A.4}$$

where N is the number of spins, g is the spectroscopic splitting factor (g-factor) of the magnetic moments for a particular direction of the applied magnetic field with respect to the crystal axes, $\mu_{\rm B}$ is the Bohr magneton, and $k_{\rm B}$ is Boltzmann's constant. Calculated $\chi(T)$ data sets for $N = 12$ were obtained by exact diagonalization assuming periodic boundary conditions (ring geometry) for J_2/J_1 ratios of -1, -0.8, ..., 2.0, 2.5, ..., 5. Examples of the calculations for a selection of J_2/J_1 values are shown in Fig. A.17. Each chain has an energy gap (spin gap) from the nonmagnetic singlet ground state to the lowest magnetic excited states.[173] No interchain (between adjacent zigzag chains) interactions are included in the calculations. These calculations are not expected to apply to our system at low temperatures where we see long-range antiferromagnetic ordering. However, we expect to be able to obtain approximate estimates of J_1 and J_2 by fitting the observed susceptibility data around the broad peak in the

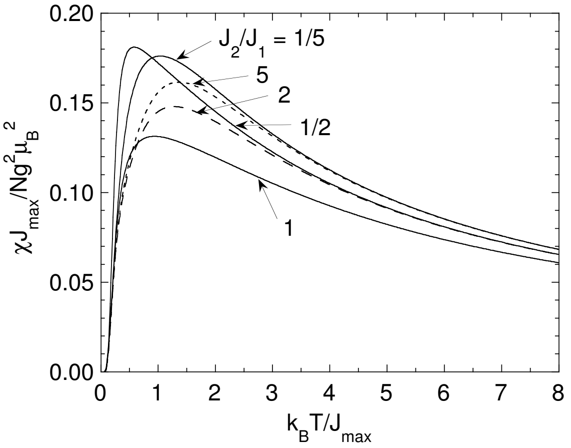

Figure A.18 Magnetic susceptibility χ versus temperature T for the spin $S = 1$ J_1-J_2 Heisenberg chain containing $N = 12$ spins. Here, $J_{\rm max} = \max(J_1, J_2)$. Pairs of curves for J_2/J_1 ratios that are reciprocals of each other become the same at high temperatures.

susceptibility at ≈ 300 K.

At high temperatures $k_{\rm B}T \gg J_{\rm max}$, where $J_{\rm max} = \max(J_1, J_2)$, one expects that the calculated $\chi J_{\rm max}$ versus $k_{\rm B}T/J_{\rm max}$ should be nearly the same upon interchange of J_1 and J_2, i.e., the same for pairs of J_2/J_1 ratios that are reciprocals of each other. [This is because all spins in the zigzag chain are equivalent, and at high temperatures the Curie-Weiss law is obtained. The Weiss temperature θ only depends on the numbers of nearest neighbors z to a given spin and the corresponding interaction strengths J ($\theta \sim z_1J_1 + z_2J_2$ with $z_1 = z_2 = 2$), which is invariant upon interchange of J_1 and J_2.] This expectation is confirmed in Fig. A.18 where such plots are shown for $J_2/J_1 = 1/5$ and 5; 1/2 and 2; and 1. The data for $J_2/J_1 = 1/2$ and 2, and for $J_2/J_1 = 1/5$ and 5, are seen to be about the same for temperatures $k_{\rm B}T/J_{\rm max} \gtrsim 4$, respectively.

The experimental magnetic susceptibility data of CaV_2O_4 will be fitted below by the calculated susceptibility $\chi(T)$ of a single $S = 1$ chain ($J_2/J_1 = 0$). Such integer-spin chains are known as Haldane chains. [174] We will therefore test here the sensitivity of the calculations to the number of spins N in the chain for this fixed J_2/J_1 value. Shown in Fig. A.19 are exact diagonalization (ED) calculations of $\chi(T)$ for $J_2/J_1 = 0$ and $N = 12$ and 14, and quantum

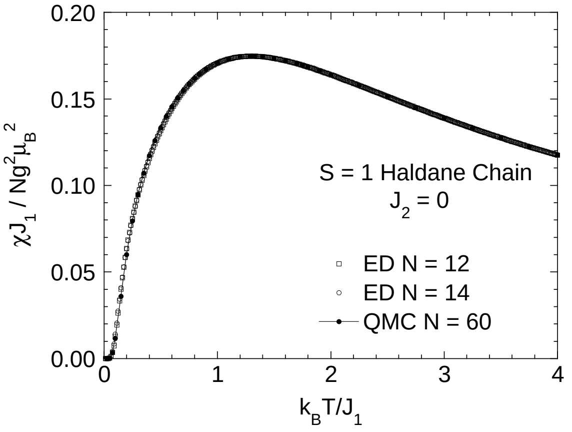

Figure A.19 Magnetic susceptibility χ versus temperature T calculations for the spin $S = 1$ Heisenberg chain with nearest neighbor exchange interaction J_1 and next-nearest-neighbor interaction $J_2 = 0$. The calculations were carried out using exact diagonalization (ED) for $N = 12$ and 14, and by quantum Monte Carlo (QMC) for $N = 60$.

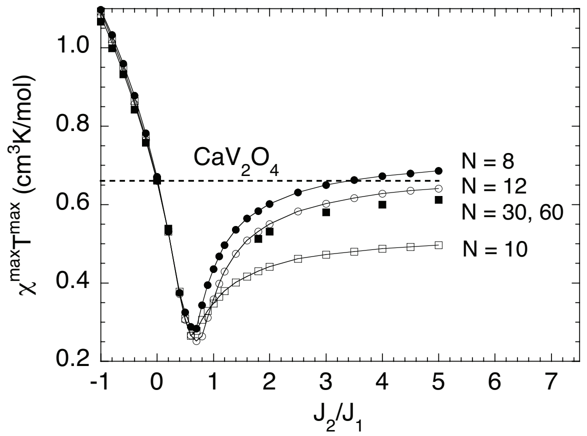

Figure A.20 The product $\chi^{\max}T^{\max}$ versus J_2/J_1 for the spin $S = 1$ J_1-J_2 Heisenberg chain containing $N = 8$, 10, 12, 30 or 60 spins, where we have assumed $N = 2N_A$ and $g = 1.97$. The data for $N = 8$, 10, and 12 were obtained using exact diagonalization calculations. The data for $N = 30$ and 60 were obtained from quantum Monte Carlo simulations; most of these data were obtained for $N = 60$, except for $J_2/J_1 = 0.2$, 1.8 and 2 where we used $N = 30$. The horizontal dashed line is the experimental value of $\chi^{\max}T^{\max}$ for CaV_2O_4 from Eq. (A.7). Comparison of this experimental value with the calculations indicates that within the J_1-J_2 model, $J_2/J_1 \approx 0$ (or $J_1/J_2 \approx 0$) in CaV_2O_4.

Monte Carlo (QMC) simulations for $J_2/J_1 = 0$ and $N = 60$. On the scale of the figure, the results of the three calculations can hardly be distinguished. These data are fully consistent with previous transfer-matrix renormalization-group results for $\chi(T)$.[175, 176] In Table A.6, the values of the maxima in the magnetic susceptibility $\chi^{\rm max}$ and also of the magnetic heat capacity $C^{\rm max}$ (see below) and the temperatures $T_\chi^{\rm max}$ and $T_C^{\rm max}$ at which they respectively occur are listed for the different calculations. For all three calculations, the maximum in the susceptibility occurs at about the same temperature $k_{\rm B}T_\chi^{\rm max}/J_1 \approx 1.30$, which may be compared with previous values of 1.35 (Ref. [177]) and 1.32(3).[178] Probably the most accurate values for the susceptibility are those of Ref. [176], as listed in Table A.6.

From the theoretical $\chi(T)$ data, for each value of J_2/J_1 one can obtain the value of the normalized temperature $k_{\rm B}T^{\rm max}/J_1$ at which the maximum in the susceptibility occurs, and the normalized value of the susceptibility $\chi^{\rm max}J_1/Ng^2\mu_{\rm B}^2$ at the maximum. For a given value of J_2/J_1, the product of these two values is a particular dimensionless number

$$\frac{\chi^{\rm max}T^{\rm max}}{Ng^2\mu_{\rm B}^2/k_{\rm B}} \tag{A.5}$$

that does not contain either exchange constant.

The spectroscopic splitting tensor (g-tensor) for vanadium cations is found to not depend much on either the oxidation (spin) state of the V cation or on its detailed environment in insulating hosts. The physical origin of this insensitivity is the small magnitude of the spin-orbit coupling constant for the vanadium atom. Typical values for the spherically-averaged g-factor $\langle g\rangle$ are between approximately 1.93 and 1.97, with the individual components of the diagonal g-tensor lying between 1.90 and 2.00. For example, for V^{+2} in single crystals of AgCl, one obtains $\langle g\rangle = 1.970(3)$;[179] for V^{+3} in guanidinium vanadium sulfate hexahydrate, $\langle g\rangle = 1.94(1)$;[180] for V^{+4} in TiO_2, $\langle g\rangle = 1.973(4)$.[181]

On the basis of the above discussion we set $g = 1.97$ for the V^{+3} spin $S = 1$ in Eq. (A.5). Then setting $N = 2N_{\rm A}$, where $N_{\rm A}$ is Avogadro's number and the factor of 2 comes from two atoms of V per formula unit of CaV_2O_4, the expression in Eq. (A.5) becomes

$$\frac{\chi^{\rm max}T^{\rm max}}{2.91\ {\rm cm^3\,K/mol}}\ , \tag{A.6}$$

Table A.6 Calculated values of the maxima in the magnetic spin susceptibility $\chi^{\rm max}$ and magnetic heat capacity $C^{\rm max}$ and temperatures $T_\chi^{\rm max}$ and $T_C^{\rm max}$ at which they occur, respectively, for the linear spin $S = 1$ Heisenberg chain (Haldane chain) with nearest-neighbor exchange interaction J_1 and next-nearest-neighbor interaction $J_2 = 0$. The results of exact diagonalization (ED) and quantum Monte Carlo (QMC) calculations are shown. Here N is the number of spins in the chain, g is the g-factor, $\mu_{\rm B}$ is the Bohr magneton, and $k_{\rm B}$ is Boltzmann's constant. Also included are the results of Ref. [176], which are probably the most accurate values currently available for the susceptibility.

	$\frac{\chi^{\rm max} J_1}{N g^2 \mu_{\rm B}^2}$	$\frac{k_{\rm B} T_\chi^{\rm max}}{J_1}$	$\frac{C^{\rm max}}{N k_{\rm B}}$	$\frac{k_{\rm B} T_C^{\rm max}}{J_1}$
QMC $N = 60$	0.174686(9)	1.301(10)	0.5431(4)	0.857(10)
ED $N = 12$	0.174662	1.2992	0.5520	0.8295
ED $N = 14$	0.174677	1.2980	0.5466	0.8398
Ref. [176]	0.17496(2)	1.2952(16)		

where a "mol" refers to a mole of $\rm CaV_2O_4$ formula units. Then from Eq. (A.6) and the calculated $\chi(T)$ data for different values of J_2/J_1, the calculated $\chi^{\rm max}T^{\rm max}$ versus J_2/J_1 for $\rm CaV_2O_4$ is shown in Fig. A.20. From the figure, the dependence of $\chi^{\rm max}T^{\rm max}$ on J_2/J_1 is about the same for N = 8, 10, and 12 for $J_2/J_1 \lesssim 0.6$ which is consistent with a short correlation length $\xi \lesssim 6$ for $0 \leq J_2/J_1 \leq 0.6$ (see Ref. [173]). However, the curves for the different values of N are quite different at larger values of J_2/J_1; the behavior versus N even becomes nonmonotonic in this parameter region. The QMC results also shown in Fig. A.20 nevertheless indicate that the ED calculations for $N = 12$ sites yield a good approximation to the infinite N limit also for $J_2/J_1 \geq 1.8$. Unfortunately, the QMC sign problems are so severe in the region $0.2 < J_2/J_1 < 1.8$ that here we cannot resolve the maximum of χ with our QMC simulations.

The experimental susceptibility $\chi_{\rm exp}(T)$ data for $\rm CaV_2O_4$ in Fig. A.10 can be written as the sum $\chi_{\rm exp}(T) = \chi(T) + \chi_0$, where $\chi(T)$ is the spin susceptibility (which is the part calculated above) and χ_0 is the temperature-independent orbital susceptibility. From the data in Ref. [129] for $\rm V_2O_3$, we estimate $\chi_0 \sim 0.4 \times 10^{-3}$ cm^3/mol for $\rm CaV_2O_4$. From Fig. A.10 we then obtain the experimental value for the *spin* susceptibility at the maximum $\chi^{\rm max} \approx 2.2 \times 10^{-3}$ cm^3/mol and for the temperature at the maximum $T_\chi^{\rm max} \approx 300$ K, yielding for $\rm CaV_2O_4$

$$\chi^{\rm max}T^{\rm max} \approx 0.66~{\rm cm^3~K/mol}~. \tag{A.7}$$

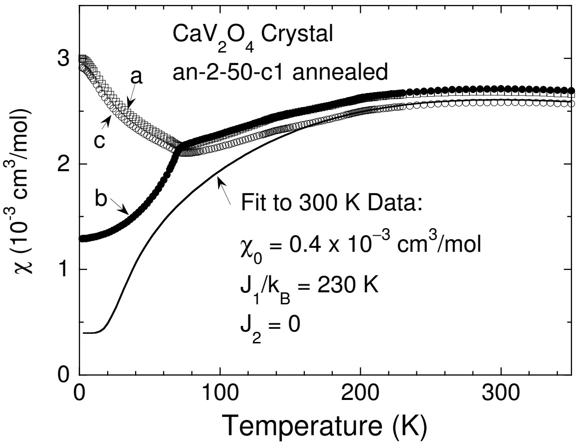

Figure A.21 Calculated magnetic susceptibility χ versus temperature T for the J_1-J_2 chain with $J_1/k_{\rm B} = 230$ K, $J_2 = 0$, and $g = 1.97$, and with a temperature-independent orbital contribution $\chi_0 = 0.4 \times 10^{-3}$ cm^3/mol (solid curve). The calculated spin susceptibility at $T = 0$ is zero, so the zero-temperature value of the calculated solid curve is χ_0. Experimental data for annealed CaV$_2$O$_4$ crystal 2-50-c1 from Fig. A.10 are also shown. Comparison of these data for $T \to 0$ with the calculated curve shows that the spin susceptibility along the easy b-axis of CaV$_2$O$_4$ is rather large for $T \to 0$.

Comparison of this value with the theoretical spin susceptibility data in Fig. A.20 yields $J_2/J_1 \approx 0$ (or $J_1/J_2 \approx 0$). This ratio of J_2/J_1 is quite different from the value of unity that we and others[11, 12] initially expected. The temperature $T_\chi^{\rm max} \approx 300$ K, combined with $k_{\rm B}T_\chi^{\rm max}/J_1 \approx 1.30$ from Table A.6, yields $J_1/k_{\rm B} = 230$ K. Although the numerical results shown in Fig. A.20 are the least accurate in the vicinity of $J_2/J_1 \approx 1$, it seems rather unlikely that the value of $\chi^{\rm max}T^{\rm max}$ obtained from the J_1-J_2 chain model in the region $0.6 \lesssim J_2/J_1 \lesssim 1.8$ could be consistent with the value in Eq. (A.7) expected for CaV$_2$O$_4$.

The calculated total susceptibility versus temperature for $J_1/k_{\rm B} = 230$ K, $J_2 = 0$ and $\chi_0 = 0.4 \times 10^{-3}$ cm^3/mol is shown in Fig. A.21. Also shown are the experimental susceptibility data for annealed CaV$_2$O$_4$ crystal an-2-50-c1 from Fig. A.10, where an excellent fit of the average anisotropic $\chi(T)$ data near 300 K is seen.

Above the Néel temperature, one sees from Figs. A.10 and A.21 that the susceptibility is nearly isotropic. The relatively small anisotropy observed can come from anisotropy in the orbital Van Vleck paramagnetic susceptibility, from g-anisotropy arising from spin-orbit interactions, from single-ion anisotropy of the form $DS_z^2 + E(S_x^2 - S_y^2)$, and/or from anisotropy in the spin exchange part of the spin Hamiltonian. The relative importances of these sources to the observed susceptibility anisotropies are not yet clear. The experimental data below 200 K in Fig. A.21 increasingly deviate from the fit with decreasing temperature. This suggests that other interactions besides J_1 and J_2 and/or the presence of magnetic anisotropies may be important to determining the spin susceptibility above $T_{\rm N}$ in $\rm CaV_2O_4$.

For collinear antiferromagnetic (AF) ordering, one nominally expects the spin susceptibility along the easy axis to go to zero as $T \to 0$. Comparison of the theoretical curve with the experimental easy axis (b-axis) data $\chi_b(T)$ in Fig. A.21 indicates that the zero-temperature b-axis spin susceptibility is not zero, but is instead a rather large value $\chi_b^{\rm spin}(T \to 0) \approx 0.9 \times 10^{-3}$ cm^3/mol. This finite spin susceptibility indicates either that the spin structure in the AF state is not collinear, that not all vanadium spins become part of the ordered magnetic structure below $T_{\rm N}$, and/or that quantum fluctuations are present that induce a nonzero spin susceptibility. Such quantum fluctuations can arise from the low-dimensionality of the spin lattice and/or from frustration effects. As discussed in the Introduction, our recent NMR and magnetic neutron diffraction experiments on single crystal $\rm CaV_2O_4$ indicated that the magnetic structure at 4 K is noncollinear,[150, 151] which can at least partially explain the nonzero spin susceptibility along the (average) easy b-axis at low temperatures. In addition, the reduction in the local ordered moment 1.0–1.6 $\mu_{\rm B}$/(V atom) of the *ordered* vanadium spins found in these studies from the expected value $gS\mu_{\rm B} = 2\ \mu_{\rm B}$/(V atom) suggests that quantum zero-point spin fluctuations could be strong and could contribute to the large finite $\chi_b^{\rm spin}(T \to 0)$.

A.4.2.2 Magnetic Heat Capacity

The magnetic heat capacity C versus temperature T was calculated by exact diagonalization for $N = 12$ spins $S = 1$ over the range $-1 \leq J_2/J_1 \leq 5$. Representative results are plotted in Fig. A.22. The variation in $C(T)$ with N is illustrated in Fig. A.23 for $J_2/J_1 = 0$ and $N = 12$ and 14 from exact diagonalization calculations, and for $N = 60$ from quantum Monte

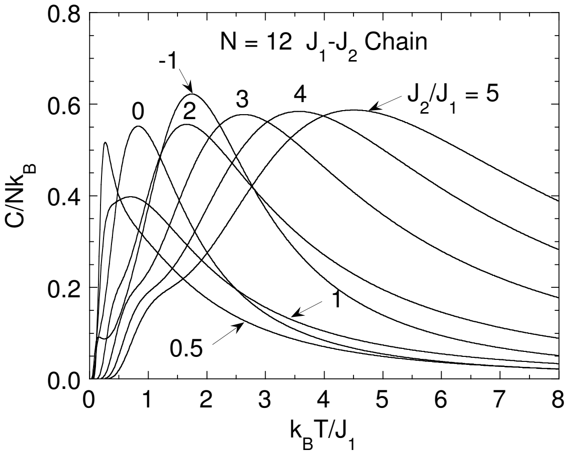

Figure A.22 Magnetic heat capacity C versus temperature T for the spin $S = 1$ J_1-J_2 Heisenberg chain with J_2/J_1 values from -1 to 5, calculated using exact diagonalization with $N = 12$. Here N is the number of spins, k_B is Boltzmann's constant, and $J_1 > 0$ and J_2 are the nearest-neighbor and next-nearest-neighbor exchange interactions, respectively.

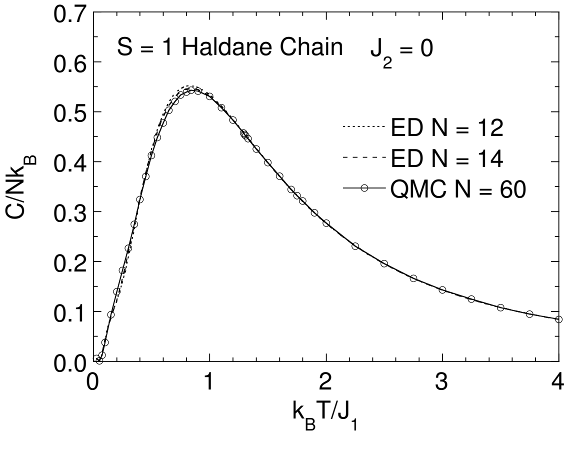

Figure A.23 Magnetic heat capacity C versus temperature T for the $S = 1$ J_1-J_2 chain with $J_2/J_1 = 0$ ("Haldane chain"), calculated using exact diagonalization (ED) with $N = 10$ and 12, and quantum Monte Carlo (QMC) simulations for $N = 60$.

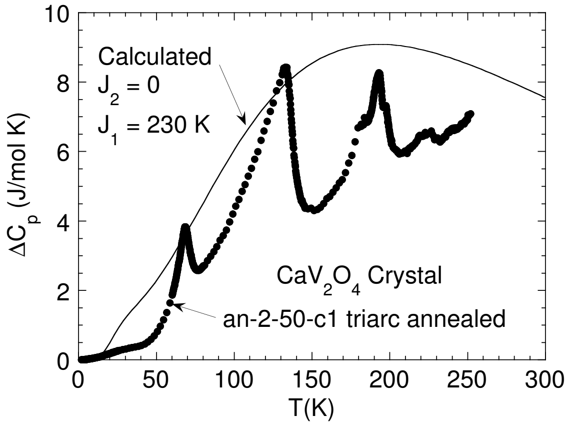

Figure A.24 Magnetic heat capacity C versus temperature T for the spin $S = 1$ J_1-J_2 chain with $J_2/J_1 = 0$ and $J_1/k_{\rm B} = 230$ K, calculated using exact diagonalization with $N = 14$ (solid curve) from Fig. A.23. The data points are the $\Delta C(T)$ data for annealed crystal an-2-50-c1 from Fig. A.15.

Carlo simulations. The data for the different N are seen to be nearly the same. The values of the maxima $C^{\rm max}$ in the magnetic heat capacity and the temperatures $T_C^{\rm max}$ at which they occur are listed above in Table A.6. Our results for the specific heat are consistent with previous transfer-matrix renormalization-group computations.[175, 176] The two transfer-matrix renormalization-group results differ at *high* temperatures. Our QMC results for C obtained from rings with $N = 60$ sites are in better agreement with the older results which apply to the infinite N limit[175] than the more recent results obtained for open chains with $N = 64$ sites.[176] The $C(T)$ data in Ref. [176] were calculated from a numerical derivative which resulted in systematic errors in the data at high temperatures.[182]

We cannot confidently derive the exchange constants in $\rm CaV_2O_4$ from fits of our heat capacity data by the theory. Extraction of the magnetic part of the experimental heat capacity is tenuous because of the presence of the orthorhombic to monoclinic structural transition at $T_{\rm S} \approx 150$ K and the transition(s) at $T_{\rm S1} \approx 200$ K. Therefore the relationship of the heat capacities $\Delta C(T)$ in Figs. A.14(a) and A.15 to the magnetic heat capacities of the samples is unclear. Here, we will just compare the theoretical magnetic heat capacity calculated for the exchange constants $J_1 = 230$ K and $J_2 = 0$, that were already deduced in the previous section, with the experimental $\Delta C(T)$ data to see if theory and experiment are at least roughly in agreement. This comparison is shown in Fig. A.24 for annealed CaV_2O_4 crystal an-2-50-c1 from Fig. A.15. Overall, the theory and experimental data have roughly the same magnitude, but the data are systematically below the theoretical prediction. This is likely caused by the heat capacity of the nonmagnetic reference compound $CaSc_2O_4$ being somewhat different from the lattice heat capacity of CaV_2O_4. We note from Fig. A.13 that a difference of 5 J/mol K between the theory and experiment in Fig. A.24 is only about 5% of the total heat capacity of the samples at 200 K. In addition, we have not included in the theory interchain couplings that lead to long-range antiferromagnetic order, or the effect of the magnetic ordering on the heat capacity including the effect of the energy gap in the spin wave spectrum below T_N.

A.4.3 Interchain Coupling

Within the $S = 1$ J_1-J_2 Heisenberg spin chain model, we found above that $J_2/J_1 \approx 0$ and $J_1 \approx 230$ K in CaV_2O_4 near room temperature. Thus the crystallographic zigzag vanadium chains in CaV_2O_4 act like $S = 1$ linear spin chains with nearest-neighbor interaction J_1. This is a so-called Haldane chain[174] with a nonmagnetic singlet ground state and an energy gap for spin excitations given by[183, 184] $\approx 0.4105J_1$. An interchain coupling $J_\perp$ must be present in order to overcome this spin gap and induce long-range antiferromagnetic ordering at T_N. Pedrini *et al.* [178, 185] have recently estimated the dependence of T_N/J_1 on $J_\perp/J_1$ using a random-phase approximation for the interchain coupling for $S = 1$ Haldane chains. Using our values $T_N = 68$ K, $J_1 = 230$ K and $T^{\max} = 300$ K, we obtain $J_\perp/J_1 \approx 0.04$ and $J_\perp = 5$–10 K. However, it should be emphasized that the treatment of Refs. [178] and [185] assumes a nonfrustrated interchain coupling geometry such that the result $J_\perp \approx 10$ K should be considered as a lower bound. Still, the value of $J_\perp/J_1$ is sufficiently small that a redetermination of J_2/J_1 and J_1, from a J_1-J_2-$J_\perp$ model fitted to the observed susceptibility data for CaV_2O_4 near room temperature, would yield very similar values of J_2/J_1 and J_1 to those we have already estimated using the isolated chain J_1-J_2 model. Additional and more conclusive information about the interchain coupling strength(s) will become available from analysis of inelastic neutron scattering measurements of the magnetic excitation dispersion relations.[153]

A.5 Summary

We have synthesized the $S = 1$ spin chain compound CaV_2O_4 in high purity polycrystalline form and as single crystals. Our magnetic susceptibility $\chi(T)$ and ac magnetic susceptibility $\chi_{\rm ac}(T)$ measurements do not show any signature of a spin glass-like transition around 20 K that was previously reported.[11, 12] We instead observe long-range antiferromagnetic ordering at sample-dependent Néel temperatures $T_{\rm N} \approx 50$–70 K as shown in Table A.4. The Néel temperature and the orthorhombic-to-monoclinic structural transition temperature $T_{\rm S}$ in Table A.4 both show a large systematic variation between different samples. Those temperatures for an unannealed crystal are each less than those for an annealed crystal which in turn are less than those for a sintered polycrystalline sample. The cause of these large temperature differences, especially between as-grown and annealed single crystals, is unclear. The transition temperature differences may arise from small changes in oxygen stoichiometry ($\lesssim 1$ at.%, below the threshold of detection by TGA or XRD) and/or from structural strain, both of which may be reduced upon annealing the as-grown crystals at 1200 °C in 5% H_2/He. In addition, other small chemical differences and/or structural defects may be relevant.

Our heat capacity $C_{\rm p}(T)$, linear thermal expansion $\alpha(T)$, and $\chi(T)$ measurements reveal distinct features at the orthorhombic-to-monoclinic structural transition temperature $T_{\rm S}$ identified from our diffraction studies.[152] We inferred from a combination of structural studies and physical property measurements that the origin of the third transition at $T_{\rm S1} \approx 200$ K in one of our annealed crystals was mostly due to the structural transition in the V_2O_3 impurity phase that grew coherently upon annealing the crystal. In the other annealed crystal, we ruled out this source and we are thus left with a transition at $T_{\rm S1}$ with unknown origin. We speculate that this transition may be the long-sought chiral phase transition originally postulated by Villain in 1977.[149]

The $\chi(T)$ shows a broad maximum at about 300 K indicating short-range antiferromagnetic (AF) ordering in a low-dimensional antiferromagnet as previously observed[11, 12] and the $\chi(T)$

above $T_{\rm N}$ in single crystals is nearly isotropic. The anisotropic $\chi(T)$ below $T_{\rm N}$ shows that the (average) easy axis of the antiferromagnetic structure is the orthorhombic b-axis. The magnetic spin susceptibility along this axis is found to be a large finite value for $T \to 0$, instead of being zero as expected for a classical collinear antiferromagnet. This result is consistent with our observed noncollinear magnetic structure below $T_{\rm N}$.[150, 151] In view of the fact that $\rm CaV_2O_4$ is a low-dimensional spin system, quantum fluctuations could also contribute to both the observed reduced zero temperature ordered moment and the relatively large zero temperature spin susceptibility.

We analyzed the $\chi(T)$ data near room temperature in terms of theory for the $S = 1$ J_1-J_2 linear Heisenberg chain, where $J_1(J_2)$ is the (next-)nearest-neighbor interaction along the chain. We obtain $J_1/k_{\rm B} \approx 230$ K, but surprisingly $J_2/J_1 \approx 0$ (or $J_1/J_2 \approx 0$), so the exchange connectivity of the spin lattice appears to correspond to linear $S = 1$ Haldane chains instead of zigzag spin chains as expected from the crystal structure. This result is consistent with analysis of our high temperature (up to 1000 K) magnetic susceptibility measurements on single crystal $\rm CaV_2O_4$.[151] We estimated here the coupling $J_\perp$ between these chains that leads to long-range AF order at $T_{\rm N}$ to be $J_\perp/J_1 \gtrsim 0.04$, i.e., only slightly larger than the value $J_\perp/J_1 \approx 0.02$ needed[178, 185] to eliminate the energy gap (Haldane gap) for magnetic excitations.

From our $C_{\rm p}(T)$ measurements, the estimated molar magnetic entropy at $T_{\rm N}$ is only $\approx 8\%$ of its maximum value $2{\rm R}\ln(2S + 1) = 2{\rm R}\ln(3)$, where R is the molar gas constant, and the heat capacity jump at $T_{\rm N}$ is only a few percent of the value expected in mean field theory for $S = 1$. Both results indicate strong short range antiferromagnetic order above $T_{\rm N}$ and large values J_1 and/or $J_2 > 100$ K, consistent with the $\chi(T)$ data. We also compared the $C_{\rm p}(T)$ data with the theoretical prediction for the magnetic heat capacity using the exchange constants found from the magnetic susceptibility analysis, and rough agreement was found. However, this comparison is not very precise or useful because the structural transition at $T_{\rm S} \sim 150$ K and the transition(s) at $T_{\rm S1} \sim 200$ K for our two annealed single crystals, make large contributions to $C_{\rm p}(T)$. In addition, the accuracy of the measured heat capacity of the nonmagnetic reference compound $CaSc_2O_4$ in representing the lattice heat capacity of CaV_2O_4 is unknown. Thus extracting the magnetic part of the heat capacity at high temperatures from the observed $C_p(T)$ data for comparison with theory is ambiguous.

In closing, we note the following additional issues that could usefully be addressed in future work. Our analyses of our $\chi(T)$ data for CaV_2O_4 to obtain the exchange constants J_1 and J_2 were based on fitting the experimental $\chi(T)$ data only near room temperature, since our calculations of $\chi(T)$ all showed nonmagnetic singlet ground states, contrary to observation, and could not reproduce the observed antiferromagnetic ordering at low temperatures. Calculations containing additional interactions (see also below) and/or anisotropies are needed for comparison with the lower temperature data.

The orthorhombic crystal structure of CaV_2O_4 at room temperature contains two crystallographically inequivalent but similar V^{+3} $S = 1$ zigzag chains. These chains may therefore have different exchange constants associated with each of them. For simplicity, our $\chi(T)$ data were analyzed assuming a single type of zigzag chain. Furthermore, the extent to which the transitions at T_{S1} and T_S affect the magnetic interactions is not yet clear.

From crystal structure considerations, one expects that $J_2/J_1 \approx 1$ in CaV_2O_4,[11, 12] instead of $J_2/J_1 \approx 0$ as found here. This suggests that additional magnetic interactions and/or anisotropy terms beyond the Heisenberg interactions J_1 and J_2 and interchain coupling $J_\perp$ considered here may be important. In addition to single ion anisotropy and other types of anisotropy, we mention as possibilities the Dzyaloshinskii-Moriya interaction, biquadratic exchange, and cyclic exchange interactions within the zigzag chains. When such additional terms are included in the analysis, the fitted value of J_2/J_1 could turn out to be closer to unity. A four-spin cyclic exchange interaction has been found to be important to the magnetic susceptibility in cuprate spin ladders.[85] In these spin ladders, there are exchange interactions J and J' between nearest-neighbor Cu^{+2} spins 1/2 along the legs and across the rungs of the spin ladder, respectively. For the $S = 1/2$ two-leg ladder compound $SrCu_2O_3$, if only J and J' are included in fits to the data, one obtains $J'/J \approx 0.5$.[85] However, by also including the theoretically derived cyclic four-spin exchange interaction, the ratio J'/J increases from 0.5 to a value closer to unity, as expected from the crystal structure.

Pieper *et al.* have recently proposed a very different and very interesting model to explain the inference that $J_2/J_1 \approx 0$ around room temperature which involves partial orbital ordering of the two *d*-electrons of V among the three t_{2g} orbitals.[151] Furthermore, in order to explain the magnetic structure at low temperatures, they deduce that the nature of the orbital ordering changes below T_S such that the effective spin lattice becomes a spin-1 two-leg ladder.

It has been well documented that fits of magnetic susceptibility data by theory tests only the consistency of a spin model with the data, and not the uniqueness of the model. A good example of this fact arose in the study of the antiferromagnetic alternating exchange chain compound vanadyl pryophosphate, $(\mathrm{VO})_2\mathrm{P}_2\mathrm{O}_2$, the history of which is described in detail in the introduction of Ref. [186]. The ultimate arbiter of the validity of a spin model is inelastic neutron scattering measurements of the magnetic excitation dispersion relations in single crystals. Theoretical calculations of the exchange interactions are much needed and would also be valuable in this regard.

Finally, the origin of the intrinsic heat capacity anomalies at $T_\mathrm{S1} \approx 200$ K for the two *annealed* single crystals of $\mathrm{CaV_2O_4}$ needs to be further studied. We speculate that this transition may be the long-sought chiral phase transition originally postulated by Villain in 1977.[149]

Note added—After this work and this paper were nearly completed, Sakurai reported a very interesting and detailed study of the magnetic and electronic phase diagram of polycrystalline samples of the solid solution $\mathrm{Ca}_{1-x}\mathrm{Na}_x\mathrm{V}_2\mathrm{O}_4$ prepared under high pressure.[44]

BIBLIOGRAPHY

[1] E. Hoschek and W. Klemm, Z. Anorg. Allg. Chem. **242**, 63 (1939).

[2] G. Andersson, Acta Chem. Scand. **8**, 1599 (1954).

[3] A. Magnéli, Acta Chem. Scand. **2**, 501 (1948).

[4] H. Kuwamoto, N. Otsuka, and H. Sato, J. Solid State Chem. **36**, 133 (1981).

[5] S. Andersson and L. Jahnberg, Ark. Kemi **21**, 413 (1963).

[6] H. Horiuchi, N. Morimoto, and M. Tokonami, J. Solid State Chem. **17**, 407 (1976).

[7] S. Kachi, K. Kosuge, and H. Okinaka, J. Solid State Chem. **6**, 258 (1973).

[8] S. Kondo, D. C. Johnston, C. A. Swenson, F. Borsa, A. V. Mahajan, L. L. Miller, T. Gu, A. I. Goldman, M. B. Maple, D. A. Gajewski, et al., Phys. Rev. Lett. **78**, 3729 (1997).

[9] B. F. Decker and J. S. Kasper, Acta Cryst. **10**, 332 (1957).

[10] J. M. Hastings, L. M. Corliss, W. Kunnmann, and S. L. Placa, J. Phys. Chem. Solids **28**, 1089 (1967).

[11] H. Fukushima, H. Kikuchi, M. Chiba, Y. Fujii, and Y. Yamamoto, Prog. Theor. Phys. Suppl. **145**, 72 (2002).

[12] H. Kikuchi, M. Chiba, and T. Kubo, Can. J. Phys. **79**, 1552 (2001).

[13] G. R. Stewart, Rev. Modern Phys. **56**, 755 (1984).

[14] A. C. Hewson, *The Kondo Problem to Heavy Fermions* (Cambridge University Press, 1993).

[15] K. Kadawaki and S. B. Woods, Solid State Communications **58**, 507 (1986).

[16] A. Shimoyamada, S. Tsuda, K. Ishizaka, T. Kiss, T. Shimojima, T. Togashi, S. Watanabe, C. Q. Zhang, C. T. Chen, Y. Matsushita, et al., Phys. Rev. Lett. **96**, 026403 (2006).

[17] V. I. Anisimov, M. A. Korotin, M. Zolfl, K. L. H. T. Pruschke, and R. T. M., Phys. Rev. Lett. **83**, 364 (1999).

[18] R. Arita, K. Held, A. V. Lukoyanov, and V. I. Anisimov, Phys. Rev. Lett. **98**, 166402 (2007).

[19] J. Hopkinson and P. Coleman, Phys. Rev. Lett. **89**, 267201 (2002).

[20] N. Shannon, Eur. Phys. J. **27**, 527 (2002).

[21] O. Chmaissem, J. D. Jorgensen, S. Kondo, and D. C. Johnston, Phys. Rev. Lett. **79**, 4866 (1997).

[22] Y. Yamashita and K. Ueda, Phys. Rev. B **67**, 195107 (2003).

[23] P. Fulde, A. N. Yaresko, A. A. Zvyagin, and Y. Grin, Europhys. Lett. **54**, 779 (2001).

[24] S. Kondo, D. C. Johnston, and L. L. Miller, Phys. Rev. B **59**, 2609 (1999).

[25] D. C. Johnston, S. H. Baek, X. Zong, F. Borsa, J. Schmalian, and S. Kondo, Phys. Rev. Lett. **95**, 176408 (2005).

[26] X. Zong, S. Das, F. Borsa, M. D. Vannette, R. Prozorov, J. Schmalian, and D. C. Johnston, Phys. Rev. B **77**, 144419 (2008).

[27] Y. Ueda, J. Kikuchi, and H. Yasuoka, J. Magn. Magn. Mater. **147**, 195 (1995).

[28] S. Nagata, P. Keesom, and S. P. Faile, Phys. Rev. B **20**, 2886 (1979).

[29] D. B. Rogers, J. L. Gillson, and T. E. Gier, Solid State Commun. **5**, 263 (1967).

[30] H. Takagi, C. Urano, S. Kondo, M. Nohara, Y. Ueda, T. Shiraki, and T. Okubo, Mater. Sci. Eng. **B63**, 147 (1999).

[31] C. Urano, M. Nohara, S. Kondo, F. Sakai, H. Takagi, T. Shiraki, and T. Okubo, Phys. Rev. Lett. **85**, 1052 (2000).

[32] D. C. Johnston, C. A. Swenson, and S. Kondo, Phys. Rev. B **59**, 2627 (1999).

[33] Y. Matsushita, H. Ueda, and Y. Ueda, Nature Mater. **4**, 845 (2005).

[34] K. Takeda, H. Hidaka, H. Kotegawa, T. C. Kobayashi, K. Shimizu, H. Harima, K. Fujiwara, K. Miyoshi, J. Takeuchi, Y. Ohishi, et al., Physica B **359-361**, 1312 (2005).

[35] K. Fujiwara, K. Miyoshi, J. Takeuchi, Y. Shimaoka, and T. Kobayashi, J. Phys. Condens. Mater. **16**, S615 (2004).

[36] L. Pinsard-Gaudart, N. Dragoe, P. Lagarde, A. M. Flank, J. P. Itie, A. Congeduti, P. Roy, S. Niitaka, and H. Takagi, Phys. Rev. B **76**, 045119 (2007).

[37] A. Kolezhuk, R. Roth, and U. Schollwock, Phys. Rev. Lett. **77**, 5142 (1997).

[38] M. Kaburagi, H. Kawamura, and T. Hikihara, J. Phys. Soc. Jpn. **68**, 3185 (1999).

[39] T. Hikihara, M. Kaburagi, H. Kawamura, and T. Tonegawa, J. Phys. Soc. Jpn. **69**, 3185 (2000).

[40] X. Zong, B. J. Suh, A. Niazi, J. Q. Yan, D. L. Schlagel, T. A. Lograsso, and D. C. Johnston, Phys. Rev. B **77**, 014412 (2008).

[41] A. Niazi, S. L. Budko, D. L. Schlagel, J. Q. Yan, T. A. Lagrasso, A. Kreyssig, S. Das, S. Nandi, A. I. Goldman, A. Honecker, et al., Phys. Rev. B **79**, 014432 (2009).

[42] O. Pieper, B. Lake, A. Daude-Aladine, M. Reehuis, K. Prokes, B. Klamke, K. Kiefer, J. Q. Yan, A. Niazi, D. C. Johnston, et al., Phys. Rev. B **79**, 180409 (2009).

[43] K. Yamaura, M. Arai, A. Sato, A. B. Karki, D. P. Young, R. Movshovich, S. Okamoto, D. Mandrus, and E. Takayama-Muromachi, Phys. Rev. Lett. **99**, 196601 (2007).

[44] H. Sakurai, Phys. Rev. B **78**, 094410 (2008).

[45] Y. Kanke and K. Kato, Chem. Mater. **9**, 141 (1997).

[46] K. Friese, Y. Kanke, A. N. Fitch, and A. Grzechnik, Chem. Mater. **19**, 4882 (2007).

[47] M. Onoda, Acta. Cryst. **B59**, 429 (2003).

[48] Y. Kamihara, T. Watanabe, M. Hirano, and H. Hosono, J. Am. Chem. Soc. **130**, 3296 (2008).

[49] X. H. Chen, T. Wu, G. Wu, R. H. Liu, H. Chen, and D. F. Fang, Nature (London) **453**, 761 (2008).

[50] G. F. Chen, Z. Li, D. Wu, G. Li, W. Z. Hu, J. Dong, P. Zheng, J. L. Luo, and N. L. Wang, Phys. Rev. Lett. **100**, 247002 (2008).

[51] Z.-A, Ren, J. Yang, W. Lu, W. Yi, X.-L. Shen, Z.-C. Li, G.-C. Che, X.-L. D. L.-L. Sun, F. Zhou, et al., Europhys. Lett. **82**, 57002 (2008).

[52] J. Yang, Z.-C. Li, W. Lu, W. Yi, X.-L. Shen, Z.-A. Ren, G.-C. Che, X.-L. Dong, L.-L. Sun, F. Zhou, et al., Supercond. Sci. Technol. **21**, 082001 (2008).

[53] J.-W. G. Bos, G. B. S. Penny, J. A. Rodgers, D. A. Sokolov, A. D. Huxley, and J. P. Attfield, Chem. Commun. p. 3634 (2008).

[54] P. Quebe, L. J. Terbuchte, and W. Jeitschko, J. Alloys Compd. **302**, 70 (2000).

[55] J. Dong, H. J. Zhang, G. Xu, Z. Li, G. Li, W. Z. Hu, D. Wu, G. F. Chen, X. Dai, J. L. Luo, et al., Europhys. Lett. **83**, 27006 (2008).

[56] H.-H. Klauss, H. Luetkens, R. Klingeler, C. Hess, F. J. Litterst, M. Kraken, M. Korshunov, I. Eremin, S.-L. Drechsler, R. Khasanov, et al., Phys. Rev. Lett. **101**, 077005 (2008).

[57] G. Giovannetti, S. Kumar, and J. van den Brink, Physica B **403**, 3653 (2008).

[58] R. W. McCallum, J.-Q. Yan, G. Rustan, E. D. Mun, Y. Singh, S. Das, R. C. Nath, S. L. Budko, K. W. Dennis, D. C. Johnston, et al., J. Appl. Phys. **105**, 123912 (2009).

[59] M. Rotter, M. Tegel, D. Johrendt, I. Schellenberg, W. Hermes, and R. Pöttgen, Phys. Rev. B **78**, 020503(R) (2008).

[60] C. Krellner, N. Caroca-Canales, A. Jesche, H. Rosner, A. Ormeci, and C. Geibel, Phys. Rev. B **78**, 100504(R) (2008).

[61] N. Ni, S. L. Bud'ko, A. Kreyssig, S. Nandi, G. E. Rustan, A. I. Goldman, J. D. C. S. Gupta, A. Kracher, and P. C. Canfield, Phys. Rev. B **78**, 014507 (2008).

[62] J.-Q. Yan, A. Kreyssig, S. Nandi, N. Ni, S. L. Budko, A. Kracher, R. J. McQueeney, R. W. McCallum, T. A. Lograsso, A. I. Goldman, et al., Phys. Rev. B **78**, 024516 (2008).

[63] N. Ni, S. Nandi, A. Kreyssig, A. I. Goldman, E. D. Mun, S. L. Budko, and P. C. Canfield, Phys. Rev. B **78**, 014523 (2008).

[64] F. Ronning, T. Klimczuk, E. D. Bauer, H. Volz, and J. D. Thompson, J. Phys. Condens. Matter **20**, 322201 (2008).

[65] A. I. Goldman, D. N. Argyriou, B. Ouladdi, T. Chatterji, A. Kreyssig, S. Nandi, N. Ni, S. L. Budko, P. C. Canfield, and R. J. McQueeney, Phys. Rev. B **78**, 100506 (2008).

[66] M. Tegel, M. Rotter, V. Weiss, F. M. Schappacher, R. Pöttgen, and D. Johrendt, J. Phys. Condens. Mater. **20**, 452201 (2008).

[67] Z. Ren, Z. Zhu, S. Jiang, X. Xu, Q. Tao, C. Wang, C. Feng, G. Cao, and Z. Xu, Phys. Rev. B **78**, 052501 (2008).

[68] H. S. Jeevan, Z. Hossain, D. Kasinathan, H. Rosner, C. Geibel, and P. Gegenwart, Phys. Rev. B **78**, 052502 (2008).

[69] M. Rotter, M. Tegel, and D. Johrendt, Phys. Rev. Lett. **101**, 107006 (2008).

[70] G. F. Chen, Z. Li, G. Li, W. Z. Hu, J. Dong, X. D. Zhang, P. Zheng, N. L. Wang, and J. L. Luo, Chin. Phys. Lett. **25**, 3403 (2008).

[71] H. S. Jeevan, Z. Hossain, D. Kasinathan, H. Rosner, C. Geibel, and P. Gegenwart, Phys. Rev. B **78**, 092406 (2008).

[72] K. Sasmal, B. Lv, B. Lorenz, A. Guloy, F. Chen, Y. Xue, and C. W. Chu, Phys. Rev. Lett. **101**, 107007 (2008).

[73] W. K.Hofmann and W. Jeitschko, Monats. fuer Chem. **116**, 569 (1985).

[74] J. M. Hill, Ph.D. thesis, Iowa State University, Ames, Iowa (2002).

[75] Quantum Design Physical Property Measurement System User's manual (2000).

[76] J. S. Hwang, K. J. Lin, and C. Tien, Rev. Sci. Instrum. **68**, 94 (1997).

[77] E. Dachs and C. Bertoldi, Eur. J. Mineral. **17**, 251 (2005).

[78] J. C. Lashley, M. F. Hundley, A. Migliori, J. L. Sarrao, P. Pagliuso, T. W. Darling, M. Jaime, J. C. Cooley, W. L. Hults, L. Morales, et al., Cryogenics **43**, 369 (2003).

[79] Alfa Aesar, 30 Bond Street, Ward Hill, MA 01835.

[80] D. L. Martin, Rev. Sci. Instrum. **58**, 639 (1986).

[81] D. L. Martin, Rev. Sci. Instrum. **8**, 5537 (1973).

[82] J. C. Holste, T. C. Cetas, and C. A. Swenson, Rev. Sci. Instrum. **43**, 670 (1972).

[83] PPMS Advanced heat capacity with Helium-3 application note from Quantum Design (2000).

[84] B. Reuter and Jascowski, Angew. Chem. **72**, 209 (1960).

[85] D. C. Johnston, Physica B **281-282**, 21 (2000).

[86] A. V. Mahajan, R. Sala, E. Lee, F. Borsa, S. Kondo, and D. C. Johnston, Phys. Rev. B **57**, 8890 (1998).

[87] A. Reisman and J. Mineo, J. Phys. Chem. **66**, 1181 (1962).

[88] R. Kohmüller and J. Martin, Bull. Soc. Chim. (France) **4**, 748 (1961).

[89] D. G. Wickham, J. Inorg. Nucl. Chem. **27**, 1939 (1965).

[90] A. Manthiram and J. B. Goodenough, Can. J. Phys. **65**, 1309 (1986).

[91] J. B. Goodenough, G. Dutta, and A. Manthiram, Phys. Rev. B **43**, 10170 (1961).

[92] D. W. Murphy, P. A. Christian, F. J. DiSalvo, and J. V. Waszczak, Inorg. Chem. **18**, 2800 (1979).

[93] E. Hoschek and W. Klemm, Z. Anorg. Allg. Chem. **242**, 63 (1939).

[94] G. Andersson, Acta Chem. Scand. **8**, 1599 (1954).

[95] F. Aebi, Helv. Chim. Acta **31**, 8 (1948).

[96] K. A. Wilhelmi and K. Waltersson, Acta Chem. Scand. **24**, 9 (1970).

[97] J. Tudo and G. Tridot, Compt. Rend. **261**, 2911 (1965).

[98] K. Kosuge, J. Phys. Chem. Solids **28**, 1613 (1966).

[99] S. Kachi and R. Roy, Second Quarterly Report on Crystal Chemistry Studies, Pennsylvania State University, 4 December (1965).

[100] International Centre for Crystal Data, 12 Campus Boulevard, Newton Square, Penssylvania 1907-3273 U. S. A. (www.icdd.com).

[101] Materials Data Inc., 1224 Concannon Blvd., Livermore, California 94550 (www.materialsdata.com).

[102] D. C. Johnston, J. Low Temp. Phys. **25**, 145 (1976).

[103] Cited in Ref.28 as B. F. Griffings (Private communication).

[104] W. Tian, M. F. Chisholm, P. G. Khalifah, R. Jin, B. C. Sales, S. E. Nagler, and D. Mandrus, Mater. Res. Bull. **39**, 1319 (2004).

[105] M. Onoda, T. Naka, and H. Nagasawa, J. Phys. Soc. Jpn. **60**, 2550 (1991).

[106] S. Das, X. Ma, X. Zong, A. Niazi, and D. C. Johnston, Phys. Rev. B **74**, 184417 (2006).

[107] H. Kaps, M. Brando, W. Trikl, N. Buttgen, A. Loidl, E.-W. Scheidt, M. Klemm, and S. Horn, J. Phys. Condens. Matter **13**, 8497 (2001).

[108] Galbraith Laboratories Inc., Knoxville, TN 37950-1610.

[109] R. H. Blessing, Acta Cryst. **A51**, 33 (1995).

[110] All software and sources of the scattering factors are contained in the SHELXTL (version 5.1) program library (G. Sheldrick, Bruker Analytical X-Ray Systems, Madison, WI). Further details of the crystal structure investigations may be obtained from Fachinformationszentrum Karlsruhe, 76344 Eggenstein-Leopoldshafen, Germany (fax: (+49)7247-808-666; e-mail: crysdata@fiz-karlsruhe.de, http://www.fiz-karlsruhe.de/ecid/Internet/en/DB/icsd/depot_anforderung.html) on quoting the deposition numbers CSD-418091 and CSD-418090.

[111] S. Das, X. Zong, A. Niazi, A. Ellern, J. Q. Yan, and D. C. JohnstonD, Phys. Rev. B **76**, 054418 (2007).

[112] A. Kreyssig, S. Chang, Y. Janssen, J. W. Kim, S. Nandi, J. Q. Yan, L. Tan, R. J. McQueeney, P. C. Canfield, and A. I. Goldman, Phys. Rev. B **76**, 054421 (2007).

[113] A. C. Larson and R. B. V. Dreele, General Structure Analysis System (GSAS), Los Alamos National Laboratory Report LAUR **86-748** (2000).

[114] T. Irifune, H. Naka, T. Sanehira, T. Inoue, and K. Funakoshi, Phys Chem Minerals **29**, 645 (2002).

[115] U. Schwingenschlögl and V. Eyert, Ann. Phys. (Leipzig) **13**, 745 (2004).

[116] D. C. Johnston, J. Low Temp. Phys. **255**, 145 (1977).

[117] A. Niazi, S. L. Budko, D. L. Schlagel, J. Q. Yan, T. A. Lagrasso, A. Kreyssig, S. Das, S. Nandi, A. I. Goldman, A. Honecker, et al., Phys. Rev. B **79**, 014432 (2009).

[118] O. Pieper, B. Lake, A. Daude-Aladine, M. Reehuis, K. Prokes, B. Klamke, K. Kiefer, J. Q. Yan, A. Niazi, D. C. Johnston, et al., Phys. Rev. B **79**, 180409(R) (2009).

[119] K. Kitayama, Bull. Chem. Soc. Jpn. **51**, 1358 (1978).

[120] A. Byström and A. M. Byström, Acta. Cryst. **3**, 146 (1950).

[121] C. C. Torardi, Mater. Res. Bull. **20**, 705 (1985).

[122] M. Isobe, S. Koishi, N. Kouno, J.-I, Yamaura, T. Yamauchi, H. Ueda, H. Gotou, T. Yagi, and Y. Ueda, J. Phys. Soc. Japan **75**, 073801 (2006).

[123] Z. Q. Mao, T. He, M. M. Rosario, K. D. Nelson, D. Okuno, B. Ueland, I. G. Deac, P. Schiffer, Y. Liu, and R. J. Cava, Phys. Rev. Lett. **90**, 186601 (2003).

[124] A. P. Holm, V. K. Pecharsky, K. A. G. Jr., R. Rink, and M. Jirmanus, Rev. Sci. Instrum. **75**, 1081 (2004).

[125] B. H. Toby, J. Appl. cryst. **34**, 210 (2001).

[126] I. D. Brown and R. D. Shannon, Acta Cryst. Sect. A **29**, 266 (1973).

[127] I. D. Brown and D. Altermatt, Acta Cryst. **B41**, 244 (1985).

[128] N. E. Brese and M. O'Keeffe, Acta Cryst. **B47**, 192 (1991).

[129] E. D. Jones, Phys. Rev. B **137**, A978 (1965).

[130] M. Takigawa, E. T. Ahrens, and Y. Ueda, Phys. Rev. Lett. **76**, 283 (1996).

[131] J. P. Pouget, D. S. Schreiber, H. Launois, D. Wohlleben, A. Casalot, and G. Villeneuve, J. Phys. Chem. Solids **33**, 1961 (1972).

[132] M. Hase, I. Terasaki, and K. Uchinokura, Phys. Rev. Lett. **70**, 3651 (1993).

[133] F. J. Morin, Phys. Rev. Lett. **3**, 34 (1959).

[134] J. P. Pouget, H. Launois, T. M. Rice, P. Dernier, A. Gossard, G. Villeneuve, and P. Hagenmuller, Phys. Rev. Lett. **10**, 1801 (1974).

[135] M. Isobe and Y. Ueda, J. Phys. Soc. Japan **71**, 1848 (2002).

[136] J. Zhou, G. Li, J. L. Luo, Y. C. Ma, D. Wu, B. P. Zhu, Z. Tang, J. Shi, and N. L. Wang, Phys. Rev. B **74**, 245102 (2006).

[137] J. B. Goodenough, J. Solid State Chem. **3**, 490 (1971).

[138] A. Puwanto, R. A. Robinson, and H. Nakotte, J. Appl. Phys. **79**, 6411 (1996).

[139] J. Kitagawa and M. Ishikawa, J. Phys. Soc. Japan **68**, 2380 (1999).

[140] Y. Singh, Y. Lee, B. N. Harmon, and D. C. Johnston, Phys. Rev. B **79**, 220401(R) (2009).

[141] Y. Singh, Y. L. S. Nandi, A. Kreyssig, A. Ellern, S. Das, R. Nath, B. N. Harmon, A. I. Goldman, and D. C. Johnston, Phys. Rev. B **78**, 104512 (2008).

[142] T. Terashima, M. Kimata, H. Satsukawa, A. Harada, K. Hazama, S. Uji, H. S. Suzuki, T. Matsumoto, and K. Murata, J. Phys. Soc. Japan **78**, 083701 (2008).

[143] E. D. Mun, S. L. Bud'ko, N. Ni, A. N. Thaler, and P. C. Canfield, Phys. Rev. B **80**, 054517 (2009).

[144] D. C. Johnston, R. K. Kremer, M. Troyer, X. Wang, A. Klümper, S. L. Bud'ko, A. F. Panchula, and P. C. Canfield, Phys. Rev. B **61**, 9558 (2000).

[145] E. Dagotto and T. M. Rice, Science **271**, 618 (2001).

[146] T. Hikihara, M. Kaburagi, H. Kawamura, and T. Tonegawa, J. Phys. Soc. Jpn. **69**, 259 (2000).

[147] T. Hikihara, M. Kaburagi, H. Kawamura, and T. Tonegawa, Phys. Rev. B **63**, 174430 (2001).

[148] H.-J. Mikeska and A. K. Kolezhuk, Lect. Notes Phys. **645** p. 1 (Springer-Verlag, Berlin, 2004).

[149] J. Villain, Ann. Israel Phys. Soc. **2**, 565 (1977).

[150] X. Zong, B. J. Suh, A. Niazi, J. Q. Yan, D. L. Schlagel, T. A. Lograsso, and D. C. Johnston, Phys. Rev. B **77**, 014412 (2008).

[151] O. Pieper, B. Lake, A. Daude-Aladine, M. Reehuis, K. Prokes, B. Klamke, K. Kiefer, J. Q. Yan, A. Niazi, D. C. Johnston, et al., Phys. Rev. B **79**, 180409(R) (2009).

[152] J. Q. Yan, M. Reehuis, O. Pieper, B. Lake, A. Daoud-Aladine, Y. Mudryk, V. Pecharsky, Y. Ren, J. Fieramosca, A. Kreyssig, et al.

[153] O. Pieper, B. Lake, M. Enderle, T. G. Perring, A. Daoud-Aladine, J. Q. Yan, A. Niazi, and D. C. Johnston.

[154] Crystals were grown in the Materials Preparation Center, Ames Laboratory-USDOE, Ames, IA, USA. See www.mpc.ameslab.gov.

[155] Rietveld analysis program DBWS-9807a release 27.02.99, ©1998 by R. A. Young, an upgrade of "DBWS-9411 - an upgrade of the DBWS programs for Rietveld Refinement with PC and mainframe computers, R. A. Young, J. Appl. Cryst. **28**, 366 (1995)".

[156] A. Kreyssig, S. Chang, Y. Janssen, J. W. Kim, S. Nandi, J. Q. Yan, L. Tan, R. J. McQueeney, P. C. Canfield, and A. I. Goldman, Phys. Rev. B **76**, 054421 (2007).

[157] D. B. McWhan and J. P. Remeika, Phys. Rev. B **2**, 3734 (1970).

[158] J. M. Honig and L. L. V. Zandt (1975).

[159] H. V. Keer, D. L. Dickerson, H. Kuwamoto, H. L. C. Barros, and J. M. Honig, J. Solid State Chem. **5**, 225 (1975).

[160] W. Bao, C. Broholm, G. Aeppli, S. A. Carter, P. Dai, T. F. Rosenbaum, J. M. Honig, P. Metcalf, and S. F. Trevino, Phys. Rev. B **58**, 12727 (1998).

[161] S. Yonezawa, Y. Muraoka, Y. Ueda, and Z. Hiroi, Solid State Commun. **129**, 245 (2004).

[162] L. L. Miller, Rev. Sci. Instrum. **67**, 3201 (1996).

[163] P. Stamenov and J. M. D. Coey, Rev. Sci. Instrum. **77**, 015106 (2006).

[164] J. R.Carter and R. S. Feigelson, J. Am. Ceram. Soc. **47**, 141 (1964).

[165] J. S. Smart, *Effective Field Theories of Magnetism* (W. B. Saunders Company, Philadelphia, 1966).

[166] G. M. Schmiedeshoff, A. W. Lounsbury, D. J. Luna, S. J. Tracy, A. J. Schramm, S. W. Tozer, V. F. Correa, S. T. Hannahs, T. P. Murphy, E. C. Palm, et al., Rev. Sci. Instrum. **77**, 123907 (2006).

[167] R. M. Moon, Phys. Rev. Lett. **25**, 527 (1970).

[168] A. Menth and J. P. Remeika, Phys. Rev. B **2**, 3756 (1970).

[169] S. A. Shivashankar and J. M. Honig, Phys. Rev. B **28**, 5695 (1983).

[170] S. A. Carter, T. F. Rosenbaum, M. Lu, H. M. Jaeger, P. Metcalf, J. M. Honig, and J. Spalek, Phys. Rev. B **49**, 7898 (1994).

[171] M. Troyer, B. Ammon and E. Heeb, Lecture Notes in Computer Science **1505**, 191 (1998); A. F. Albuquerque, F. Alet, P. Corboz, P. Dayal, A. Feiguin, S. Fuchs, L. Gamper, E. Gull, S. Gürtler, A. Honecker, R. Igarashi, M. Körner, A. Kozhevnikov, A. Läuchli, S. R. Manmana, M. Matsumoto, I. P. McCulloch, F. Michel, R. M. Noack, G. Pawłowski, L. Pollet, T. Pruschke, U. Schollwöck, S. Todo, S. Trebst, M. Troyer, P. Werner, and S. Wessel, *The ALPS Project Release 1.3: Open Source Software for Strongly Correlated Systems*, J. Magn. Magn. Mater. **310**, 1187 (2007); F. Alet, S. Wessel, and M. Troyer, Phys. Rev. E **71**, 036706 (2005); see also http://alps.comp-phys.org.

[172] O. F. Syljuåsen and A. W. Sandvik, Phys. Rev. E **66**, 046701 (2002).

[173] A. Kolezhuk, R. Roth, and U. Schollwock, Phys. Rev. Lett. **77**, 5142 (1997).

[174] F. D. M. Haldane, Phys. Rev. Lett. **50**, 1153 (1983).

[175] T. Xiang, Phys. Rev. B **58**, 9142 (1998).

[176] A. E. Feiguin and S. R. White, Phys. Rev. B **72**, 220401(R) (2005).

[177] L. J. de Jongh and A. R. Miedema, Adv. Phys. **50**, 947 (2001).

[178] B. Pedrini, J. L. Gavilano, D. Rau, H. R. Ott, S. M. Kazakov, J. Karpinski, and S. Wessel, Phys. Rev. B **70**, 024421 (2004).

[179] L. Shields, J. Chem. Soc. (A) p. 303 (1970).

[180] J. Ashkin and N. S. Vanderven, Physica B+C **95**, 1 (1978).

[181] F. Kubec and Z. Sroubek, J. Chem Phys. **57**, 1660 (1972).

[182] A. E. Feiguin, private communication (2008).

[183] O. Golinelli, T. Jolicœur, and R. Lacaze, Phys. Rev. B **50**, 3037 (1994).

[184] S. R. White and D. A. Huse, Phys. Rev. B **48**, 3844 (1993).

[185] B. Pedrini, S. Wessel, J. L. Gavilano, H. R. Ott, S. M. Kazakov, and J. Karpinski, Eur. Phys. J. B **55**, 219 (2007).

[186] D. C. Johnston, T. Saito, M. Azuma, T. Y. M. Takano, and Y. Ueda, Phys. Rev. B **64**, 134403 (2001).